

UNIVERSITE DE NANTES

ÉCOLE DOCTORALE

SCIENCES ET TECHNOLOGIES
DE L'INFORMATION ET DES MATERIAUX
Année : 2006

Thèse de Doctorat de l'Université de Nantes

Spécialité : SCIENCES DES MATERIAUX

Présentée et soutenue publiquement par

Ludovic Godet

Le 07 juillet 2006

à Nantes

TITRE

Development of pulsed plasma doping system for semiconductor processing: characterization of the plasma and its interaction with the materials.

Jury

Président : Guy Turban.....IMN, Université de Nantes, Nantes, France

Rapporteurs : Ch. Hollenstein Ecole Polytechnique Fédérale de Lausanne, Switzerland
J.-M. Layet Laboratoire PIIM, Université de Provence, Marseille, France

Examineurs : D. Lenoble STmicroelectronics, Crolles, France
J. Scheuer Varian Semiconductor Equipment Associates, Gloucester, MA, USA
S. Radovanov Varian Semiconductor Equipment Associates, Gloucester, MA, USA
C. Cardinaud IMN, Université de Nantes, Nantes, France
G. Cartry IMN, Université de Nantes, Nantes, France

Directeur de Thèse : Christophe Cardinaud

Laboratoire : IMN

Co-encadrant : Gilles Cartry

Laboratoire : IMN

Composante de rattachement du directeur de thèse :

N° ED 366-277

L. Godet

Acknowledgments

Acknowledgement is gratefully made to Varian Semiconductor Equipment Associates, Inc. for sponsoring my doctoral research. Special thanks to Jay Scheuer, my advisor at VSEA who gave me judicious advice when needed and helped me to untangle tricky situations. I would also like to warmly thank my second VSEA advisor Svetlana Radovanov for our long discussions about plasma, for her support and help during all those years.

I would like to thank my dissertation advisors Christophe Cardinaud and Gilles Cartry for their expert advice and long scientific discussions that were of great help for my research work. Many thanks also for their good company during their stays in the US.

I gratefully thank all the persons from VSEA who helped me and more particularly Ziwei Fang, John Koo and Steve Walther for their valuable advice and scientific discussions. Particular thanks are due to Harold Persing for our discussion about negative ions, Tim Miller for his helpful advice, James Buff and Rajesh Dorai for their help with plasma and electrostatic simulations, George Unger for his help with the PLAD power supplies, Leo Klos as well as all the technicians who were always of great help.

I would also like to gratefully acknowledge ST for offering me the opportunity to work with them while in France. Special thanks to André Grouillet, Damien Lenoble, Stéphane Courault, Jean-Philippe Reynard and Yannick Rault for having shared a few years of the history of PLAD with me.

I would also like to express my gratitude to my first supervisors: Serge Campion and David Hacker for their valuable advice. I would like to show my gratitude to Thierry Josselin, Yuri Erokhin, Bob Simmons, Olivier Joubert and Nader Sadeghi for their encouragements and support.

I'm also grateful to the jury members, i.e. Ch. Hollenstein, J.-M. Layet and the President of the jury, Guy Turban, whose comments and analyses are of great value to me.

Finally, I would like to thank the University of Nantes and more particularly the Institut des Matériaux de Nantes (IMN) for having given me the opportunity to work with them during those doctoral years.

Many thanks to all my friends and PhD fellows: Fabrice Lallement, Vanessa Raballand and Elise Lafosse.

Contents

Abbreviations	13
Symbols	15
Physical Constants and Conversion Factors.....	18
General introduction, goals and motivations.....	19
Chapter I Semiconductor device and ultra-shallow junction requirements for ion implantation technology	23
I.1 MOS transistor	24
I.1.1 Principle of operation.....	24
I.1.1.1 Low-inversion mode.....	25
I.1.1.2 High inversion mode	25
I.1.2 Short Channel Effect (SCE) and Drain-Induced Barrier Lowering (DIBL)	26
I.1.3 Optimization of the transistor's performance	27
I.1.3.1 Control of Short Channel Effect.....	27
I.1.3.2 Reduction of in-series resistance	28
I.2 Ion implantation technology.....	30
I.2.1 Ion implantation for CMOS technology	30
I.2.2 Ion implantation system.....	31
I.2.2.1 Crystal damage after ion implantation	33
I.2.2.2 Ion distribution after ion implantation.....	33
I.2.2.3 Channelling effect	35
I.2.2.4 Dopant activation after implantation.....	36

I.3	Ultra Shallow Junction	38
I.3.1	Requirements	38
I.3.2	Low-energy ion implantation.....	39
I.3.2.1	Molecular ion implantation	40
I.3.2.2	Deceleration mode.....	41
I.3.2.3	Plasma-Based implantation	42
 Chapter II PLAsma Doping System		 44
II.1	Brief historical background of PLAD	45
II.2	Description of the technique.....	48
II.2.1	Principle of operation.....	48
II.2.2	Pulsed DC Glow Discharge (GD).....	49
II.2.2.1	Plasma Ignition.....	49
II.2.2.2	Very low energies PLAD implantation	50
	a) Hollow cathode mode	50
	b) Pulsed anode mode	52
II.2.2.3	Characteristics of a dc glow discharge	53
II.2.2.4	Cathode bias characteristics	54
	a) Cathode voltage	54
	b) Power supply overshoot.....	55
	c) Cathode current.....	55
	d) Secondary electron current	56
	e) Displacement current	57
II.3	General presentation of the equipment.....	58
II.3.1	Vacuum system and pressure control	59
II.3.2	Gas in-used and applications	61
II.3.2.1	Boron Trifluoride (BF ₃).....	61
II.3.2.2	Arsenic Pentafluoride (AsF ₅)	62
II.3.2.3	Rare gases.....	63

II.3.2.4	Oxygen (O ₂)	63
II.3.3	Process chamber.....	64
II.3.3.1	Dose control	65
II.4	PLAD performance and process repeatability.....	66
II.5	Different applications of PLAD	69
II.5.1	Ultra-Shallow junction.....	69
II.5.2	Imaging applications.....	71
II.5.3	Conformal doping	72

Chapter III Plasma diagnostics and surface characterization 74

III.1	Mass spectrometry.....	75
III.1.1	Brief history of mass spectrometry	75
III.1.2	Electrostatic Quadrupole Probe (EQP)	76
III.1.2.1	Extraction optics.....	77
III.1.2.2	Ionization source	78
III.1.2.3	Deceleration stage	80
III.1.2.4	Energy analyzer.....	81
III.1.2.5	Quadrupole mass filter	82
III.1.2.6	Detector	85
III.1.3	Time-resolved mass energy spectrometry	86
III.1.4	Transit time	87
III.1.5	Mass spectrometer considerations and experimental set-up.....	89
III.1.5.1	Mass spectrometry goal and motivations for this study.....	89
III.1.5.2	Modification of the optics voltage set-up.....	90
III.1.5.3	Mass spectrometer transmission and angular acceptance	94
III.1.5.4	Experimental study of the mass spectrometer transmission.....	95
III.1.5.5	Bulk plasma study: mass spectrometer inside the anode	102
III.1.5.6	Study of ions traversing the sheath: mass spectrometer inside the cathode.....	105

III.1.6	Mass spectrometry measurement in a pulsed DC plasma.....	109
III.1.6.1	Mass distribution concerns	109
III.1.6.2	Measurement of IED:	110
a)	Bulk plasma: Energy scan.....	111
b)	Ions accelerated by the high-voltage sheath: Reference scan.....	112
III.1.6.3	Ions accelerated across the sheath during time-resolved measurements	114
a)	Ions across the sheath: What can be learned from the rise and fall times of the pulse	114
b)	Mass spectrometer calibration and transit time concern.....	116
c)	Validation of the energetic ion measurements.....	118
III.2	Langmuir probe	120
III.2.1	Principle	120
III.2.2	Experimental settings.....	121
III.2.3	Extraction of the plasma parameters.....	123
III.2.3.1	Electron energy distribution function.....	125
III.2.3.2	Fast electron	126
III.3	Characterization method used	128
III.3.1	Secondary Ion Mass Spectrometry (SIMS)	128
III.3.2	Sheet-resistance measurement with four-point probe.....	130
 Chapter IV Plasma doping of silicon with BF₃ chemistry		134
IV.1	Electron Kinetics in BF ₃ plasma	135
IV.1.1	BF ₃ cross sections	136
IV.1.2	Electron-impact dissociation measurements.....	138
IV.1.3	Time evolution of the electron temperature and density in the pulsed discharge	140
IV.1.3.1	Electron energy distribution function measurements.....	143
IV.1.3.2	Time evolution of the radial distribution of the plasma density.....	144

IV.1.4	Concluding remarks	145
IV.2	Ion behavior.....	146
IV.2.1	Time evolution of the ion density in the pulsed discharge	146
IV.2.2	Description of the high-voltage sheath	149
IV.2.2.1	Matrix sheath.....	150
IV.2.2.2	Collision-less sheath.....	151
IV.2.2.3	Collisional sheath	153
IV.2.3	Ion processes inside a collisional sheath.....	154
IV.2.3.1	Elastic scattering.....	155
IV.2.3.2	Charge transfer	155
IV.2.3.3	Ion dissociation.....	156
IV.2.3.4	Ionization inside the sheath by secondary electrons	156
a)	Discussion on ion angular dispersion in a collisional sheath.....	157
IV.2.4	Davis and Vanderslice model	157
IV.2.5	Ion energy distribution in BF_3 plasma	161
IV.2.5.1	Overview	162
a)	Boron containing ions in the bulk plasma.....	162
b)	Boron containing ions in the plasma sheath	163
c)	Ion energy distribution in collision-less sheath and transition to collisional sheath	164
d)	Ion energy distribution for collisional sheath	171
e)	Parameter driving the shape of ion energy distribution shapes	173
IV.2.5.2	Ion energy distributions discussion	176
a)	Observations and comments	176
b)	B^+ ion energy distribution.....	177
c)	BF^+ ion energy distribution.....	182
d)	BF_2^+ ion energy distribution	185
e)	BF_3^+ ion energy distribution	190
f)	Heavy ions	191
IV.2.5.3	Role of negative Ion:	194
IV.2.5.4	Concluding remarks	196

Chapter V	Understanding, control and optimization of the process	198
V.1	PLAD process control	199
V.1.1	Chamber conditioning.....	199
V.1.1.1	Observation	199
V.1.1.2	Description of the experiments.....	200
V.1.1.3	Conditioning test results	201
V.1.1.4	Conditioning optimization.....	211
V.1.2	Plasma and R_s uniformity	211
V.1.3	Plasma etching	215
V.1.4	Conclusion	217
V.2	Depth profile simulation.....	218
V.2.1	Principle	218
V.2.2	Results and comparison	222
V.2.3	Validation.....	224
V.2.3.1	Mass transmission inside the mass spectrometer	224
V.2.3.2	Higher implantation energy.....	225
V.2.3.3	Collisional and collision-less sheath	226
V.2.4	Dopant profile prediction: Conclusion.....	227
V.3	Control of the dopant depth profile	229
V.3.1	Cathode voltage	229
V.3.1.1	Diode configuration: without hollow cathode.....	229
V.3.1.2	Triode configuration: hollow cathode mode	232
V.3.2	High pressure to increase the number of collisions	234
V.3.3	Reduction in the number of collisions	241
V.3.3.1	Hollow cathode mode.....	241
a)	Anode-to-cathode spacing and process implications	242
b)	Hollow cathode voltage	251

V.3.3.2	Pulsed anode configuration	255
V.3.4	Optimum conditions and conclusions	258
Chapter VI Conclusion		259
Reference	262
List of Figures	277
List of Tables	294
Appendix 1a: Mass spectrometer old configuration.....		295
Appendix 1b: Mass spectrometer new configuration.....		296
Appendix 2: PLAD chamber diagnostic.....		297
Appendix 3: Electron temperature calculation		298
Appendix 4: EEDF and EEPF calculation.....		299
Appendix 5: IED for different HC voltage 20mTorr with 500 V cathode bias		301
Appendix 6: Pulsed anode voltage variation		303
Appendix 7: 1kV no HC Frequency Variation.....		304

Abbreviations

a.u.	Arbitrary unit
AsF ₅	Arsenic Pentafluoride
amu	Atomic mass unit
BF ₃	Boron Trifluoride
CMOS	Complementary Metal-Oxide-Semiconductor
dc	Direct current
DIBL	Drain induced Barrier Lowering
EC	Energy Contamination
EEDF	Electron Energy Distribution Function
EEPF	Electron Energy Probability Function
EQP	Electrostatic Quadrupole Probe
ESA	Electrostatic Sector Analyzer
eV	Electronvolt
GD	Glow Discharge
HC	Hollow Cathode
IED	Ion energy Distribution
ITRS	International Technology Roadmap for Semiconductors
JAP	Journal of Applied Physics
JVST	Journal of Vacuum Science and Technology
KeV	Kiloelectronvolt
MeV	Megaelectronvolt
NRA	Nuclear Reaction Analysis
OES	Optical Emission Spectrometry
PAI	Pre-Amorphized Implantation
PIII	Plasma Immersion Ion Implantation
PLAD	PLAsma Doping
ppm	Particle per million
QMS	Quadrupole Mass Spectrometer

RBS	Rutherford Backscattering Spectrometry
RIE	Reactive Ion Etching
RGA	Residual Gas Analysis
RTP	Rapid Thermal Process
SCE	Short Channel Effect
SD	Source/Drain
SDE	Source/Drain Extension
SEM	Scanning Electron Microscopy
Si	Silicon
SIMS	Secondary Ion Mass Spectrometry
SOI	Silicon On Insulator
SPE	Solid Phase Epitaxy
SRIM	Stopping Range of Ions in Matter
STI	Shallow Trench Isolation
TRIM	Transport and Range of Ions in Matter
TTL	Transistor Transistor Logic
ULE	Ultra-Low Energy
USJ	Ultra- Shallow Junction
VCS	Varian System Control
VSEA	Varian Semiconductor Equipment Associates

Symbols

μ	Charge carrier mobility
θ	Sector angle of the electrostatic energy analyzer
σ	cross section
τ	Transit time inside the mass spectrometer
τ_{det}	Transit time inside the detector section
ΔE	Mass spectrometer energy resolution
τ_{ena}	Transit time inside the energy analyzer section
τ_{ext}	Transit time inside the extraction section
τ_{mass}	Transit time inside the mass filter section
a_c	Cathode area
A	Mass spectrometer entrance aperture area
A_p	physical collecting area of the Langmuir probe
A_E	Activation efficiency
C_{ox}	Gate oxide capacitance
d	Inter-electrode distance
e	Elementary charge
ε	Energy
$\langle \varepsilon_e \rangle$	Average electron energy
ε_e	Electron energy
ε_0	Permittivity of free space
E_t	Transmission energy
E_z	Ion energy in the z direction of the quadrupole
γ	Secondary Electron Emission Coefficient
I	Current
I_c	Cathode current
I_D	Drain current
I_{disp}	Displacement current

I_e	Electron current
I_{Faraday}	Faraday current
I_{ions}	Ion Current
I_{on}	Saturation current
I_{off}	Leakage current
I_{sec}	Secondary Electron Current
I_{th}	Current threshold
j_i	ion implantation current density
K	Boltzmann's constant
L	Gate Length
L_q	Length of the quadrupole
K_1	Mass conversion factor (cold cathode gauge)
K	Transmission coefficient at the entrance aperture of the mass spectrometer
k	Boltzmann constant
L_{ext}	Extension length
M	Mass of any ion
m_e	Electron mass
n_e	Electron density
n_i	Ion density
N_j	Active dopant concentration
P	Discharge Pressure
p	Neutral-gas pressure
P_{PLAD}	PLAD process chamber pressure
P_s	Pressure inside the mass spectrometer
Q_{PLAD}	Gas flow into the PLAD process chamber
Q_s	Gas flow into the mass spectrometer
R_{contact}	Contact resistance
$R_{\text{extension}}$	Source drain extension resistance
R_j	Extension layer resistance
R_{layer}	Layer resistance
R_s	Sheet-resistance of the thin doped layer

R_s^{total}	Total sheet resistance calculated
$R_{S/D}$	Source/drain resistance
R_{series}	In series resistance
S	Solubility
S_{PLAD}	Pumping speed into the PLAD process chamber
S_s	Mass spectrometer pumping speed
s	Sheath Thickness
T_e	Electron Temperature
T_{eff}	Effective electron temperature
T_g	Gas Temperature
u_B	Bohm Speed
V	Voltage
V_0	Cathode Voltage
V_b	Bias voltage
V_{bd}	Cathode voltage
V_D	Drain Voltage
V_f	Floating potential
V_G	Gate voltage
V_p	Plasma potential
V_{te}	Transit-energy voltage at the entrance and exit of the quadrupole
V_{th}	Threshold voltage
W	Gate Width
X_j	Junction depth
Z	Relative charge on an ion, in unit of e

Physical Constants and Conversion Factors

<u>Quantity</u>	<u>Symbol</u>	<u>Value</u>
Avogadro number (molecules/mol)	N_A	6.0220×10^{23}
Atomic mass unit (amu)	amu	$1.6606 \times 10^{-27} \text{ kg}$
Boltzmann constant	k	$1.3807 \times 10^{-23} \text{ J / K}$
Elementary charge	e	$1.6022 \times 10^{-19} \text{ C}$
Electron mass	m_e	$9.1095 \times 10^{-31} \text{ kg}$
Proton mass	M_i	$1.6726 \times 10^{-27} \text{ kg}$
Permittivity of free space	ϵ_0	$8.8542 \times 10^{-12} \text{ F / m}$
Standard temperature (25°)	T_0	298.5 K
Standard pressure	p^o	$1.0133 \times 10^5 \text{ Pa}$

Conversion factors of units

Length	1 m = 39.4 in. = 3.28 ft
	1 ft = 12 in. = 30.48 cm
	1 in. = 2.54 cm
Volume	1 U. S. gallon = 3.785 l
Weight	1 ounce (oz) = 28.35 g
	1 pound (lb) = 16 oz = 0.454 kg
Energy and temperature	1 eV = 11605K = $1.6022 \times 10^{-19} \text{ J}$
	$^{\circ}\text{C} \rightarrow \text{K}: ^{\circ}\text{C} + 273.15 = \text{K}$
	$^{\circ}\text{F} \rightarrow ^{\circ}\text{C}: (^{\circ}\text{F} - 32) \times \frac{5}{9} = ^{\circ}\text{C}$
Pressure	1 Torr = 1 mmHg = 133.32 Pa
	1 atm = 760 Torr = 1.0133 bars
	1 psi = 704 Pa = 5.3 Torr

General introduction, goals and motivations

In the past three decades, the speed and packing density of integrated circuits have dramatically increased following Moore's law, which predicts that the number of transistors is multiplied by four every three years. The semiconductor device dimensions continue to shrink in order to implement more transistors on the same microelectronic chip area, and to produce more powerful and cheaper electronic systems. All the transistor dimensions, such as the gate, the gate oxide and the source drain extensions need to be reduced at the same time. This brings many technological challenges and constraints for each new device node. For example, in order to reach the new doping requirements for the source drain extension, the ion implantation energy needs to be further reduced with a higher dopant concentration. The physical limitations (space charge during beam transport) of the traditional beamline approach are reached, and new beamline techniques such as ion implantation with a deceleration mode, are being developed. Unfortunately, this method suffers from energy contamination for very low-energy implantation, causing deeper junction depth than expected. Plasma-based ion implantation is emerging as a viable technique that can meet the doping requirements of future device nodes if associated with an adequate dopant activation technique. In particular, pulsed PLASMA Doping (PLAD) offers the capability of operating at very low energies for a lower cost and at a higher ion flux than with the traditional beamline ion implantation. With the PLAD technique, the silicon wafer is directly immersed in the plasma. The ions present in the bulk plasma are extracted through the high voltage applied on the cathode and are implanted into the wafer with the desired energy. The pulsed nature of the plasma minimizes the etching of the silicon substrate.

One of the features that made ion implantation so successful in semiconductor fabrication is the high degree of control and repeatability of the dopant depth profile. By selecting a unique ion mass, ion charge, ion energy and implant angle, an ideal beamline tool offers a high degree of control over the dopant depth profile. Real-world implementations of beamline technology maintain a high degree of repeatability, but often introduce compromises, such as energetic contamination, which takes place when

decelerating the beam, or angle spread, which is due to lack of angle correction after mass resolution. As a competing technology, plasma-based implantation must feature a comparable level of control and repeatability, despite using a mixture of ion species and a variety of ion energies. To compete with traditional mass-resolving beamline systems, a plasma implant must produce the same ion composition from day to day and across the wafer. Additionally, the implanted ion energy distribution, which is a function of the acceleration of ions across the plasma sheath and any collision effects within the sheath, must be repeatable and tolerant of typical process fluctuations.

In traditional beamline implantation, the incident ion mass and energy are well-known parameters, and simulation programs are available to predict the implant profiles. In plasma-based ion implantation, all ionized species present in the plasma are extracted and implanted by applying negative voltage pulses to the wafer. Therefore, the prediction of implant profiles is more complicated since it requires the knowledge of each ion relative abundances, as well as their energy distributions, prior to entering the wafer surface. This information is not readily available when using conventional plasma characterization techniques, because most of them measure plasma bulk properties. One of the thesis goals is to develop an in-situ technique to measure the energy distribution of the different dopant ions reaching the silicon wafer after their acceleration inside the high-voltage sheath. Another goal is to predict the dopant depth profile according to these measurements.

The research presented here sets out to provide the practical and theoretical underpinnings upon which the technique of plasma doping can be built. The research scope was designed mainly for silicon technology. It includes the use of p-type dopants that are derived from boron tri-fluoride [BF₃ (g)] plasma. The scientific objective was to characterize in detail the plasma phase and how the plasma interacts with the semiconductor material. The main part of the work consists of studying the plasma composition by using a mass spectrometry diagnostic. Langmuir probe measurements are used to determine plasma parameters, such as electron energy distribution and plasma potential. The characterization of pulsed plasmas has led to the modification of the

existing system and has required the development of time-resolved measurements. One particularly important feature was the installation of the mass spectrometer set-up within the pulse-powered electrode. The identification and the quantification of the various plasma charged species, as well as the ion energy distribution measurements, give information on the mechanisms of interaction with the material. The research aims is to provide a better understanding of the key parameters that control the nature, the concentration and the depth distribution of the implanted species. These results provide the necessary information to achieve the industrial objective of developing the PLAD process and a pre-industrial product. With a better understanding of the collision processes that occur inside the high-voltage sheath, the doping process can be optimized. Based on the ion energy distributions measured with the mass spectrometer, the dopant depth profile can be predicted and the plasma parameters can be tuned in order to obtain shallower dopant depth distribution in the silicon after plasma doping implantation.

The goal of the first chapter is to give the basics of CMOS and ion implantation technologies, which are needed to understand the key challenges of low-energy implantation. This chapter also addresses the actual beamline limitations, the solutions used by the conventional ion implantation technology and the need for new techniques, such as the plasma-based ion implantation system, to meet the requirements of the next generation of semiconductor devices.

The second chapter discusses the plasma-doping technology in detail. It gives first the history of plasma-based ion implantation and explains the principle of plasma doping. The VSEA equipment used for plasma doping is also presented. Finally, the PLAD performance and its different applications are reviewed and discussed.

Chapter three describes the main plasma diagnostics used during this research. The mass spectrometry is described in detail starting with a small history, then reviewing the different part of the mass spectrometer and finally presenting the mass spectrometer set-up and the mode of operation. The Langmuir probe is also quickly introduced. The different post implantation surface characterizations used such as secondary ion mass spectrometry are also briefly explained.

The characterization of the plasma-doping system in a BF₃ plasma, including the electron and ion kinetics, the description of different collision processes occurring inside

the high-voltage sheath and a detail description of the energy distributions of ions reaching the cathode, is presented in chapter four.

The understanding, control and optimization of the process are introduced in chapter five. The PLAD conditioning step is described in details. A model, based on ion energy distribution measurements, allowing for the prediction of the dopant depth profile is presented and validated by comparison to SIMS measurements. Finally, a review of the method to obtain shallower junctions is also presented.

Chapter I Semiconductor device and ultra-shallow junction requirements for ion implantation technology

The goal of this chapter is to give the reader the basics of CMOS and ion implantation technology, which are needed to understand the key challenges of low-energy implantation. This chapter also addresses the actual beamline limitations, the solutions used by the conventional ion implantation technology and the need for new techniques, such as the plasma-based ion implantation system, to meet the requirements of the next generation of semiconductor devices.

I.1 MOS transistor

This part briefly describes the mode of operation of a Metal Oxide Semiconductor, or MOS, structure and particularly the influence of the source drain extensions on the MOS performance. More details can be found in [Sze 2002, Lenoble 2000]

Principle of operation

A MOS transistor is designed to perform the modulation of the electrical carriers' density in a semiconductor material using an electric field. This electric field is applied to the command electrode, also called the gate through an insulator (gate dielectric). The mobile carrier charges created by the electric field are electrons in the case of the N-MOS and holes in the case of the P-MOS. When the voltage applied is higher than a threshold voltage (V_{th}), a conduction channel is created by the carriers between the source and the drain.

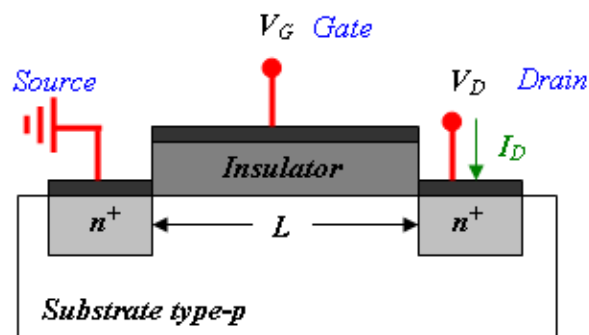


Figure 1: Schematic representation of a MOS Transistor type-N

In the case of a N-MOS (See Fig. 1), a positive voltage is applied between the gate and the substrate. The electric field, which will thus attract the electrons and repel the holes at the surface of the P-Type substrate, will create a superficial channel of N-type when $V_G > V_{th}$. When a potential is applied between the drain and the source, electrons will flow from the source to the drain (the corresponding current will flow from the drain to the source) through the conducting channel. The conductance of this channel can be

modulated by varying the gate voltage. The electrons are then collected by the drain when the transistor is in high inversion mode (transistor turned on). When the gate voltage is not high enough to create the inversion layer, the transistor is in low-inversion mode (transistor blocked). The MOS transistor is thus used to regulate a current between two electrodes through a control voltage (V_G).

Low-inversion mode

In the low-inversion mode, the drain current should ideally be null, even if a voltage is applied between the source and the drain ($V_D \neq 0$). Unfortunately, a leakage current I_{off} is often unavoidable [Skotnicki 1996]:

$$I_{off} = I_{th} \times \exp\left[\frac{-V_{th} \ln 10}{S}\right] \quad \{I.1\}$$

where I_{th} is the current at the voltage threshold and S corresponds to the gate voltage augmentation needed to increase the current of one decade. S needs to be as small as possible to minimize the leakage current which is dependant on the threshold voltage.

High inversion mode

When the concentration of the charge carrier on the surface channel becomes important (i.e. $V_G > V_{th}$), two different cases can be distinguished according to the value of V_D , which is used to modulate the channel resistivity.

- When $V_D < V_G - V_{th}$, the channel acts as a resistor and the drain current is proportional to the drain voltage. The transistor thus operates in a linear mode.
- When $V_D > V_G - V_{th}$, the drain current remains the same and the number of carriers arriving from the source, or the current flowing from the drain to the source, remain constant. This is the saturation region. The saturation current I_{on} is defined by the following equation:

$$I_{\text{on}} = \frac{1}{2} \mu C_{\text{ox}} \frac{W}{L} (V_G - V_{\text{th}})^2 \quad \{1.2\}$$

where C_{ox} is the gate oxide capacitance, μ is the electron's mobility (N-MOS) or hole's mobility (P-MOS) in the channel, W is the gate width and L is the gate length. V_G and V_{th} are defined for each technology node. In order to increase the I_{on} for a defined gate width, the carrier mobility needs to be improved, the channel length needs to be reduced and the C_{ox} need to be increased by reducing the gate oxide thickness,.

In short, the electrical performance of a MOS transistor is defined by the leakage current I_{off} and the saturation current I_{on} . In order to improve the transistor performance, the I_{off} needs to be maintained at an acceptable level and the I_{on} needs to be increased to its maximum. In the next two parts, we will explain the physical limitation of the transistor and look at how to optimize the transistor's performance.

Short Channel Effect (SCE) and Drain-Induced Barrier Lowering (DIBL)

Smaller device size enables higher device density in an integrated circuit. In addition, a smaller channel length improves the drive current and thus, the operation performance. The influence of the channel's side regions (i.e. source, drain, isolation edge) becomes significant as the device dimensions are reduced, leading to the Short Channel Effect (SCE).

When the channel side effect becomes non-negligible, the threshold voltage in the linear region usually becomes less positive as the channel length decreases for N-channel MOS. An increase of the V_D polarization produces an extension of the space charge area which contributes to a further reduction of the threshold voltage. This effect is known as the Drain-Induced Barrier Lowering (DIBL).

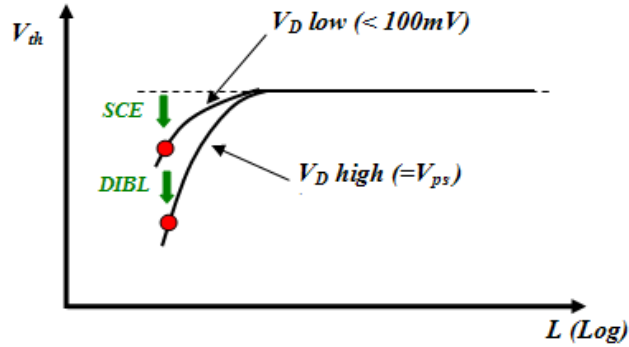


Figure 2: Evolution of V_{th} for different gate lengths as a function of the drain voltage

With the reduction of the gate length, these two effects become critical for the transistor's performance. They also reduce the threshold voltage, thereby creating a deterioration of the gate control for the carrier's density and mobility inside the channel. The SCE and DIBL are important limitations for the technology miniaturization as they reduce the V_{th} and increase the I_{off} .

Optimization of the transistor's performance

Control of Short Channel Effect

In order to control the short channel effect, the effective length L_{eff} of the channel needs to be maximized. The L_{eff} is limited by the lateral spread ΔL due to the lateral propagation of the dopant during ion implantation, along with the lateral diffusion of the dopant during activation (see Fig. 3). A compromise on ΔL is necessary. A spread that is too large is not acceptable for the device's performance but ΔL is necessary to maintain a good contact between the Source Drain Extensions (SDE) and the channel. Calculations relating to a 0° tilt implant have shown that the dependence of the junction depth (X_j) and ΔL is [Lenoble 2000]:

$$\Delta L = \rho \times X_j \quad \{I.3\}$$

where ρ is a scalar factor (dependant on the dopant atom, ρ is between 0.5 and 1).

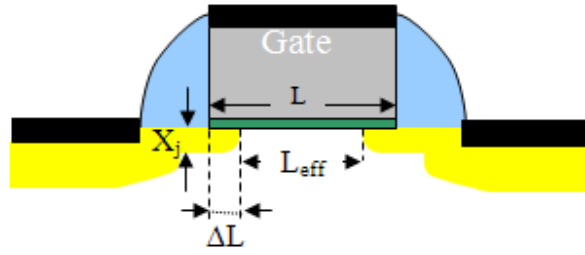


Figure 3: Schematic representation of the channel-effective length and the spread under the gate

In order to reduce the short channel effect, a reduced of the junction depth is necessary along with a controlled dopant diffusion during the anneal step. Enough diffusion of the dopant under the gate needs to be kept to maintain the contact between the SDE and the channel.

Reduction of in-series resistance

The minimization of the transistor's in-series resistance, R_{series} , is important to improve the device's performance [Lallement 2005]. The drain current flowing through the channel is directly impacted by the in-series resistance (see Fig. 4).

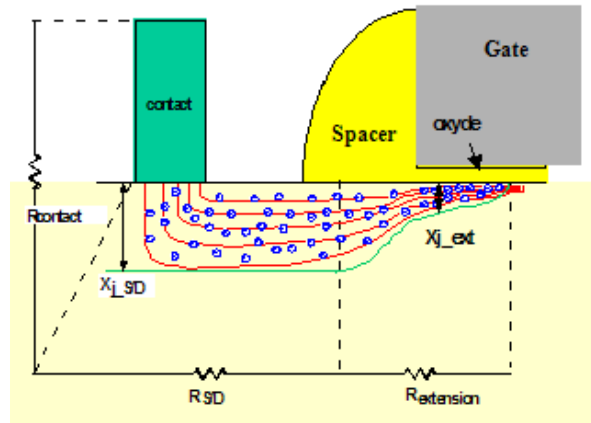


Figure 4: Representation of the in-series resistance's components [Lallement 2005]

The R_{series} needs to be minimized to increase the I_{on} in the saturation mode. The R_{series} is the sum of the contact resistance $R_{contact}$, the source/drain resistance $R_{S/D}$ and the SDE resistance $R_{extension}$:

$$R_{series} = R_{contact} + R_{S/D} + R_{extension} \quad \{I.4\}$$

The contact resistance R_{contact} comes from the contact between the silicide and the source/drain junction. R_{contact} depends on the quality of the silicon/silicide interface and the surface doping [Lenoble 2000]. Its value is around $10\Omega\cdot\mu\text{m}$.

The junction resistances $R_{\text{S/D}}$ and $R_{\text{extension}}$ are called layer resistance, R_{layer} . The source/drain area is less resistive (higher dose implanted) than the extension area. The $R_{\text{S/D}}$ is negligible compared to $R_{\text{extension}}$.

$$R_{\text{layer}} = R_{\text{S/D}} + R_{\text{extension}} \approx R_{\text{extension}} \quad \{\text{I.5}\}$$

$$R_{\text{extension}} = R_j \times L_{\text{ext}} \quad \{\text{I.6}\}$$

where R_j is the resistance of the extension layer and L_{ext} is the total length of the extension. In the case of uniform and very abrupt junctions, R_j is defined as:

$$R_j = \frac{1}{qN_j\mu X_j} \quad [\Omega\cdot\mu\text{m}] \quad \{\text{I.7}\}$$

where N_j is the active dopant concentration and X_j is the junction depth.

Reducing the in-series resistance of the transistor implies reducing either the extension length or the layer resistance of the source/drain extensions. As ΔL is already minimal to guarantee a good control of the short channel effect, L_{ext} is fixed. Only higher active dopant concentration of the SDE can thus give a higher I_{on} .

In order to reduce the junction's in-series resistance, the transistors need to have abrupt shallow junctions with a high dopant concentration.

I.2 Ion implantation technology

Ion implantation for CMOS technology

The ion implantation steps represent around twelve percent of the total number of process steps needed to build a microelectronic chip. Fig. 5 shows the different implanted zones of the MOS transistor in the front end of line.

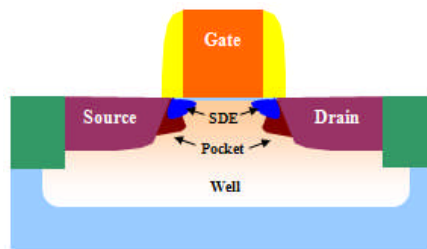


Figure 5: Schematic of the different zones implanted for a MOS transistor

The main transistor doping zones are the well, the source, the drain, the SDE, the pockets and the gate. In order to put the dopant where it is needed, each doping area requires a proper implantation species, energy, dose and angle control.

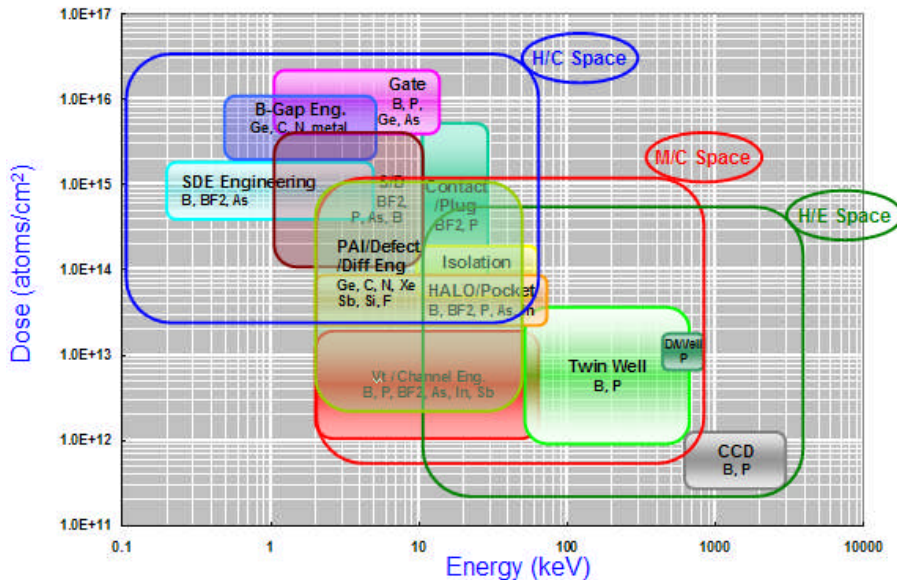


Figure 6: A map of application areas for high-current (H/C), medium-current (M/C) and high-energy (H/E) implanters as a function of dose and energy

Traditional implant applications cover a broad range of dose, energy and species, as illustrated in Fig. 6. Ion implantation technology provides the control required to ensure that the dopant atoms are implanted where they are needed.

Ion implantation system

Ion implantation is used to bombard a material with dopant ions at the desired energy and dose. An ion implanter is a collection of very sophisticated subsystems (see Fig. 7), each performing a specific action on the ions. The main subsystems include an ion source, an extracting and ion-analyzing section, an accelerating column, a scanning system and a target chamber.

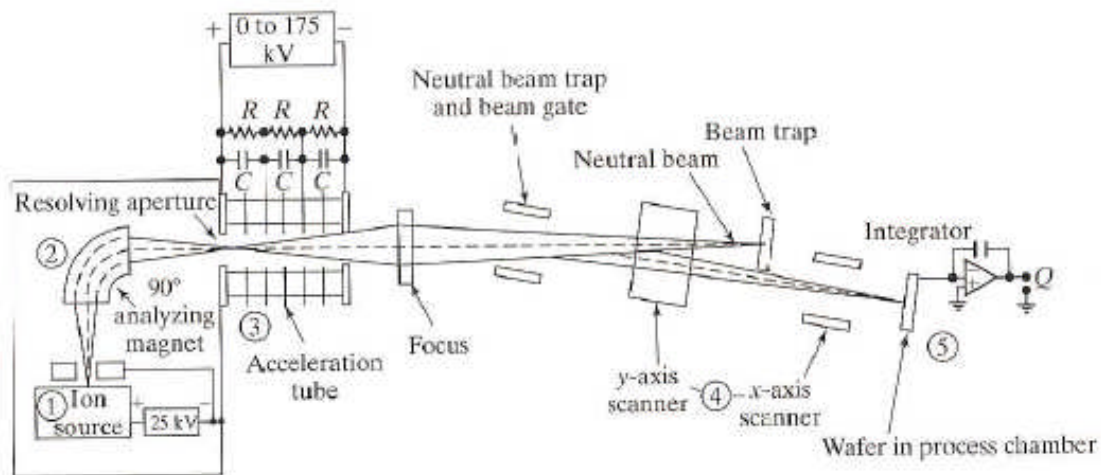


Figure 7: Schematic drawing of a typical ion implanter showing (1) the ion source, (2) the ion-analyzing mechanism, (3) the accelerating column, (4) the scanning system, (5) the target chamber [Jaeger 2002]

All the ions produced inside an ion source are extracted through an extraction system and then analyzed by mass through the ion-mass analyzing system. The magnetic field of the analyzer is set so that only ions with a desired mass-to-charge ratio can travel through it without being filtered. The selected ions enter the acceleration tube, where they are accelerated to the desired energy as they move from high voltage to ground. Apertures are used to ensure that the ion beam is well collimated. A good pressure is maintained inside the implanter to minimize ions scattering because of gas molecules. The ion beam is then scanned over the wafer surface using electrostatic deflection plates

and the ions are implanted into the semiconductor target. The main advantages of the ion implantation technology are:

- The implanted dopant distributions inside the substrate are controlled by the incident energy of the ion beam.
- The total dose of dopant inside the substrate is easily calculated by measuring the implantation current generated by the charge particle at the surface of the target. A precise dose from 10^{10} to 10^{16} atoms/cm² can be achieved.
- Ion implantation is performed at low temperatures (<85°C) and is compatible with the photoresist process. Low temperature processing prevents undesired diffusion.
- Ion implantation provides a minimal lateral diffusion of the dopant and assures the control of the implant angle.
- The substrate can be doped at a level above the solid solubility limit.
- Ion implanters can be used for a large number of different dopants (As, P, In, B, Ge...). In theory, any element that can be ionized can be introduced into the wafer through implantation.

Three different families of implanters are used to cover the full energy range of the implanted ions, from a few hundred electronvolts (eV) to a few Megaelectronvolts (MeV) (see Fig. 6).

- The high-current implanters are able to deliver high productivity for low-energy implant applications. They provide high dose doping for implant energies between 200eV to 60 keV and can achieve a current of up to 25 mA. The typical dose ranges from $1E13$ to $5E16$ dopant atoms per square centimeter, with a uniformity and repeatability below 1.5%. The principal applications of the high current implanter are gate doping, pocket doping, source/drain (SD) and source/drain extension doping (SDE).
- The medium-current implanters are able to deliver high productivity (up to 500 wafers per hour) and precise doping. The implant energy ranges from 2 to 810

kilo-electronvolts (keV), with an implant current up to 5 milli-amperes. The typical dose ranges from $1E13$ to $1E16$ dopant per square centimeter, with a uniformity and repeatability below 0.5 %.

- The high-energy implanters are able to deliver ion implantation energies ranging from 10keV to 3 MeV. The typical dose ranges from $5E10$ to $1E16$ dopant per square centimeter, with a uniformity and repeatability below 0.5%. The implantation current for this type of implanters is only reaches of several hundred micro-amperes. The high-energy implanters are mainly used for Well doping.

Crystal damage after ion implantation

While penetrating the silicon substrate, the ion loses its energy by colliding with the target's atoms. During the implantation process, a large amount of the projectile's kinetic energy is transferred to the atoms of the target, displacing them from the lattice sites. The energy threshold required to eject a silicon atom from its lattice position is about 15eV. The most common defect is a vacancy-interstitial that is created when an incident ion knocks a target atom from a lattice site; the displaced atom then comes to rest in a nonlattice position. Light atoms, such as boron, produce a smaller number of displaced atoms than heavier atoms, such as phosphorus and arsenic. When the density of the defects reaches a critical density, an amorphous layer is formed on the surface of the target wafer. The depth of the amorphous layer is more important when it comes to higher incident-ion energies and higher implanted doses. Because of this damaged region and the disorder that results from the implantation step, most of the as-implanted ions are not located in substitutional sites, leading to severely degraded semiconductor parameters such as mobility and lifetime.

Ion distribution after ion implantation

The distance that an ion travels before being stopped by the semiconductor material is called its range, R , and is illustrated in Fig. 8. The projection of this distance along the

axis of incidence is called the projected range, R_p . As the ion beam is mono-energetic and the collision process is random, the ion distribution can be approximated to a Gaussian for low dose implantation:

$$C(x) = \frac{D}{\sqrt{2\pi}\sigma_p} \exp\left[-\frac{(x - R_p)^2}{2\sigma_p^2}\right] \quad \{I.1\}$$

where $C(x)$ is the dopant concentration at depth x , D is the dopant dose and σ_p is the statistical fluctuations of the R_p call projected straggle. The dopant profile obtained after ion implantation is then a Gaussian centered at a depth R_p (see Fig. 9a) and characterized by the σ_p .

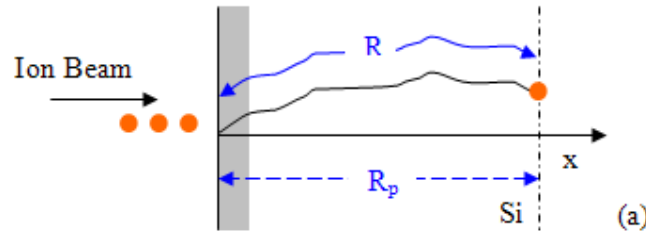


Figure 8: Schematic of the ion range and projected range R_p

The Transport of Ions in Matter (TRIM) software developed by Ziegler [Ziegler 1985] determines ion ranges and damage distributions, as well as angular and energy distributions of the backscattered and transmitted ions. It provides high computer efficiency while maintaining accuracy [Nastasi 1996]. TRIM is the most commonly cited software for range and damage distributions in amorphous materials. An example of a B^+ 5000 eV TRIM simulation is shown in Fig. 9.

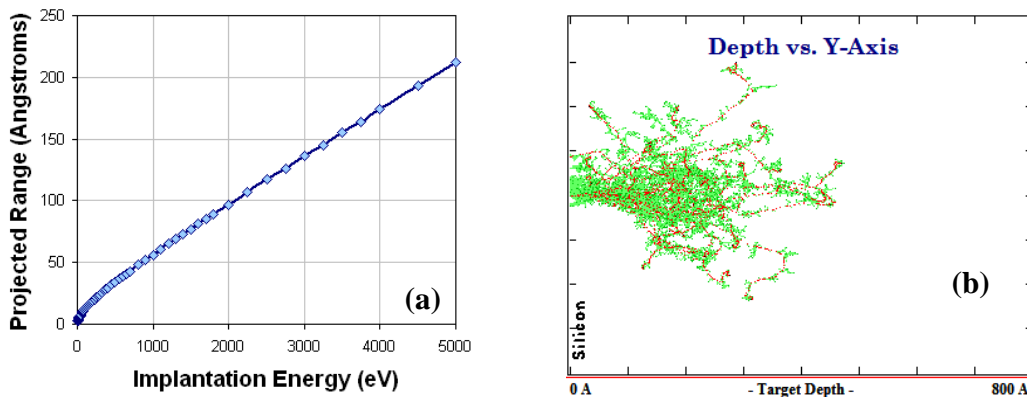


Figure 9:; (a) Projected range simulated for B^+ implanted into silicon with an energy ranging from 10 to 5000 eV, (b) TRIM calculation example of B^+ 5000 eV implant into silicon

There are two mechanisms that can be used to stop an energetic ion after it enters a semiconductor target. The first is by transferring the ion's energy to the target nuclei. This causes the deflection of the incident ion (see red trajectories in Fig. 9b) and it also displaces many target nuclei from their original lattice sites (see green trajectories in Fig. 9b). The second stopping mechanism takes place through the interaction of the incident ion with the cloud of electron surrounding the target's atoms. The ion loses energy as it collides with electrons through Coulomb interactions. The electron can be excited to higher energy levels (excitation) or they can be ejected from the atom (ionization). The average rate of energy loss with distance is given by the sum of the nuclear stopping power and the electronic stopping power [Lenoble 2000]:

$$\frac{dE}{dx} = -N \times [S_n(E) + S_e(E)] \quad \{I.2\}$$

where E is the energy of the ion at any point x along its path, N is the atomic density of the target ($N = 5 \times 10^{22} \text{cm}^{-3}$ for the silicon), $S_n(E) \equiv (dE/dx)_n$ is the nuclear stopping power and $S_e(E) = (dE/dx)_e$ is the electronic stopping power.

For low-energy implantation, nuclear stopping is the dominant mechanism used, with more than sixty percent of the total stopping power in the case of boron implantation below 2keV. The contribution of the nuclear stopping power is reduced for lighter ions, which are more sensitive to the electronic stopping power [Lenoble 2000]. At higher energy, the S_n is reduced and S_e can become the dominant mechanism because the fast particle may not have sufficient interaction time with the target atoms to achieve an effective energy transfer.

Channelling effect

A regular arrangement of atoms in the crystal lattice leaves a large amount of open space in the mono-crystalline silicon substrate. For example, Fig. 10a shows a view through the silicon lattice in the $\langle 110 \rangle$ direction. When the direction of the incident ions is improperly oriented, the ions will "channel" much more and will be implanted deeply into the silicon. This phenomenon, which is called channeling, is sensitive to the

orientation of the ion beam and to the ions' energy. Ion channeling is particularly critical for low-energy implantation when very shallow junction is needed.

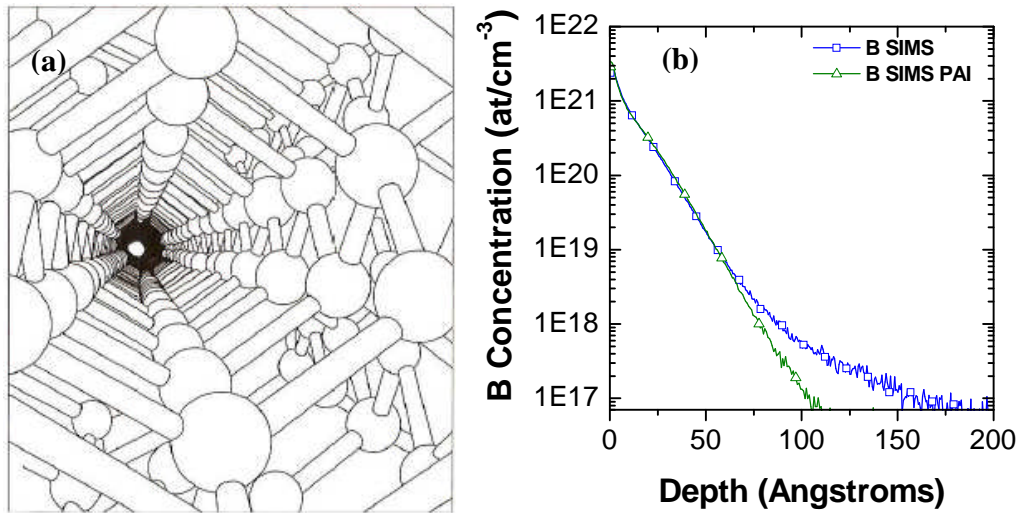


Figure 10: (a) The silicon lattice viewed along the <110> axis [Pauling 1964], (b) Comparison of a boron as-implanted SIMS profile after 500V implantation into a crystalline and a pre-amorphized (PAI) silicon wafer [Godet 2006]

Channeling can be minimized by creating an amorphous layer at the surface of the wafer through the implantation of non-dopant impurities into the silicon. In this case, a Germanium 20 keV beamline implantation is resorted to when pre-amorphized wafers are used. Another approach toward reducing channeling is the use of tilt angle implantation (7 to 10 degrees). In Fig 10b, a comparison of an as-implanted boron SIMS profile after a 500V implantation into a crystalline with a PAI silicon wafer is shown. As expected, boron ions are implanted deeper into the silicon in the non-amorphized substrate.

Dopant activation after implantation

In order to repair the damage induced by the ion implantation and to activate the dopant ions, the substrate needs to be annealed using an appropriate combination of activation time and temperature. However, in order to minimize the diffusion, the thermal budget of activation needs to be maintained at a level as low as possible. Rapid Thermal Annealing (RTA), systems use high-intensity lamps to rapidly heat the wafer to the desired annealing temperature (e.g., 950-1100°C) in a very short time (from a few

minutes to a few seconds). RTA is still the activation technology of choice for today's semiconductor manufacturing equipment.

In most of the cases here, dopant activation is performed through an optimized Rapid Thermal Process (RTP) spike anneal in a Mattson 3000 plus RTP system [Bayha 2002]. This system is equipped with a wafer rotation system and an edge guard ring at the wafer level to optimize uniformity. The ramp-up rate to the pre-stabilization temperature is 50°C/s. The pre-stabilization step is performed at 650°C for 10 seconds [Bayha 2002]. A 250°C/s ramp-up rate is used to reach the final temperature of 1050°C. The ramp-down rate was 50°C/s. All wafers are processed with a rotation speed of 90 revolutions per minute. The partial pressure of oxygen is 100 ppm in an N₂ ambient at atmospheric pressure.

I.3 Ultra Shallow Junction

Requirements

The front end process International Technology Roadmap of Semiconductors (ITRS) [ITRS 2005] defines the future requirements of the key technologies needed for the front end wafer fabrication process and suggests potential solutions for any problems that might arise. It also looks at the materials associated with these devices. It gives a clear indication of the next challenges that will need to be met in order to follow the governing Moore's law. One of the next challenges facing the doping of CMOS transistors is the Source Drain Extension (SDE) doping as discussed previously.

Year	2005	2006	2008	2010	2012
Node (nm)	80	70	57	45	36
gate length (nm)	32	28	23	18	14
X _j (nm)	11	9	7.5	6.5	4.5
Maximum R _s (ohm/sq)	653	674	740	650	593
Lateral Abruptness (nm/decade)	3.5	3.1	2.5	2	1.5
Channel doping concentration(cm ⁻³)	3.7E+18	4.6E+18	7.3E+18	8.9E+18	8.8E+18

Table 1: Key Ultra-Shallow Junction (USJ) doping requirements for CMOS [ITRS 2005]

Table 1 shows the USJ doping requirements for future device generations up to 2012. The sheet resistance of the doped layer R_s (described in section III.3.2), the junction depth X_j and the dopant lateral abruptness are the main parameters involved in the USJ requirements. A curve $R_s(X_j)$ is very often used to characterize the junction.

In order to achieve the ITRS requirements, the SDE USJ depth needs to be decreased and the dopant profile needs to be more abrupt, which implies improving the dopant placement precision and lowering the ion implantation energies with higher doses. The realization of ultra-shallow source and drain extension junction depths, which are vertically and laterally abrupt, requires not only the development of new and enhanced methods for implanting the doping species, but also the development of thermal

activation processes that have an extremely small thermal budget [ITRS 2005]. In order to reduce the thermal budget, the anneal temperature or the anneal time needs to be reduced. However a reduction of the anneal temperature implies a reduction of the solid solubility limit into the silicon. It is thus necessary to anneal the wafer with high temperatures and a reduced annealing time. New anneal technologies including flash anneal, laser anneal and the Solid Phase Epitaxy (SPE) technique are being developed to meet the anneal requirements of the future device generations. Details on these techniques can be found in the Lallement thesis [Lallement 2005].

Low-energy ion implantation

In order to follow the International Technology Roadmap of Semiconductors (ITRS) and continue to reduce the device sizes, the implantation energy needs to be increasingly reduced to lower values while keeping the same or even better throughput. Reducing the implantation energy below 3keV while maintaining high productivity, is a challenge for the implantation industry. The maximum ion current that can be transported inside the beamline decreases as the implantation energy is reduced. It can be calculated using the Child-Langmuir equation, assuming that there are no collisions between particles under high vacuum (see equation {I. 1}).

$$j = \frac{4\epsilon_0}{9} \times \sqrt{\frac{2e}{m_i}} \times \frac{V_{\text{ext}}^{3/2}}{x^2} \quad \{\text{I.1}\}$$

where j is the implantation current, e is the elementary charge, m_i is the mass of the dopant, V_{ext} is the extraction potential and x is the length where the potential is applied.

$$v_i = \sqrt{\frac{2E}{M_i}} \quad \{\text{I.2}\}$$

When the ion beam energy is reduced, the velocity of the ions is decreased (see equation {I.2}). The ions are thus exposed longer to the electrostatic force of neighboring ions, making the beam diverge. Beam current is lost by the divergent beam striking on optical elements and apertures of the implanter. Two methods can be used to solve the beam transport limitation at low energies, the molecular ion implantation and deceleration-mode ion implantation (Ultra-Low Energy or ULE implanters). Another

technique used for low-energy implantation is plasma-based ion implantation. These three different methods will be discussed in the next three sections.

Molecular ion implantation

The idea of molecular implantation is to use heavy molecular ions which will be then implanted shallower than mono-atomic ions. Consequently, for a given initial implantation energy, the dopant profile will be shallower. When a molecular ion is implanted into the substrate, the molecules split into atoms after interacting with the first layers of the target. Each atom of the initial molecule has an equivalent energy of $E_{molecule} \times \left(\frac{M_{atom}}{M_{molecule}} \right)$. The boron-equivalent energies of different boron molecular ions are presented in Table 2.

Molecular ion mass	11	30	49	68	117	220
Molecular ion implanted	B ⁺	BF ⁺	BF ₂ ⁺	BF ₃ ⁺	B ₂ F ₅ ⁺	B ₁₈ H ₂₂ ⁺
Boron equivalent energy (keV)	10.00	3.67	2.24	1.62	0.94	0.50
R _p (Angstroms)	400	163	107	81	55	34

Table 2: Boron equivalent energies and projected range of different molecular boron ions implanted with an energy of 10 keV

Using molecular ion implantation, higher energy can be used to achieve smaller implantation depth into the target with an acceptable beam current. One of the most commonly implanted molecules is BF₂⁺, which has been used for many years now to implant the boron atoms at 11/49 times the energy of the BF₂ ion. Other molecular ions are sometimes used, such as arsenic dimer As₂⁺, Diborane (B₂H₆) and decaborane (B₁₀H₁₄). The ultimate extension of this approach is cluster-ion beam implantation, where hundreds or even thousands of weakly bound atoms are ionized and then implanted as a cluster [Takagi 1978]. Unfortunately, this approach also presents some issues, as the beam current is usually significantly reduced when extracting molecular ions. The beam

transport and also the mass resolution cause special issues when using molecular ions such as decaborane [Perel 2000]. For instance, stoichiometry of ions extracted from the ion source strongly depends on the parameters in the ion source and vacuum conditions. It can change during the source life time, leading to a non-repeatable setup performance and complicate beamline tuning [Renau 2002].

Deceleration mode

In order to solve the beam transport limitations at low energy, the implanter can be running in deceleration mode. The ions are extracted and transported at a higher energy than the final implant energy. Before reaching the wafer, they are decelerated to the final energy through an electrostatic lens. The ultra-low energy implanters that use this method give a good uniformity and high implantation current. Unfortunately, the process is very sensitive to the residual gas inside the beam line. Ions can collide with molecules from the residual gas or with the surface and become neutralized through charge exchange. The neutrals are not affected by the deceleration field and reach the wafer with a high energy and are implanted in the wafer at an undesired depth. These high energy neutrals are referred as energy contamination (EC).

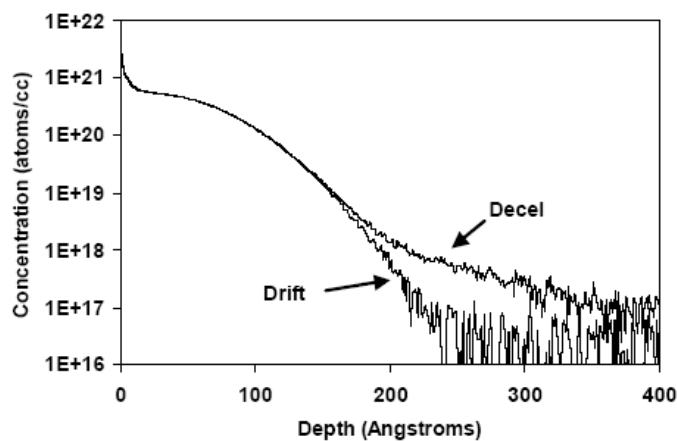


Figure 11: Comparison of drift and decel implants of 1 keV $5E^{14}$ boron [Renau 2002]

Fig. 11 shows the SIMS profile for a 1 keV boron implants that is implanted in drift mode (without deceleration) and another that is implanted through the deceleration of the ion beam before it reaches the wafer. The decelerated beam (from 3.5keV to 1

keV) shows an energy contamination of 0.2%. The EC is important enough to affect the depth of the boron dopant distribution. At a level of 10^{18} boron atoms per cubic centimeter, the deceleration mode dopant distribution is nine angstroms deeper than in the drift mode one.

Plasma-Based implantation

Another alternative for dealing with the beam transport at low energies is to use plasma-based ion implantation. Through this technique, the wafer is immersed directly in dopant plasma, which is created by a negative pulsed voltage applied on the cathode. The ions are accelerated across the plasma sheath and implanted directly into the wafer. Each negative pulse ignites and maintains the plasma.

No beam transport is necessary with this technique, making the plasma-based ion implanters much simpler machines than the conventional ion implanters. Another significant advantage is that the entire wafer is implanted at once with high wafer current. An example of the VSEA plasma-based ion implantation machine, PLAsma Doping (PLAD), is shown in Fig. 12.

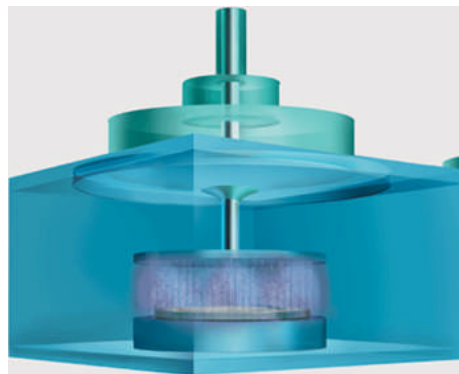


Figure 12: PLAD concept

Trough this technique, a large number of wafers can be implanted per hour, even at very low energies. PLAD is starting to be adopted for the new device nodes by the chip-manufacturing companies. PLAD principle of operation will be described in detail in Chapter 2.

Chapter II PLAsma Doping System

The goal of this chapter is to discuss the plasma-doping technology in detail. First, we will give the history of plasma-based ion implantation and explain the principle of plasma doping. We will then present the VSEA equipment used for plasma doping. Finally, we will discuss the PLAD performance and its different applications.

II.1 Brief historical background of PLAD

The first method used to introduce dopant into semiconductor materials was the thermal diffusion of the dopant from a deposited layer or a vapor source. In 1958, W. Shockley [Shockley 1958] proposed the method of using ion implantation to dope the semiconductors with precision by controlling the energy and number of implanted ions. The first direct plasma implantation was done by Hans Strack in 1963 [Strack 1963]. He followed a recommendation given by Shockley [Shockley 1957], which called for low-energy dopant ion bombardment to be used to provide a source for vacancies and interstitials. The method could also affect the diffusion of substitutional atoms into the substrate.

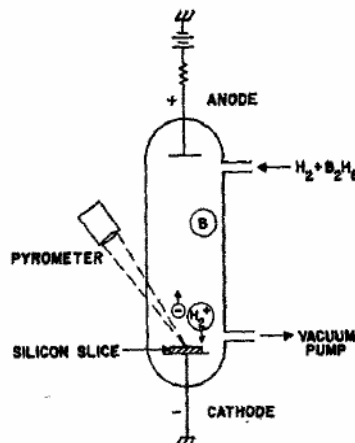


Figure 13: Hans Strack's plasma immersion system [Strack 1963]

The apparatus used by Strack is shown in Fig. 13. The silicon wafer was immersed in diborane or phosphine plasma, which was diluted in a gas made of 99 % hydrogen. The wafer was then installed on the cathode and surrounded by a silicon or graphite cylinder to enhance the plasma density, so that the wafer could be simultaneously heated during the implant. The dose and the dopant diffusion into the wafer were controlled by the implant time. The implant voltage was in the range of 700 to 1200 V, so that the dopant was deposited primarily in a shallow surface region. Implant time was in the order of hours to obtain the diffused junction in the μm range. This technique led to higher diffusion rates than the classical diffusion technique, but the

lack of independent dose and depth control, as well as the poor beam species purity, made this approach less attractive than beamline implantation. Conventional beamline implantation was used for material modification work during the 1970s and the 1980s, but beamline implanters were highly directional and could not implant irregularly shaped surfaces [Conrad 2000]. In order to implant irregular surfaces (see Fig. 14), the plasma-immersion ion implantation (PIII) was revived in 1986 through the work of Conrad [Conrad 1987a].

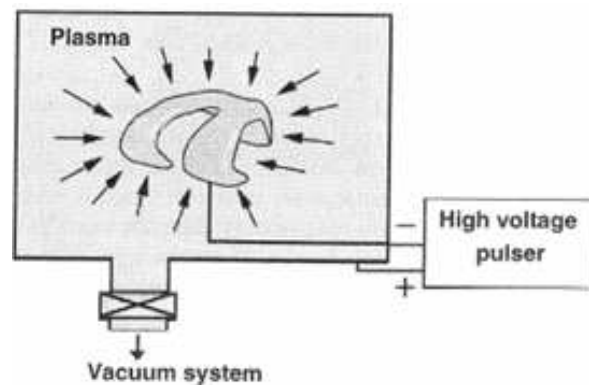


Figure 14: Plasma-Immersion Ion Implantation (PIII) [Conrad 2000]

In PIII, the workpiece is directly immersed inside the plasma, which is created through a negative pulse voltage. A plasma sheath then forms around the workpiece. Ions are implanted conformally into the workpiece as long as the plasma sheath dimensions remain less than the workpiece feature sizes. Conrad and Lieberman started the theoretical work on and modeling of PIII in the late 1980s [Conrad 1987b, Liebermann 1989]. After 1988, many applications of PIII appeared in the semiconductor research industry, for instance as conformal doping of trench sidewalls [Mizuno 1987 and 1988, Qian 1991a] and junction fabrication [Qian 1991b]. Since the 1990s, many new applications using PIII have appeared for material modifications or semiconductor doping. More details on the history of PIII can be found in [Conrad 2000] and [Walther 2006a].

In the 1980s, Varian started research on plasma-based ion implantation and PLAsma Doping (PLAD) in particular. VSEA started this research on a PLAD test stand (see Fig. 15) at Varian's research center in Palo Alto, CA, USA. Under the original configuration, a vacuum loadlock was attached to the main chamber for wafer handling.

The BF_3 gas entered from the chamber bottom and was pumped out from the top of the chamber. The silicon wafer was fixed on a wafer chuck that was located on the top plate of the chamber. An anode facing the wafer chuck was used as a ground plate. A high-voltage negative pulse was applied to the cathode, and each pulse created the plasma. The ions were then extracted across the sheath and implanted into the silicon wafer. Many studies were conducted to demonstrate the suitability of PLAD to meet the goals defined by ITRS and demonstrate the technological compatibility of PLAD with semiconductor process requirements [Felch 1992, 1998, 1999, Sheng 1993, Matyi 1997, Ha 1998, Goeckner 1999, Chu 1999, Lenoble 1999, Yeap 1999].

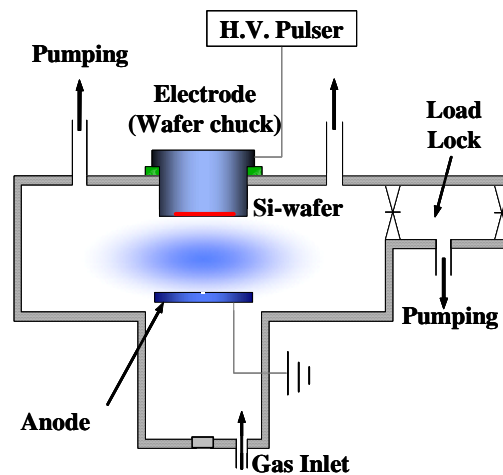


Figure 15: Varian plasma-doping system first prototype [Lenoble 2000]

The first manufacturing PLAD system was developed in 2000 and 2001 at VSEA in Gloucester, MA, USA. The semiconductor applications that use plasma-based ion implantation developed with the VSEA system will be described in section II.5.

II.2 Description of the technique

Principle of operation

The glow-discharge PLAD chamber consists of a cathode, which holds the wafer being implanted, and an anode (see Fig. 16). A negative DC voltage pulse is applied to the cathode, which generates a glow discharge in the volume adjacent to the wafer.

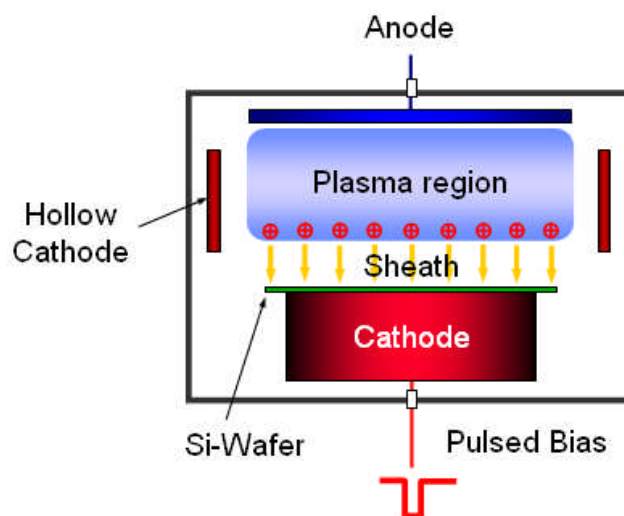


Figure 16: Principle of PLAD

The plasma is ignited by each voltage pulse applied to the wafer. When the pulse ends, the plasma follows a natural decay process. During the pulse-on period, ions in the plasma are accelerated by the electric field across the plasma sheath and are subsequently implanted into the wafer. The energy of the ions striking the wafer during the pulse-on period is mainly controlled by the applied voltage. Other parameters, such as pulse width, frequency, gas pressure, flow rate, surface condition and the geometry of the electrodes, can also affect the implant process by changing the plasma composition, the ion flux and the number of collisions inside the sheath. Short pulse-on periods provide short plasma exposure, good charge control and minimal etching and deposition effects and maintain high dose rates even at low energies (<1 keV).

Pulsed DC Glow Discharge (GD)

Plasma Ignition

A DC glow discharge is produced by applying a DC voltage between two conductive electrodes inserted into a gas at low pressure. As the voltage applied to the gas in the discharge chamber is gradually increased, the available free electrons present inside the gas are accelerated by the electric field and gain some kinetic energy. These electrons then collide with the atoms or molecules of the gas. Initially, the energy of the electron is too low to excite or ionize a target and the collisions are thus elastic. Meanwhile, the electrons continue to gain energy between collisions until they attain sufficient energy to ionize the target through inelastic collisions. The new electrons produced in the ionization process are in turn accelerated by the electric field and produce further ionization by impact with neutral atoms or molecules of the gas. An electron multiplication process thus takes place.

The minimal threshold voltage required to produce the glow discharge is called the breakdown voltage. In a DC discharge, the breakdown voltage is determined by the discharge gas, the discharge pressure, and the anode-to-cathode distance. The dependence of the breakdown voltage (V_{bd}) on gas pressure (P) and the anode-to-cathode distance (d) can be expressed as [Cecchi 1990, Raizer 1997]:

$$V_{bd} = \frac{C_1 \times (P \times d)}{C_2 + \ln(P \times d)}, \quad C_2 = \ln \left[\frac{A}{\ln(1/\gamma + 1)} \right] \quad \{\text{II.2.1}\}$$

where A, C_1 and C_2 are coefficients that change with the nature of the gas and γ is the secondary electron-emission coefficient. For each specific gas, the breakdown voltage only depends on the product $P \times d$. This dependence is called Paschen's law, which reflects the dependence of the DC glow discharge on the secondary electrons. When the anode-to-cathode distance is small or the pressure is low, the secondary electrons emitted from the cathode can reach the anode while undergoing only a very small number of collisions and do not create a sufficient number of ions for the regeneration of secondary

electrons. When the pressure is too high, the electrons cannot acquire enough energy between collisions to produce enough ions.

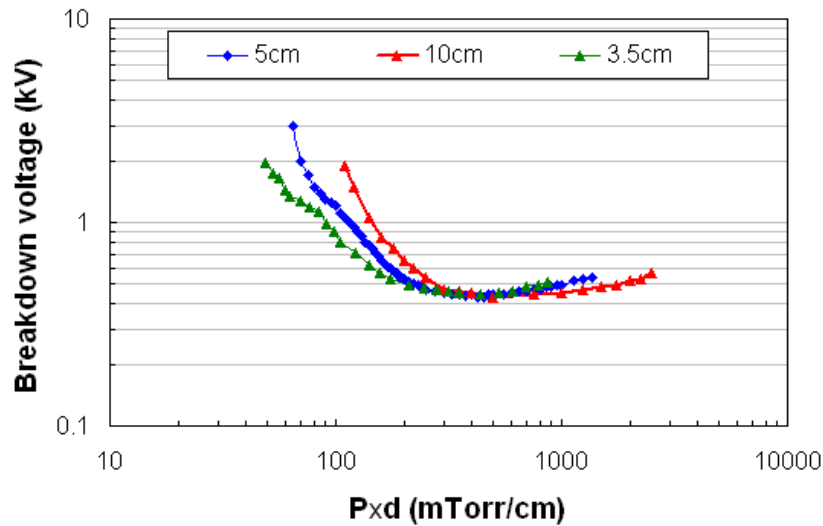


Figure 17: Experimental Paschen's curves showing the evolution of the breakdown voltage of a BF_3 discharge as a function of the product $P \times d$

If the distance between the electrodes is too large, only a small fraction of the produced ions will be able to reach the cathode with sufficient energy to create more secondary electrons. At both extremes of the $P \times d$ product's value, the probability of ionization is small and the breakdown voltage required to ignite the discharge is too high. The breakdown voltage reaches a minimum between the two extremes. This behavior is described by Paschen's curves, which are shown in Fig. 17 for BF_3 GD plasma at different anode-to-cathode distance. The minimum breakdown voltage in the BF_3 GD is around 450V.

Very low energies PLAD implantation

The pulsed glow discharge cannot be operated below 450V unless an external plasma source is used. Two different configurations are presented here:

a) Hollow cathode mode

Shown in Fig. 16 is a Hollow Cathode (HC) ring that is used here as an external plasma source to self-sustain the discharge for low-energy implantation (below 600V). The HC assembly is composed of a 10 cm tall aluminum spray coated silicon ring installed between the anode and cathode. The ring which has a radius of 25 cm is positioned at 2.5 cm from the cathode. The moveable anode can penetrate inside the HC ring. The HC is negatively pulsed with a dc power supply that can be synchronized to the cathode voltage pulse.

The hollow cathode ring provides a mirror electric field for electrons as well as an electron-confinement mechanism in this area. It is used to increase the plasma density, and the discharge can be operated at low pressure, even at very low cathode voltages (up to 50 eV) with high ion current density (see Fig 18). The advantage of operating with a lower pressure discharge is to increase the ion-neutral mean free path and to reduce the number of collisions inside the sheath.

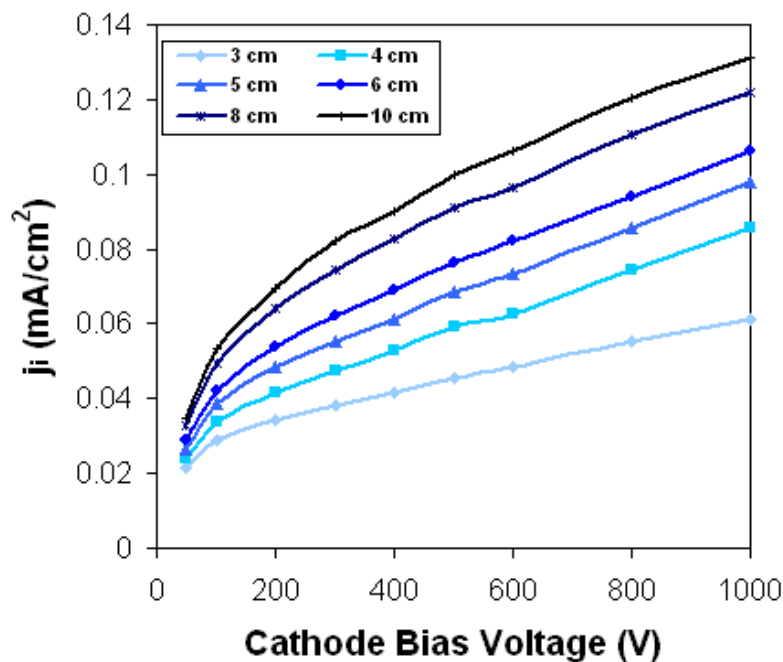


Figure 18: Ion current density as a function of cathode bias voltage and anode-to-cathode spacing at 30mTorr for a hollow cathode plasma operated at -1500 V

When the anode-to-cathode spacing is reduced, the effective hollow cathode surface is decreased. Reducing the effective hollow cathode surface implies a reduction of the cathode current due to the plasma density decrease between the anode and cathode

spacing. Larger anode-to-cathode spacing produced higher plasma density which leads to higher power supply current as indicated in Fig. 18. The anode-to cathode gap is used to control the plasma density and uniformity by adjusting the effective HC surface.

In most cases, the HC voltage is set as around 1500 V and is coincident with the cathode pulse, so that no time delay is introduced between the pulses. This configuration has been found to maximize the plasma density and uniformity.

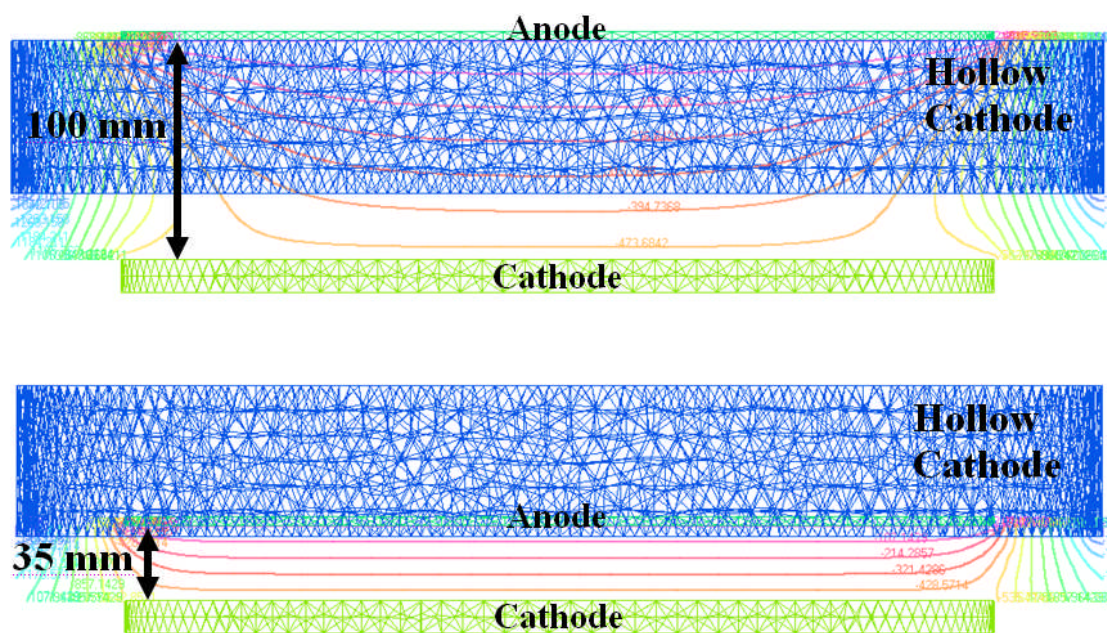


Figure 19: Electric field distribution calculated using Opera 3D with -500 V on the cathode and -1500 V on the hollow cathode for two different anode-to-cathode spacing (100 and 35 mm)

When the anode-to-cathode spacing is reduced, the electric field near the cathode becomes more uniform (see Fig. 19) and the effective hollow cathode surface is decreased.

b) *Pulsed anode mode*

Another alternative developed during this work to increase the plasma density is the pulsed anode configuration. The anode can be pulsed synchronously or not with the

cathode pulse up to -1500 V. In this mode of operation, the hollow cathode is grounded. The vacuum electric field is uniform near the cathode in this configuration (see Fig. 20).

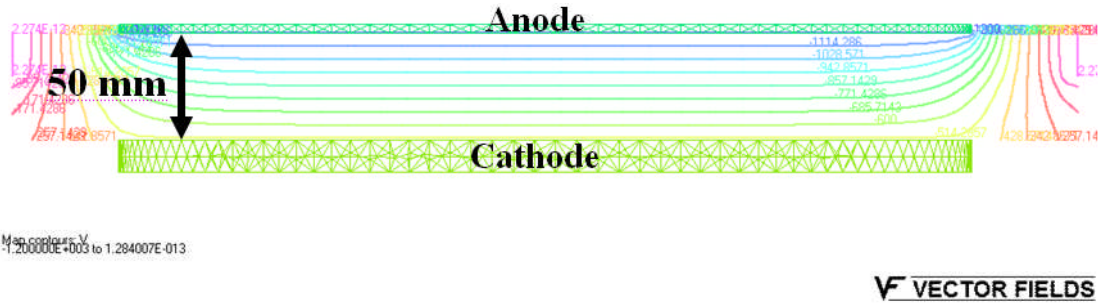


Figure 20: Electric field distribution calculated using Opera 3D with -500 V on the cathode and -1200 V on the pulsed anode for an 5cm anode-to cathode spacing

Characteristics of a dc glow discharge

After the plasma is ignited, three different regions will form between the anode and the cathode: the anode region, the bulk plasma and the cathode region (see Fig. 21).

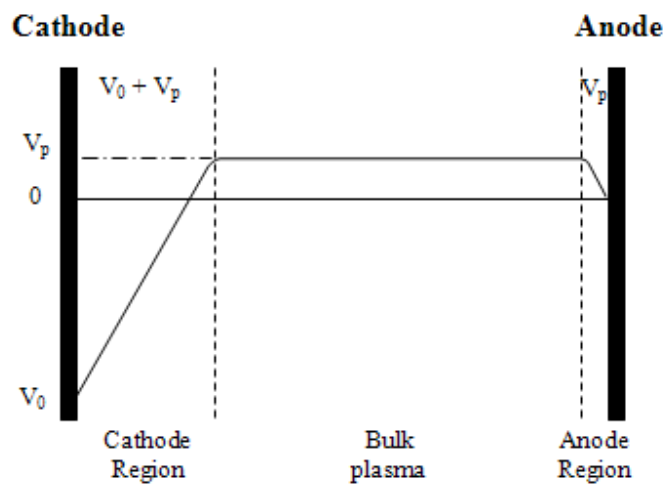


Figure 21: Voltage distribution in a dc glow discharge process [Chapman 1980]

In order to maintain the positive and negative charge equilibrium inside the bulk plasma, the flow of positive and negative carriers is balanced by a potential called plasma potential (V_p). In the usual situation of electropositive plasma, consisting of equal numbers of positive ions and electrons, the electrons are far more mobile than the ions. The plasma will adjust itself and be charged positively with respect to the grounded wall.

The non neutral potential region between the plasma and the surface is called a sheath. Only electrons having sufficiently high thermal energy will be able to penetrate through the sheath and reach the surface, which, being at a negative potential relative to the plasma, tends to repel the electrons.

When a voltage bias is applied on the cathode, an ion sheath is formed. The positive ions are accelerated across the sheath and implanted into the target with an energy lower than or equal to $(V_0 + V_p) \times e$.

Cathode bias characteristics

c) Cathode voltage

The high-voltage pulses applied to the cathode are generated by a high-voltage dc power supply. Fig. 22 shows an example of voltage waveforms measured during a 1 kV, 2.5 kHz, 40 mTorr BF₃ discharge.

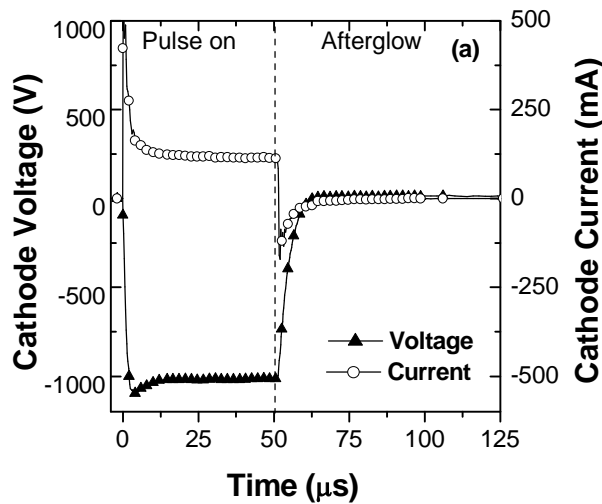


Figure 22: Cathode voltage and current waveforms for a 1kV, 40mTorr, 50µs, 2.5 kHz BF₃ discharge

The typical high voltage rise and fall times are 1 to 5µs and 5-30 µs, respectively, at operating pressures of 10 – 300 mTorr, with a pulse width of 10 to 50 µs and a 1 to 15 % duty cycle.

d) Power supply overshoot

A cathode voltage overshoot is shown in Fig. 23. The pulsed bias overshoot is caused by the non-ideal power supply. Typically, the bias overshoots to positive values (<15 V) during the afterglow.

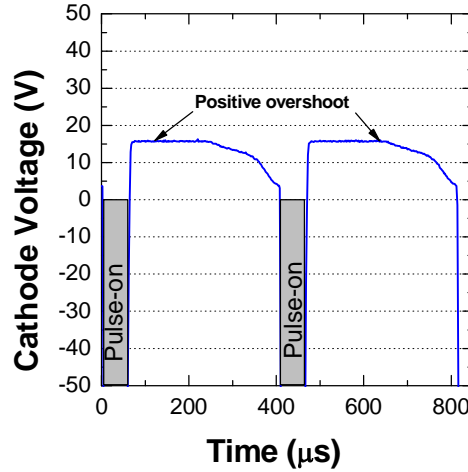


Figure 23: Typical cathode voltage overshoot for 1kV, 40mTorr, 50μs, 2.5 kHz BF₃ discharge

The presence of the overshoot significantly affects the ion-energy distributions in Ar and BF₃ discharges and was described in detail by Koo and Radovanov [Koo 2004, Radovanov 2005].

e) Cathode current

Fig. 22 shows an example of a cathode current waveforms measured during a 1 kV, 2.5 kHz, 40 mTorr BF₃ discharge. The measured cathode current (I_c) is a combination of ion current (I_{ions}), electron current (I_e), secondary electron current (I_{sec}) and the displacement current (I_{disp}).

$$I_c = I_{ions} + I_e + I_{sec} + I_{disp} \quad \{\text{II.3.1}\}$$

Since the electron density is small compared to the ion density inside the sheath, the electron current measured on the cathode is negligible.

$$I_c = I_{ions} + I_{sec} + I_{disp} \quad \{\text{II.3.2}\}$$

At the end of the pulse, the available electrons neutralize the wafer surface charge, which has built up during the voltage pulse. The pulse width is limited by the need to maintain the charge-up voltage below the damage threshold [Cheung 1991, Liebert 2000a].

f) Secondary electron current

The secondary electron current is related to the electron emission after the energetic ion impact on the cathode and can be expressed as follows:

$$I_{\text{sec}} = \gamma \times I_{\text{ions}} \quad \{\text{II.3.2}\}$$

The number of electrons ejected per incident particle is called the secondary electron coefficient (γ). γ was measured experimentally and is dependant on the cathode voltage (ie ion energy), as can be seen in Fig. 24. When the voltage is raised the number of electrons ejected by the incident ions is increased.

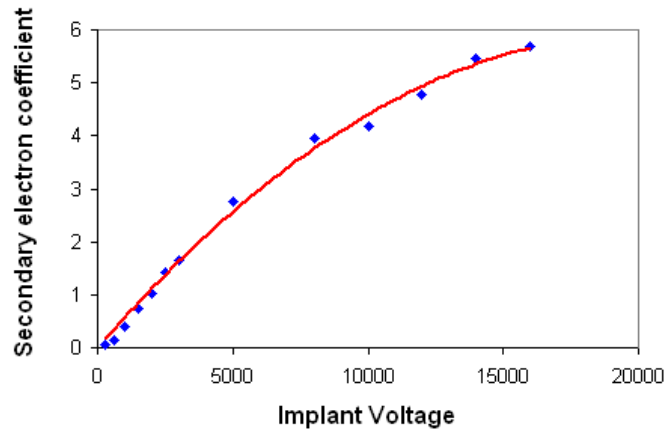


Figure 24: Secondary electron coefficient at different cathode voltages [Miller]

It is also noticeable that the fast neutrals created through charge exchange collisions inside the sheath can eject some electrons. For low energies (< 1keV), experimental results suggest that electron emission induced by the neutral bombardment are negligible compared to the electron emission induced by the ion bombardment [Medved 1963].

g) Displacement current

The displacement current which is created during the rise and fall of the cathode voltage pulse is defined by the following equation:

$$I_{disp} = C_s \times \frac{dV}{dt} + V \frac{dC_s}{dt} \quad \{II.3.3\}$$

Where $C_s = \epsilon_0 \times \frac{S}{s}$ is the ion sheath capacity, S is the sheath surface area, s is the sheath thickness and ϵ_0 is the permittivity of the free space.

In the case of the PLAD technique, the afterglow plasma density before the ignition is very low, making the displacement current quasi-independent of the plasma parameters and close to the vacuum displacement current. The displacement current can be considered to correspond to the capacitance charge created by two electrodes that are in series with the capacitance of the power-supply. The displacement current without gas is assumed to be equivalent to the displacement current when the plasma is ignited. It was demonstrated by Lenoble that the displacement current is mainly due to the PLAD hardware (cable, power supply, anode, cathode...) and not to the plasma parameters [Lenoble 2000]. An example of the displacement current in a chamber without gas is shown in Fig. 25.

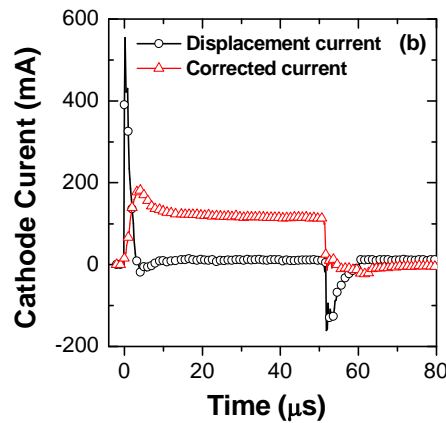


Figure 25: Displacement current measured without gas inside the process chamber

A corrected cathode current can then be estimated by subtracting the displacement current without gas from the original cathode current.

II.3 General presentation of the equipment

The PLAD system layout developed by VSEA is shown in Fig. 26. A PLAD system is composed of two loadlocks that can be configured for twenty-five 200mm or 300 mm wafers, a transfer chamber and two-process chambers.

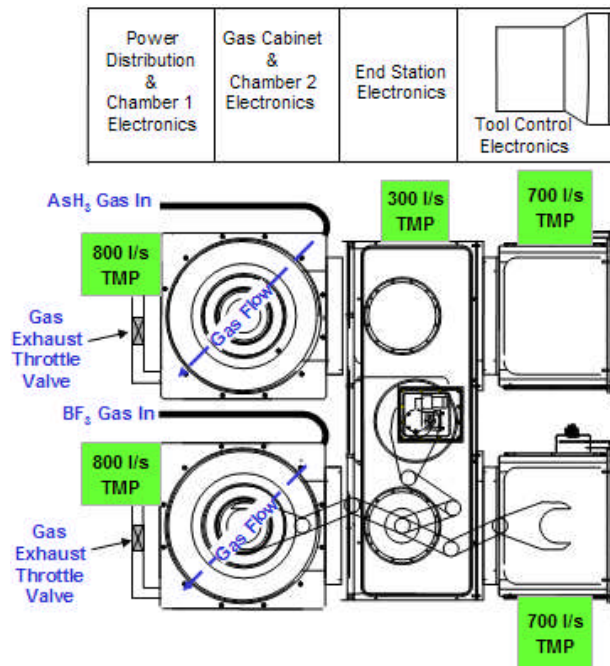


Figure 26: VIISa PLAD system layout

In order to orient the wafer, it is transported from the loadlock to the wafer orientation station by two handling robots inside the end station. The orientation of the wafer is important, even if the entire wafer is implanted at one time, as it allows us to see any repeatable pattern on the wafer after implantation. The wafer is then transported from the orientation station to one of the two process chambers where the wafer will be implanted. Each chamber can be operated at the same time with a different process gas. Once it is implanted, the wafer is transported back to one of the loadlocks by the same handling system.

All the PLAD system is controlled by the Varian Control System (or VCS) software developed by VSEA for a Windows platform.

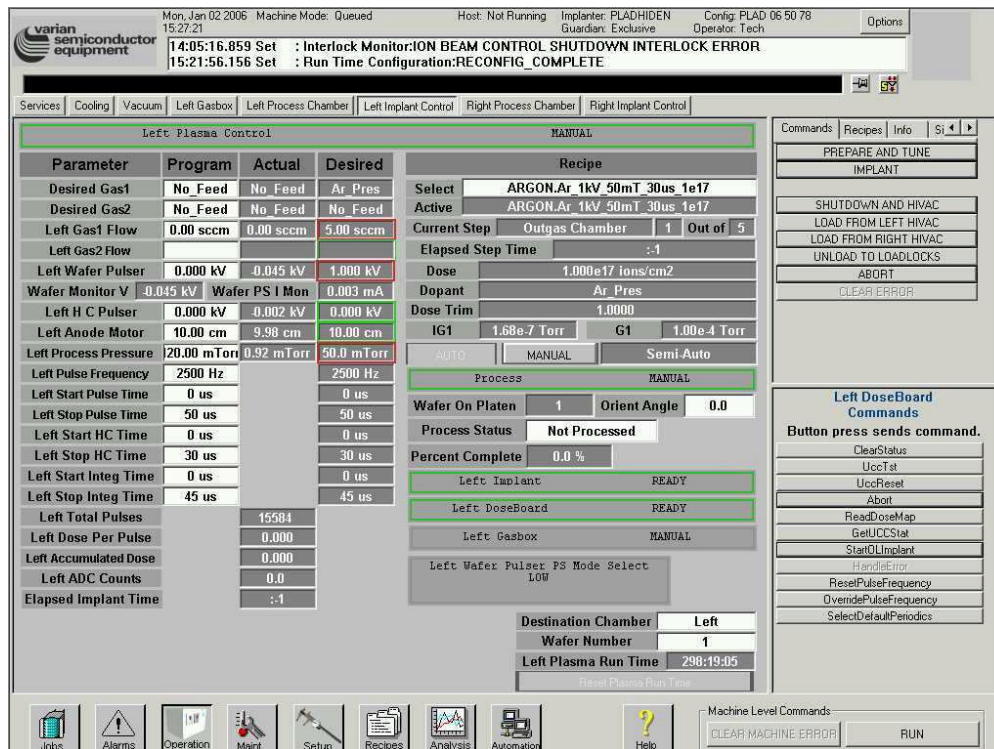


Figure 27: PLAD parameter control screen

With VCS, we can generate process recipes that control all of the implant parameters, such as the process pressure, the cathode voltage, the implant dose and the cathode duty factor. The wafer implantation can thus be fully automatic for production purposes. The process conditions can also be manually modified during the recipe optimization by using the VCS screen shown above in Fig. 27. VCS also controls all of the safety interlocks and cleaning protocols of the machine.

Vacuum system and pressure control

The base vacuum is maintained below 10^{-6} Torr inside the loadlocks and the transfer chamber, while it is kept below $5 \cdot 10^{-7}$ Torr inside the process chamber. The VCS chamber vacuum screen is shown in Fig. 28. The low chamber pressure is obtained through the use of a turbo-molecular pump from Seiko, model STP A803C, which gives a pumping speed of 800l/s.

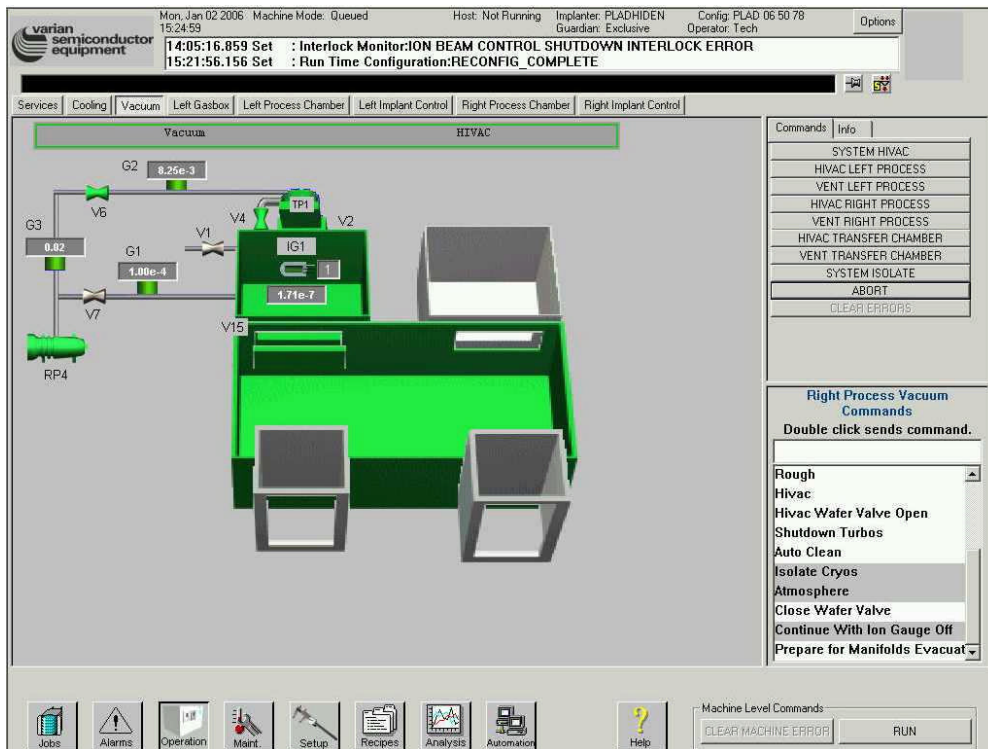


Figure 28: Varian Control System's, vacuum control screen

Each process chamber has independent pressure and gas flow control for process gases, which are delivered through a coaxial gas line for safety purposes. When the wafer is loaded, the isolation valve V2 (see Fig. 28) between the chamber and the turbo-molecular TP1, as well as the valve V15 between the end station and the chamber, are closed. The process-chamber pressure is adjusted up to the required pressure and is regulated by a variable throttle valve (V4) of MKS type 653b. It is also sensed by a MKS 120AA Baratron gauge. The process chamber is exhausted to a high-vacuum pressure before the isolation valves are opened. After a new wafer is loaded, the process chamber is refilled to process-gas pressure. The gas flow inside the process chamber is maintained through a mass-flow controller, which can deliver gas flow ranging from 2 to 50 sccm. Each chamber can have a maximum of eight gas lines and mass flows. Fig. 29 shows one of the VCS gas control screen for one chamber with three gas lines in use.

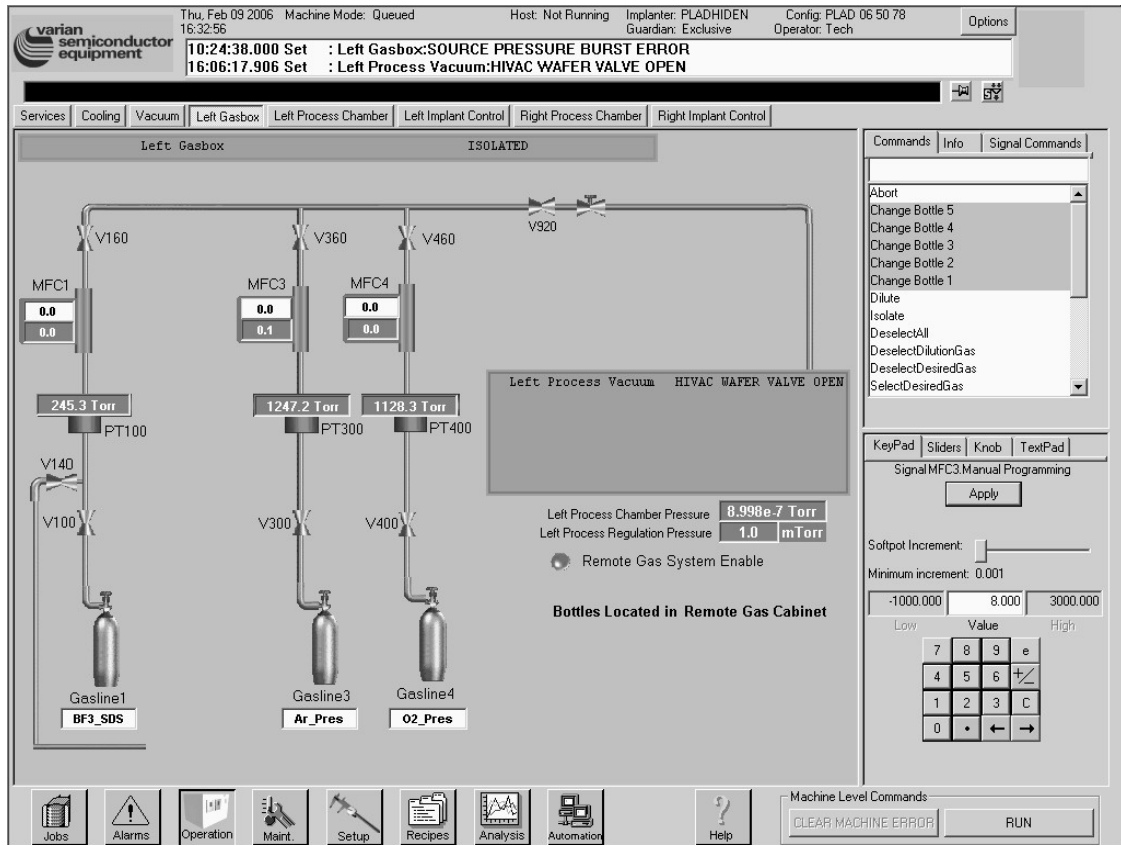


Figure 29: Gas delivery control system

Gas in-used and applications

For this thesis, the following gases with the PLAD system were used:

Boron Trifluoride (BF₃)

Boron or boron molecular ions (BF_x^+ , BF_2^+ , B_xH_y^+) are the most common dopants used for P-type doping of the semiconductor junction, because of its high solubility in the silicon. Boron trifluoride is one of the gases used to create the boron molecular ions. The purity of the gas used is very important for ion implantation, and in particular during plasma doping where no mass selection is performed.

In this case, the P-type dopant used is SDS BF_3 (Safe Delivery Source) from Matheson. In a SDS bottle, the dopant gas is maintained below one atmosphere and is

extracted through the pressure differential between the bottle and the ion implantation chamber, thus eliminating the risk of an uncontrolled release. The BF_3 purity is superior to 99.9%. In addition, the concentration of the enriched boron trifluoride dopant is 25% higher than that of natural boron ($^{11}\text{BF}_3 \geq 99.7\%$). A typical ion spectrum of a 1 kV BF_3 plasma is shown in Fig. 30. The BF_3 plasma is the main plasma studied in this thesis.

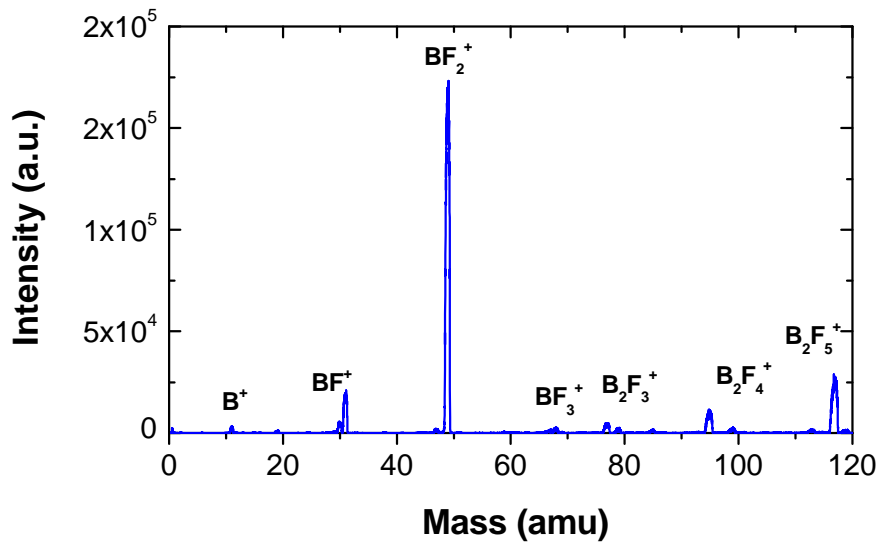


Figure 30: Typical BF_3 ion spectrum for bulk plasma during the pulse-on period at 1kV 50 μs

Arsenic Pentafluoride (AsF_5)

Arsenic or arsenic molecular ions (AsH_x^+ , As_xH_y^+ , As_xF_y^+) are one of the more commonly used N-type dopants due to their high solubilities into the silicon. Arsenic Pentafluoride is one of the gases used to create arsenic molecular ions. An SDS AsF_5 dopant was used for the N-type doping. A typical ion spectrum of a 1kV AsF_5 plasma is shown in Fig. 31.

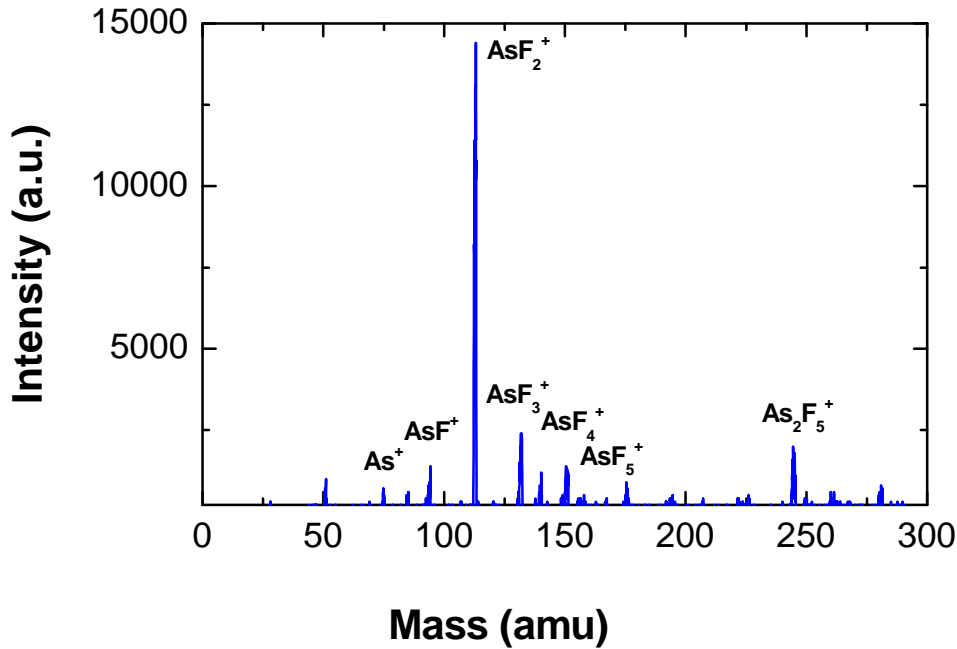


Figure 31: Typical AsF_5 ion spectrum for bulk plasma during the pulse-on period at 1kV 50 μs

The dominant ion in the bulk plasma during the plasma on-period is the AsF_2^+ , followed by AsF_3^+ and As_2F_5^+ , which is created by recombination during the afterglow period. The AsF_5 was used to fabricate an N+/P ultra-shallow junction. We will not provide a detailed discussion of the AsF_5 plasma in this thesis, but some device results using AsF_5 can be found in [Lallement 2004, Lallement 2005].

Rare gases

Many different rare gases, such as Helium, Neon, Argon and Xenon, were used to dilute BF_3 or to condition the chamber after a maintenance opening. The dilution of BF_3 with rare gases will be discussed in chapter V.

Oxygen (O_2)

A O_2 - BF_3 mixture was used for the chamber-cleaning after a BF_3 photoresist implantation. The clean-up is designed to eliminate process drift (dose non-repeatability

and non-uniformity, concentration of non-dopant co-implants) associated with the deposition of materials released on components of the plasma-implanter chamber during the ion implantation of photoresist wafers. The ionized and dissociated species in the O₂-BF₃ plasma are effective at removing carbon-based and other chamber deposits. This oxygen/dopant combination also prevents over-cleaning, as it will not remove protective coatings.

Process chamber

The PLAD process chamber is shown in Fig. 32. It is composed of a spray-coated silicon anode and cathode shield ring. The wafer sits in the middle of the cathode on a gravity platen or an electrostatic chuck (e-clamp). The electrical contact between the high-voltage supply and the wafer is made through sharp metallic pins at the back of the wafer. The cathode is water-cooled to keep the wafer temperature under 85°C. The wafer is installed or removed from the platen using a pneumatic lift-pin system, which moves the wafer up or down.

Special liners are used on the top, bottom and side of the chamber in order to avoid any aluminum contamination and keep the metal level under control during the implantation process.

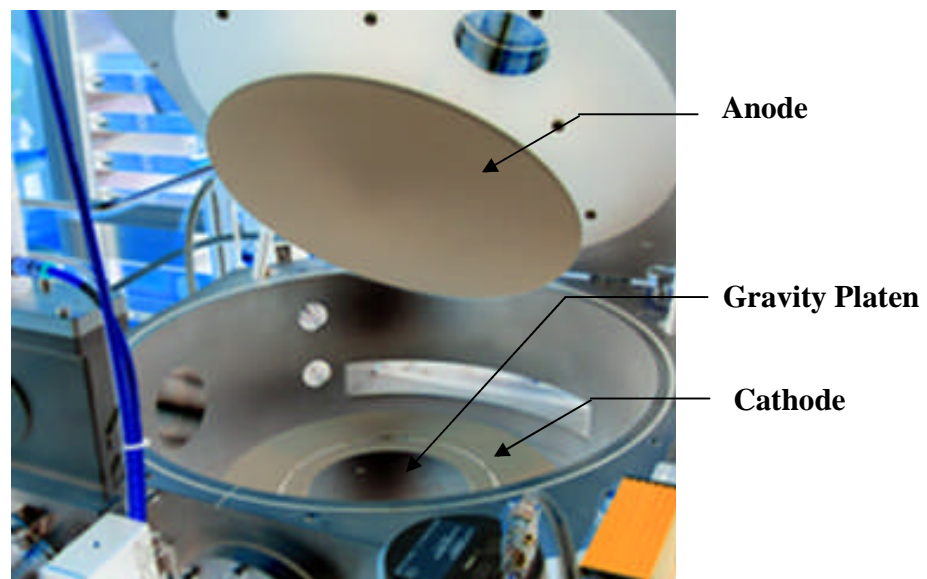


Figure 32: PLAD process chamber with spray-coated silicon anode and cathode

The dose uniformity optimization for the full energy range is achieved by adjusting both the pressure and the anode-to-cathode spacing. An anode assembly driven by a servo-motor is used to cover an anode-to-cathode spacing range from 2.5 to 12cm.

Dose control

As discussed previously, the cathode current does not allow for accurate measurement of the dopant dose implanted into the wafer because the measured cathode current does not correspond to the implanted ion current. The measured cathode current is a combination of the ion current, the electron current, the secondary electrons current and the displacement current created during the rise and fall parts of the pulse due to the cathode capacitance.

A special dosimetry system is then required to accurately measure the in-situ dopant dose. Compared to the conventional ion-implantation systems, the plasma-doping dosimetry systems face a number of challenges [Liebert 2000]. The dose needs to be measured at a high voltage when the plasma is present. Meanwhile, the charge collection has to eliminate the effect of the secondary electrons and the displacement current affecting the implant dose.

A special annular graphite Faraday cup [Lallement 2005] was designed to accurately measure the ion current of the ions reaching the cathode. The Faraday dosimetry system is positioned inside the high-voltage cathode, around the wafer. Since the whole Faraday dosimetry system floats at the same potential as the cathode, the electron current measured by the Faraday cup is now negligible. In order to trap the secondary electrons emitted from the Faraday graphite, a magnetic field is applied to the Faraday cup by permanent magnets. The magnetic confinement also effectively stops electrons in the ion beam from entering the dose cup.

The Faraday cup allows accurate measurement of the ion current. The ion dose implanted can be monitored and good process repeatability can then be reached. The use of a Faraday cup provides efficient process control.

II.4 PLAD performance and process repeatability

As a technology that competes with beamline implantation, plasma-based implantation must demonstrate a comparable level of control and repeatability, even though it uses a mixture of ion species and a wide distribution of ion energies. The dopant profile in the silicon is mainly controlled by the cathode voltage. An example of boron SIMS profiles for BF_3 plasma at different cathode voltages are shown in Fig. 33. Lower voltages provide shallower dopant distributions in the silicon.

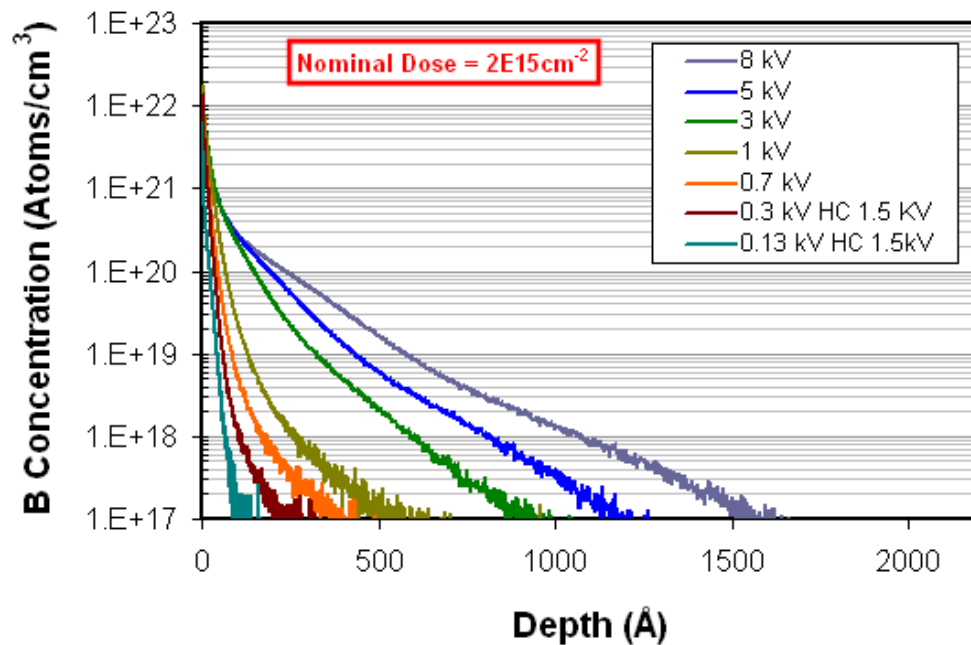


Figure 33: As-implanted boron SIMS profile after a 2.10^{15} PLAD implant at different cathode voltage using crystalline wafers

The dopant depth distribution is mainly controlled by the cathode voltage, bulk plasma ion composition and the number of collision inside the sheath. In general, a shallower junction is obtained when the cathode voltage is reduced.

As can be seen in Fig. 34, the particle level after a N or P-type plasma doping implantation stays below the specifications of the ITRS (60 particles added per wafer)

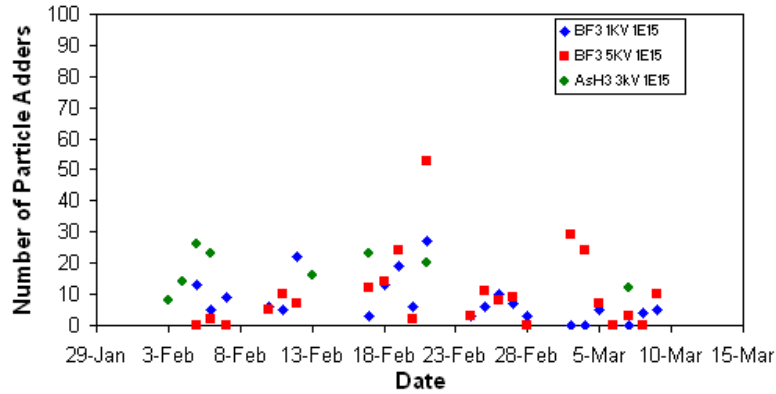


Figure 34: Particle contamination on 200mm wafers for AsH₃ and BF₃ implants

Metal contamination was one of the major challenges to overcome so as to demonstrate the compatibility of the PLAD process for the CMOS technology. After major material modifications to the process chamber, all the metal levels were below the specifications, as can be seen in Fig. 35. The aluminum level is now below 10¹¹, and the sum of all the other metals is below 5x10¹⁰ particles per cubic centimeter (cm⁻³) after a BF₃ 5 and 10kV implant with a 5x10¹⁵ dose.

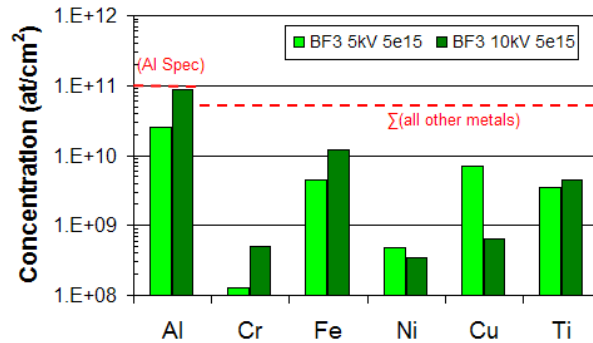


Figure 35: Metal contamination during 5E15 BF₃ PLAD implantation at 5 and 10kV

Fig. 36 shows a plot of a repeatability run on PLAD for the 32 nm node condition [Arevalo] of 1kV, 7.5e14/cm² BF₃ into a pre-amorphized 30keV implant, annealed using SPE by RTP at 650°C for 60s in 100 ppm O₂ in N₂. during this run, 75 wafers were implanted in three cassettes. Twenty-one of these wafers were prime-process wafers, which were evenly distributed throughout the cassettes and subsequently annealed and probed for Rs. The average Rs for these wafers was 798 Ω/sq, with a one sigma repeatability of 0.89% and an average non-uniformity of 0.76%.

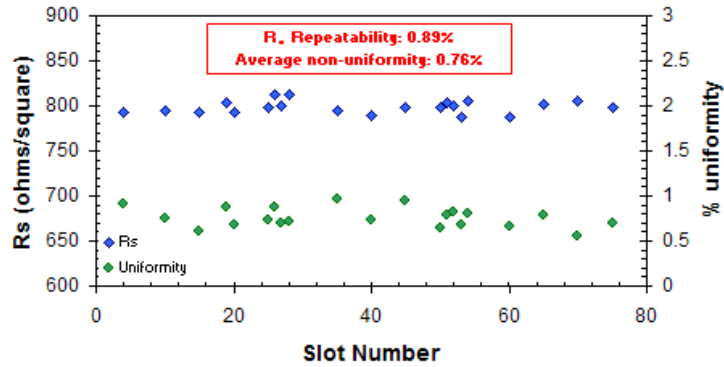


Figure 36: PLAD Uniformity and repeatability of a 1kV, 7.10^{14} dose, 40mTorr, PAI: Ge^+ 30keV $1e15$ dose, SPE annealed by RTP 650°C 60sec in 100ppm O_2 [Arevalo]

In Fig. 37, we show five boron SIMS profiles after a 500V, 30mTorr, BF_3 PLAD implant performed at five different locations on the wafer (center, left, right, top and bottom). A 1.17% X_j uniformity is obtained after a PLAD implantation at low energy (no edge effect observed) and the SIMS profile is repeatable.

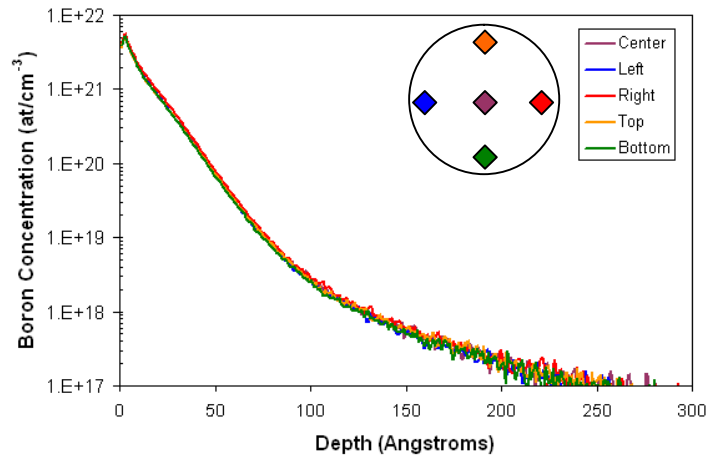


Figure 37: Across wafer X_j uniformity for 500V, BF_3 PLAD as-implanted SIMS boron profiles

Plasma doping is a stable and repeatable process that has demonstrated dose uniformity and repeatability, metal purity and particle performance comparable to that attainable with beamline implants [Scheuer 2004]. During the past 10 years, PLAD has demonstrated its compatibility with the CMOS technology.

II.5 Different applications of PLAD

One of the driving applications for PLAD is “gate doping”. Poly-silicon gate doping requires a very high dopant dose (10^{16} - 10^{17} atoms/cm²). PLAD is able to deliver a very high dose along with a very high throughput (80 to 120 wafers per hour) compared to the 10-40 wafers per hour for conventional beamline implantation. A review of the different PLAD applications and production worthiness can be found in the following articles [Walther 2006a, Fang 2005]. In this section, only the main low-energy applications will be briefly described.

Ultra-Shallow junction

For previous device nodes, the fabrication of the required USJ had been achieved through the reduction of the ion-implantation energy and the emergence of a high-ramp rate spike annealing process. For future technologies, diffusion-less activation techniques (solid-phase epitaxy (SPE), flash or laser anneals...) have been widely studied but have lead to many integrations issues (poly-silicon gate activation, dopants de-activation, system on chip integration etc.). Consequently, the high-temperature spike annealing process is still the most common activation technique, but the transistors architecture has been complicated with the introduction of offset spacers prior to the SDE implantation. Using PLAD overcomes these issues for PMOS and NMOS transistors and allows the continuous shrink of the standard CMOS architecture when using a conventional spike annealing tool [Lallement 2004, Lallement 2005 and Dumont 2005].

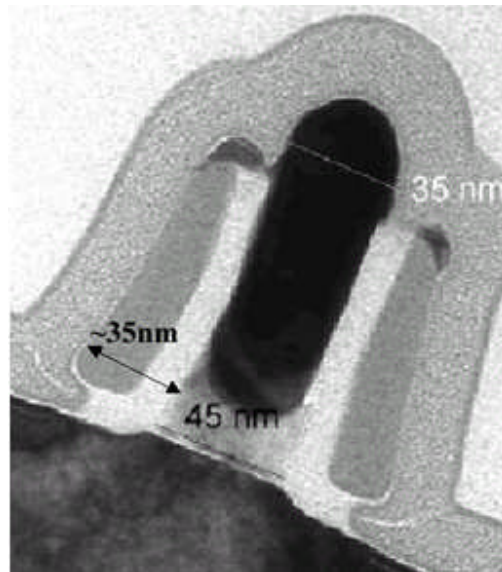


Figure 38: A cross section of a 65 nm transistor fabricated by plasma implant without a sacrificial offset spacer [Lallement 2004, Walther 2006]

N-type and P-type plasma doping processes have been developed to fabricate the ultra-shallow junctions needed for the 65nm CMOS technology. For the first time, the strong benefit of PLAD, as compared to ultra-low energy implantations, for the fabrication of sub-25nm USJ was demonstrated when the standard activation technique was used. Such plasma-doped USJ were successfully integrated into a simplified 65 nm CMOS architecture (no offset spacers, low ramp rate spike annealing < 75 °C/s) for the SDE doping. Lallement demonstrated the capability of fabricating 45nm gate-length CMOS transistors without offset spacers and while using high temperatures and a conventional spike anneal (see Fig. 38). This ultra-low cost architecture leads to the following transistor performance: drive currents of $720 \mu\text{A}/\mu\text{m}$ and $330 \mu\text{A}/\mu\text{m}$, for NMOS and PMOS respectively, are obtained at $V_{\text{dd}}=0.9\text{V}$, $I_{\text{off}}=100 \text{ nA}/\mu\text{m}$. The I_{on} is increased for the NMOS transistor. In addition, the junction leakage current was significantly improved (>1 decade) and the junction capacitance was reduced by 15% for NMOS.

Plasma doping is a very promising candidate for source-drain extension doping, as it can provide low-energy implantation and very high doses. It allows for less integration steps (no offset spacers) and better or equal electrical performance as compared to traditional ion implantation.

Imaging applications

With the digital revolution of photography and the new cell phone generation, the photosensitive sensor type CMOS photodiode represents a simple and cheap solution for commercial use. A photodiode is basically a p-n junction operated under reverse bias. When an optical signal impinges on the photodiode, the depletion region serves to separate the photo-generated electron-hole pairs, and an electrical current flows in the external circuit. A parasitic current is observed even when the photodiode is not illuminated; this phenomenon is called dark current. The dark current is generated by the parasites at the periphery of the photodiode and poses a problem for the photodiode integration into the CMOS photosensors. The dark current is principally created near the interface of the Shallow Trench Isolation (STI) side wall (Zone Z_1 in Fig. 39) and the transfer gate TG (Zone Z_2) [Lallement 2005].

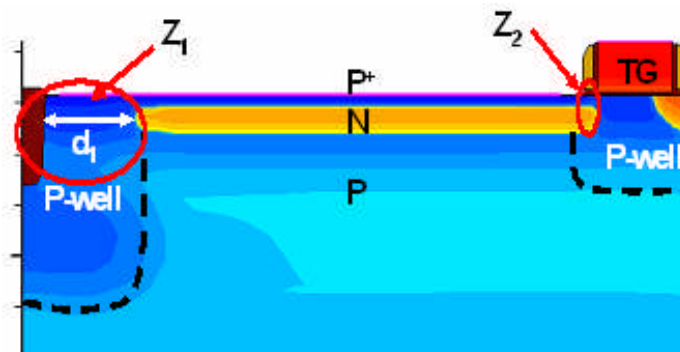


Figure 39: Photodiode implanted area [Lallement 2005]

The problems with the Z_1 zone can be solved by a tilted implant near the STI-substrate interface, which will reduce the production of the parasite electrons in this area. In order to reduce the dark current of the Z_2 zone created by the electron migration at the interface of the spacer-silicon and the N-doped zone, a low-dose, shallow implantation of P-type dopant can be performed. The junction created needs to be very shallow with a low dose to avoid disturbing the transfer of the photoelectrons from the channel when the transfer gate is polarized. Plasma doping is a good candidate to reduce the dark current. The dark current was drastically reduced after optimization of the PLAD process, and the

electron transport from the photodiode to the gate transfer was not disrupted [Lallement 2005].

Conformal doping

Multi-Gate Transistors (MUGFETs), such as triple-gate transistors, have been extensively investigated to replace the planar transistors, because of their excellent short-channel effect control when the device gate is scaled down to 35nm and below. An example of a FinFET is shown in Fig. 40. The non-planar transistor is built on a Silicon On Insulator (SOI) substrate. The silicon is then etched to create a Fin and the gate is created around the Fin.

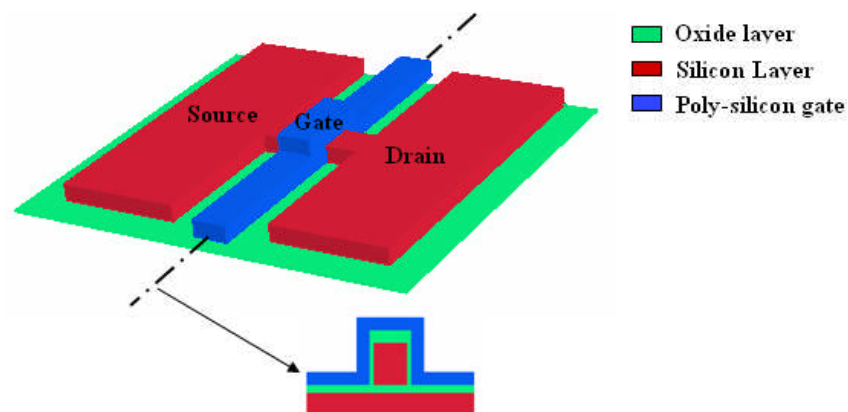


Figure 40: Schematic representation of a FinFET transistor

The doping of SDE in the non-planar transistor is a real challenge for the ion-implantation technology [Lenoble 2006]. When the realistic 32 nm node design rules are taken into account, the maximum ion-beam angle produced by conventional beamline implanters is limited to 10° because of the shadowing from adjacent devices. Since the formation of conformal junctions is not possible with the beamline implantation technique, Lenoble and coworkers investigated the use of plasma doping with tall Fins for a PMOS MUGFET [Lenoble 2006].

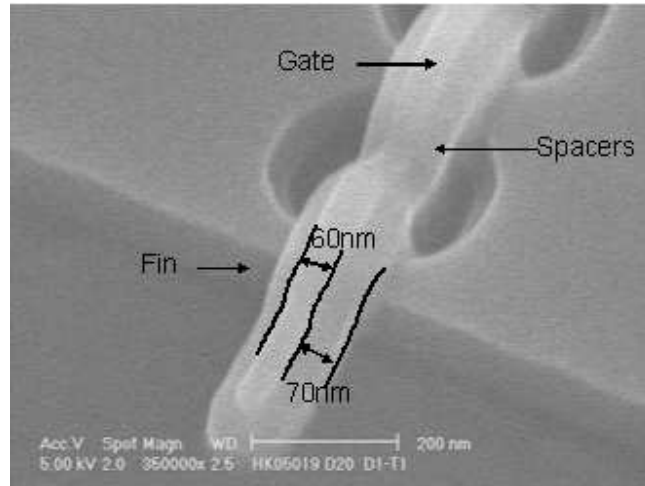


Figure 41: SEM picture of the fabricated MUGFETs with BF_3 plasma-doped SDE. TiCN/HfO₂ gate stack is used on 20nm width/60nm height Fin

The experimental conditions used during plasma-doping implantations are under industrial confidentiality and will not be described in this manuscript. Lenoble has demonstrated that specific plasma-doping processes can be successfully integrated into triple metal-gate FinFets devices, so as to obtain a conformal doping of the SDE over the Fin (see Fig. 41). This specific process leads to a significant improvement (24%) of the drive current (at $I_{off} = 20$ A/ μ m), which may be further increased through the optimization of annealing conditions. PLAD is a promising candidate for non-planar transistor doping.

Chapter III Plasma diagnostics and surface characterization

Several plasma diagnostic instruments were used through out this work: a mass spectrometer and a Langmuir probe.

III.1 Mass spectrometry

The mass spectrometer was the main diagnostic instrument used to probe both the energetic ions reaching the cathode and the ions from the bulk plasma. The mass spectrometry technique and operating modes are described in detail below.

Brief history of mass spectrometry

In 1912, the first apparatus for ion mass analysis was built by Thompson [Hoffman 2002]. It was called a parabola spectrograph [Thompson 1913]. Ions created by a direct current (dc) glow discharge were passed into electric and magnetic fields, which made the ions follow parabolic trajectories. The rays were then detected on a fluorescent screen or a photographic plate. The ion current intensity was determined by the blackening of the photographic plate and the length of the parabola connected to the ion energy distribution. With this apparatus, Thompson detected the Ne isotopes ^{20}Ne and ^{22}Ne .

The mass spectrograph created by Aston [Aston 1919] is often said to be the first mass spectrometer with a velocity focusing feature, but until the work of Herzog and Mattauch [Herzog 1934a, Herzog 1934b] mass spectrometry did not really progress. Their research on ion optics solved the issues of ion beam energy transport and beam angular dispersion. The progress in ion optics, vacuum technologies and electronic detection systems allowed high-resolution mass spectrometry and many other new applications to emerge and led to the detection of atoms, neutral particles and ions.

Industrial mass spectrometer instruments (such as the one used here) appeared along with many new applications after the development of the quadrupole mass filter by Paul and Steinwendel [Paul 1953]. It is a useful diagnostic instrument for gas discharge physics, as it can be used to detect ions directly extracted from the plasma, or created after an ionization of a neutral particle inside the probe. Whenever the system is equipped with an energy filter, it can also determine the energy distribution of these ions.

Electrostatic Quadrupole Probe (EQP)

The commercial instrument used for all the mass spectrometer experiments presented here is the EQP 300 from Hiden Analytical, Inc. The Hiden EQP system consists of a 45° electrostatic ion energy analyzer (ESA), as well as a quadrupole mass spectrometer (QMS). This apparatus allows a mass detection ranging from 0.4 to 300 amu, with an energy range between 0 to 1100eV. It can also detect and analyze neutral particles, along with positive and negative ions in the studied plasma.

A diagram of the EQP is shown in Fig. 42. The mass spectrometer has two modes of operation: the Residual Gas Analysis (RGA) mode, which is used for neutral species (radicals, molecules, atoms) detection from the gas or the plasma, and the Secondary Ion Mass Spectrometry (SIMS) mode, which is used for positive and negative ion analysis. The ionization chamber is only used with the RGA mode.

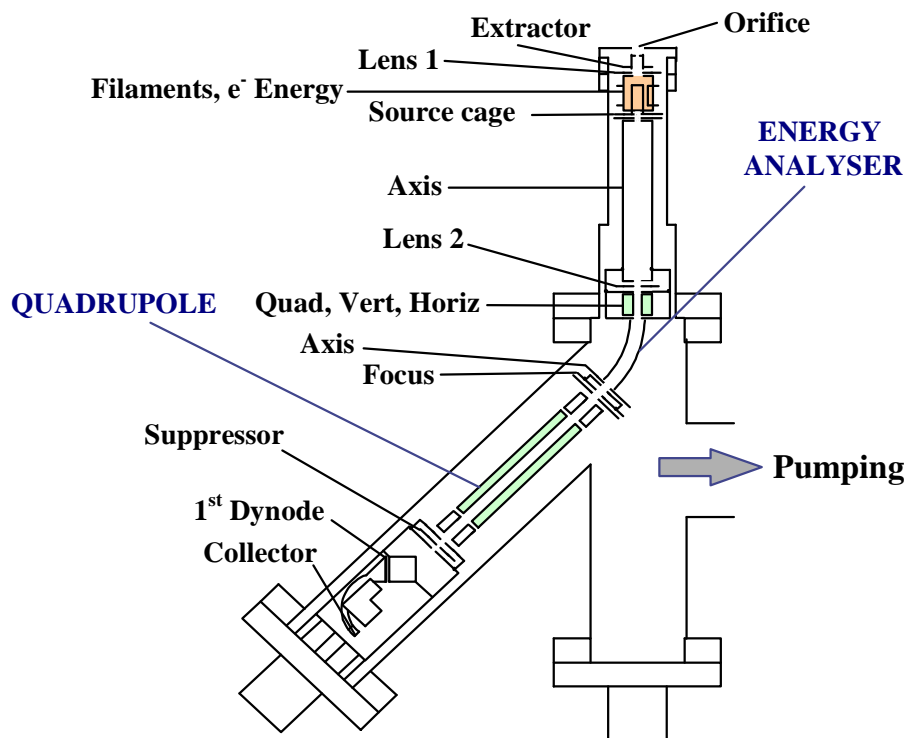


Figure 42: Diagram of the Hiden EQP mass spectrometer

The mass spectrometer is maintained under good vacuum ($< 5e-7$ Torr) through a Pfeiffer turbo pump with a pumping speed of $53 \text{ l}\times\text{s}^{-1}$ (TMU 064). The pump is

connected to the side of the mass spectrometer and the vacuum is controlled by a cold cathode pressure gauge (Pfeiffer Vacuum model TSF 012). The pressure inside the mass spectrometer versus the pressure in the process chamber is plotted in Fig. 43. This low pressure level inside the mass spectrometer is necessary to minimize the number collision between gas species.

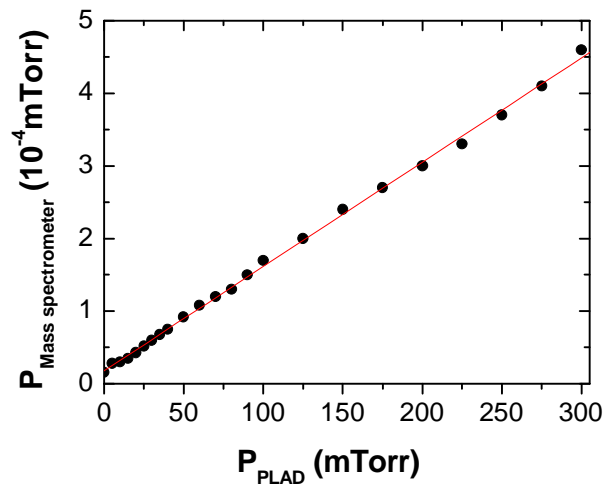


Figure 43: Linear relation between EQP pressure and PLAD process chamber for BF_3

The mass spectrometer is controlled by the MASsoft software, version 3.06, from Hiden Analytical. This software, which operates within a Windows environment controls all the potentials of the instrument different elements and allows for the visualization of the spectra. It enables us to use an “autotune method”, which consists of scanning all the mass spectrometer parameters and selecting for each value that maximizes the signal intensity. The mass spectrometer data is then handled using Origin 7.5 or Excel 2003 software.

Following a particle trajectory from the entrance to the detector, the mass spectrometer is composed of extraction optics (Extractor, Lens 1), an ionization source, a deceleration stage (Axis, Lens2, Quad Lens (Quad, Vert, Horiz)), an energy analyzer, a quadrupole mass filter and a detector. The role of each section is described in detail below.

Extraction optics

The first section of the mass spectrometer (see Fig. 44) is the electrostatic extraction optics. It is composed of an extractor and a focusing lens (Lens1). The extraction sector has two functions. First, it allows for the neutral particle present in the process chamber to penetrate into the mass spectrometer. Second, it is also used to extract positive or negative ions from the plasma.

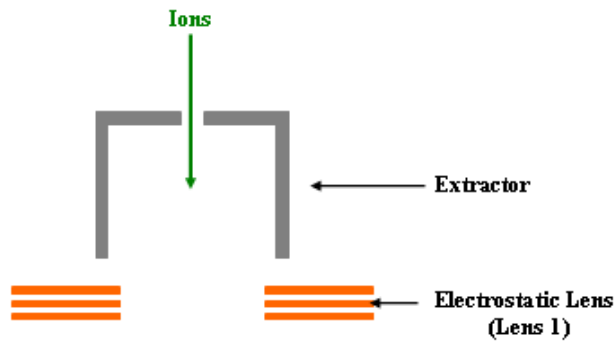


Figure 44: Mass spectrometer extraction section

In the case of neutral analysis, the neutral particles diffuse into the mass spectrometer through the extraction sector. To stop ions from penetrating into the probe and disrupting the neutral analysis, a low positive voltage (10 or 20 V) is applied to the extractor. In the case of positive ion analysis, a negative voltage (-50 to -10 V) is applied to the extractor so as to attract positive ions and proceed to the analysis. In the case of negative ion analysis, a positive voltage (50 to 100 V) is applied to the extractor. The extractor is followed by an electrostatic lens (Lens 1) that is used to focus the extracted ion beam.

Ionization source

In the case of neutral particle analysis, the extraction optics (Extractor and Lens1) are not used. The particles diffuse through the extractor aperture and are ionized by electron impact inside the ionization chamber (Fig. 45).

The ionization chamber is composed of two tungsten filaments and a cage. Using thermo-emission, an electron beam is created by heating up one of the filaments. The electrons are accelerated toward the ionization cage where neutrals are ionized. The

energy of this electron beam is fixed and controlled by applying a potential bias between the filament and the ionization cage.

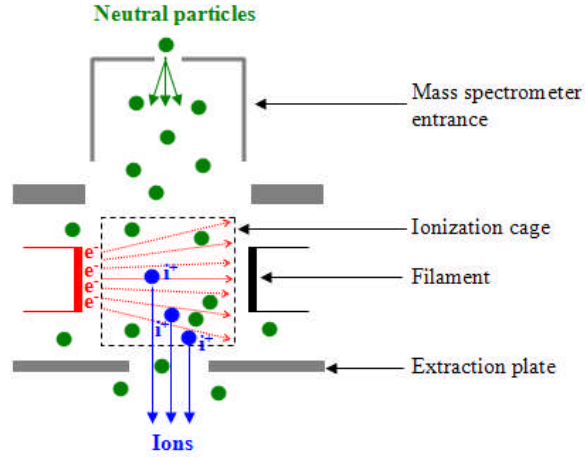


Figure 45: Principle of an ionization chamber by electron impact

The electron impact is a common method used for ion formation [Dawson 1995]. Atoms and molecules are ionized through the following processes [Hippler 2001]:

Ionization of atoms



Direct ionization of molecules



Dissociative ionization



Electrons with high energies can also produce multiply charged ions, such as A^{++} or AB^{++} . The probability of ionization is quantified by the value of the ionization cross-section. For most molecules, single ionization reaches a maximum around 70eV. Therefore, the electron energy is often fixed at 70eV. In the EQP 300, the electron energy can be adjusted from 0 to 150eV, with a step size of 0.1eV, and can be used for threshold ionization mass spectrometry measurements [Kae-nune 1995], [Schwarzenbach1999], [Rolland 2000], [Gaboriau 2006].

Deceleration stage

Subsequently to the extraction stage, a drift tube is positioned after the Lens 1 (see Fig. 46).

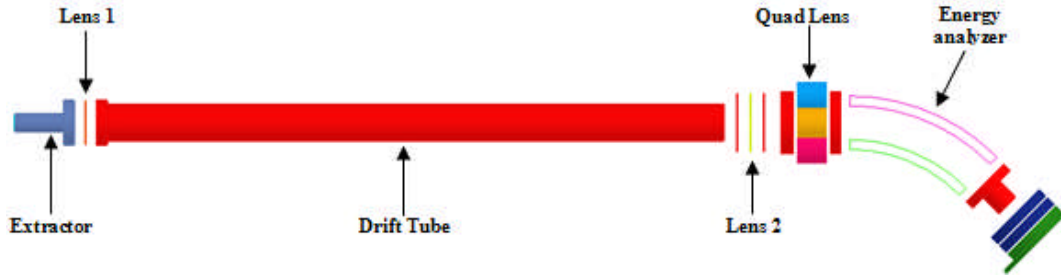


Figure 46: Schematic of the first sections of the EQP mass spectrometer

In the long drift tube of the mass spectrometer, the ions are focused by Lens 2 and decelerated to the energy, which is required to pass through the energy analyzer. The ion transport energy inside the drift tube E_T is fixed by the “Axis potential” ($e \times \text{Axis} = E_T$), usually set to 40eV. The electric field created by the energy analyzer is not null at its entrance and is increasing when the ions come close to it. In order to maintain the ion beam centered inside the EQP, a quad lens is installed in front of the energy analyzer to adjust the beam and correct the beam distortions induced by the electric field at the entrance edge of the 45° electrostatic analyzer.

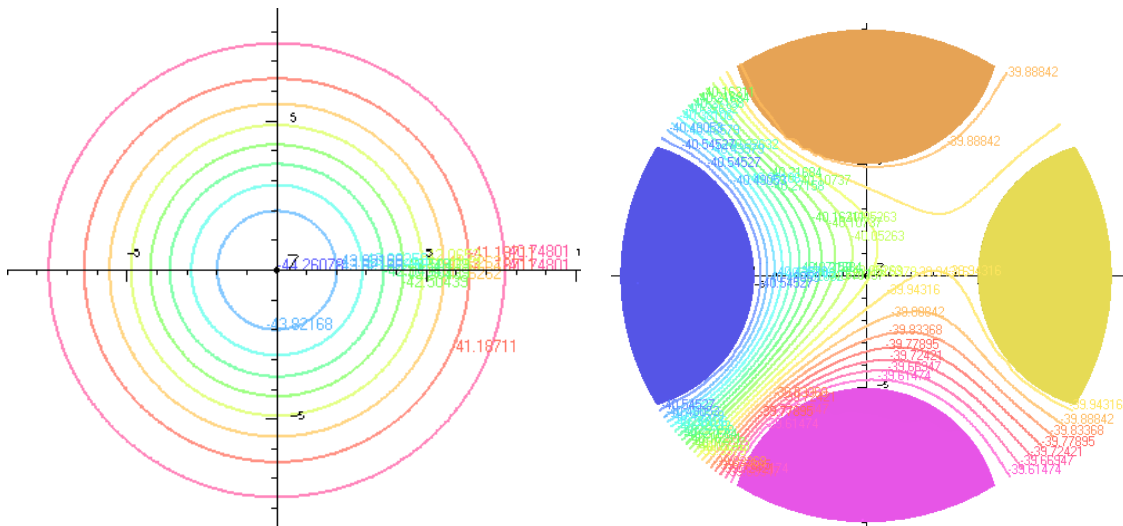
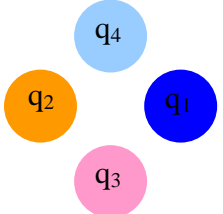


Figure 47: Equipotential distribution inside the mass spectrometer, (right) after the drift tube and before the quad lens, (left) inside the quad lens sector

A non-symmetric electric field is then created by the quad lens. Fig. 47 shows a typical example of the use of the Quad Lens. The equipotential lines are not symmetric after the Quad Lens, which allows for the correction of the ion beam distortions at the entrance of the energy analyzer. The Quad lens also maximizes the number of ions entering the analyzer.

The quad lens is made up four small rods (q_1 , q_2 , q_3 and q_4) on which different voltages are applied. This small device is tuned using 3 different values (Vert, Horiz and D.C. Quad) through the following equations:



$$\left\{ \begin{array}{l} q_1 = 0.02 \times (\text{D.C. Quad}) + 0.04 \times \text{Horiz} \\ q_2 = 0.02 \times (\text{D.C. Quad}) - 0.04 \times \text{Horiz} \\ q_3 = -0.02 \times (\text{D.C. Quad}) + 0.04 \times \text{Vert} \\ q_4 = -0.02 \times (\text{D.C. Quad}) + 0.04 \times \text{Vert} \end{array} \right. \quad \{\text{III.1.5}\}$$

Energy analyzer

The ion energy is then analyzed by a 45° sector electrostatic energy analyzer composed of two cylindrical plates (plate 1 and 2), to which an electric field is applied (Figure 48).

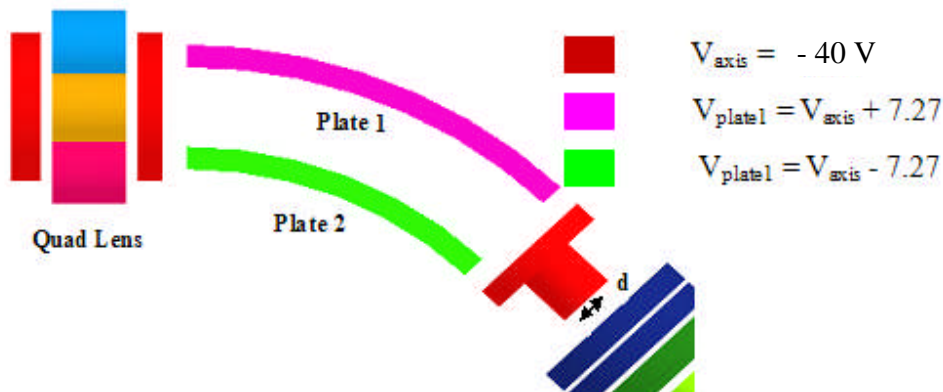


Figure 48: Electrostatic sector analyzer

By applying a potential between plate 1 and plate 2, an electric field is created that deflects ions according to their kinetic energy. To be able to pass through the aperture (d) at the end of the cylindrical energy analyzer, an ion needs to have the energy (E_T) defined by the V_{axis} potential ($E_T = eV_{\text{axis}}$), usually set at 40eV. The energy resolution, ΔE , [Hiden] is:

$$\Delta E = \frac{d \times E_T}{R(1 - \cos \theta) + L \sin \theta} \quad \{\text{III.1.4}\}$$

where the sector angle, mean sector radius, transmission energy and the distance to the exit aperture are defined as θ , R , E_T and L respectively. Under the standard configuration, the exit aperture is 3 mm, the transmission energy is 40eV and the energy resolution is 2.6eV. The energy resolution can be improved by reducing the transmission energy. A complete ion energy distribution can also be obtained by floating the mass spectrometer, using a reference potential from -1000V to +1000V. This way, ions with different initial energies at the entrance of the mass spectrometer will be measured after they are accelerated or decelerated to the correct transmission energy.

Quadrupole mass filter

The quadrupole mass spectrometer (QMS) is the most widely used analyzer for low-resolution applications and is the most important in plasma diagnostics [Paul 1953, Drawin 1968, Dawson 1995 and Vasile 1989]. Only the main characteristics of the quadrupole devices will be reviewed here, more details can be found in Edmond Hoffmann and Peter Dawson's books [Dawson 1995, Hippler 2001, Hoffmann 2002]. The quadrupole mass filter ideally consists of four, parallel, hyperbolic, conducting rods, but cylindrical rods are used in practice. A potential that combines a dc potential (U_{dc}) with a radiofrequency potential ($V_{\text{rf}} \cos(\omega t)$) of frequency $f = \omega/2\pi$ is applied on each rod; the opposite rod has the same potential (Fig. 49).

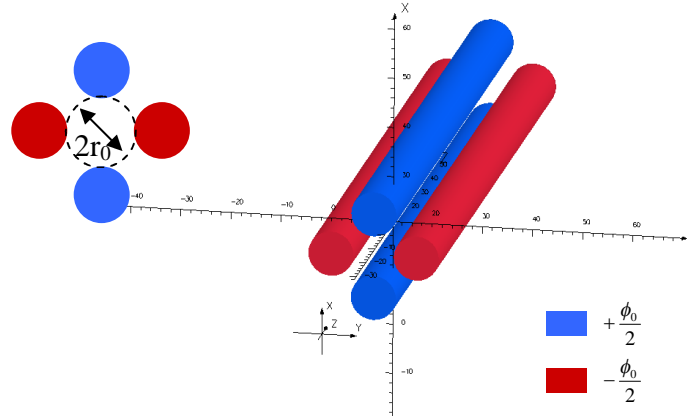


Figure 49: Quadrupole with cylindrical rods and applied potentials

The trajectories of ions of mass M and charge Ze are governed by the following equations:

$$\frac{d^2x}{dt^2} + \frac{Ze}{Mr_0^2} (U_{dc} - V_{rf} \cos \omega t)x = 0, \quad \{\text{III.1.6}\}$$

$$\frac{d^2y}{dt^2} - \frac{Ze}{Mr_0^2} (U_{dc} - V_{rf} \cos \omega t)y = 0, \quad \{\text{III.1.7}\}$$

$$\frac{d^2z}{dt^2} = 0, \quad \{\text{III.1.8}\}$$

The ions maintain their velocity in the z direction and oscillate transversally in the x and y directions. Their movement in the axial direction near the center of this system is described by the Mathieu differential equation [Dawson 1995]:

$$\frac{d^2u}{d\xi^2} + (a - 2b \cos 2\xi)u = 0 \quad \{\text{III.1.9}\}$$

where $u = x$ or y , $\xi = \frac{\omega t}{2}$, $a = a_x = -a_y = U_{dc} \frac{Ze}{M} \frac{4}{\omega^2 r_0^2}$ and $b = b_x = -b_y = V_{rf} \frac{Ze}{M} \frac{2}{\omega^2 r_0^2}$

The solution to Mathieu's equation can be expressed by:

$$u(\xi) = \alpha' e^{\beta\xi} \sum_{n=-\infty}^{+\infty} C_{2n} e^{2in\xi} + \alpha'' e^{-\beta\xi} \sum_{n=-\infty}^{+\infty} C_{2n} e^{-2in\xi} \quad \{\text{III.1.10}\}$$

where α' and α'' are the integral constants, which depend on the initial conditions at the mass filter entrance. The constants C_{2n} , β and the nature of the ion motion depend on the values of a and b and not on the initial conditions. This is an important characteristic of the Mathieu equation. The solutions of the Mathieu equation are sinusoidal or exponential. If the oscillation amplitude is small, the ions can pass through the mass filter, but for larger oscillations, the ions will be lost and neutralized by striking one of the rods.

The conditions of the ion trajectories stability are presented in Fig. 50. The quadrupole of the EQP 300amu operates at a constant frequency of 1.6 MHz. For an ion of any mass, x and y can be determined and stability regions can be defined on Fig 50. Ions with masses below the stable region on the diagram of stability are deflected along the x -direction toward the rods. The ions with masses above this region are deflected along the y -direction.

The operational lines are defined by different values of U_{dc} and V_{rf} with constant U_{dc}/V_{rf} ratio. Fig. 50 shows that if the operation line crosses the top of the stability regions, a good mass resolution can be achieved (M_1 and M_2 are well separated). On the contrary, if the slope of the line is lower, the resolution is reduced (M_1 and M_2 are not resolved when the operation line slope is too low). The mass resolution is then controlled by the operation line slope. By changing the U_{dc} and V_{rf} through a constant ratio (thus changing a and b while keeping the same operational line), other ions can pass through the mass filter and reach the detector. This is the way that a mass spectrum is scanned.

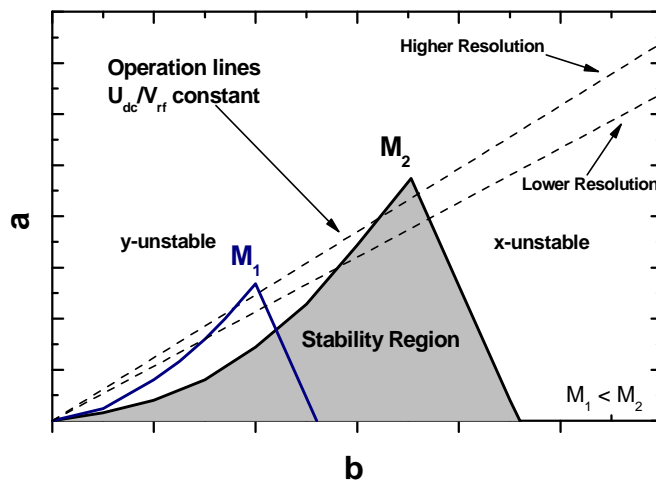


Figure 50: Mathieu diagram of stability of the ion movement in a quadrupole field for two different mass ($M_1 < M_2$)

The mass resolution of the quadrupole, which depends on the number n of ion oscillation cycles through the quadrupole, is defined by the following empiric relation [Dawson 1995, Perrin 1997]:

$$\frac{M}{\Delta M} = \frac{n^2}{12.2} \quad \text{With } n = \omega L_q \sqrt{\frac{M}{2E_z}} \quad \{\text{III.1.11}\}$$

where L_q is the length of the quadrupole and E_z is the ion energy in the z direction of the quadrupole.

Detector

After the quadrupole, the ion strikes the input face of the channeltron (Fig. 51) and typically produces two to three secondary electrons. The input face of the channeltron is a secondary emitting surface. These electrons are accelerated inside the detector through a positive bias. They then strike the channel walls and produce additional electrons. This phenomenon occurs several times and is called a cascade of electrons. At the end of the channel, a pulse of 10^7 to 10^8 electrons emerges for one impinging ion. For positive ion detection, the first dynode is usually at a negative voltage of around -1200V and the output is at a positive voltage. The detection efficiency is defined as the probability of an incident-charged particle to produce an output pulse and create a count. This parameter depends on the ion energy at the point of impact and the ion mass to charge ratio (m/z) [Reagan 1987]. Usually channeltron detection efficiency decreases with the ion mass.

This kind of device does have several drawbacks, including its limitation to 5×10^6 counts per second. However, the output signal does not need to be amplified, which allows a low count per second detection due to the low signal-to-noise ratio.

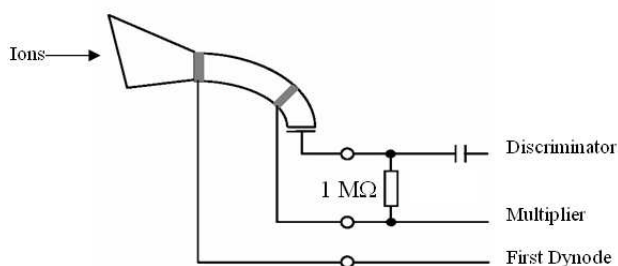


Figure 51: Channeltron Electron Multiplier [Hiden]

In order to maintain a stable measurement, the operational stability of the detector needs to be checked regularly, and the detector should operate at a voltage just below the plateau region where the number of counts does not change with the multiplier voltage (Figure 52).

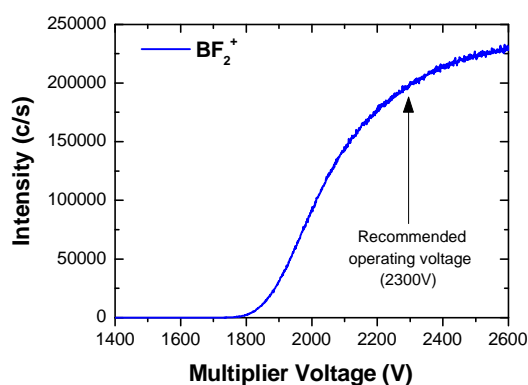


Figure 52: Typical Detector operating curve

The supplier [Hiden] recommends to set the multiplier at 90% of the maximum intensity (the plateau area). The lifetime of the detector can be improved a hundred times when the mass spectrometer pressure is reduced from 1×10^{-6} to 1×10^{-8} Torr. The sensitivity of the channeltron electron multiplier is not constant; as the multiplier inner surface ages, the voltage must be increased. In this study, the Multiplier's voltage has been increased from 1850V to 2300V during the whole experimental period and has been weekly calibrated in RGA mode.

Time-resolved mass energy spectrometry

In order to perform time-resolved measurements, the EQP analyzer is gated by a TTL pulse (5V positive square pulse) that is synchronized with the PLAD voltage pulse (Fig. 53). A delay generator synchronized to the PLAD voltage pulse is used to vary the delay time between 0 and 500 μ s. A 2 μ s time resolution is achievable and the delay time between the TTL pulse and PLAD pulse is adjustable, so as to allow ion sampling at the beginning, middle or end of the PLAD pulse. A narrow TTL pulse leads to a good time resolution, but low count rate, and usually a balance between resolution and statistics is necessary. The acquisition time slot was set from 5 to 50 μ s. For all measurements in this work, $t=0$ was defined by the start of the wafer bias voltage.

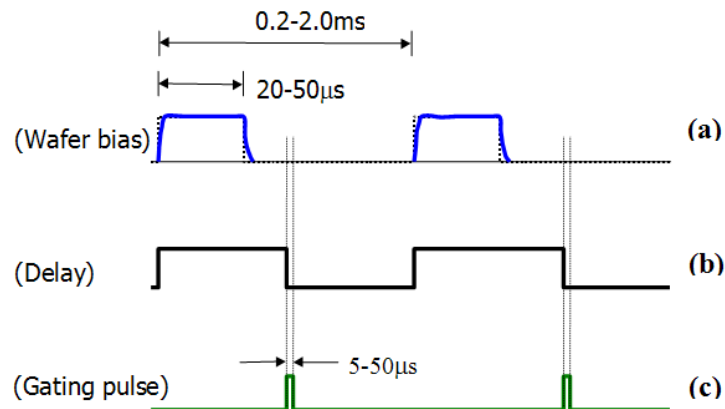


Figure 53: Schematic timing diagram of the time-resolved ion mass and energy measurements. Shown above are the timing scales for time-resolved ion mass and energy measurements: (a) the wafer bias voltage, (b) delay signal, and (c) gating pulse [Koo 2004].

Transit time

For time-resolved acquisition, the transit time of the ions inside the mass spectrometer must be known. In order to estimate this transit time, the apparatus will be divided into four sections [Hiden] (Fig. 54):

- Extraction section
- Energy analyzer section
- Mass filter section
- Detector section

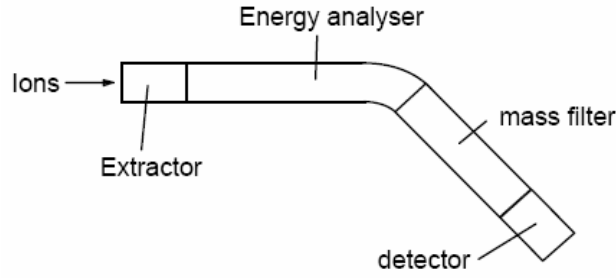


Figure 54: Transit time inside the mass spectrometer divided in four sections [Hiden]

The total transit time inside the mass spectrometer is defined by:

$$\tau = \tau_{\text{ext}} + \tau_{\text{ena}} + \tau_{\text{mass}} + \tau_{\text{det}} \quad \{\text{III.1.12}\}$$

The extractor and energy analyzer are treated with a 3D electrostatic model (described later) for better accuracy, while the mass and detection sections are treated analytically.

- **Mass Filter Sector**

Ions transit through this sector with an energy defined by the entrance and exit energy called Transit-Energy (voltage V_{te}), which is adjustable. The transit time is [Hiden]:

$$\tau_{\text{mass}} = s_{\text{mass}} \sqrt{\frac{M}{2eV_{\text{te}}}} \quad \{\text{III.1.13}\}$$

with s_{mass} being the length of the mass filter sector. In our case, s_{mass} is equal to 0.1778m.

- **Detector section**

When the ions enter this section with a constant energy, they are accelerated through the first dynode potential. The entry energy for this section will be neglected and set to zero, which does not cause a significant error. The transit time inside this section is [Hiden]:

$$\tau_{\text{det}} = s_{\text{det}} \sqrt{\frac{2M}{eV_{\text{dyn}}}} \quad \{\text{III.1.14}\}$$

with s_{det} being the length of the detector section and V_{dyn} the first dynode voltage. In our case, s_{det} is equal to 0.0415m.

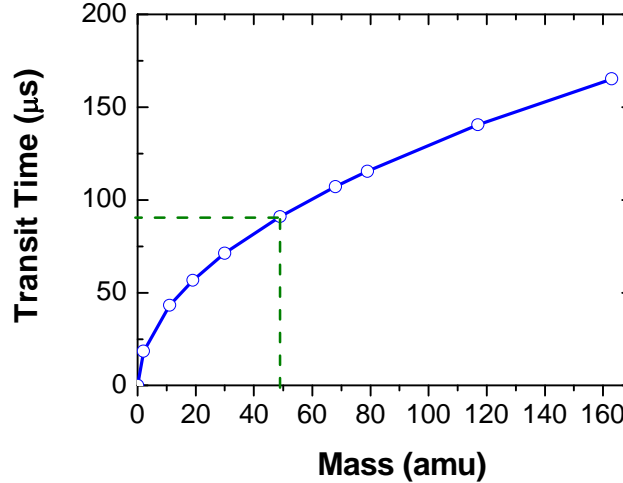


Figure 55: Calculated transit time into the mass spectrometer for different masses with the calibration set-up of a 500V 75mTorr PLAD implantation

Fig. 55 shows the calculated ion transit time into the EQP as a function of the ion mass using the experimental calibration set-up of a 500 eV ion during a 500 V 75 mTorr PLAD implantation. As expected, the transit time into the mass spectrometer is longer in the case of higher ion masses. The ion transit time difference between 500 eV and 10 eV BF_2^+ is less than 1 μs and will be neglected in all the time resolved mass spectrometry measurements.

Mass spectrometer considerations and experimental set-up

Mass spectrometry goal and motivations for this study

The main goal of this mass spectrometer study is to accurately measure the Ion Energy Distribution (IED) of the ions reaching the PLAD cathode for the sub-KeV plasma-based ion implantation. The energy and mass transmission inside the mass spectrometer need to be investigated and optimized to obtain an accurate result. A three-dimensional (3D) electrostatic model of the mass spectrometer was developed to

optimize the transmission and calculate the ion transit time as well as the angular acceptance of the mass spectrometer.

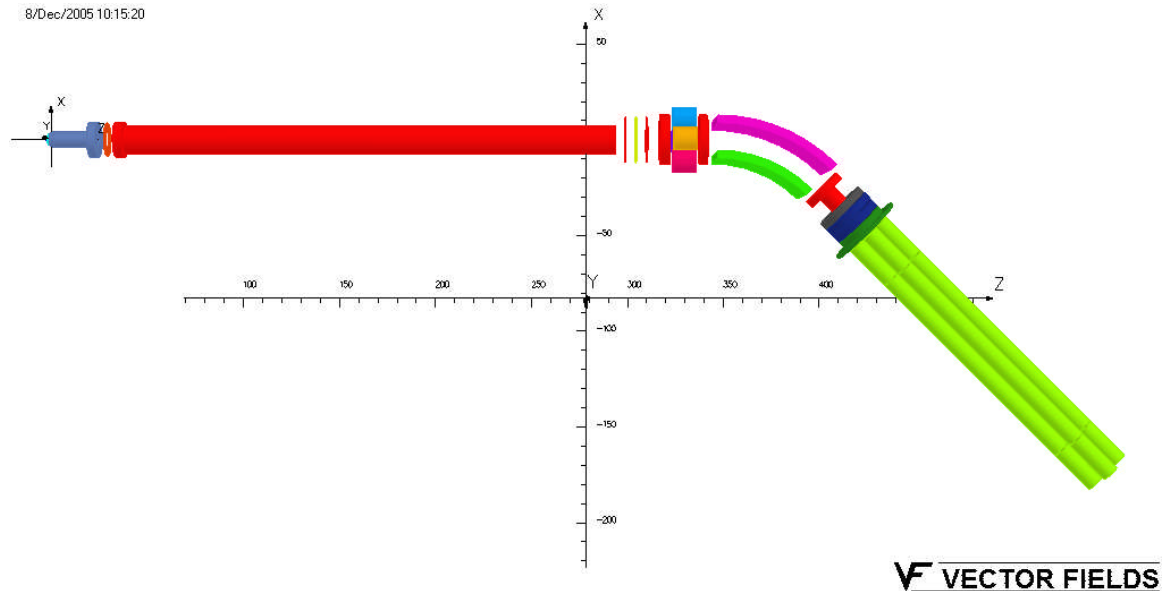


Figure 56: 3D electrostatic model of the EQP

The model was created using Opera 3D software from Vector Fields. Previous electrostatic simulations [Hiden, Budtz-Jorgensen01 and Low 1995] were made using two-dimensional electrostatic software reaching up to the entrance of the energy analyzer. The non-linear parts of the EQP, such as the quad lens in front of the energy analyzer, need to be simulated using a 3D model. Fig. 56 shows a picture of the 3D model used here. It is composed of the extraction optics, the drift tube, the quad lens, the energy analyzer and the focusing lens.

Modification of the optics voltage set-up

- *Original configuration :*

In the original configuration of the mass spectrometer, the extractor and Lens 1 voltage were controlled by an external power supply. All the other voltage settings of the mass spectrometer were connected to a reference voltage, which was scanned to measure

ions with energies ranging from 0 to 1000eV. This configuration proved to be inadequate for a time-resolved pulsed plasma study.

In this particular configuration, as Extractor and Lens 1 potentials were fixed, all the ions from the plasma penetrated into the mass spectrometer. Energetic ions were decelerated after Lens 1. As the deceleration took place after the first electrostatic lens, there was no focusing lens before the drift tube. The divergent ion beam was thus propagated up to the entrance of the energy analyzer, diverging inside the drift tube. The ion beam angular spread was too large and all the ions could not pass through the three-millimeter aperture at the end of the energy analyzer, as illustrated in Fig. 57.

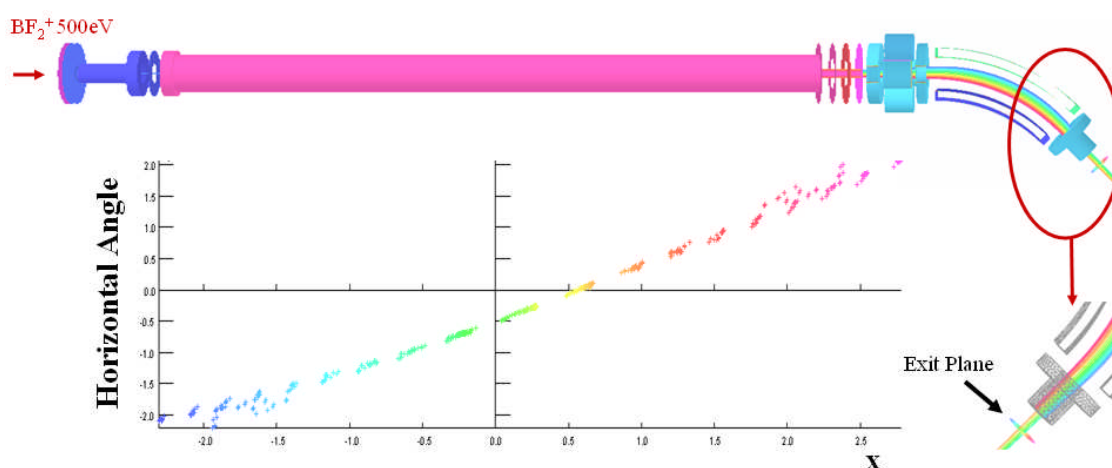


Figure 57: Beam trajectory inside the mass spectrometer model and divergence angle of a 500eV BF_2^+ measured at the exit plane of the energy analyzer and zoom on the exit of the electrostatic energy analyzer of the mass spectrometer model

Moreover, the extractor voltage needed to be set to a lower value than the cathode voltage to be able to monitor all ions whatever their energy (from 0 to 1000eV). When the cathode voltage was returned to zero volts during the pulse-off period, ions from the afterglow were accelerated and detected as energetic ions.

This configuration created several transmission problems for the energetic ions inside the mass spectrometer. As shown in Fig. 58, the calculated transmission efficiency of normal incident ions inside the mass spectrometer was not constant for the range of ion energies studied. It rapidly decreased for ion energies higher than 200eV.

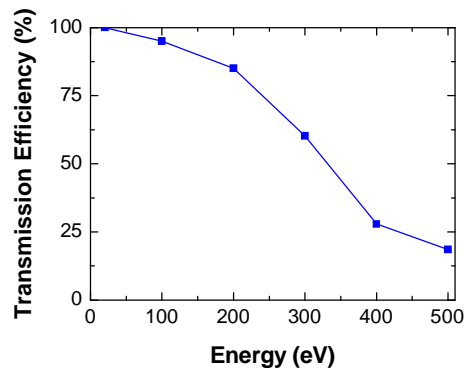


Figure 58: Calculated transmission efficiency of 100 to 500 eV BF_2^+ ion with normal incidence at the entrance of the mass spectrometer

This was confirmed by the ion energy distribution of BF_2^+ ions reaching the cathode with different cathode voltages as shown in Fig. 59. These distributions were experimentally measured during the pulse-on period. Depending on the wafer current density, the relative total ion flux should increase with the cathode voltage (see section II.2.2.2.a). However, the measured relative BF_2^+ flux is strongly decreased when the cathode voltage is raised.

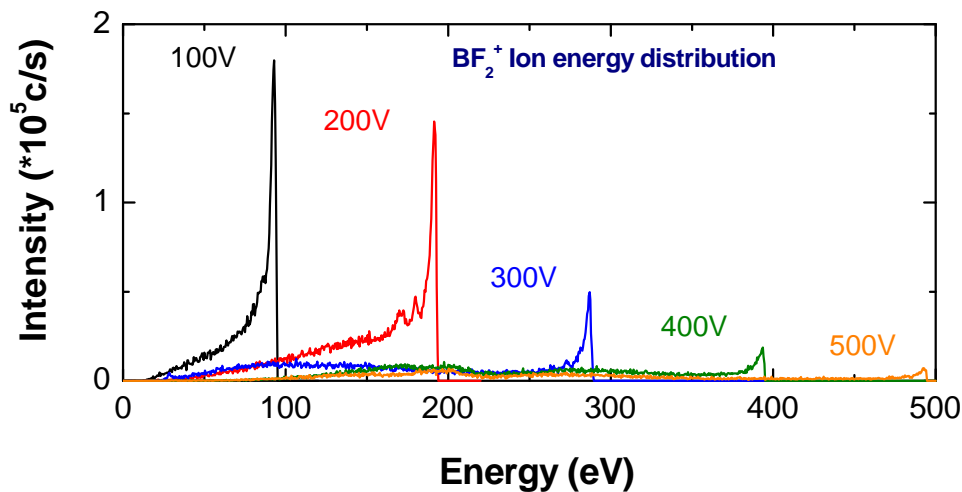


Figure 59: BF_2^+ ion energy distribution measured during the pulse-on period at different cathode voltage from 100 V to 500 V at 30 mTorr, 2500 Hz with 10 cm anode to cathode spacing in the hollow cathode mode pulsed at 1500 V

In short, this mass spectrometer operation set-up was not suitable for our purposes, because it presented problems with the time-resolved measurements and with the transmission efficiencies of the energetic ions.

- ***Pulsed extraction configuration:***

In order to solve the transit-time problem inside the mass spectrometer, a pulsed extraction system linked to the cathode-pulsed voltage was used. A constant dc voltage was added to the cathode voltage. This mode of operation led to a constant extraction voltage during the pulse-on and the afterglow and the afterglow, ions were thus not measured as energetic ions. However, the energetic ions from the pulse-on period still decelerate after the Lens1. The energetic ion transmission inside the mass spectrometer still remains a problem under this mode of operation.

- ***Extraction optics voltage linked to the reference potential:***

Following this first set of experiments, a further configuration of the mass spectrometer was investigated. Based on the mass spectrometer's electrostatic simulation, the extraction sector's voltage set-up was modified. The whole mass spectrometer can thus be floated from 0 to -1000 V, which allows us to scan ion energies ranging from 0eV to 1000eV. The extractor and Lens 1 voltages are now linked to the reference potential of the mass spectrometer (see Fig. 60).

A comparison of the different potentials applied on the front of the mass spectrometer under the new configuration and the original configuration, with the calibration used for a 500V implantation, can be found in Appendixes 1a and b. Under this mode of operation, the energetic ions are decelerated between the cathode and the extractor, and the focal point is optimized by Lens 1 to obtain a better focusing of the beam. Appendix 1 also shows a comparison of the divergence angles of 500 eV BF_2^+ at the end of the mass spectrometer drift tube for the original and new electrostatic lenses set up at the entrance of the mass spectrometer. The angular spread created by the

deceleration is reduced by a factor of 3 when the Extractor and Lens 1 are linked to the reference.

In the case of a cathode voltage of -1000V, with the reference voltage at 0V, ions of 1000eV are measured; with a reference voltage of -500V, ions of 500eV are measured; and with a reference voltage of -1000V, low-energy ions are measured.

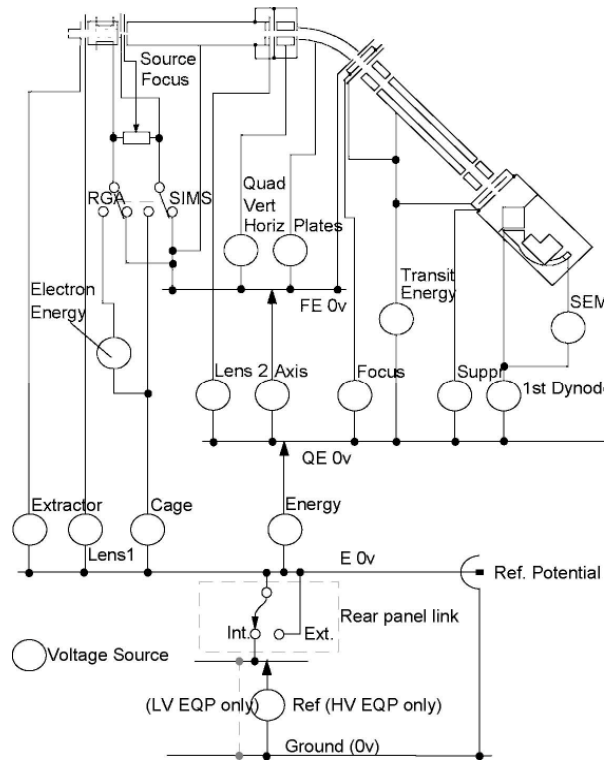


Figure 60: Mass spectrometer voltage set-up

The ion calculated transmission efficiency is constant inside the mass spectrometer for the full range of ion energies analyzed here. When using time-resolved measurement, ions from the pulse-on and from the pulse-off can be easily separated. This mode will be the one used in all of the following experiments.

Mass spectrometer transmission and angular acceptance

Under all the experimental conditions used ($V_b = -1000 \text{ V}$ to 0 V), all ions with a normal incidence angle has 100 % transmission efficiency inside the mass spectrometer up to the entrance of the quadrupole. As all the operating voltages are floated on the

reference potential and the deceleration of the energetic ions occurs before the entrance of the mass spectrometer, the EQP operates in a correct manner. The Lens 1 can focus the ion beam before the drift tube and a good transmission is achievable.

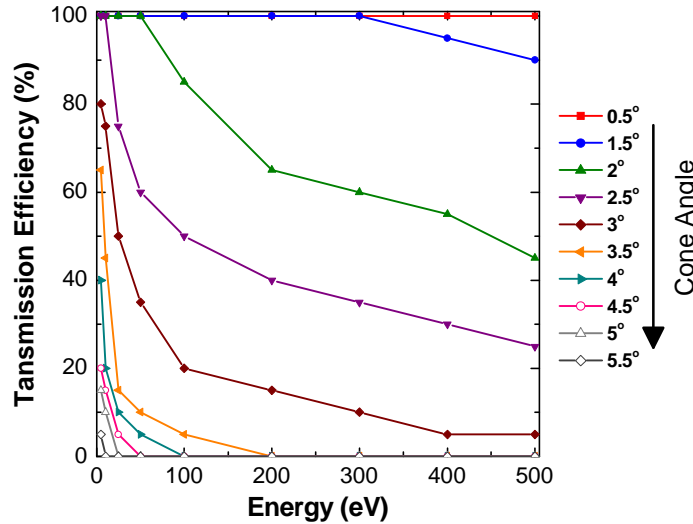


Figure 61: BF_2^+ transmission efficiency inside the mass spectrometer with different cone angle at the entrance of the EQP with the experimental settings of a 500V 100mT PLAD implant

A simulation of the transmission efficiency of BF_2^+ ions when using different entrance angles ranging from 0.5° to 5.5° is presented in Fig. 61. The experimental calibration of the EQP during a 500V 100mT PLAD implant is used as an input for the simulation. The transmission efficiency is maintained at 100% for incident angles up to 1° , while it decreases quickly for incident angles greater than 2° . However, under our experimental conditions, ions are suspected to have a low incidence angle ($< 1^\circ$) [Vahedi 1992].

Experimental study of the mass spectrometer transmission

The goal of this section is to establish the experimental mass transmission inside the mass spectrometer when the mass spectrometer is operated in SIMS mode. As it is difficult to compare directly the incident number of ion entering the EQP to the number of ions detected by the channeltron, the calibration is performed using the EQP RGA mode.

The global mass transmission inside the mass spectrometer is estimated using the RGA operation mode at a constant gas pressure, with different rare gases of mass m such as helium, neon, argon and xenon. Each ion specie m_j created through electron impact ionization of the parent molecule inside the ionization chamber is accelerated to 40eV before reaching the detector. The intensity of each ion species of mass m_j that is detected can be expressed as [Chevolleau 1998, Singh 1999]:

$$I(m_j) \propto n_s(m) \times I_e \times F(m_j) \times \sigma(m_j) \quad \{\text{III.1.15}\}$$

with

- $I(m_j)$: the measured relative intensity of the ion with mass m_j
- $n_s(m)$: gas density inside the mass spectrometer
- I_e : electronic emission current
- $F(m_j)$: transmission factor of an ion with a mass m_j inside the mass spectrometer
- $\sigma(m_j)$: ionization cross-section of neutral particle of mass m into an ion of mass m_j

For all of the different rare gases used, the extraction efficiency from the ionization cage is estimated to be constant [Singh 2000]. As the pressure inside the process chamber is linearly proportional to the mass spectrometer pressure for the pressure range used, the relation {II.1.15} becomes:

$$I(m_j) \propto n_{\text{PLAD}}(m) \times I_e \times K(m) \times F(m_j) \times \sigma(m_j) \quad \{\text{III.1.16}\}$$

with

- $n_{\text{PLAD}}(m)$: gas density inside the PLAD process chamber
- $K(m) = \frac{n_s(m)}{n_{\text{PLAD}}(m)} = \frac{P_s}{P_{\text{PLAD}}}$: transmission coefficient of the mass spectrometer entrance aperture for a gas of mass m

The transmission coefficient of the mass spectrometer aperture is equal to the ratio of pressure inside the mass spectrometer P_s to the pressure inside the process chamber P_{PLAD} . As the pressure of the mass spectrometer is measured using a cold cathode gauge, the pressure measured for different gases needs to be corrected using a compensation factor supplied by Pfeiffer Vacuum [Pfeiffer]. In the range below 10^{-5} mTorr, the pressure correction is linear with pressure. For gases other than air, the pressure can be determined through a simple formula:

$$P_s = K1 \times \text{Pressure indicated} \quad \{\text{III.1.17}\}$$

The K1 conversion factor is shown in table 3.

Gas type	K1
Air (N2, O2, CO)	1
Xe	0.4
Kr	0.5
Ar	0.8
Ne	4.1
He	5.9

Table 3: Conversion factor for different gases for the cold cathode pressure gauge Pfeiffer Vacuum model TSF 012

Using conversion factor from table 3, the pressure inside the mass spectrometer is corrected and plotted as a function of the pressure inside the PLAD process chamber ranging from 0 to 300mTorr in Fig. 62 for helium, neon, argon and xenon.

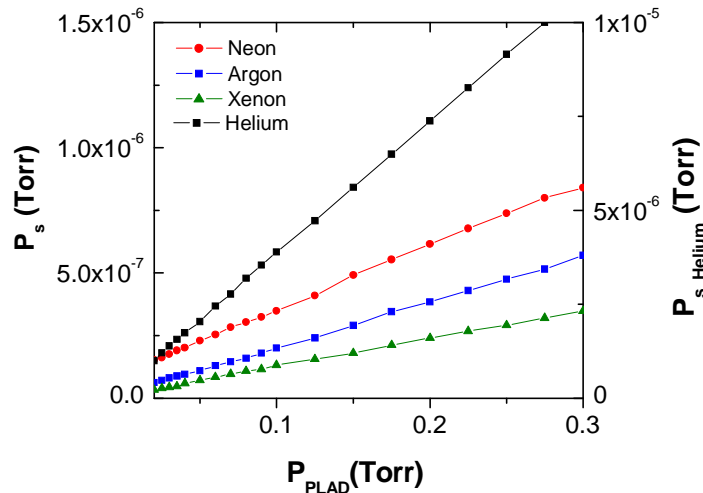


Figure 62: Mass spectrometer corrected pressure P_s versus the PLAD process chamber pressure for helium, neon, argon and xenon

The coefficient $K(m)$ is estimated using the slope of the straight line P_s versus P_{PLAD} for different gases. The transmission coefficient at the entrance of the mass spectrometer rapidly decreases when the mass rises and is inversely proportional to the square root of the mass. Fig. 63 shows its evolution for different gases.

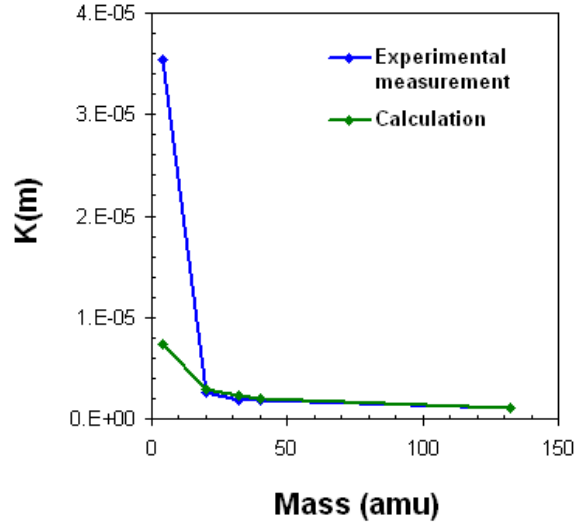


Figure 63: Experimental and calculated entrance aperture transmission factor as a function of mass

The $K(m)$ can also be calculated analytically using the conductance of the entrance aperture. The thickness of the aperture will be neglected in this calculation and a simple schematic of the experimental set-up is shown in Fig. 64.

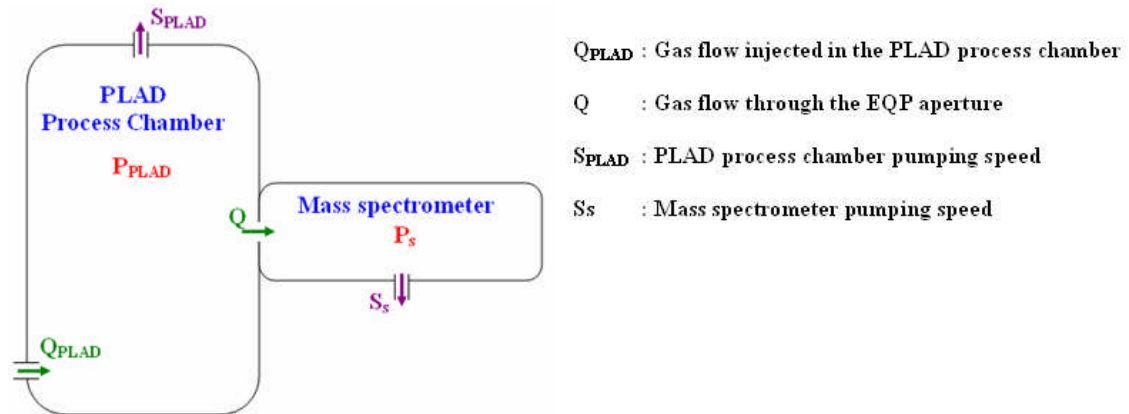


Figure 64: Schematic of the experimental system

In the case of molecular flow, the gas flow through an entrance aperture is governed by the following equation [O'Hanlon 2003]:

$$Q = A \times \left(\frac{kT}{2\pi m} \right)^{1/2} \times (P_{PLAD} - P_S) \quad \{\text{III.1.18}\}$$

where A is the area of the mass spectrometer entrance orifice. As observed previously, P_{PLAD} is much higher than P_S , so equation {III.1.18} becomes:

$$Q = A \times \left(\frac{kT}{2\pi m} \right)^{1/2} \times (P_{PLAD}) \quad \{\text{III.1.19}\}$$

The gas flow Q can also be expressed as a function of mass spectrometer pressure P_S and pumping speed S_S :

$$Q = P_S \times S_S \quad \{\text{III.1.20}\}$$

Using the equations {III.1.19} and {III.1.20}, which linked the flux Q as a function of P_{PLAD} and P_S , the entrance aperture transmission factor can be expressed by the following equation:

$$K(m) = \frac{P_S}{P_{PLAD}} = \frac{A}{S_S} \times \left(\frac{kT}{2\pi m} \right)^{1/2} \quad \{\text{III.1.21}\}$$

This analytical aperture transmission factor is then inversely proportional to the square root of the mass and can explain the shape of the K(m) obtained experimentally in Fig. 63.

The calculated K(m) is in good agreement with the one experimentally measured for masses greater than 20 amu but in the case of helium a strong disagreement is observed. K(M) experimentally was measured using the reading of a cold cathode gauge. According to the gauge supplier, the conversion factor inaccuracy of the type of gauge that is used on the mass spectrometer is greater than 15%.

When the mass of the parent molecule is identical to the ion mass created ($m = m_j$), the global transmission coefficient T(m) of the mass spectrometer $T(m) = K(m) F(m)$. {II.2.13} becomes:

$$I(m_j) \propto n_{\text{PLAD}}(m) \times I_e \times T(m) \times \sigma(m_j) \quad \{\text{III.1.22}\}$$

In order to experimentally estimate the global transmission coefficient, we kept a constant pressure of 50mTorr inside the process chamber for each gas used (He, Ne, Ar, Xe). A constant emission current of 100 μ A and a 70eV electron energy was maintained inside the ionization chamber. The electron impact cross-section at ionization energy of 70eV for the different gases is presented in Table 4, based on the compilation of electron cross-sections by A. V. Phelps [Phelps].

Gas Species	Ion Species	Ionization cross section at 70eV 10^{-16} cm^2
He	He ⁺	0.313
Ne	Ne ⁺	0.5139
Ar	Ar ⁺	2.675
Xe	Xe ⁺	5.146

Table 4: Ionization cross section at 70eV for different gases [Phelps]

Fig. 65 shows the evolution of the global transmission factor, T(m) for different gases. The coefficient T(m) decreases rapidly when the mass is increased, for masses ranging from 0 to 20amu. For masses higher than 20amu, the coefficient is mostly constant.

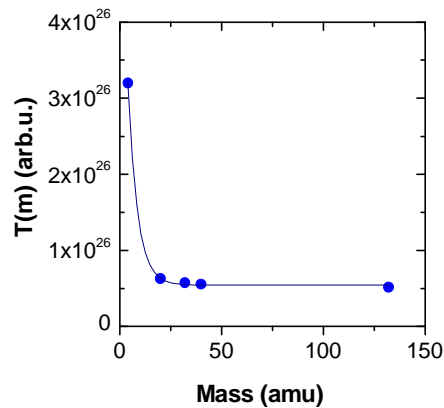


Figure 65: Mass spectrometer global transmission factor as a function of mass

The mass spectrometer transmission $F(m)$ is estimated using the global transmission factor and the entrance aperture transmission factor through the following relation:

$$F(m) = \frac{T(m)}{K(m)} \quad \{\text{III.1.23}\}$$

$F(m)$ has been normalized by $F(40\text{amu})$. Fig. 66 shows the normalized transmission inside the mass spectrometer (energy analyzer, quadrupole and channeltron). The experimental transmission based on the measured $K(m)$ and the calculated $K(m)$ are in good agreement except for the helium point.

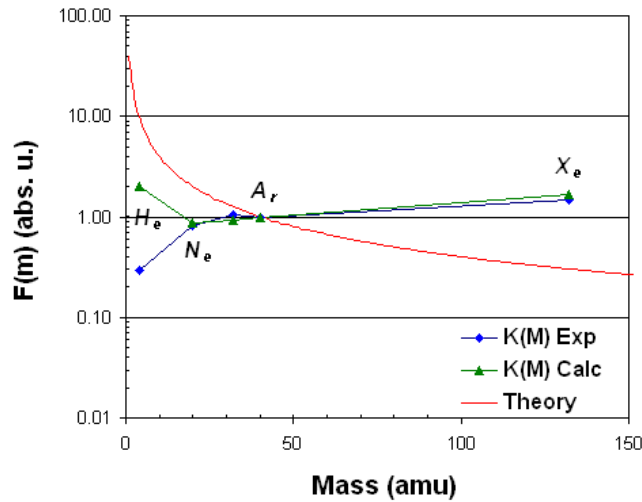


Figure 66: Mass spectrometer transmission factor as a function of mass normalized to the argon transmission using the experimentally measured and calculated $K(M)$ and compared to the theoretical mass spectrometer transmission

The mass transmission inside the mass spectrometer given by the supplier is proportional to the product of the transmission efficiency of the quadrupole mass filter, $t(m)$ and the detection efficiency of the channeltron detector $\theta(m)$ and is estimated to follow a curve $1/m$ [Dawson 1995, Kessels 1999].

$$F(m) \propto t(m) \times \theta(m) \approx m^{-0.5} \times m^{-0.5} \approx m^{-1} \quad \{\text{III.1.24}\}$$

The expected transmission curve normalized to the argon transmission is plotted in red in Fig 66. However, this curve does not fit the experimental points with the calculated $K(m)$ or the experimentally measured $K(m)$. One of the possible explanations for the difference between expected transmission and the measured transmission maybe due to the way the calibration was performed. The measurements of IED for different gases were performed using the Argon calibration. The transmission of the mass 40 was then optimum but most probably the optimized argon settings are not the optimum setting for the masses 20 or 4. The mass 40 is then privileged compared to the light masses and the transmission does not follow an $1/m$ equation.

In chapter V, part 2, the dopant depth profile is predicted based on the measured IED. This correlation shows that the simulation and SIMS profile are in good agreement and therefore confirms that the mass transmission is not proportional to $1/m$ equation (the prediction profile will not match the measured dopant depth profile if the mass transmission varied as m^{-1}).

In summary, when settings are optimized for argon (mass 40), the transmission slightly decreases for lighter ion masses. In the following, settings are optimized for BF_2^+ (mass 49) and the transmission probably slightly decreases for masses lighter than 49 (B, $m = 10$ for example). However, due to the uncertainties listed above the relative ion fraction will not be corrected and the mass transmission will be assumed to be constant for the whole range of mass studied (1 to 150 amu).

Bulk plasma study: mass spectrometer inside the anode

For Bulk plasma studies, a special anode was designed to insert the mass spectrometer in the middle of the grounded electrode. As shown in Fig. 67, the ion mass and energy analyzer (EQP) was installed above the anode plate.

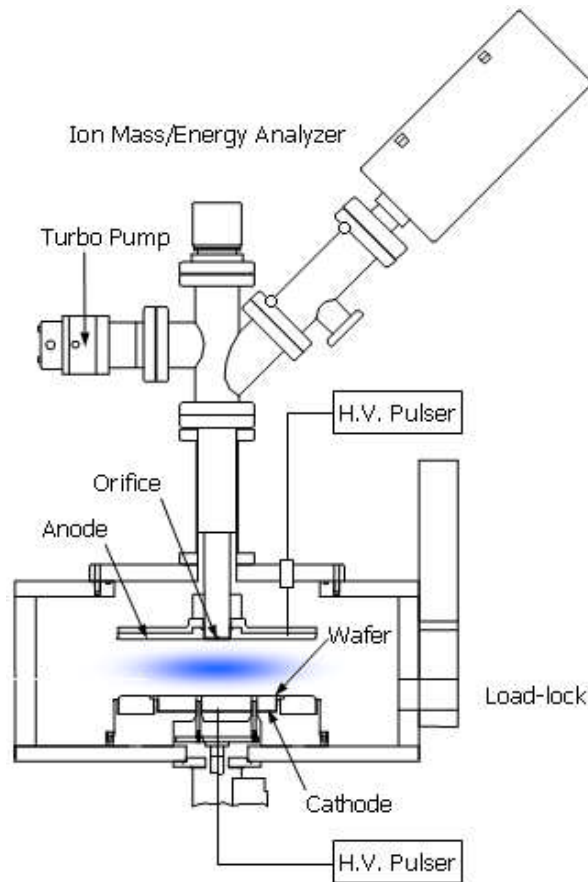


Figure 67: Schematic diagram of PLAD process chamber with an ion mass and energy analyzer installed in the center of the anode

The EQP analyzer is electrically isolated from the anode plate by a small vacuum gap. Ions reaching the anode enter the probe through a 100 μm diameter aperture at the center of the anode. The 100 μm diameter aperture also provides the differential pumping needed to reach high vacuum ($<1.5 \times 10^{-6}$ Torr) inside the EQP probe. The small aperture on the anode also minimizes disturbances to the local plasma and electric field. The bulk plasma ion species could be studied using this mass spectrometer set-up. An example of time resolved measured ion energy distributions for a Ar^+ , 3 kV, 30 mTorr discharge is presented in Fig. 68.

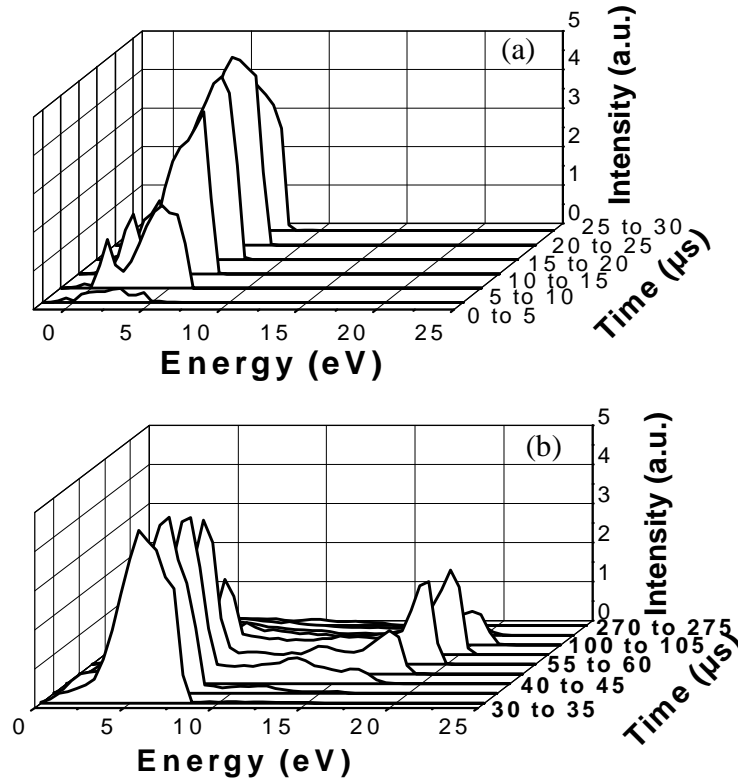


Figure 68: Time-resolved IEDs of Ar^+ ion incident to a grounded anode surface, 3 kV bias, 30 μs pulse, 2500 Hz frequency, and 30 mTorr. (a) Pulse-on, (b) pulse-off [Radovanov 2005]

The distributions are measured from 0 - 30 μs during the pulse on and from 30 to 275 μs during the pulse-off period with a time resolution of 5 μs . The shape and average energy during the pulse on and pulse-off periods depend on the time over which the distributions are accumulated.

The build up of the ion-energy distributions approaching the steady state is evident from the time resolved distributions shown in Fig 68a. The IEDs at the beginning of the pulse have two peaks, one at ~ 1 eV and the other at ~ 5 eV. The small peak at the lower energy level is related to the initial stage of the pulse-on period, while the larger peak at the higher energy level corresponds to the fully developed plasma and the early stage of afterglow. The energy of the larger peak is approximately equal to the plasma potential as measured by the Langmuir probe. The plasma potential peak is not only determined by the pulse voltage and pressure, but also by the pulse width, duty cycle ratio, electrode surface conditions and plasma chemistry. Due to the positive voltage overshoot, the plasma is maintained after the pulse is switched off. The plasma response

to the overshoot is visible in the Ar^+ IEDs during the afterglow (see Fig 23 and Fig 68b), which is centered at a new V_p value around 20eV. After the pulse-on, cold plasma decays for several hundred microseconds and never completely extinguishes before the start of the next pulse.

The bulk plasma measurements were also performed in a reverse bias configuration. The mass spectrometer is installed inside the cathode, which is grounded for bulk plasma experiments and the anode is pulsed negatively.

Study of ions traversing the sheath: mass spectrometer inside the cathode

The configuration of the mass spectrometer inside the high voltage electrode is shown in Fig. 69. Here, the cathode can be negatively pulsed between 0.1 kV to 5 kV and the mass spectrometer can float negatively between 0 and 1 kV.

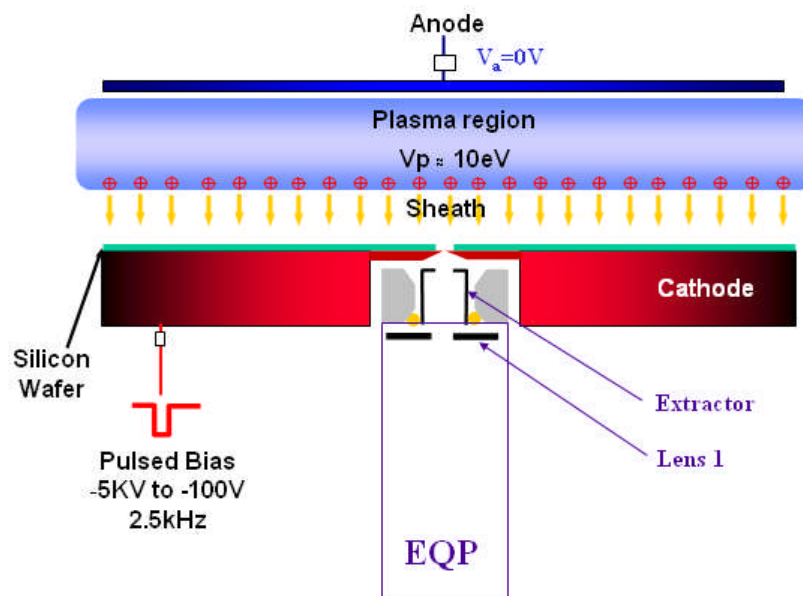


Figure 69: Schematic diagram of the mass spectrometer installed in the middle of the PLAD cathode

In order to install the mass spectrometer in the middle of the cathode, the bottom of the cathode was redesigned, as illustrated in Fig. 70 and 71. A special water-cooled aluminum gravity platen was designed. The wafer-lift pin assembly system was also modified.

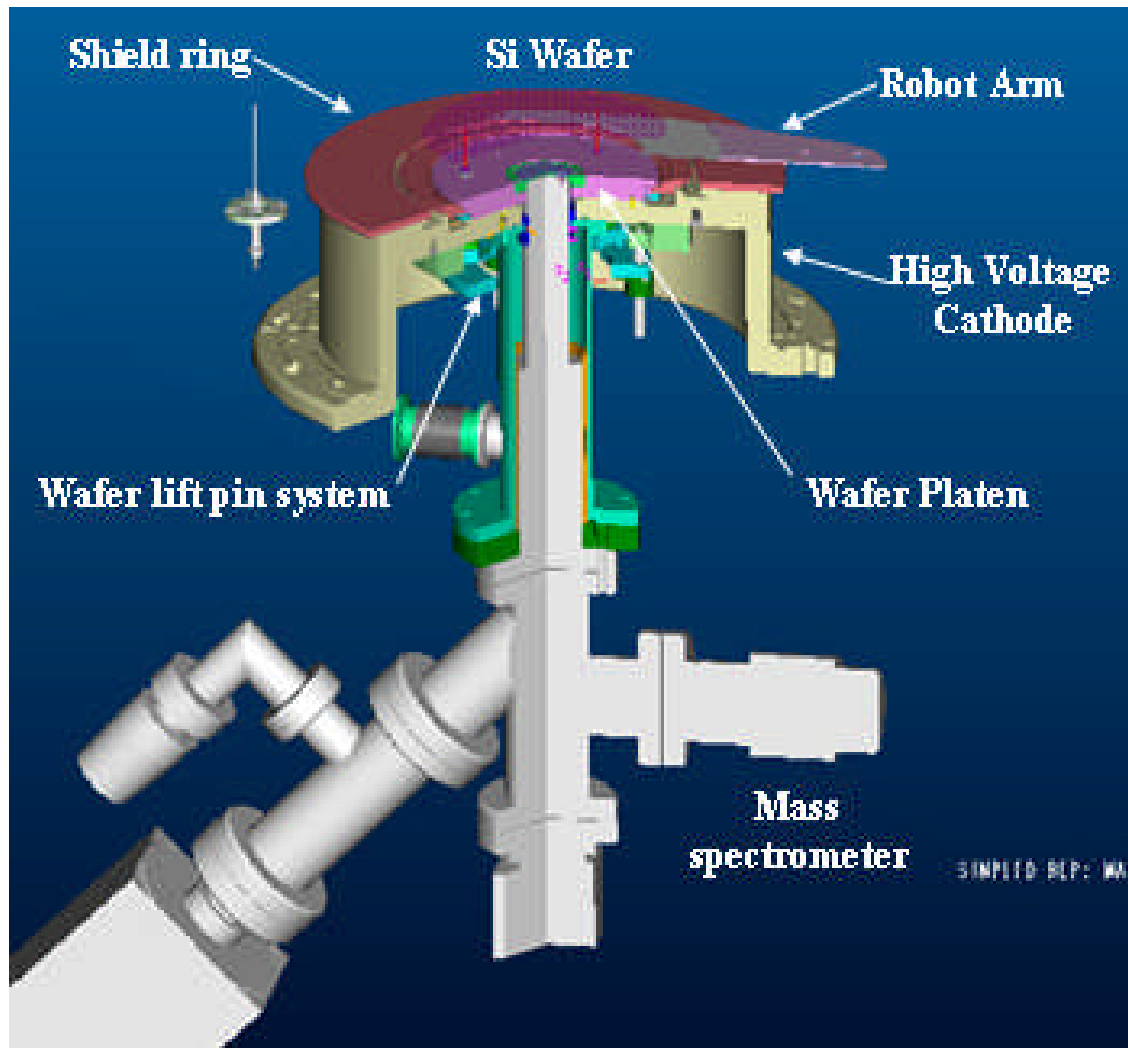


Figure 70: Design of EQP Mass spectrometer inside the PLAD cathode

The power supply matching unit was also modified; the cathode and HC matching unit is now separated into two pieces (cf Appendix 2). The special platen is composed of two pieces (see pink and green pieces Fig. 70 and 71). A $75\mu\text{m}$ aperture was located in the middle of the “center platen” (in green in Fig. 70 and 71). This center piece could be replaced for cleaning or maintenance purpose. As the alignment of the mass spectrometer and the cathode is very important to obtain a correct measurement, the entire cathode was designed with very tight precision. In order to correctly align the mass spectrometer, a special adjustment platen was developed to replace the “center platen” during the mass spectrometer alignment.

The body of the mass spectrometer was insulated from the high voltage cathode (Fig. 71). A differentially pumped system was used to ensure that a good vacuum is maintained between the mass spectrometer and the cathode, and to avoid arcing between the mass spectrometer's body and the PLAD cathode.

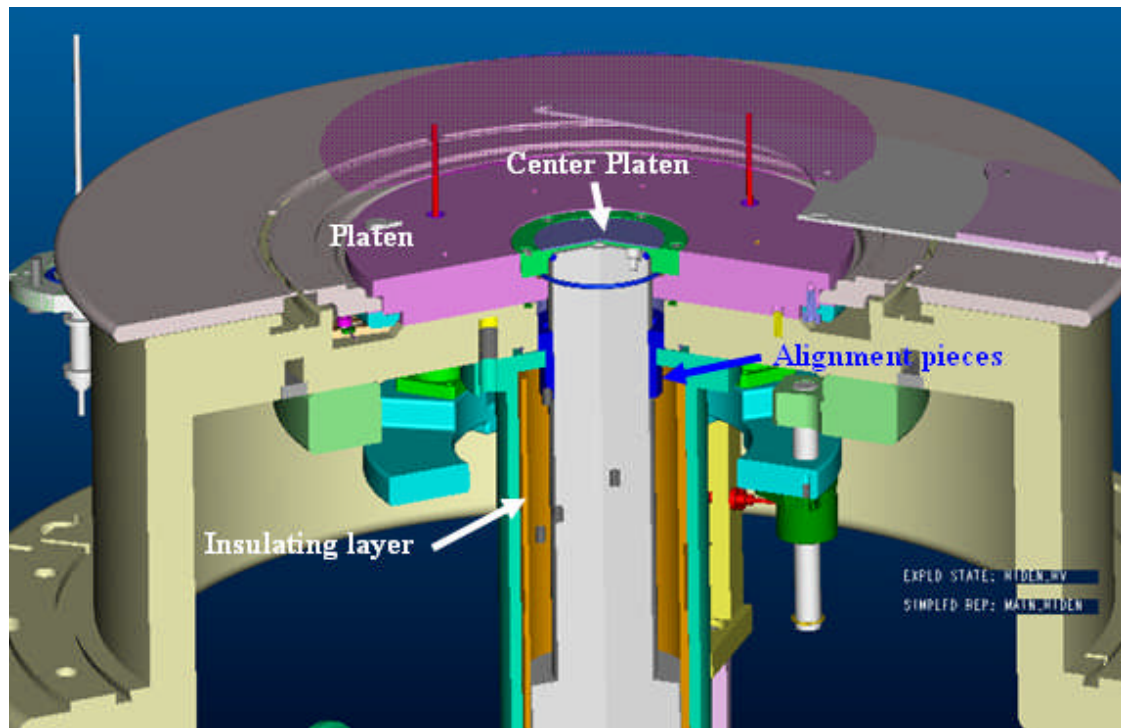


Figure 71: Mass spectrometer insulated from the cathode

In order to collect IED data during the plasma doping process, a 200 mm silicon wafer with a laser cut aperture in its center was introduced under vacuum inside the process chamber through an isolation valve between the load-lock and the process chamber using a wafer-handling robot. The special 200mm wafer site on the redesigned cathode and can be replaced under vacuum. When the plasma is on, the ions are extracted directly from the plasma through the aperture drilled into the center of the wafer. The extractor aperture was set to 2 mm (Fig. 72) to achieve a good transmission and a good pumping speed, and to reduce collisions during the ion transport to the EQP. A 1mm gap was kept between the mass spectrometer and the cathode to avoid any arcing. By using a differential pumping system, a base pressure of 2×10^{-8} Torr inside the mass spectrometer can be achieved.

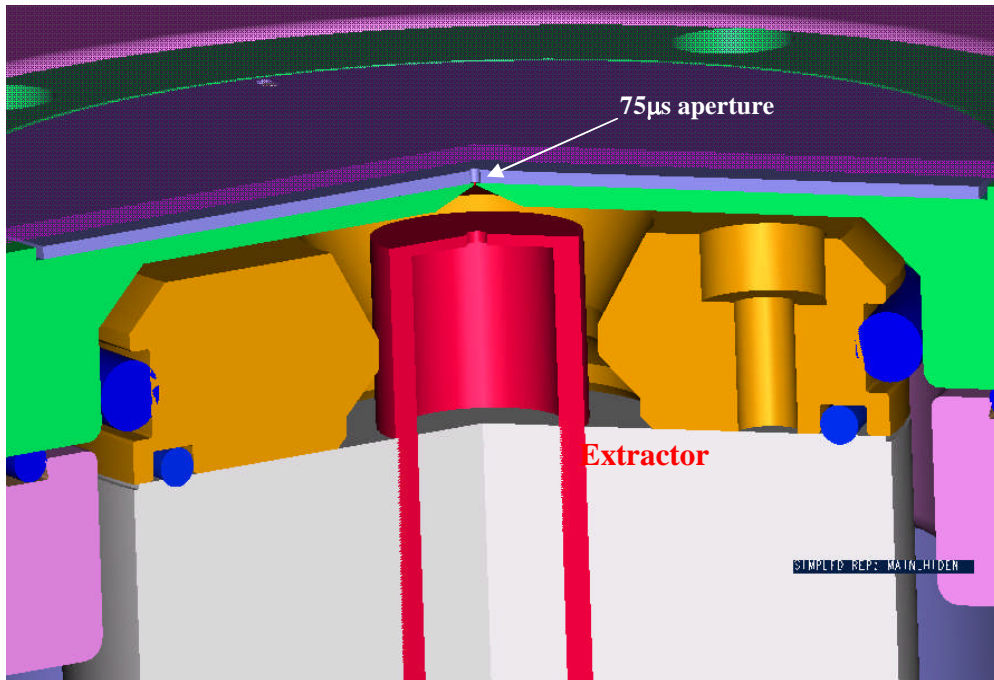


Figure 72: Wafer, platen and Mass spectrometer extraction optics set up

In order to increase the transmission efficiency of the extraction optics and minimize the effects of field perturbations and gas collisions, detailed optimizations were made using 2-dimensional electrostatic models. In essence, the flat extraction lenses normally used were replaced by conical Pierce-angled optics and the inter-electrode gaps between the extractor and the PLAD platen were modified. The new geometry, in addition to lowering perturbations of electric field, also allows for better gas pumping thus lowering losses due to collisions. The modified spectrometer operates in a more efficient way that is suitable to the study of pulsed DC plasma. This scheme allowed collection of the ion species from the cathode sheath during the discharge.

An example of typical measured ion energy distributions in BF_3 plasma of the ions that cross the high-voltage sheath is shown in Fig. 73. The shape of each IED will be described in detail in chapter IV.

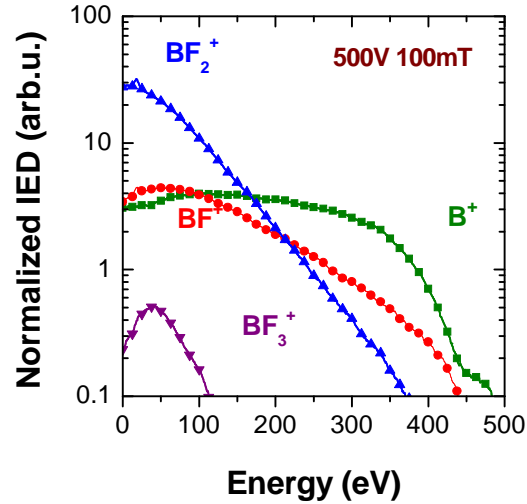


Figure 73: B^+ , BF^+ , BF_2^+ , BF_3^+ IED normalized to the total ion flux for a 500 V BF_3 plasma at 100 mTorr and 2500 Hz

In order to have a stable PLAD configuration (not submitted to production or development constraints), a special PLAD test stand was developed during this thesis. The test stand is composed of an industrial PLAD process chamber, a manual 200mm loadlock, a Langmuir probe installed on the side of the chamber, a mass spectrometer installed in the center of the high voltage cathode and an optical emission spectrometer (see Appendix 2). It is operated using the same software and same hardware as the industrial PLAD machine.

Mass spectrometry measurement in a pulsed DC plasma

In this section a general discussion on the method used to obtain an accurate measurement for a pulsed DC plasma with high-energy ions is presented.

Mass distribution concerns

When a mass distribution scan is performed using the EQP, the ion energy analyzer setting is optimized for a specific ion mass. In order to compare the relative abundance of ions based on the mass distribution, the assumption is that all ions have the same maximum energy ($\varepsilon_{Max} \pm \Delta\varepsilon$).

For example, when the bulk plasma is studied, ion energy spread is usually small. A mass distribution is thus acceptable to compare the relative ion abundance from the bulk plasma. When it comes to measuring energetic ions accelerated across the sheath, ion energy is strongly dependant on the sheath collision processes, which vary for different ion masses and the ion energy spread is large.

For example (based on Fig.73), when acquiring a mass distribution, the ion energy is set to collect ions with 20 eV energy, where BF_2^+ ion is measured as the dominant ion. However, when the energy is set to collect ions with 300 eV, B^+ ion becomes the dominant species. When the energy is further increased to 450 eV, only B^+ is detected in the mass distribution spectrum. Therefore, a mass spectrum does not always reflect the correct relative abundance of the different ions reaching the cathode, but only their relative ratios for a certain energy. As different ions have different transit times inside the mass spectrometer, the mass distribution does not accurately estimate the ratio between the different ions during the time-resolved measurements when pulsed plasmas are in use.

To summarize, mass distribution acquisition will not be shown for time-resolved measurement when measuring energetic ions. It will be used only to characterize bulk plasma with time average measurements. The acquisition of IED for each ion reaching the cathode is thus a better way to estimate the relative abundance between the different ions of the plasma.

Measurement of IED:

This section will present how the IED are collected with the mass spectrometer. Two different modes of acquisition are available: the Energy scan and the Reference scan (see Fig.60).

a) Bulk plasma: Energy scan

In the case of the energy scan, ions with energies between 0 and 100 eV can be measured. Under this configuration, Extractor and Lens 1 voltages are fixed to a certain value during the acquisition, while the other voltages, such as Lens 2 and Focus 2 are linked to the Energy potential. This configuration is similar to the one used prior to the modification of the voltage setup as described in section (III.1.5.1). This configuration provides good ion energy transmission inside the mass spectrometer for ion energies below 100 eV.

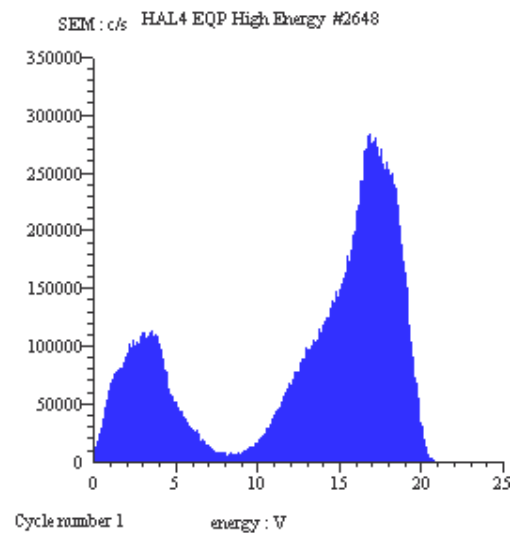


Figure 74: Bulk plasma time average Energy scan spectrum of Ar^+ during a 3kV 30mTorr 10cm 2500 Hz Argon glow discharge

As can be seen in Fig. 74, an Energy scan provides a direct reading of the ion energy. This method is used for the bulk plasma study when the ion energy is lower than 50 eV.

In order to understand the shape of the IED in the pulsed plasma and analyze the origin of each peak in its distribution, a time-resolved measurement is needed. For example in Fig.74, two peaks were observed in the Ar^+ time-averaged IED. It is not possible to explain how these two peaks are created without performing time-resolved measurements by mass spectrometry or Langmuir probe (measuring the evolution of plasma potential during the pulse could help understand the origin of peaks in the IED).

Once time-resolved measurements are performed (see Fig. 68), the two peaks can be identified: the low-energy peak at 4eV corresponds to the ion energy during the pulse-on period, while the peak at 18eV corresponds to the energy of the ion during the afterglow.

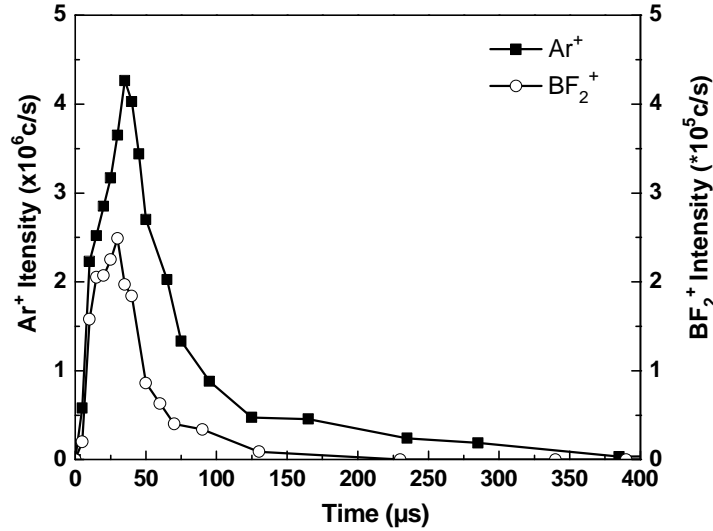


Figure 75: Time evolution of maximum intensity of BF_2^+ ion, -1 kV, 41 mTorr, 2500 Hz and of Ar^+ ion, 3 kV, 30 mTorr, 30 μs .

Time-resolved measurements are also necessary to study the ion flux increase and decay during the pulse development. An example of the time evolution of the maximum of intensity for BF_2^+ and Ar^+ is shown in Fig. 75.

b) Ions accelerated by the high-voltage sheath: Reference scan

In the case of a Reference scan, ions with energies between 0 to 1000 eV can be detected. This is accomplished by changing the reference voltage with all other electrostatic lenses floating above the Reference voltage. As this is the only way to measure the energy distribution up to 1000eV, this mode is the one required for monitoring the energy of the ions accelerated by the high-voltage sheath. An example of an Ar^+ Reference scan performed in an argon plasma at 50 mTorr, with 1 kV applied to the cathode, is shown in Fig. 76.

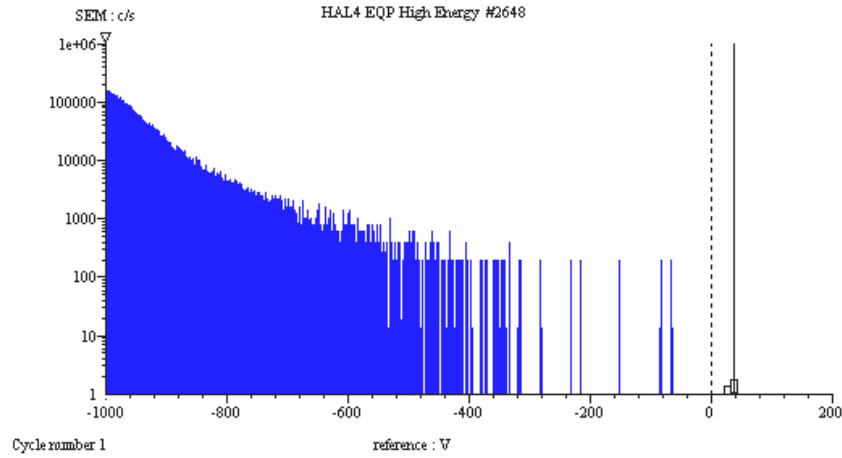


Figure 76: Pulse-on period time-resolved measurement of Ar^+ reaching the cathode for a 1 kV 50 mTorr $50\mu s$ 2500 Hz 5 sccm, 5 cm implantation. Reference scan measurement is used

As discussed previously (III.1.5.2), when the reference is equal to the cathode voltage, ions experience no acceleration or deceleration before entering the mass spectrometer and the energy of detected ions is equivalent to zero electron-volt ions. Conversely, when the reference is set at zero volt, only the energetic ions with the full sheath acceleration can penetrate inside the mass spectrometer. These ions have an energy equal to $e \times V_c$ (see Fig. 77).

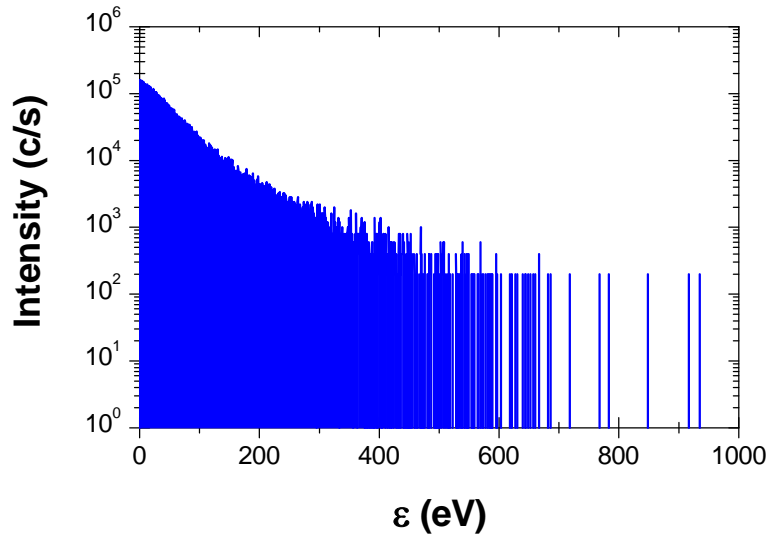


Figure 77: Pulse-on period time-resolved measurement of Ar^+ IED measured at the cathode for a 1 kV 50 mTorr $50\mu s$ 2500 Hz implantation

In order to convert the Reference scan into an actual IED, each reference voltage bin needs to be converted to the correct energy through the following equation:

$$E = e \times (V_{reference} - V_c) \quad \{\text{III.1.25}\}$$

The Ar^+ ion energy distribution is presented in Fig. 77. In this manuscript, all the IED will be presented through this conversion.

Ions accelerated across the sheath during time-resolved measurements

Due to the fast changes of the electric field during the plasma rise and fall time, measuring the IED of ions accelerated by the high-voltage sheath becomes more challenging.

c) Ions across the sheath: What can be learned from the rise and fall times of the pulse

For time-resolved measurements, the EQP analyzer is gated by a TTL pulse that is synchronized with the PLAD voltage pulse. A 2 μs time resolution is achievable with the current EQP probe. The delay time between the TTL pulse and PLAD pulse is adjustable to allow ion sampling at the beginning, middle and end of the PLAD pulse. The TTL pulse width is optimized, taking into account the trade-off between time resolution and count rate. In the steady state, the energy of each ion is well defined and the mass spectrometer time resolution is adequate. During the rise time and fall time of the pulse, the time resolution of 2 μs is insufficient to accurately determine the shape of the IED. As the cathode voltage is rapidly changing during the measurement, the conversion defined by equation {III.1.25} is not valid.

An example of a time-resolved BF_2^+ IED during the entire pulse-on period is shown in Fig. 78, with a 10 μs time resolution for a 500 V, 100 mTorr and 2500 Hz BF_3 glow discharge. During the first 5 μs , the cathode voltage decreases from 0 to -565V and the IED between -5 to 5 μs is a combination of those ions that undergo different cathode

accelerations. Therefore, the determination of their energy distributions is made impossible. In most cases, 15 μs is the necessary time to reach the steady state cathode voltage. The same observation is valid when the pulse ends, between 50 to 65 μs , the ion exact energy is not known. The IED measured between 55 and 65 μs clearly shows the decay part of the pulse ({II.1.25} is again non-valid).

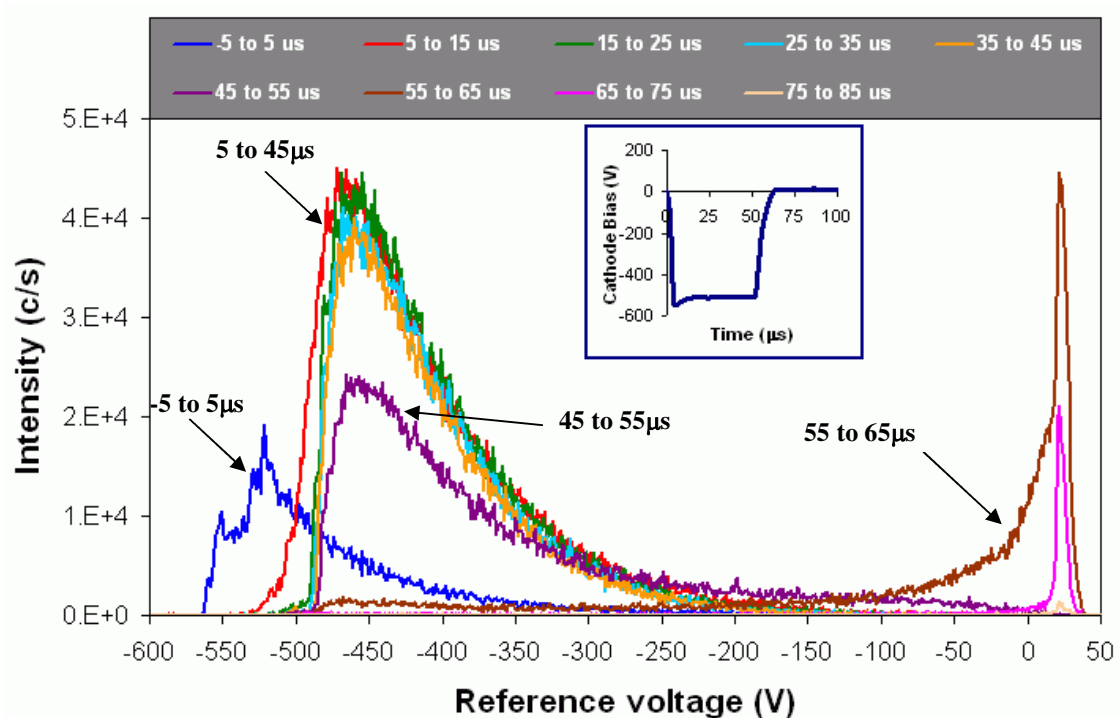


Figure 78: Time resolved BF_2^+ IED measured by the mass spectrometer installed in the center of the high-voltage cathode, with a time resolution of 10 μs for a 500 V, 100 mTorr, 50 μs , 5sccm, BF_3 glow discharge plasma at 2500Hz

An accurate IED measurement during the rise time and fall time of the cathode pulse will thus not be possible because of the time-step resolution limitation of the mass spectrometer. However, during these dynamic changes, the number of ions detected by the mass spectrometer is still accurate (only the exact energy of each ion is unknown) and the relative ion flux measured remains valid.

A concern associated with the rise and fall time of the pulse is that it may affect the ion mass and energy distributions, thus changing the implant profile. This concern was ruled out in early studies of low-energy BF_3 PLAD implantation, as boron SIMS profiles

showed no difference for different pulse-on widths (20 to 60 μs) [Lenoble 2000] with constant rise and decay times. The IEDs change during the rise and fall times of the pulse, but during these dynamic changes, the ion density and the ion energy are lower than during the steady state. Therefore no influence appears on the implant profile.

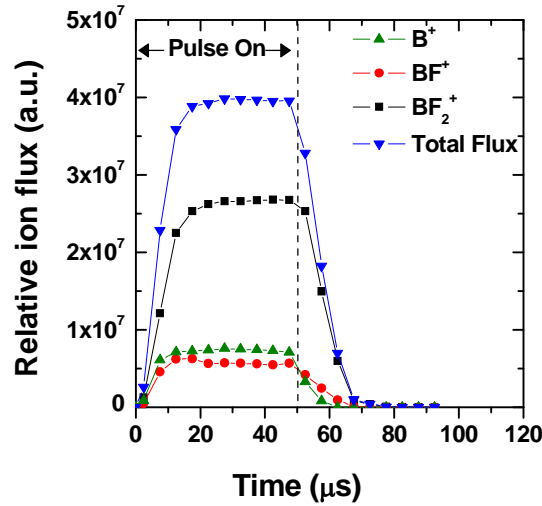


Figure 79: Evolution during the pulse of the relative total ion flux and B^+ , BF^+ and BF_2^+ ion relative fluxes measured through time resolved mass spectrometry

The time evolution of the different ion fluxes measured by the mass spectrometer during the PLAD pulse is shown in Fig. 79 (Ion flux is defined here as the integral of the IED). During the first 10 μs of the pulse-on, the sheath is expanding and the relative ion flux is increasing. After 15 μs , the relative total ion flux is stabilized and the IED of the different ions remain the same. During the decay, the total ion flux decreases as the sheath collapses. This observation allows us to improve the statistics of the EQP system by employing a wide TTL gate pulse, starting at 20 μs after the beginning of the pulse and ending at 50 μs .

In the next section, all IEDs are measured in the high-voltage sheath when the cathode voltage is constant and the energy of each ion is well defined. Large TTL gate pulse will be employed, starting after 15 μs and stopping at the end of the pulse.

d) Mass spectrometer calibration and transit time concern

During the calibration of the mass spectrometer, the Quad Lens parameters (Vert, Horiz and D.C. Quad) are very sensitive.

An incorrect calibration affects the transit time of ions inside the mass spectrometer. Even if the autotune method is used, a significant error could be made in the time-resolved acquisition mode. This occurs particularly in cases where signal to noise ratio is low. By monitoring the ions reaching the detector with a fast-acquisition oscilloscope, the above mentioned parameters can be set correctly. Fig. 80 shows an example of the vertical voltage (Vert) calibration, as well as the effect of an incorrect set-up. In Fig 80, the set-up (a) is a correct one, where ion signal duration is coincident with the pulse length. On the other hand, set up (b) is incorrect because energetic ions with 1000 eV are still detected even 100 μ s after the end of the high voltage pulse.

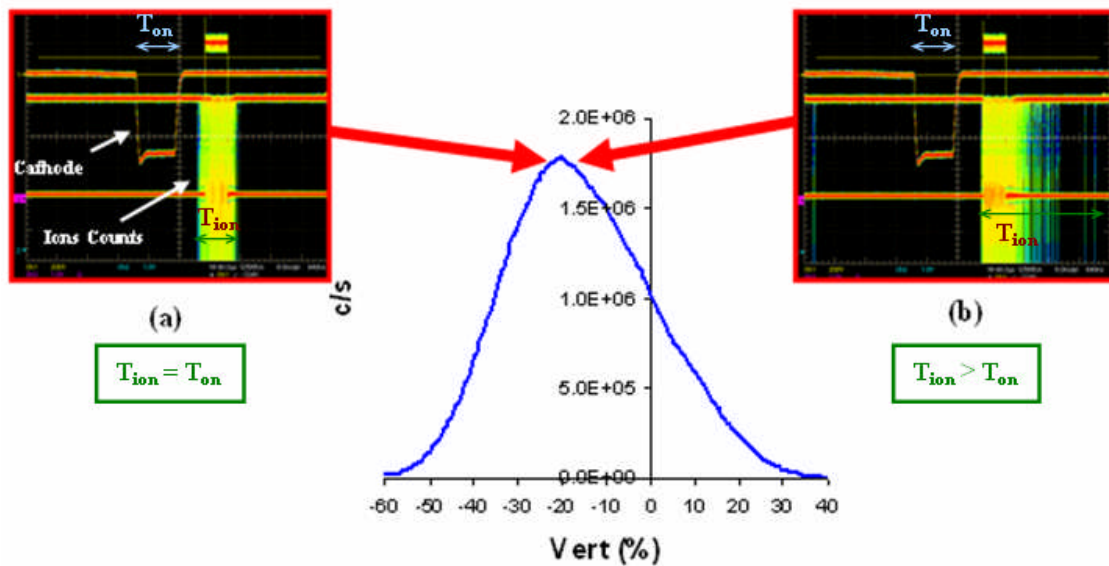


Figure 80: Correct and incorrect setting of the Vert parameter during its calibration are represented in (a) and (b), both of which are monitored with a fast-acquisition oscilloscope. The ion energy was set to 1000 eV. T_{on} is the pulse-on period and T_{ion} is the time over which the energetic ions are detected.

As mentioned previously, in order to perform an accurate time-resolved measurement with the mass spectrometer, it is necessary to monitor the output ion count signal of the detector with an oscilloscope and carefully adjust the voltage setup of the Quad Lens and the other relevant optical elements.

e) Validation of the energetic ion measurements

One way to verify if the transmission efficiency is constant inside the mass spectrometer is to check the proportionality between the total relative ion flux, which is measured with the mass spectrometer, and the ion current density.

Fig. 81 shows the relative total ion flux measured by the mass spectrometer, as a function of the ion current density under several different plasma conditions: 1kV (30 to 70 mTorr; 500Hz to 3000Hz), 750V (40 to 70 mTorr) and 500V (100 to 250 mTorr) The relative ion flux is calculated by summation of the integrated ion energy distributions for all ions reaching the cathode. The ion current density is calculated using the following formula:

$$j_i = \frac{I_c}{a_c \times (1 + \gamma)} \quad \{\text{III.1.26}\}$$

where I_c is the measured cathode current, a_c is the cathode area and γ is the secondary electron emission coefficient.

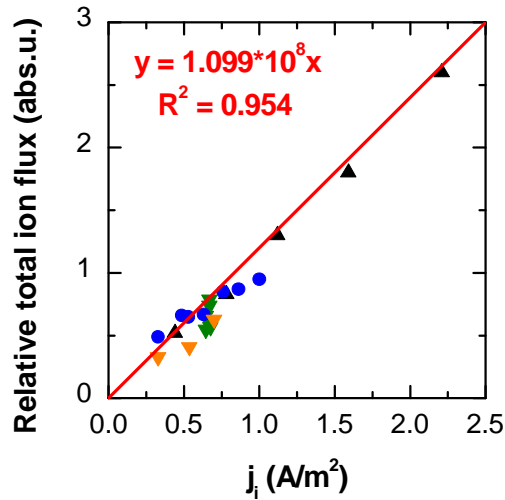


Figure 81: Relative total ion flux measured with the mass spectrometer as a function of the ion current density for 1kV (30 to 70mTorr, 500Hz to 3000Hz), 750V (40 to 70mTorr) and 500V (75 to 250mTorr) BF_3 plasma

A linear relationship is observed between the ion current density and the relative total ion flux. The linear response of ion flux to pressure suggests a good ion detection efficiency and constant transmission inside the mass spectrometer in this pressure range.

III.2 Langmuir probe

A basic Langmuir probe consisting of a simple metal wire inside a plasma was first developed by Irving Langmuir and his coworkers in the 1920's [Langmuir 1924], [Mott-Smith 1926]. In this work, a moveable Langmuir probe, commercialized by Scientific System, was employed to measure plasma parameters including the electron density n_e , the ion density n_i , the electron temperature T_e , the plasma potential V_p , the floating potential V_f and the Electron Energy Distribution Function EEDF under different plasma conditions. In addition, the ion flux ϕ_i of the ions reaching the surface exposed to the plasma can be estimated. More information on the Langmuir probe can be found in the following books: Hershkovitz [Hershkovitz 1989], Lieberman [Lieberman 2005] and Ruzic [Ruzic 1994].

Principle

Fig. 82 shows the variation of the total electric current I measured by of the probe as a function of the probe potential V_b . The current I collected at different voltages V_b is the sum of the electron current I_e and the ion current I_i .

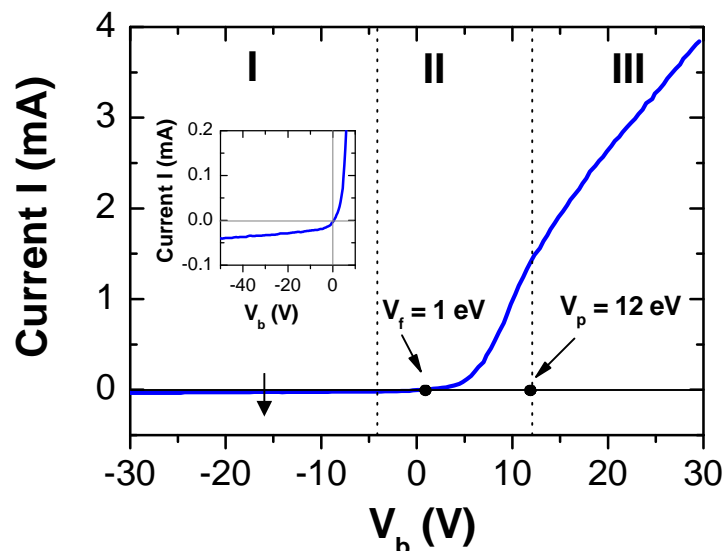


Figure 82: Example of a typical I-V characteristic measured in argon plasma at 300V 45mTorr. Three regions can be distinguished (I,II,III) as well as the potentials V_p and V_f . A zoom of the ion saturation current is also presented.

The plasma parameters are derived from the probe characteristic, which is measured by varying the voltage applied to the probe and measuring the resulting current. An example of a typical $I(V_b)$ characteristic during an Argon implant at 300V 45mTorr is shown in Fig.82.

Three distinct regions can be distinguished on a probe characteristic. In the first region, all the electrons are repelled by the low negative probe bias voltage and only positive ions contribute to the probe current. This part of the curve defines the ion-saturation current (see in the zoom of this region in Fig.82).

In the second region, when V_b is closer to the plasma potential V_p , energetic electrons are able to cross the potential barrier. The probe then collects electrons and ions at the same time. When the electron flux and ion flux are equal, the probe current is zero at a certain voltage V_f referred to as the floating potential. The floating potential also corresponds to the potential that an insulated object will have inside the plasma. At a certain voltage, electrons are neither attracted nor repelled by the voltage, and the sheath does not exist. The probe current is then mainly due to the electron thermal motion. At this point, the probe characteristic shows an inflexion point known as the plasma potential, V_p . The potential is approximately the point where $I = e \times I_e$ where I_e is the electron current. If the voltage is superior to the plasma potential, the electron current cannot increase any further and all the electrons are collected.

In the last region, the probe attracts the electrons and repels the ions. An electron sheath is formed around the probe tip. The collected current is purely electronic and is referred to as electron saturation current.

Experimental settings

An automated Langmuir probe supplied by Scientific System was installed on the side of the PLAD process chamber (Fig. 83).

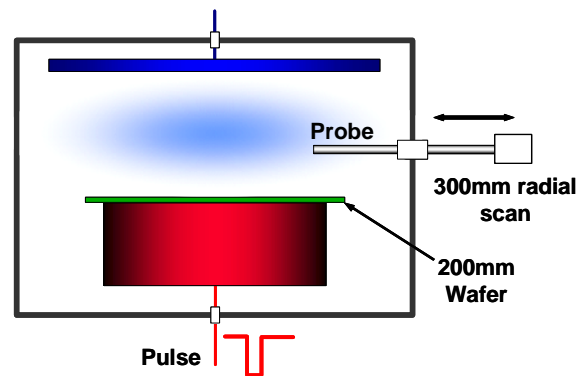


Figure 83: Schematic diagram of a Langmuir probe installed on the PLAD process chamber

The probe is controlled by the SmartSoft software, which can directly extract the plasma parameters from the probe characteristic. The software also controls the radial position of the probe inside the discharge chamber. A radial distribution of the plasma parameters from the center of the wafer to the edge of the cathode can be obtained using this set-up. In order to perform the acquisition outside of the cathode sheath for all the experimental conditions, the air-cooled Langmuir probe is installed at 3.5 cm above the cathode. The cylindrical probe tip material used for all experiments is tungsten.

The probe tip can be automatically cleaned between each $I(V_b)$ characteristic. While studying BF_3 discharges, a drift of V_p and V_f is observed when no automatic probe cleaning is used. After ten acquisitions without cleaning, the whole curve is shifted positively and no V_p can be measured. The probe was cleaned by heating the filament two seconds between each $I(V_b)$ acquisition. In order to maintain a good signal to noise ratio, the current I for each V_b is averaged over 10 measurements and an averaged of five $I(V_b)$ characteristics is calculated.

Due to the pulsed nature of the plasma, its characteristics change over time during its rise time and decay. Therefore, time-resolved measurements are necessary. In order to perform a time resolved acquisition, the Langmuir probe is synchronized to the PLAD pulse (see section III.1.3). A time resolution of up to $1 \mu\text{s}$ is achievable with the present Langmuir probe.

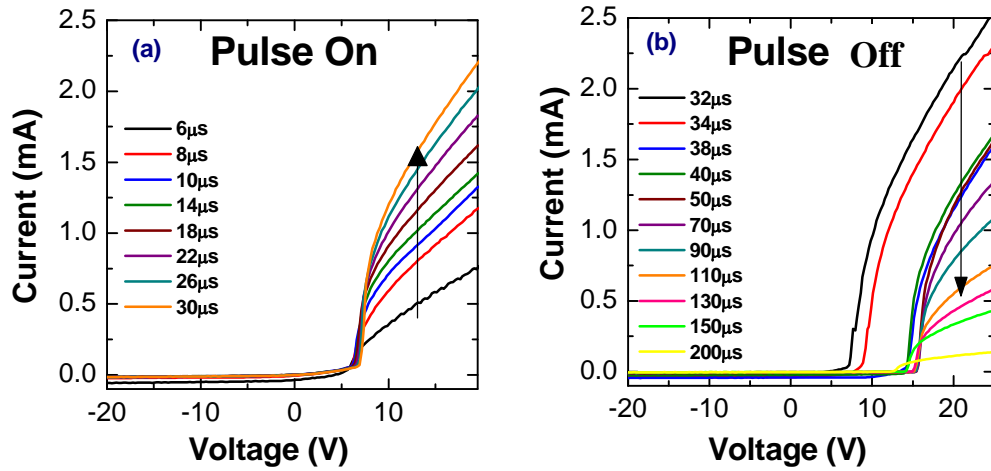


Figure 84: Pulse-on period (a) and afterglow (b) time resolved Langmuir probe for a 1kV 40mT 30µs BF_3 implant,

Fig. 84 shows an example of the time development of the probe characteristic measurements in a BF_3 plasma during a 1kV, 40 mT, 30 µs pulse-on at a pulse frequency of 2500 Hz. The electron saturation current increases during the pulse-on period and then slowly decreases during the afterglow period, showing the increase and decrease of plasma density at ignition and extinguishing of the DC plasma.

Extraction of the plasma parameters

The plasma's parameters are extracted directly from the $I(V_b)$ characteristics using the SmartProbe software [Scientific sys] with a cylindrical tip. An explanation of the analysis method is presented below.

- The **floating potential** is the potential during which the current is measured as equal to zero ampere.
- The **plasma potential** is the potential during which the second derivative of the $I(V_b)$ curve is equal to zero ($d^2I/dV_b^2 = 0$)

- The **electron temperature** T_e is calculated by dividing the integral of the $I(V_b)$ curve between V_f and V_p by the current measured at the plasma potential $I(V_p)$:

$$\frac{kT_e}{e} = \frac{\int_{V_f}^{V_p} I(V_b) dV_b}{I(V_p)} \quad \{\text{III.2.1}\}$$

A demonstration of this formula can be found in Appendix 3. The electron temperature is often expressed in electron-volts rather than in joules.

- The **electron density** n_e is calculated based on the current $I(V_p)$, as measured at the plasma potential using the following equation:

$$n_e = \frac{I(V_p)}{eA_p} \sqrt{\frac{2\pi \times m_e}{kT_e}} \quad \{\text{III.2.2}\}$$

where A_p is the probe physical collecting area. The assumption in the use of these two last formulas is that the electron distribution function follows a Maxwellian distribution.

- Another important plasma parameter is its Debye length. The plasma can be considered as neutral inside a sphere of radius λ_d . When the electron density and electron temperature are known, the **Debye length** can be calculated using the following formula:

$$\lambda_d = \sqrt{\frac{\epsilon_0 kT_e}{e^2 n_e}} \quad \{\text{III.2.10}\}$$

- When the electron density and temperature are known, the flux of ions reaching a surface inside the plasma can be calculated. This flux is known as the **Bohm flux** and can be calculated using the Bohm criteria:

$$\phi_i = 0.6n_i \sqrt{\frac{kT_e}{m_i}} \quad \{\text{III.2.11}\}$$

where n_i is the ion density (m^{-3}) and m_i is the ion's mass (kg).

Electron energy distribution function

Another method can be used to calculate n_e and T_e based on the electron energy-distribution function, when the distribution is non-Maxwellian. This method consists of calculating the **Electron Energy Distribution Function (EEDF)**. EEDF gives a measure of the number density of electrons as a function of electron energy. For an arbitrary distribution function, the EEDF $g_e(\varepsilon)$ can be calculated using the following formula [Lieberman 2005]:

$$g_e(\varepsilon) = \frac{2}{e^3 A_p} (2m\varepsilon)^{1/2} \frac{d^2 I}{dV_b^2} \quad \{\text{III.2.6}\}$$

where $\varepsilon = V_p - V_b$, the $d^2 I/dV_b^2$ function can be calculated by differentiating $I(V_b)$. SmartSoft can also calculate the function directly.

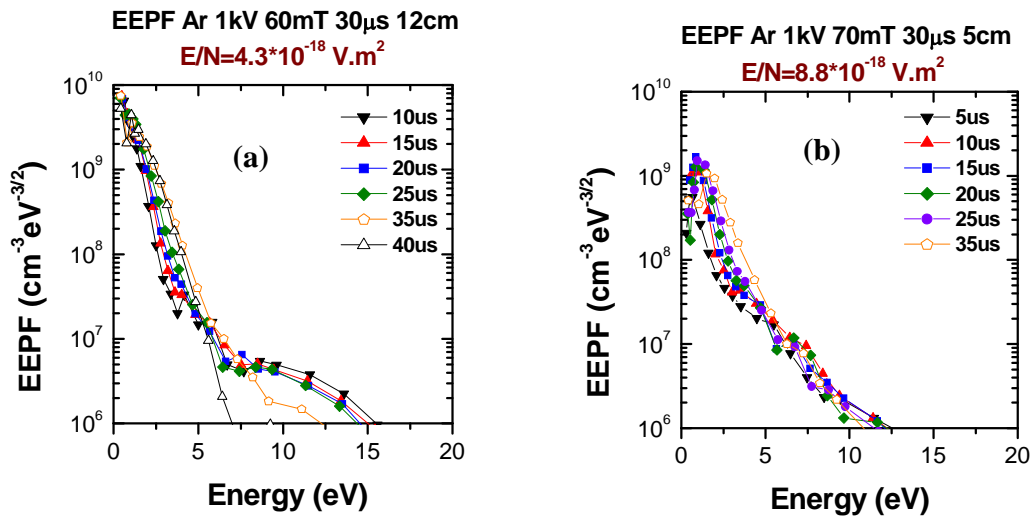


Figure 85: Experimental time-resolved EEPF for Argon plasma under two different plasma conditions
(a): 1 kV 60 mTorr 30 μ s 12 cm 2500Hz, (b): 1 kV 70 mTorr 30 μ s 5 cm 2500Hz

The electron energy distribution function is a very important parameter of the discharge as it allows for knowing the electron energy available to dissociate the gas and to excite or ionize the different species present in the plasma. The Electron Energy Probability Function (EPPF) $g_p(\varepsilon) = \varepsilon^{-1/2} g_e(\varepsilon)$ is sometimes introduced instead the

EEDF. In the case of the electron energy distribution is Maxwellian; the EEPF is a linear curve when logarithmic representation is used. A typical EEPF measured using SmartProbe for an argon plasma is shown in Fig. 85.

Two different linear slopes are observed on the EEPF in Fig. 85a, the EEPF is clearly a non-Maxwellian distribution. The electron density n_e , the average energy $\langle \varepsilon_e \rangle$ and the effective electron temperature T_{eff} can then be determined (even in the non-Maxwellian distribution) as:

$$n_e = \int_0^{\infty} g_e(\varepsilon) d\varepsilon \quad \{\text{III.2.7}\}$$

$$\langle \varepsilon_e \rangle = \frac{1}{n_e} \int_0^{\infty} \varepsilon_e \times g_e(\varepsilon) d\varepsilon \quad \{\text{III.2.8}\}$$

and

$$T_{eff} = \frac{2}{3} \langle \varepsilon_e \rangle \quad \{\text{III.2.9}\}$$

Fast electron

The fast electron analysis routine is based upon the Laframboise theory [Hopkins 1986] which calculates the values of the fast electron temperature kT_{fe} and density n_{fe} . The current to the probe through the collection of the fast electrons $I_{fe}(\chi)$ is calculated for negative values of χ as follows:

$$I(\chi) = I_+(\chi) + I_e(\chi) + I_{fe}(\chi) \quad \{\text{III.2.12}\}$$

where $I(\chi)$ is the measured current to the probe with $\chi = (V_b - V_p) / kT_e$, I_e is the thermal bulk electron contribution and I_+ is the ion contribution.

Thus,

$$I_{fe}(\chi) = I(\chi) + en_e R_p \sqrt{\frac{2\pi kT_e}{m_e}} \exp(\chi) - en_+ R_p \sqrt{\frac{2\pi kT_e}{m_+}} f\left(\frac{R_p}{\lambda_d}, \chi\right) \quad \{\text{III.2.13}\}$$

where $\chi < 0$.

The initial calculation of $I_{fe}(\chi)$ is restricted to the region $\chi < -10$, as the bulk thermal contribution is effectively zero in this case. The calculation of $I_{fe}(\chi)$ is not sensitive to the value of kT_e/e . The current to the probe due to the fast electrons is fitted by the least square exponential regression to:

$$I_{fe}(\chi) = I_{ofe} \exp\left(\frac{\chi \times kT_e}{kT_{fe}}\right) \quad \{\text{III.2.14}\}$$

where I_{ofe} is the fast electron thermal flux to the probe at V_p and kT_{fe} is the fast electron temperature. This method assumes a good calculation of ion saturation current to separate I_+ from I_{fe} . The fast electron techniques give at least qualitative information on of fast electrons.

III.3 Characterization method used

In order to characterize the implant profile and dopant concentration before and after activation, Secondary Ion Mass Spectrometry (SIMS) is used to measure the dopant concentration as a function of depth inside the silicon wafer. The sheet resistance of the dopant film is measured after anneal using the four-point probe technique. These two characterizations, SIMS and the four-probe technique, are presented below.

Secondary Ion Mass Spectrometry (SIMS)

Secondary Ion Mass Spectrometry (SIMS) allows for the measurement of dopant or impurities depth profiles present in small quantities in a solid material, such as semiconductors. This method is very commonly used in microelectronics, but the technique is facing some big challenges, such as the characterization of ultra-shallow junctions. A control process for the SIMS technique and its protocols thus becomes very important for an accurate measurement.

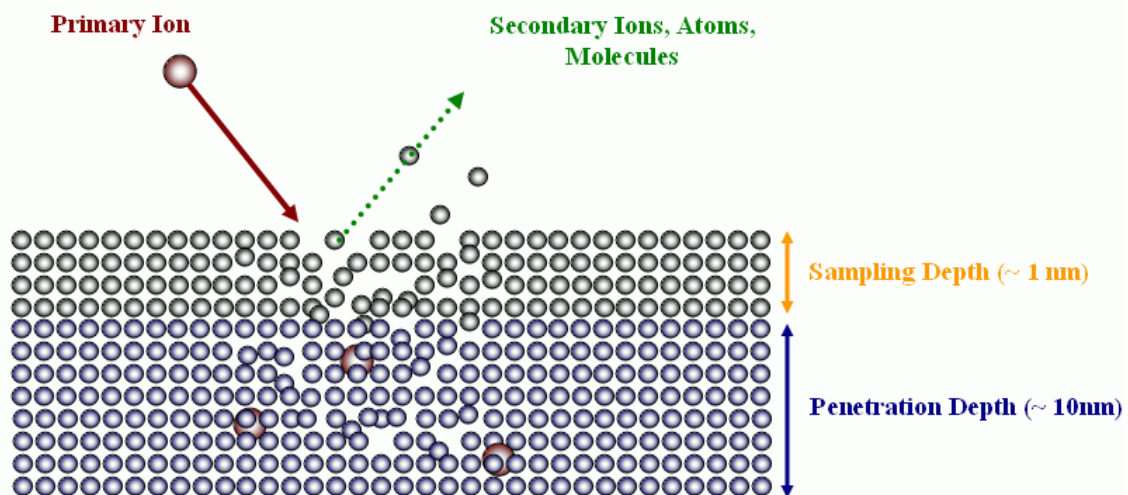


Figure 86: Primary ion interaction with the solid target and sputtering effects. The SIMS technique is based on the analysis of the secondary ions ejected from the target through mass spectrometry

During a SIMS analysis (see Fig. 86), a primary ion beam with an energy of around a 1000eV bombards the surface of a sample maintained under vacuum. Under the

ion bombardment, a cascade of collisions is produced at the surface of the sample with some particles, such as electrons, atoms, molecules or ions, ejected from the sample surface. The secondary particles carry negative, positive and neutral charges and they have kinetic energies that range from zero to several hundred electronvolts. The ions ejected from the sample surface are then analyzed through mass spectrometry. Due to the erosion of the surface by the ion bombardment, a depth analysis of the sample is possible and a dopant concentration depth profile can be performed.

The ionization yield and the energy of the secondary ions is strongly dependant on the primary ion used, its energy and incidence angle. In order to maximize the ionization yield, reactive ions such as O_2^+ and Cs^+ are used. Throughout the analysis, the reactive ions are implanted. The analysis first passes through a transition regime, where the number of ions implanted in the target increase simultaneously with the target erosion. A stable regime is then obtained when the reactive species flux is equal to the flux loss through sputtering or desorption. Due to the dynamic changes during the transition period, the signal measured cannot be analyzed. In this period, a target surface up to a few nanometers cannot be analyzed properly. The interpretation of the results becomes especially difficult for junction depths below 20 nanometers. In order to improve the depth resolution and reduce the transition regime, the primary ion energy is reduced and its incident angle with the target surface is increased.

For all experiment done here, N-type prime (100) Silicon wafers with 12 Angstroms of control oxide were implanted using PLAD under different plasma parameters. The as-implanted boron profiles following a PLAD implantation are analyzed using SIMS, with 700eV O_2^+ at a 45° incidence angle with an O_2 leak. As the co-implanted fluorine plays an important role during the activation of the dopant [Ishida 1999], the as-implanted fluorine profiles are also collected using SIMS, with 500eV Cs^+ at a 60° incidence angle and no O_2 leak. The dose errors for all measurements are expected to be below 20%. The absolute error in the junction depth, X_j , should be less than 10%. This absolute error is mainly due to discrepancies among laboratories and the techniques (e.g. NRA, RBS, etc.) they used to calibrate the SIMS equipments [Buyuklimanli 2006]. The SIMS conditions mentioned above allow for an accurate

measurement of the profile shape, but a less accurate measurement of the total dose. The chemical junction depth throughout this manuscript is defined as the depth where the total boron concentration, sum of electrically and non-electrically active species, falls below a level of $3E18/cm^3$ in the SIMS profile. All the SIMS measurements presented were performed by Evans East [Evans East].

Sheet-resistance measurement with four-point probe

The four-point probe technique is the most common method used to measure the semiconductor resistivity [Van Zant 2004]. In this case, it is used to measure the sheet-resistance of the doped layer of a silicon wafer after the activation of the implanted dopant. Through this non-destructive method, the voltage V between two contact points (point 2 and 3) is measured when a current I is applied to the two other contact points (point 1 and 4) as shown in Fig. 87.

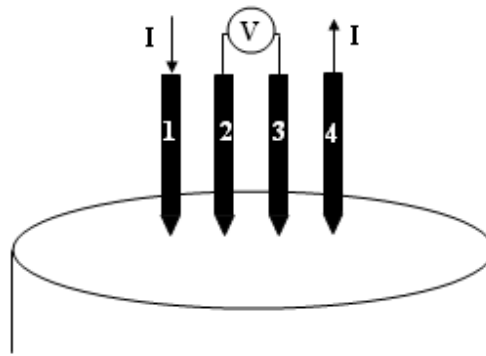


Figure 87: Four-Point probe schematic

Assuming that the studied sample is homogenous, infinite compared to the measurement system and the gap between two contacts is larger than the studied thin film thickness, the sheet-resistance of the thin doped layer can be deduced based on the following formula:

$$R_s = \frac{\pi}{\ln 2} \times \frac{V}{I} \quad \{\text{III.3.1}\}$$

where R_s is the sheet-resistance of the thin doped layer listed in ohms per square (Ω/\square).

This technique is used to monitor the implant and anneal non-uniformity of the entire wafer surface by measuring the local sheet-resistance of the thin layer in several points. When the thickness of the dopant layer X_j (also called junction depth) is known, the resistivity ρ can be deduced through the following equation:

$$\rho = R_s \times X_j \quad \{\text{III.3.2}\}$$

The average active dopant concentration N of the doped layer can be expressed by the following equation:

$$N = \frac{1}{q \times \rho \times \mu} \quad \{\text{III.3.3}\}$$

As the carrier motility μ is not constant with N , this formula is only valid as a first approximation. For improved precision, the active dopant concentration for different depth in the substrate need to be taking into account and the calculated sheet resistance becomes an integral over the junction depth [Lallement 2005]:

$$R_s^{\text{total}} = \int_0^{x_j} \frac{dx}{q \times N(x) \times \mu(N(x))} \quad \{\text{III.3.4}\}$$

The sheet resistance is calculated by integrating the atoms from the SIMS chemical dopant profile below the solid solubility limit at the annealing temperature and assuming that all the dopant atoms below this limit are electrically active.

At a given temperature, there is an upper limit to the amount of an impurity that can be absorbed by silicon. This is called the solid-solubility limit. The boron solubility (at/cm^3) into the silicon follows an Arrhenius law [Armigliato 1977]:

$$S = A \times \exp(-E/kT) \quad \{\text{III.3.6}\}$$

where $A = 9.25 \times 10^{22} \text{ at}/\text{cm}^2$ and $E = 0.73\text{eV}$.

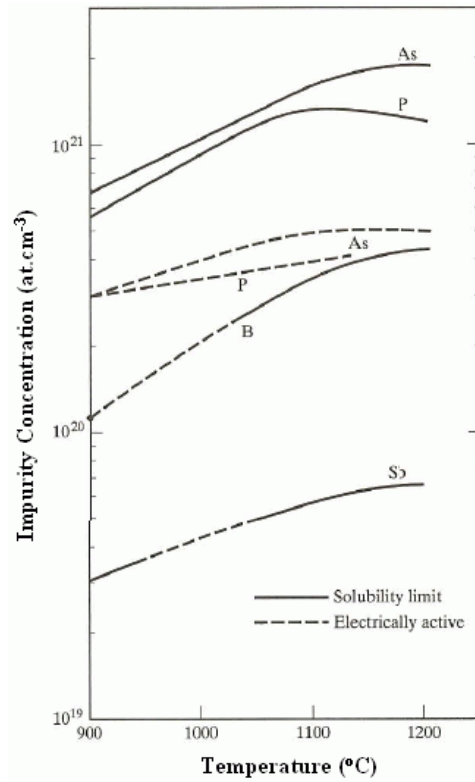


Figure 88: Solid-solubility and electrically active impurity-concentration limits in silicon for antimony, arsenic, boron and phosphorus [Jaeger 2002]

With this formula, the maximum boron concentration can be determined for each annealing temperature and is indicated by solid line in Fig. 88 for boron, phosphorus, antimony and arsenic. The electrically active impurity concentration, which is the maximum of impurities electrically active after activation, is also presented in Fig.88. For the anneal recipe used in all the manuscript (see I.2.2.4), the boron solid solubility limit and electrically active boron-concentration limits is 1.54×10^{20} atoms per cubic centimeter.

The carrier mobility as a function of the depth and the active dopant density can be expressed by the following formula [Masetti 1983]:

$$\mu(x) = \mu_{\min} + \frac{\mu_{\max} - \mu_{\min}}{1 + \left(\frac{N(x)}{N_r}\right)^\alpha} \quad \{\text{III.3.5}\}$$

For boron dopant: $\mu_{\min} = 44.9 \text{ cm}^2/\text{Vs}$

$$\mu_{\max} = 470.5 \text{ cm}^2/\text{Vs}$$

$$N_r = 2.23 \times 10^{17} \text{ cm}^{-3}$$

$$\alpha = 0.719$$

The activation efficiency (A_E) is defined as the ratio of the calculated total sheet resistance to the measured sheet resistance (by the four-point probe) in percent:

$$A_E = \frac{R_s^{\text{total}}}{R_s} \times 100 \quad \{\text{III.3.7}\}$$

The error in this calculation is mostly determined by the uncertainty of the SIMS measurement. The activation efficiency is a good relative measure which defines the percentage of annealed dopants residing below the electrical solid solubility limit that are electrical active. A greater value than 100% could result from inaccuracies in the SIMS profile, a result of higher than assumed electrical solid solubility, or of additional activation from non-conventional mechanisms. Activation efficiency is a more valid indicator than the curve $R_s(x_j)$ plots in determining the extent of activation [Downey 2003].

In all our experiments, the sheet resistance was measured by a KLA-Tencor Rs-100 four point probe using tips of type C with a circular 49 point pattern and 194mm test diameter.

Chapter IV Plasma doping of silicon with BF_3 chemistry

Although, the electron and ion densities (n_e and n_i) can be several orders of magnitude lower than the gas density, the charged particles play a central role in sustaining the discharge as well as in the implantation process. The role of electrons and ions in the discharge as well as their interactions with neutral particles of the plasma are presented in this chapter. In particular, collision processes inside the sheath will be reviewed and discussed in order to obtain a better understanding of the energy distribution shape of the ions striking the wafer.

IV.1 Electron Kinetics in BF₃ plasma

The collisions of low-energy electrons with atoms and molecules can be direct or indirect. The principal direct elastic and inelastic electron-scattering processes are [Christophorou 2004]:

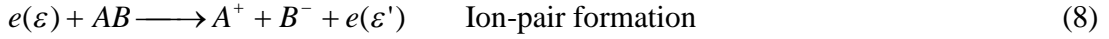
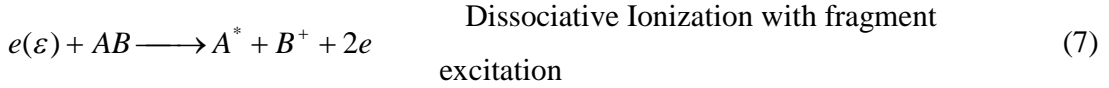
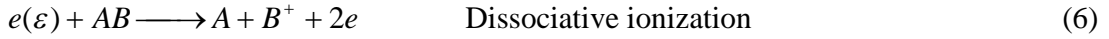
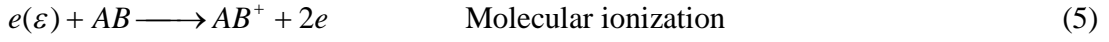
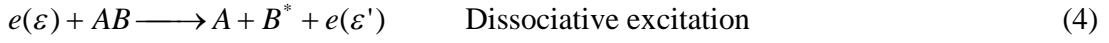
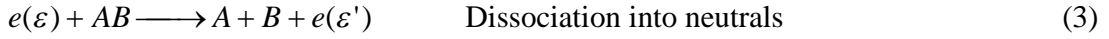
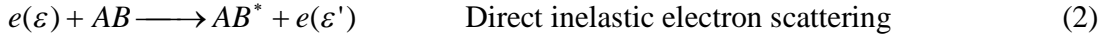
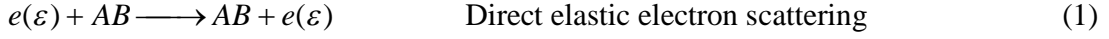
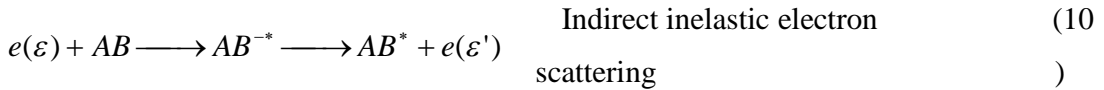


Table 5: Principal direct elastic and inelastic electron scattering processes

In the above reactions, $e(\varepsilon)$ and $e(\varepsilon')$ represent the incident electron with energy ε and the scattered electron with energy ε' respectively. The notations AB, AB^{*} and AB⁺ represent ground-state, excited and ionized molecules respectively. Similarly, the notations A and B, B^{*}, B⁺, A⁺, and B⁻ represent ground-state fragments, excited fragments, positive ion fragments and stable negative ion fragments respectively. In the case of indirect electron-collision processes, the electrons can be captured by the molecule AB to form transient (metastable) negative ions AB^{-*}. The principal indirect electron-collision processes are:



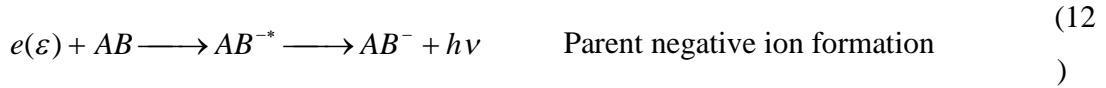


Table 6: Principal indirect elastic and inelastic electron scattering processes

The probabilities of various processes in an electron-molecule collision are described by the corresponding cross-section $\sigma(\varepsilon)$ for each reaction. For a particle A of energy ε , and for a certain type of reaction R, the mean free path between the interactions of type R, λ_{AB} , is defined as the average distance that a particle of type A will traverse through a group of particle of type B before undergoing the reaction R and is given by:

$$\lambda_{AB}(\varepsilon) = \frac{1}{\sigma_{AB}n_B} \quad \{\text{IV.1.5}\}$$

where σ_{AB} is the cross section for the interaction and n_B is the density of particle of type B.

BF₃ cross sections

Fig. 89 shows the set of cross sections for some of the processes mentioned in the previous paragraph that occur during BF₃ plasma processing.

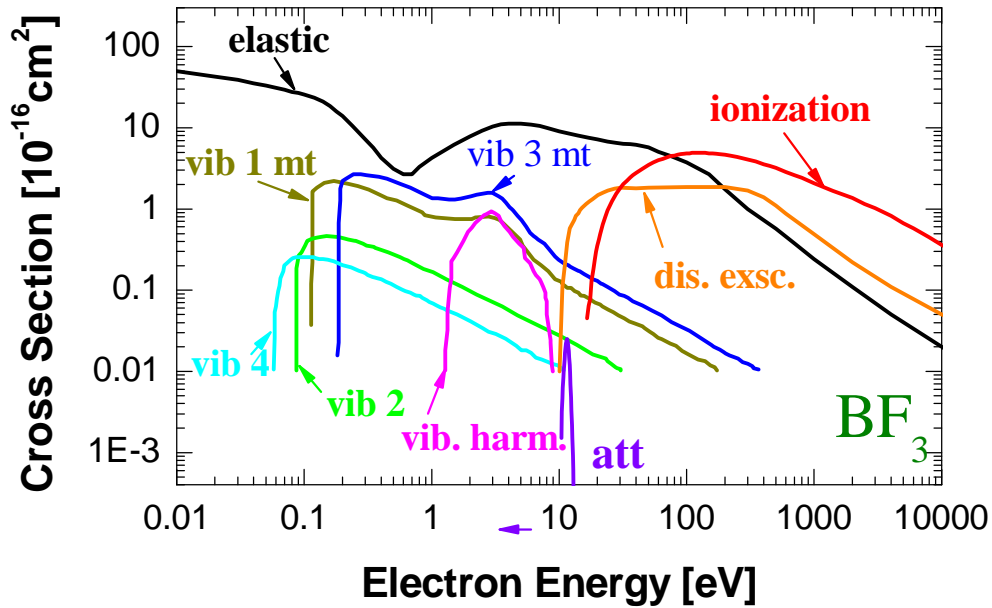
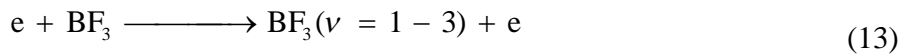


Figure 89: BF₃ cross section calculated by S. Biagi [Šašić 2005] for direct and indirect electron collision processes

The cross section for elastic scattering is seen to be large over a wide range of electron energies. With the exception of elastic electron scattering, the cross-section for each of the other processes has an energy threshold that depends on the physical process itself. The thresholds for molecular dissociation and ionization are much higher than those for direct vibrational excitation. The ionization process begins at 15.6 eV and the peak ionization probability is reached for electron energy around 120 eV.

When the electron temperature is below 1 eV energy is primarily deposited into vibrational excitations (see reaction 13) and partially into momentum transfer collisions.



The vibrationally excited BF₃ likely provides extra enhancement to the electron attachment processes, as observed in other electronegative afterglow plasmas [Midha 2001, Ramamurthi 2002, Ohtake 1996].

In contrast with the direct electron-collision processes for which the cross-sections are substantial over a wide range of electron energies, electrons in the low-energy region (usually around 20 eV) can be selectively captured by the molecule AB to form metastable negative ions AB^{-*} (see attachment cross section on Fig. 89). The transient negative ions live for approximately 10⁻¹⁵ to 10⁻² s [Christophorou 1984]. They decay by auto-detachment, leaving the neutral molecule AB with or without excess internal energy, or via the processes of dissociation electron attachments. They can also form a stable parent negative ion AB⁻.

Fig. 89 gives BF₃ ionization cross section but does not provide any information on the relative abundance of the ions created by ionization. As the focus of this work is to study positive ions, electron-impact ionization measurements for BF₃(g) were performed and are described below.

Electron-impact dissociation measurements

Employing the mass spectrometer described in chapter III, mass spectrometric measurements without plasma, in RGA mode, were made of the different ions produced during electron impact of BF₃(g) at a constant pressure of 50 mTorr inside the PLAD process chamber.

In order to obtain an accurate measurement of the appearance potential or ionization threshold, the energy scale measured by the mass spectrometer needs to be calibrated using a gas with a known appearance potential, such as argon. The measured appearance potential of Ar⁺ for Argon was measured to be 15.8 eV, which corresponds well to the first ionization potential of Argon into Ar⁺ (15.6 eV). The mass spectrometer is then correctly energy-calibrated.

The ionization efficiencies of the ion species BF₃⁺, BF₂⁺, BF⁺, B⁺ and F⁺ as a function of the electron impact energy, are presented in Fig. 90.

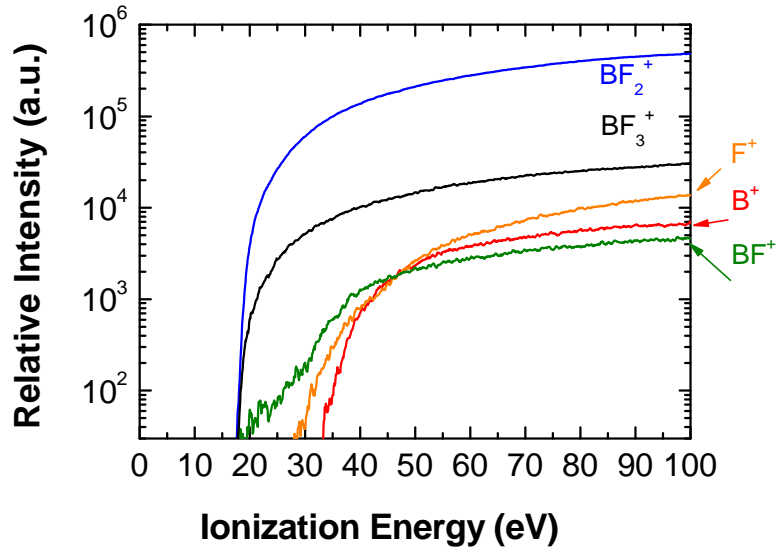


Figure 90: Ions produced through electron impact fragmentation of $BF_3(g)$, as function of electron energy

The measured appearance potential in $BF_3(g)$ corresponds to previous data [Osberghaus 1950, Farber 1984] for BF_3^+ , BF_2^+ and F^+ . No measurements of B^+ were reported in earlier work. This is a list of the reactions that occur by electron impact dissociation:

Reaction	AP (eV)
$e^- + BF_3(g) \xrightarrow{(1)} BF_3^+ + 2e^-$	15.6
$e^- + BF_3(g) \xrightarrow{(2)} BF_2^+ + F(g) + 2e^-$	15.9
$e^- + BF_3(g) \xrightarrow{(3)} BF^+ + 2F(g) + 2e^-$	15.2
$e^- + BF_3(g) \xrightarrow{(4)} B^+ + 3F(g) + 2e^-$	32.4
$e^- + BF_3(g) \xrightarrow{(5)} BF(g) + F^+ + F(g) + 2e^-$	29.8
or $BF_2(g) + F^+ = 2e^-$	

Table 7: Products of electron impact in $BF_3(g)$

The BF_3^+ appearance potential is found to be 15.6 eV, which corresponds to the values obtained from photo-ionization studies by Diebler and Batten [Diebler 1968,

Batten 1978], who reported values of 15.55 and 15.74 eV. The BF₂⁺ appearance potential from the electron impact dissociation of BF₃ occurs at an electron energy only 0.3 eV higher than that required for BF₃ ionization. It corresponds well to the Diebler experiments, which reported values of 15.81 eV for the BF₂⁺ appearance potential. The appearance potential of the reaction number 5 (29.8 eV) from Table 7 corresponds to the work of Farber and Marriott [Farber 1984, Marriott 1957], who reported values of 29.65 and 31.5 ± 2eV respectively. But the measurement of the appearance potential for BF⁺ is different than the one reported by Marriott and Osberghaus, who reported values of 27.2 ± 1eV and 25.2 ± 1eV. Our measurement of BF⁺ presents two different slopes in the low-energy part. The first slope may be due to the thermal dissociation of BF₃(g) into BF(g), due to the presence of the hot filament (1100°C) or the ionization of the fragments of BF₃ produced during the electron impact measurement. If the first slope is ignored, a value of 27.5eV can be obtained for the BF⁺ appearance potential, which is closer to other literature values.

At 18 eV, the relative abundance for BF₂⁺ and BF₃⁺ are nearly equal. At higher dissociation energies, BF₂⁺ rapidly becomes the more abundant ion. B⁺, BF⁺ and F⁺ only represent a minor fraction (2 orders of magnitude lower) of the ions created by electron impact in BF₃(g). In conclusion, a large concentration of BF₂⁺ and small concentrations of B⁺, BF⁺ and F⁺ created by electron impacts are expected in the BF₃ plasma.

Time evolution of the electron temperature and density in the pulsed discharge

In this section the time evolution of the electron temperature and density in the diode configuration (cathode negatively biased and anode grounded) and in the triode configuration (cathode and hollow cathode negatively biased and anode grounded) are presented. Fig. 91a shows the evolution of cold and fast electron densities during an entire period of a 1 kV 40 mTorr, 30μs, 2500Hz BF₃ pulsed glow discharge. Fig. 91c shows the evolution of the cold and fast electron density during a BF₃ glow discharge in a

- 300 V, 30 mTorr, 30 μ s, 2500Hz plasma, with the hollow cathode biased at - 1500V and synchronized to the cathode bias voltage.

Due to the displacement current (see II.2.2.4.e), Langmuir probe data was not analyzed during the first five microseconds of the pulse-on period. During the pulse-on period in the diode configuration, the electron density increases from 0 to 2.5×10^9 electrons per cubic centimeter, while the fast electron density increases from 0 to 1.5×10^7 electrons per cubic centimeter. During the pulse-on period in the triode configuration, the electron density increases from 0 to 5.8×10^9 electrons per cubic centimetre and stabilizes after 24 μ s. As expected, the plasma density is higher when the hollow cathode is used. The fast electron fraction is constant during the whole pulse-on period at around 2.2×10^7 electrons per cubic centimetre. In both cases, the fast electrons constitute less than 1 % of the total electron population during the pulse – on period. The existence of the fast electrons is mainly due to the secondary electrons emitted from the cathode, which are accelerated away from the cathode through the high-voltage sheath. They are thus mainly present during the pulse-on period.

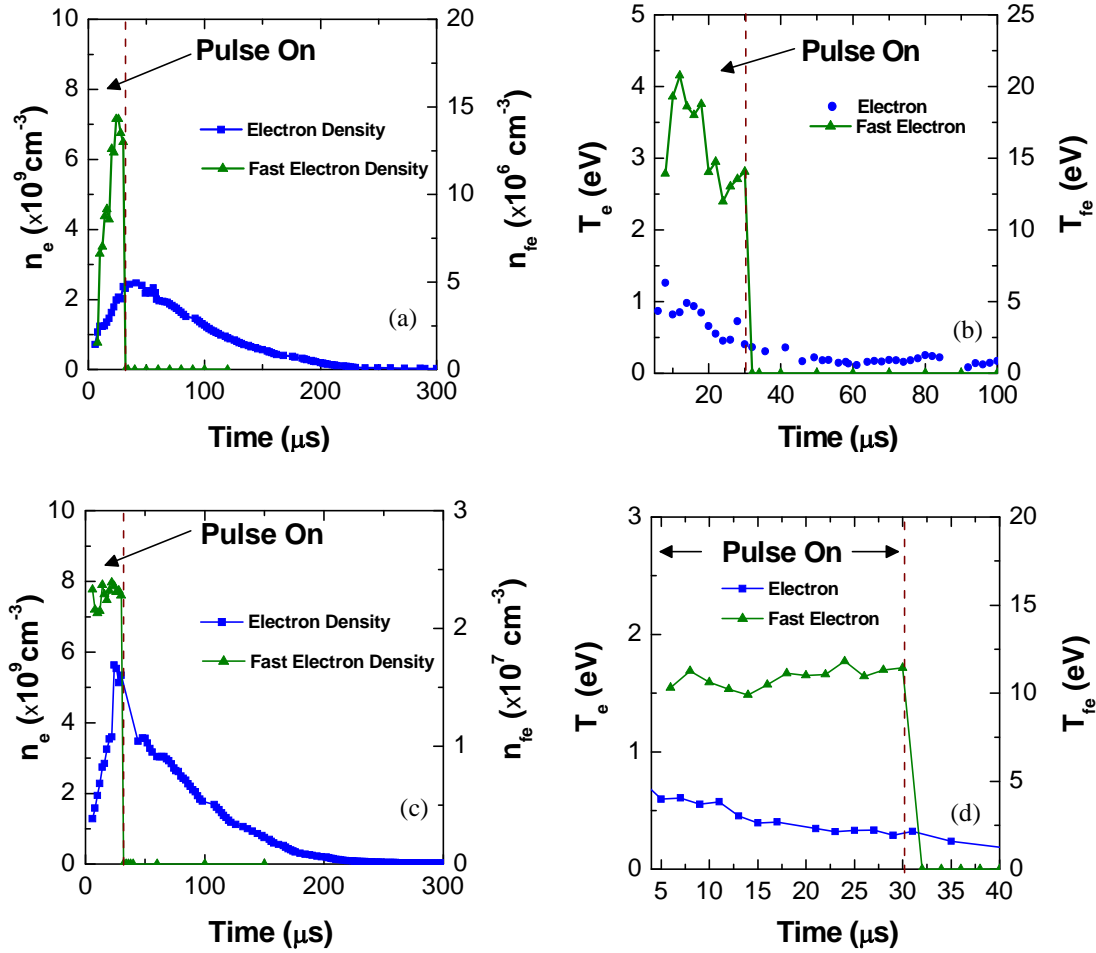


Figure 91: (a) Electron and fast electron density evolution (n_e and n_{fe}) and (b) electron and fast electron temperatures (T_e and T_{fe}) during an entire period of a BF_3 1 kV 40 mTorr, 30 μ s, 2500 Hz glow discharge plasma,

(c) Electron density evolution (n_e and n_{fe}) and (d) electron temperature (T_e and T_{fe}) during an entire period of a 300V 30 mTorr, 30 μ s, 2500 Hz BF_3 glow discharge plasma with the hollow cathode at 1500V

As two different types of electrons were detected (low-energy electrons and fast electrons), an electron temperature for the two electron populations was calculated. Fig. 91b and 91d show time evolution of the temperatures for the cold and fast electrons for the same BF_3 glow discharge. The temperature of the low-energy electrons is below 1 eV \pm 0.5 eV during the pulse-on period, and their density decays slowly during the afterglow. The average energy of these electrons is thus below the ionization threshold, and they do not participate efficiently to the ionization inside the bulk plasma.

In contrast, the fast electron temperature is around 15 to 20 eV in the diode configuration and around 12 eV in the triode configuration. The fast electrons are likely to ionize efficiently neutral particles inside the bulk. Based on the result of the electron impact experiments, the fast electrons will mainly, they will mainly create BF₂⁺ and only a minor fraction of B⁺, BF⁺ and BF₃⁺. When the high-voltage sheath disappears at the end of the pulse, the electrons do not have enough energy to ionize neutrals efficiently. The electron density decays slowly during the afterglow. At 200 μs after the end of the pulse, the electron density is under the detectable limit of the Langmuir probe technique and thus can not be detected.

Electron energy distribution function measurements

The Electron Energy Distribution Function was calculated (see Appendix 4) during the pulse-on and pulse-off periods under the plasma conditions that have been described in this section (see Fig. 92 and 93). Two different populations of electrons can be observed on the EEDF during the pulse-on period, with different electron temperatures.

The detection limit of the EEDF measurement is around $10^7 \text{ cm}^{-3} \times \text{eV}^{-3/2}$ and is relatively low due to the noise created by the numerical calculation (First and the second derivative of I(V_b)).

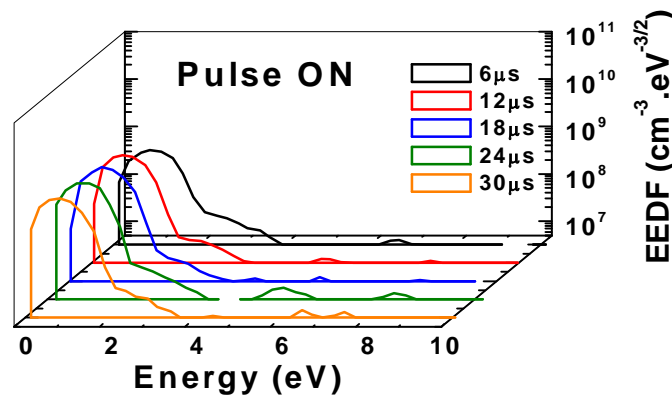


Figure 92: Calculated EEDF time evolution extracted from the I-V curves during the pulse-on period of a 1 kV, 40 mTorr, 30 μs, 2500Hz, 5sccm PLAD implantation

The hot electron tail visible during the plasma-on period of a 1 kV 40 mTorr implantation comes from the electrons emitted from the cathode and accelerated across

the sheath. These electrons are strongly decelerated by collisions inside the negative glow. As soon as the cathode voltage is turned off, the hot electron tail disappears (see Fig. 93).

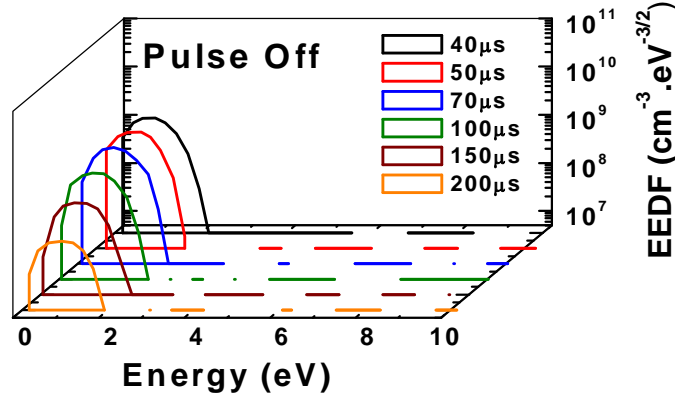


Figure 93: EEDF time evolution extracted from the I-V curves during the pulse-off period of a 1 kV, 40 mTorr, 30 μs, 2500Hz, 5sccm PLAD implantation

The EEDF method gives similar results as the fast electron measurements described in section (III.2.3.2).

Time evolution of the radial distribution of the plasma density

The temporal development of the radial electron density distribution was obtained under the same BF₃ glow discharge as before using the Langmuir probe measurement at different radial positions inside the process chamber (see Fig 94).

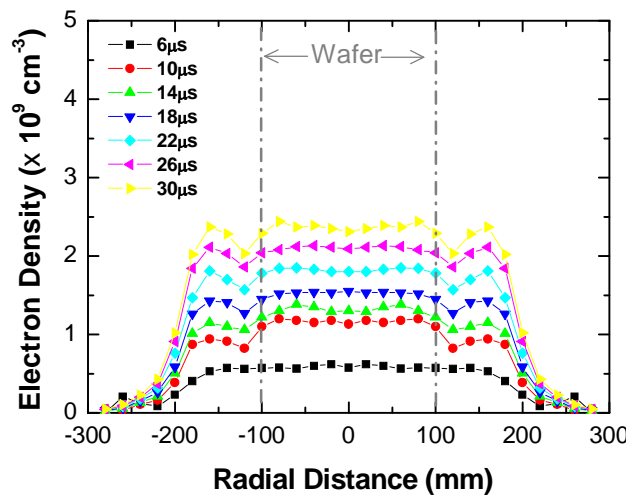


Figure 94: Time evolution during the pulse-on period of the electron density radial distribution measured by the Langmuir probe during a 1 kV 40 mTorr 30 μs BF₃ glow discharge

At the beginning of the pulse, the electron density is uniform. The electron density slowly increases with time during the pulse-on period. During the whole pulse, the electron density is uniform in the area near the wafer and strongly decreases at the edge of the cathode (radial distance equal to 200 mm). A small drop in the electron density is observed at about 120 mm from the centre of the wafer, which is where the annular Faraday cup is positioned. As discussed previously, the Faraday cup suppresses the secondary electrons emitted by the ions inside the cup. These electrons cannot participate in the ionization, and the electron density is locally reduced near the Faraday cup. This is a confirmation of the role of secondary electron emitted from the cathode.

Concluding remarks

In this section, the different elastic and inelastic collisions for the BF₃ electron cross-section processes were briefly reviewed. Electron-impact dissociation measurements for BF₃ have shown that BF₂⁺ is the dominant ion created by this reaction channel. Its relative abundance intensity is two decades higher than that for B⁺, F⁺, BF⁺ and BF₃⁺.

The time evolution of the electron temperature and plasma density was also presented. Two different electron populations were measured: the low-energy electrons that make up the majority of the electrons and the fast electrons that represent less than 1 % of the electrons and are present only during the pulse-on period. The electron density increases during the pulse-on and decreases slowly during the afterglow period. As expected, higher electron density is measured when the hollow cathode is used. The radial electron density shows a uniform electron density over the whole cathode, for the plasma conditions detailed here.

IV.2 Ion behavior

In the first part of this chapter, the electron behavior in the bulk plasma was detailed, along with the bulk plasma uniformity during pulsed-plasma processes. In this section, the time evolution of the ion density in the pulsed discharge and the sheath dynamics (collisional, collision-less sheath) will be discussed, so as to better understand the shape of the ion energy distributions for the different ions collected at the cathode surface by the mass spectrometer.

Time evolution of the ion density in the pulsed discharge

Fig 95a shows the evolution of the plasma potential V_p and floating potential V_f measured by the Langmuir probe during the whole period of a 1 kV 40 mTorr, 30 μ s, 2500 Hz, BF_3 glow discharge. After the pulse ignition, V_p and V_f quickly reach a constant value, which is maintained during the pulse-on period. V_p is measured around 8 eV. The maximum energy of an ion accelerated across the high-voltage sheath will thus be equal to 1008 eV. When the pulse is terminated, V_p and V_f increase due to the overshoot of the power supply but the difference $V_p - V_f$ strongly decreases due to the decrease of the average electron energy.

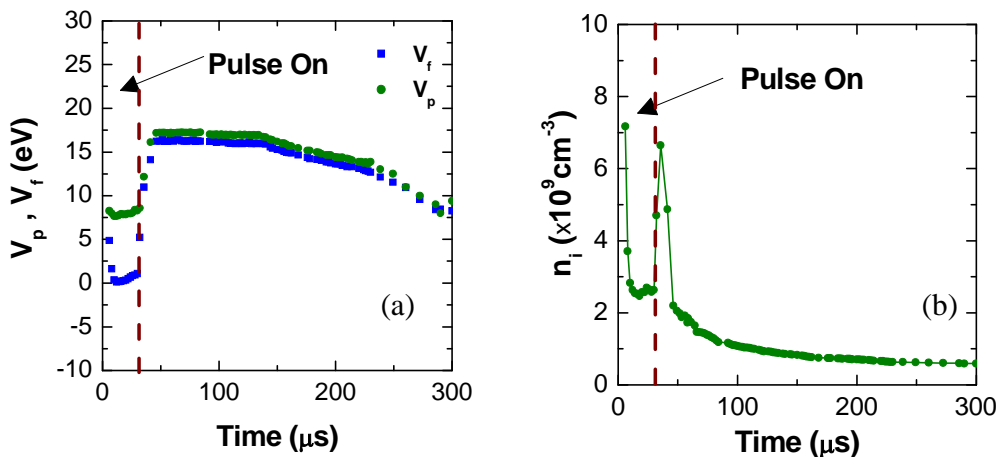


Figure 95: (a) Plasma potential and floating potential evolution (V_p and V_f) and (b) ion density evolution (n_i) during the whole period of a 1 kV 40 mTorr, 30 μ s, 2500 Hz BF_3 glow discharge plasma

The evolution of the ion density is shown as measured by Langmuir probe in Fig 95.b. The peaks obtained at the beginning and at the end of the pulse are artefacts due to the displacement current created by the rise and fall portions of the pulse (see Chapter II). The time-resolved mass spectrometer data under the same conditions (see Fig 79) shows that the ion density increases during the rise part of the pulse and stabilizes after 10 μ s or 15 μ s. This confirms that the ion density peak measured at the beginning of the pulse is not real and is due to the displacement current. A similar observation can be made at the end of the high-voltage pulse.

After 15 μ s, the ion density is stabilized as also indicated by the mass spectrometer data. The ion density decays slowly during the afterglow period, but the decay is much slower than for the electrons. When the new pulse restarts, the ion density is still at $5 \times 10^8 \text{ ions/cm}^3$ while the majority of the electrons is gone. The positive ion and electron densities are almost in equilibrium when the pulse ends. At the middle of the pulse, the ion density is higher than the electron density. Since an electro-negative gas (BF₃) is used, the presence of negative ions needs to be taken into account. When the pulse ends, the electrons quickly thermalize and thus enhance the negative ion creation by dissociative electron attachment. The plasma slowly becomes an ion-ion plasma composed of positive and negative ions.

The temporal development of the radial plasma potential distribution was measured under the same BF₃ glow discharge as before, using Langmuir probe measurements at different radial positions inside the process chamber, as shown in Fig 96a. As can be seen, the plasma potential is quickly stabilized after the beginning of the pulse. The plasma potential fluctuations measured above the wafer plane were not more than 1 eV. However, the plasma potential drops at the edge of the cathode.

The temporal development of the radial ion density distribution was also extracted from the $I(V_b)$ curve measured by Langmuir probe at different radial positions inside the process chamber, and is shown in Fig 96b.

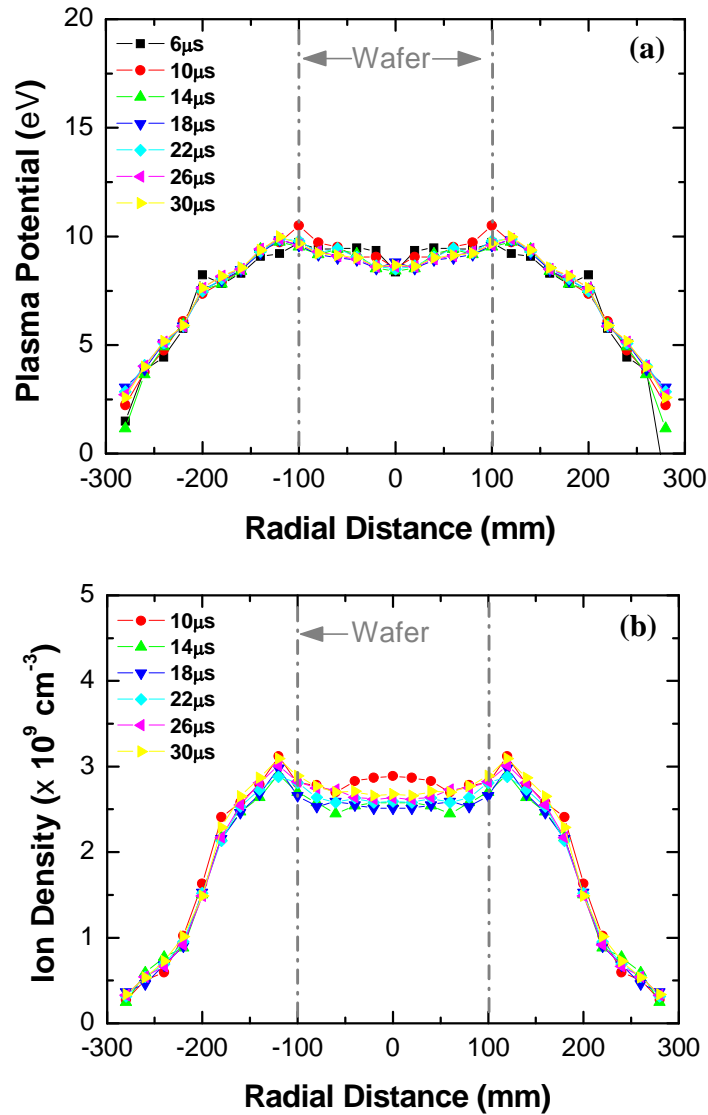


Figure 96: (a) Time evolution during the pulse-on period of the plasma potential radial distribution as measured by the Langmuir probe during a 1 kV 40 mTorr 30 μs BF_3 glow discharge (b) Time evolution during the pulse-on period of the ion density radial distribution as measured by the Langmuir probe during a 1 kV 40 mTorr 30 μs BF_3 glow discharge

As discussed previously, the ion density stabilizes after 15 μs and does not change up to the end of the pulse. In essence, these time evolution measurements confirm stable conditions throughout the implant. In contrast, the low energy population of electron increases and reaches a steady state only after 40 μs. This observation may be explained by the presence of negative ions at the beginning of the pulse. The fraction of negative ions is then slowly decreasing during the pulse on- period.

The ion density is uniform across the wafer but some uniformity distortions can be observed at the edge of the wafer. The ion density decreases quickly on the 5 cm edge of the cathode. Higher n_i can be detected between the edge of the wafer and the Faraday cup. This phenomenon will be explained and discussed in detail in section {V.1.2}.

Description of the high-voltage sheath

When a sudden negative voltage is applied to the target, electrons near the surface are initially driven away from the cathode during the time scale of the inverse electron plasma frequency ω_{pe}^{-1} , leaving behind a uniform ion density known as the ion “matrix” sheath [Lieberman 1989]. On the time scale of the inverse ion plasma frequency ω_{pi}^{-1} , ions present inside the sheath are accelerated toward the target. This, in turn, drives the sheath-plasma edge farther away, exposing to the electric field new ions that are extracted. On a longer time scale, the system evolves toward a steady state Child law [Child 1911] sheath. The electron and ion plasma frequencies are defined by the following equations:

$$\omega_{pe} = \left(\frac{e^2 n_e}{\epsilon_0 m_e} \right)^{1/2} \quad \omega_{pi} = \left(\frac{e^2 n_i}{\epsilon_0 M_i} \right)^{1/2} \quad \{\text{IV.2.1}\} \text{ and } \{\text{IV.2.2}\}$$

where n_e is the electron density, m_e is the electron mass, ϵ_0 is the permittivity of free space, n_i is the ion density and M_i is the ion mass.

A good understanding of sheath dynamics is necessary to understand the shape of the energy distributions for the different ion species reaching the cathode. In this section, we will briefly discuss the dynamic models for Plasma Immersion Ion Implantation sheath formation in the collision-less and collisional regimes. These models were developed by Lieberman and coworkers [Lieberman 1989, Stewart 1991, Vahedi 1991, and Lieberman 2005]. In the case of PIII, the plasma steady state is created by an RF source (constant plasma density), and each negative pulse applied on the wafer accelerates the ions from the bulk plasma up to the wafer target. In our case, as the plasma is ignited periodically by the negative pulse applied to the cathode, the plasma density does not remain constant during the whole period. The Lieberman’s model is

slightly modified here, so as to take into account the evolution of the plasma density during the pulse.

Matrix sheath

As explained in the previous paragraph, when a sudden negative voltage is applied on the cathode, on a very short time scale, a matrix sheath is formed. The voltage drop inside the sheath is large compared to the bulk plasma electron temperature. As the potential in the sheath is highly negative with respect to the plasma, it is assumed that only ions are present inside the sheath of thickness (s) with a uniform ion density ($n_i = n_s$). The matrix sheath thickness can be estimated with the following formula [Anders 2000]:

$$s = \left(\frac{2\varepsilon_0 V_c}{en_s} \right)^{1/2} \quad \text{\{IV.2.3\}}$$

where n_s is the ion density inside the sheath. Lieberman estimated that the time (t) required to implant all the ions of the matrix sheath was proportional to the inverse of the ion plasma frequency [Lieberman 1989]:

$$t \approx \frac{2.7}{\omega_{pi}} \quad \text{\{IV.2.4\}}$$

The electron and ion plasma frequency as well as the time necessary to implant all the ions from the matrix sheath for different plasma density is presented in Table 8.

	Plasma density (cm ⁻³)				
	2.E+08	5.E+08	1.E+09	2.E+09	5.E+09
ω_{pe} (Hz)	8.E+08	1.E+09	2.E+09	3.E+09	4.E+09
ω_{pi} (Hz)	3.E+06	4.E+06	6.E+06	8.E+06	1.E+07
$\tau_{\text{matrix sheath}}$ (μs)	1.0	0.6	0.5	0.3	0.2

Table 8: Electron and ion plasma frequency, matrix sheath time length after the beginning of the pulse as a function of the plasma density

In the case of the plasma doping system, the ion density is not constant during the entire pulse period. Typical ion density before the beginning of the negative pulse is between 2×10^8 and 5×10^8 ions/cm³. All the ions of the matrix sheath are implanted in less than 1 μs , therefore matrix sheath will not be considered in the following work.

Collision-less sheath

Following the matrix sheath, ions are accelerated toward the cathode. This drives the sheath-plasma edge further away. In case of collision-less motion of ions inside the sheath, calculation of the time taken to reach the stable Child law sheath can be performed. This is the aim of this paragraph.

In case of collision less sheath, the potential inside the sheath follows a $x^{4/3}$ dependence [Lieberman 2005]:

$$\phi(x) = -\frac{3}{2} \left(\frac{j_c}{\epsilon_0} \right)^{2/3} \times \left(\frac{M}{2e} \right)^{1/3} \times x^{4/3}$$

where j_c is the current density, ϵ_0 is the free-space permittivity, e and M are the ion charge and mass and $x = 0$ at sheath edge.

The Child law current density j_c for a voltage V_c across a sheath thickness (s) is defined by the following equation [Child 1911]:

$$j_c = \frac{4}{9} \epsilon_0 \times \left(\frac{2e}{M} \right)^{1/2} \times \frac{V_0^{3/2}}{s^2} \quad \{\text{IV.2.5}\}$$

Assuming that there are two sources of ions in the sheath (ions streaming into the sheath at the Bohm velocity and ions uncovered by the expanding sheath) and equating j_c to the charge per unit time crossing the sheath boundary [Lieberman 1989]:

$$en_0 \times \left(\frac{ds}{dt} + u_B \right) = j_c \quad \{\text{IV.2.6}\}$$

Assuming that there is a constant plasma density, the motion of the pulsed plasma sheath (s) in a collision-less PIII was modeled by Lieberman using the following equation:

$$en_0 \left(\frac{ds}{dt} + u_B \right) = \frac{4}{9} \epsilon_0 \times \sqrt{\frac{2e}{M}} \times \frac{V^{3/2}}{s^2} \quad \{\text{IV.2.7}\}$$

where e is the ion charge, n_0 is the plasma density in the bulk, s is the sheath thickness, u_B is the Bohm speed, ϵ_0 is the permittivity of free space, M is the ion mass and V is the applied voltage.

In our case, the bulk plasma density is not constant during the entire pulse, the equation which takes into account the plasma density variations ($n(t)$) should be used [Radovanov 2005]:

$$en(t)\left(\frac{ds}{dt} + u_B\right) = \frac{4}{9}\epsilon_0 \times \sqrt{\frac{2e}{M}} \times \frac{V^{3/2}}{s^2} \quad \{\text{IV.2.8}\}$$

The time scale (t_c) for establishing the steady-state Child law sheath is then [Anders 2000]:

$$t_c \approx \left(\frac{\sqrt{2}}{9}\right) \times \omega_{pi}^{-1} \times \left(\frac{2V_c}{T_e}\right)^{3/4} \quad \{\text{IV.2.9}\}$$

The time necessary to establish the steady-state Child law sheath for different plasma density and cathode voltage is calculated in Table 9. As can be seen, the time needed to reach the steady-state sheath is dependant of the plasma density and cathode voltage. The steady state is reached faster at higher plasma densities and lower cathode voltages. In most of the cases studied here, a quasi steady state sheath is reached during the first 10 μ s of the high-voltage sheath.

			Plasma density (cm ⁻³)				
			2.E+08	5.E+08	1.E+09	2.E+09	5.E+09
Cathode Voltage (V)	250	$\tau_{\text{child sheath}} (\mu\text{s})$	6.2	4.0	2.8	2.0	1.2
	500	$\tau_{\text{child sheath}} (\mu\text{s})$	10.5	6.6	4.7	3.3	2.1
	1000	$\tau_{\text{child sheath}} (\mu\text{s})$	17.7	11.2	7.9	5.6	3.5

Table 9: Time necessary to establish the steady-state Child law sheath for different plasma density and cathode voltage

An example of a calculated sheath thickness as a function of time is presented in Fig. 97 for a 1kV 40 mTorr BF₃ glow discharge.

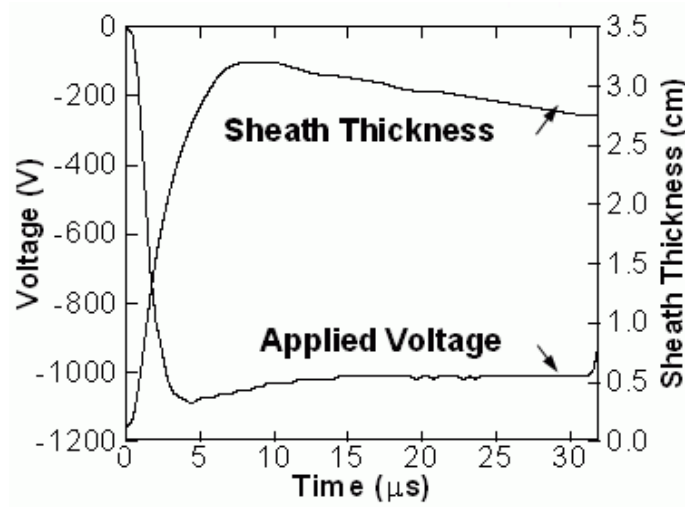


Figure 97: Sheath thickness calculated using {IV.2.8} for a 1kV 40mTorr 30μs BF₃ glow discharge the plasma parameters, such as $n(t)$, were measured by a Langmuir probe

The cathode voltage and temporal evolution of the plasma parameters measured by the Langmuir probe were used as an input for the calculation, assuming a collisionless sheath. With an increasing dc bias voltage, the sheath expands. As the dc bias voltage and the bulk plasma density reach a steady state, the sheath thickness tends to a constant value.

Collisional sheath

This section describes the equations governing the collisional sheath. Assuming that the ion motion is highly collisional, the Child law can be written as follows [Vahedi 1990, Lieberman 2005, Budtz-Jorgensen01]:

$$j_i = \varepsilon_0 \left(\frac{2}{3}\right) \times \left(\frac{5}{3}\right)^{3/2} \times \left(\frac{2e\lambda_i}{\pi M}\right)^{1/2} \times \frac{V^{3/2}}{s^{5/2}} \quad \{\text{IV.2.10}\}$$

where ε_0 is the permittivity of free space, e is the charge of an ion of mass M , V_0 is the cathode voltage, λ_i is the ion mean free path and j_i is the ion current density. The sheath potential $\phi(x)$ at a distance x inside the sheath can be expressed by the following equation ($x = 0$ at sheath edge):

$$\phi(x) = -\frac{3}{5} \left(\frac{3}{2\epsilon_0} \right)^{2/3} \times \left(\frac{\pi M \times j_i^2}{2e\lambda_i} \right)^{1/3} \times x^{5/3} \quad \{\text{IV.2.11}\}$$

The number of collisions (s/λ) inside a sheath is calculated based on {IV.2.10} using the following formula:

$$\frac{s}{\lambda} = \frac{1}{3} \times \left(\frac{e}{\pi M} \right)^{1/5} \times \left(\frac{\epsilon_0}{j_i} \right)^{2/5} \times (10\text{V})^{3/5} \times \left(\frac{\sigma \times p}{kT_g} \right)^{4/5} \quad \{\text{IV.2.12}\}$$

where σ is the ion neutral cross-section, k is Boltzmann's constant, T_g is the gas temperature and p is the neutral gas pressure.

Ion processes inside a collisional sheath

Fig. 98 is a representation of the two types of sheaths: a collision-less and collisional sheath

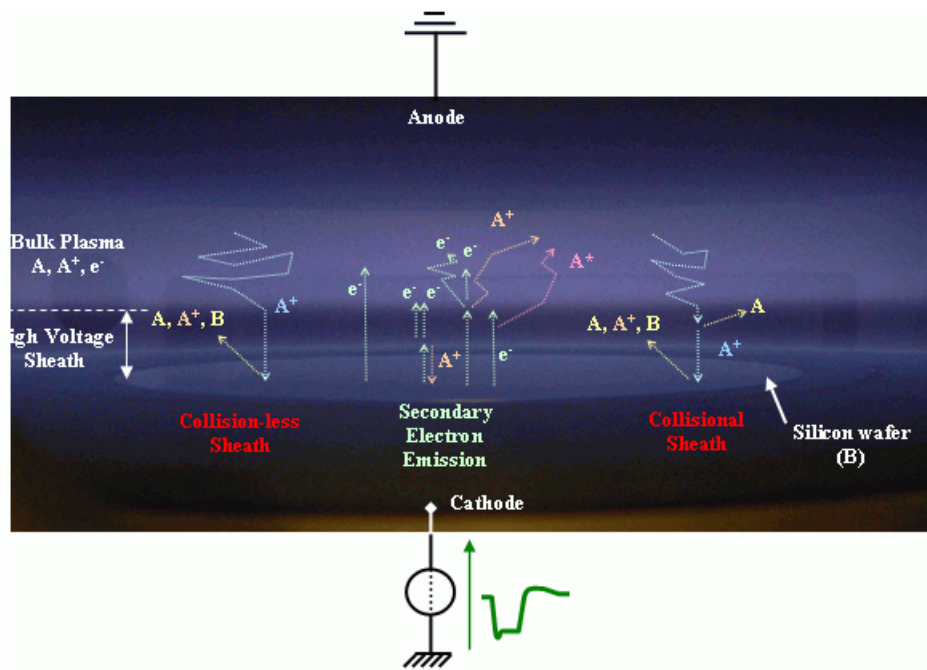
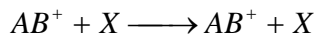


Figure 98: Representation of the different particle interaction in a collision-less sheath or collisional sheath, as well as the secondary electron emission from the cathode

It also shows the secondary electron emission processes and the interactions of these electrons with the gas phase. The present section gives a brief summary of the main collision processes inside a collisional sheath (see Fig. 98). Elastic (polarization) scattering, charge transfer, molecular ion dissociation and ionization are the main collision processes occurring inside a collisional sheath and are described in the following.

Elastic scattering

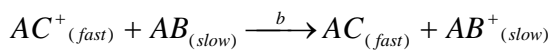
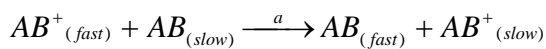
An elastic collisions can be represent by the following reaction



where X can be an electron, an neutral or an ion. An estimation of elastic scattering cross sections can be made using the hard sphere model. The radius of the molecule BF₃ is 0.129 [HCP 1981] while the one of BF₂ radical is 0.125 [Lenoble 2000], giving cross sections for elastic scattering equal to respectively $2.1 \times 10^{-19} \text{ m}^2$ and $1.96 \times 10^{-19} \text{ m}^2$.

Charge transfer

Two different kinds of charge exchange collisions can be distinguished, the symmetric charge transfer between a positive ion AB⁺ and its parent molecule AB (reaction a) or an asymmetric charge transfer between a positive ion AB⁺ with another molecule AC (reaction b).



The charge exchange process creates a fast neutral particle that reaches the cathode with an energy lower than the sheath voltage and is implanted into the target. It also creates a slow ion that is accelerated by the high voltage sheath, but will not reach the full energy.

Ion dissociation

As indicated by Stoffels and al [Stoffels 2001], because of the high ion energy inside the sheath, in addition to well known elastic scattering and charge exchange collisions, many other ion processes can occur. These mechanisms are less studied and less known. During the acceleration inside the sheath, fast positive molecular ions (AB^+) can collide with the background gas (C). The molecular ion dissociates and can create lighter positive ions (A^+ , B^+) and can be described by the following reaction:

	Reaction
Simple dissociation	$AB^+ + C \longrightarrow A + B^+ + C$ $A^+ + B + C$
Ionizing dissociation	$AB^+ + C \longrightarrow A^+ + B^+ + C + e^-$
Electron capture and dissociation	$AB^+ + C \longrightarrow A + B + C^+$
Simple electron capture (charge exchange)	$AB^+ + C \longrightarrow AB + C^+$
Background gas ionization	$AB^+ + C \longrightarrow AB^+ + C^+ + e^-$

Table 10: Products of dissociation of fast molecular ion (AB^+) by collision with the background gas (C) inside the high-voltage sheath [Suzuki 1986]

These different reactions were reported by Suzuki and coworkers as the main dissociation reaction processes that can occur during the dissociation of fast (> 4 keV) molecular ions (AB^+ : CO^+ and CF^+) and different background gases (C: He, Ne and Ar) [Suzuki 1986]. Each collision process present different cross sections but from a general point of view, simple dissociation was found to be the main mechanism. In our case AB^+ can be assimilated to BF^+ , BF_2^+ , BF_3^+ or other heavier ions such as $B_xF_y^+$. However no cross section measurements are available for boron containing ions in $BF_3(g)$.

Ionization inside the sheath by secondary electrons

The secondary electrons emitted from the cathode and accelerated by the cathode high voltage can gain enough energy to ionize neutral particles during their travel through the sheath. The same reaction channels than the one for electron impact describe in section (IV.1.2) are still valid in the high-voltage sheath.

a) Discussion on ion angular dispersion in a collisional sheath

Vahedi and coworkers [Vahedi 1992] have developed an analytical model for the angular distribution of the ion flux at the cathode in a collisional sheath due to ion-neutral scattering collisions, when charge exchange is the dominant collision mechanism. The shape of the angular distribution function was found to be insensitive to variations in pressure and correspond to particle-in-cell simulations. They showed that the average angle for all ions was less than 3° during discharge conditions close to the ones used here (pressure of 50 to 100 mTorr, cathode voltage 500 V), when the ratio of charge transfer cross-section to the elastic scattering cross section was equal to 6. The average angle for all ions is proportional to this ratio. The average angle was further reduced when the ratio was increased. Average angle distribution remains below 1° degree when an ion-neutral charge exchange is the dominant reaction channel inside the sheath.

Davis and Vanderslice model

Davis and Vanderslice were among the firsts to accurately measure and model the ion energy distribution for a cathode sheath during a d.c. glow discharge in 1963 [Davis 1963].

A slightly modified version of their model is described below. The model illustrated in Fig. 99 assumes that:

- No ionization occurs inside the sheath (all the ions reaching the cathode comes from the bulk plasma).

- Charge exchange is the only ion-neutral collision mechanism taking place (the momentum transfer is ignored).
- The charge exchange cross-section is energy-independent.
- The sheath potential is governed by the Child law [Lieberman 1989]. As the measured of the ion energy distributions are typically made 20 μs after the beginning of the pulse when the Child law is valid (see section IV.2.2.2, Tab. 9):

$$\Phi(x) = (V_c - V_p) \times \left(1 - \frac{x}{s}\right)^{5/3} + V_p \quad \{\text{IV.2.13}\}$$

In their original paper, Davis and Vanderslice assume there is a linear electric field, but according to equation {IV.2.11} the potential in the sheath should have a $x^{5/3}$ dependence.

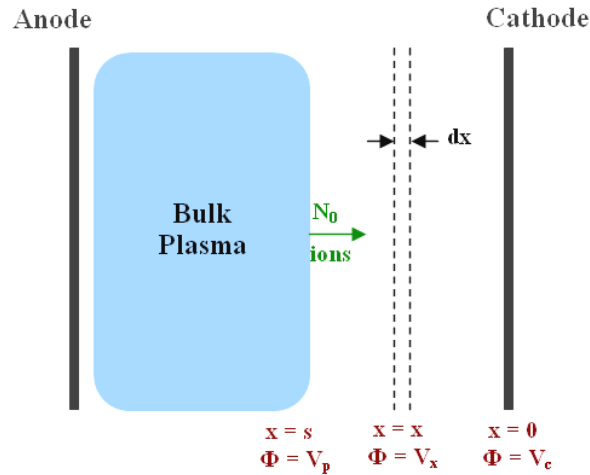


Figure 99: Modified Davis and Vanderslice model for the ion energy distribution measured at the cathode

The only way for an ion to strike the cathode with an energy eV_x is to undergo a charge transfer collision at a point x and then travel all the way to the cathode without further collision. Making the mean free path for a charge exchange as λ_i and assuming that ϕ_0 , the ion flux at the sheath edge, remains constant all the way to the cathode, the

number of collisions per surface and time units that occur in the region dx is $\phi_0(dx / \lambda_i)$. The probability for any of these ions to reach the cathode without further charge exchange is given by e^{-x/λ_i} . The number of ions per surface and time units detected at energy eV_x is then given by:

$$d\phi = \left(\frac{\phi_0}{\lambda_i} \right) \times e^{-x/\lambda_i} dx \quad \{\text{IV.2.14}\}$$

Using equation {IV.2.6} and setting $\Phi(x) = V_x$, the following equation is obtained:

$$x = s \left[1 - \left(\frac{V_x - V_p}{V_c - V_p} \right)^{3/5} \right] \quad \{\text{IV.2.15}\}$$

and

$$dx = -\frac{3s}{5} \times \left[\frac{V_x - V_p}{V_c - V_p} \right]^{-2/5} d \left(\frac{V_x - V_p}{V_c - V_p} \right) \quad \{\text{IV.2.16}\}$$

By substituting {IV.2.15} and {IV.2.16} into {IV.2.14} the modified Davis and Vanderslice equation {IV. 2.17} is obtained giving a theoretical expression for IEDs:

$$\frac{1}{\phi_0} \times \frac{d\phi}{dV_x} = \frac{3}{5} \times \frac{s}{\lambda_i} \times \frac{1}{(-V_c + V_p)} \times \left(\frac{V_x - V_p}{V_c - V_p} \right)^{-2/5} \times \exp \left[-\frac{s}{\lambda_i} \left(1 - \left(\frac{V_x - V_p}{V_c - V_p} \right)^{3/5} \right) \right]$$

The fraction of ions that cross the entire sheath without any collisions, e^{-s/λ_i} is not included in the equation {IV.2.17}. The controlling parameter of the equation is s/λ_i , which is the mean number of collisions that an ion undergoes on its way through the sheath. An example of calculated ion energy distributions for different numbers of collisions inside the sheath ($\frac{s}{\lambda_i}$ from 1 to 100 collisions) is presented in Fig. 100.

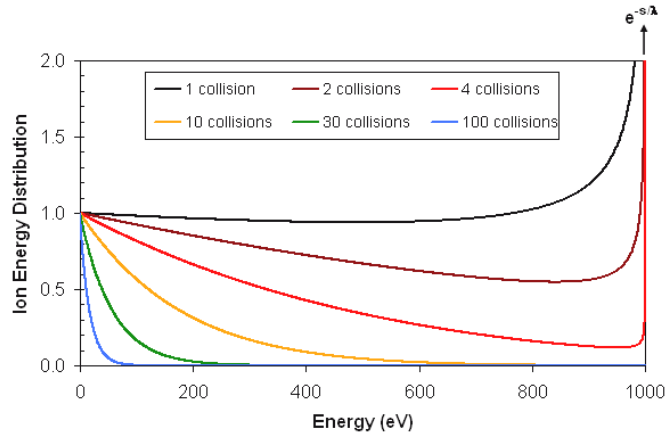


Figure 100: Theoretical cathode ion energy distributions for different numbers of collisions inside the sheath (from 1 to 100). All the curves have been normalized at $E = 0$ eV.

In order to validate their model, Davis and Vanderslice have performed ion energy distribution measurements of Ar^+ and Ne^+ in argon and neon plasmas using mass spectrometry. Charge exchange was expected to be the dominant ion-neutral collision process, since symmetric charge exchange (Ar^+ with Ar and Ne^+ with Ne) under these conditions is known to be very efficient. Fig. 101 shows a comparison of experimental Ne^+ and Ar^+ ion energy distributions with their theoretical curves calculated with the Davis and Vanderslice model using s/λ , as the fitting parameter. The IED curves for these two ions follow an exponential decay and match the Davis and Vanderslice theory well.

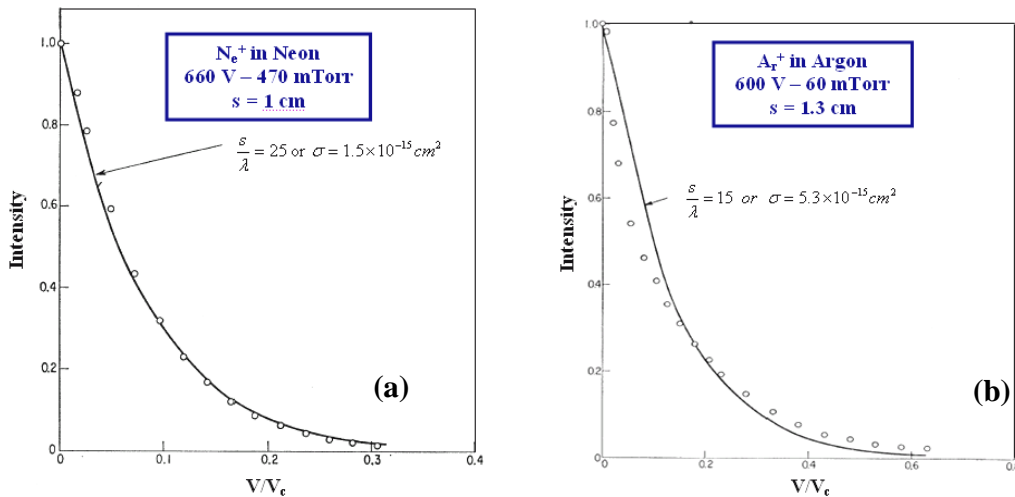


Figure 101: Energy distribution for Ne^+ in Neon discharge (660 V 470 mTorr) and for Ar^+ in Argon discharge (600 V 60 mTorr). The circles are the experimental data and the full lines are the theoretical curve fitted to the experimental points [Davis 1963]

It should be noted that the high energy ion fraction decreases rapidly when the number of collisions inside the sheath increases (see Fig 100).

From the IED, the mean ion energy can be calculated for different numbers of collisions using the following formula:

$$\langle E \rangle = \frac{\int E \times f(E) \times dE}{\int f(E) \times dE} \quad \text{\{IV.2.18\}}$$

As expected, the mean ion energy is reduced when the number of collisions inside the sheath increases (see Fig. 102). It should be noted that only three collisions are enough to decrease $\langle E \rangle$ to $E_{\max}/2$.

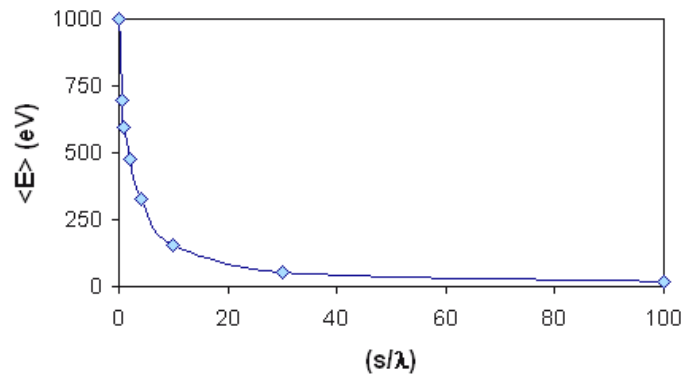


Figure 102: Calculated mean energy as a function of the number of collisions based on the Davis and Vanderslice model

This modified Davis and Vanderslice model will be used to fit the experimental IED measured in the BF₃ plasma, as discussed in the next section.

Ion energy distribution in BF₃ plasma

The main goal of this section is to understand the shape of ion energy distribution of the different ions reaching the cathode in BF₃ plasma. In this aim, an overview of different boron containing ions in the bulk plasma and in the high-voltage sheath will first be presented. The ion energy distributions (IED) of the boron containing ions reaching

the cathode will then be presented under various plasma and discharge conditions. The shape of the IED are then analyzed and discussed.

Overview

b) Boron containing ions in the bulk plasma

Fig. 103 shows the relative abundances of the major ionic species B^+ , BF^+ , BF_2^+ , BF_3^+ , $B_2F_3^+$ and $B_2F_5^+$ in the BF_3 plasma. These ions are measured during the pulse-on period and under various operating discharge conditions (different pressures, frequencies and cathode voltages) and various modes of operation of the discharge (with or without hollow cathode, pulsed anode mode (see section {V.3.3.2}) with the mass spectrometer installed inside the anode

Under all the different operating conditions, BF_2^+ is the dominant ion of the bulk plasma ion population, followed by the heavier molecular ions such as $B_2F_3^+$ and $B_2F_5^+$. The bulk plasma relative abundance of B^+ , BF^+ and BF_3^+ always remains below 3 %.

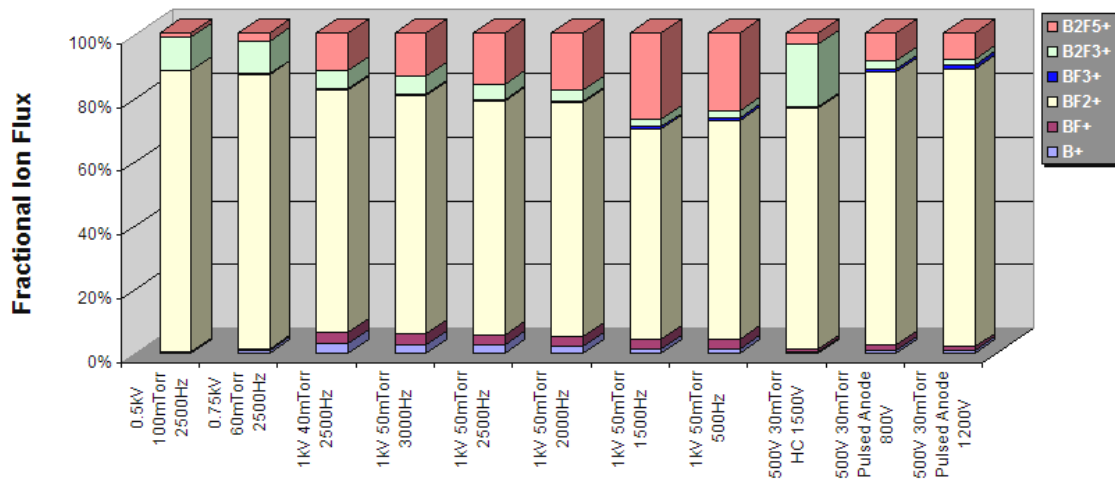


Figure 103: Bulk plasma boron ions fractions normalized to the total flux of boron containing ions in BF_3 plasma for different cathode voltage biases, pressures and frequencies measured by the mass spectrometer during the pulse-on period installed on the anode in a reversed bias configuration

These data are in good agreement with the electron-impact dissociation measurements in BF₃(g) and with mass spectrometric measurements made in BF₃ bulk RF plasma by Kaepelin [Kaepelin 2002] who found that BF₂⁺ was the main ion. The heavier ions detected in the bulk plasma are probably created by three body recombination with neutral particles.

c) Boron containing ions in the plasma sheath

Fig. 104 shows the relative abundances of the major ionic species B⁺, BF⁺, BF₂⁺, BF₃⁺, B₂F₃⁺ and B₂F₅⁺ in BF₃ plasma. These ions are measured during the pulse-on period with the mass spectrometer installed inside the high-voltage cathode under the same discharge conditions as those discussed previously.

Under all the different operating conditions, BF₂⁺ is the dominant ion striking the cathode followed by B⁺ and BF⁺. B⁺ and BF⁺ fractions represent up to 25% of the total flux of boron ions. Under all the conditions, the BF₃⁺, B₂F₃⁺ and B₂F₅⁺ ion fractions represent only a minor fraction of the total flux of boron ions (less than 3% of the total ion flux).

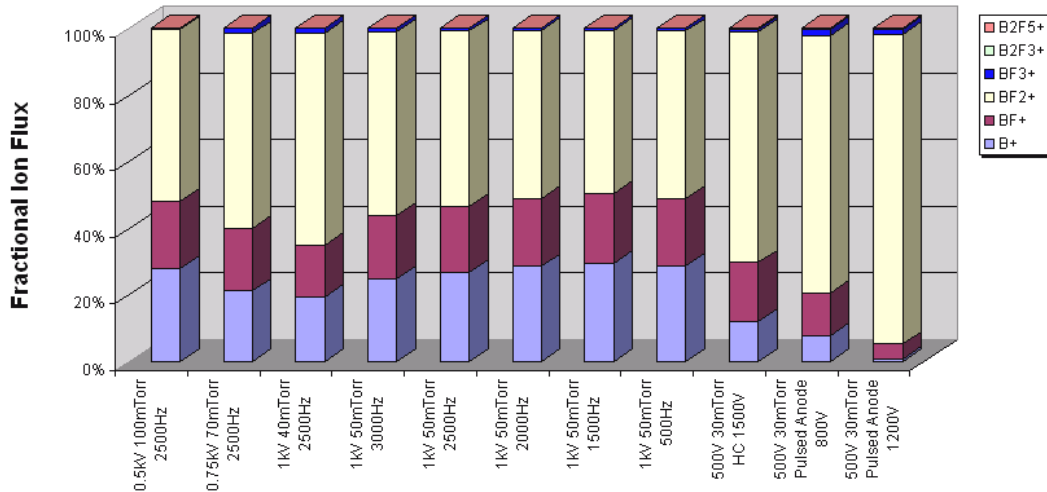


Figure 104: Boron ions and molecular ions fraction normalized to the total flux of boron ions of the ions reaching the cathode, as measured during the pulse-on period in BF₃ plasma for different cathode voltage biases, pressures and frequencies by the mass spectrometer installed on the cathode

Compared to the bulk plasma ion species, the relative abundance of B⁺ and BF⁺ is in general strongly increased from a few percent up to 25 %, and B₂F₃⁺ and B₂F₅⁺ are largely reduced. Even if, the BF₂⁺ ion remains the dominant ion, its fraction is significantly reduced after acceleration inside the sheath. The ion population is thus changed significantly after crossing the plasma sheath. This observation indicates that bulk plasma diagnostics is not sufficient to predict the ion population that reaches the cathode and implants onto the wafer. It should be noted that in the case of the hollow cathode and pulsed anode modes, the B⁺ and BF⁺ fractions do not increase as much as in the other cases. A general presentation of the IED will now be given for the cases of collision-less and collisional sheaths.

d) Ion energy distribution in collision-less sheath and transition to collisional sheath

In this section, ion energy distributions in BF₃ plasma are presented under various discharge operation in the case of the triode configuration (anode grounded, cathode and hollow cathode pulsed synchronously), where the sheath is expected to be collision-less. As discussed previously, when a hollow cathode is used, higher plasma density than in the diode configuration is achievable and the collision-less sheath condition can be reached. Fig. 105, 106 and 107 show B⁺, BF⁺, BF₂⁺, BF₃⁺, B₂F₃⁺ and B₂F₅⁺ IEDs normalized to the total flux of boron ions for various cathode biases (50, 100, 300, 500, 750 and 1000V). The discharge is created and maintained by hollow cathode at a constant negative bias (1500 V) in a 30mTorr BF₃ plasma.

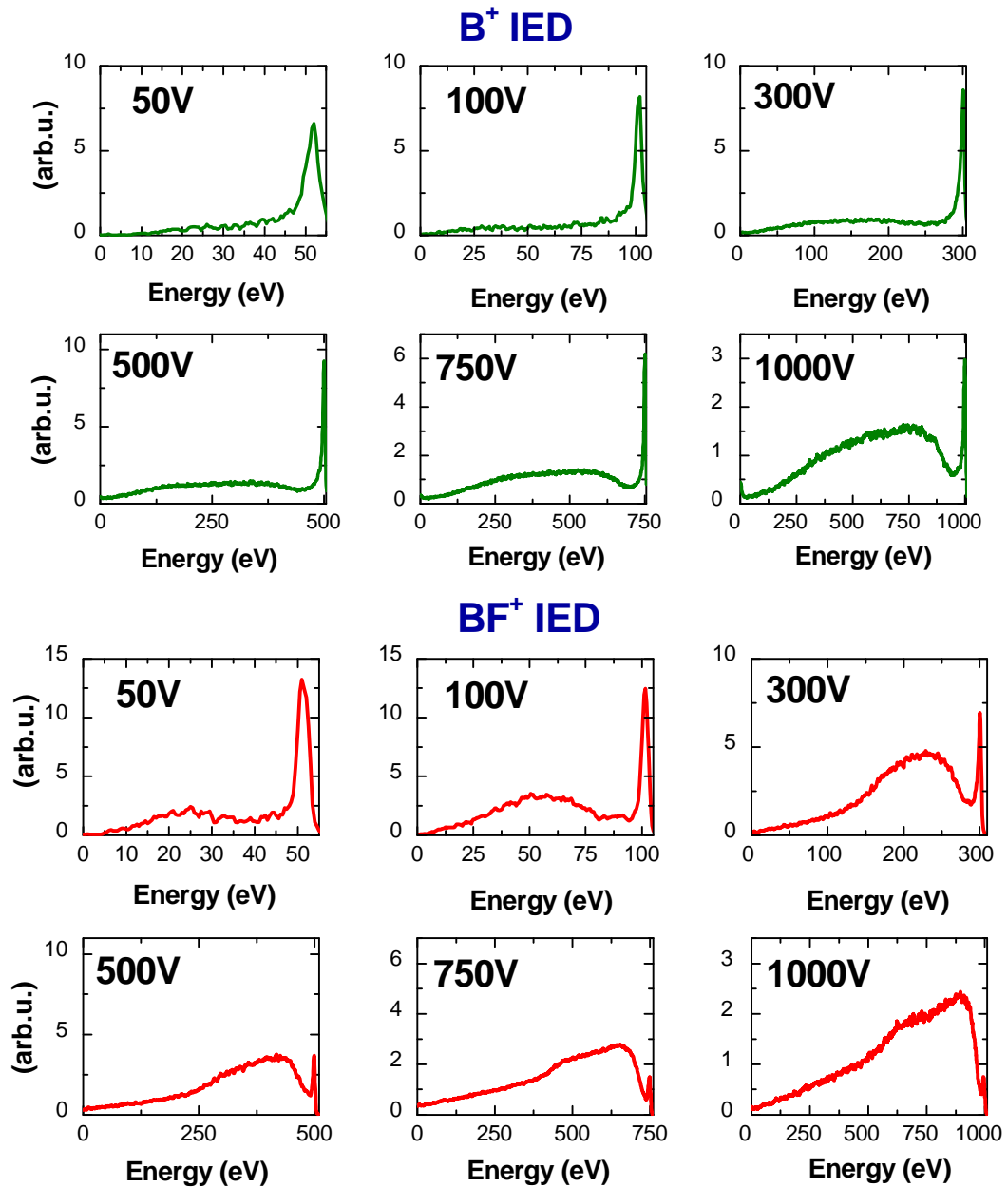


Figure 105: B^+ and BF^+ IEDs normalized to the total ion flux for different cathode voltages (50, 100, 300, 500, 750 and 1000 V), for a 30 mTorr, 5sccm, 2500 Hz BF_3 glow discharge created using the hollow cathode at 1500V

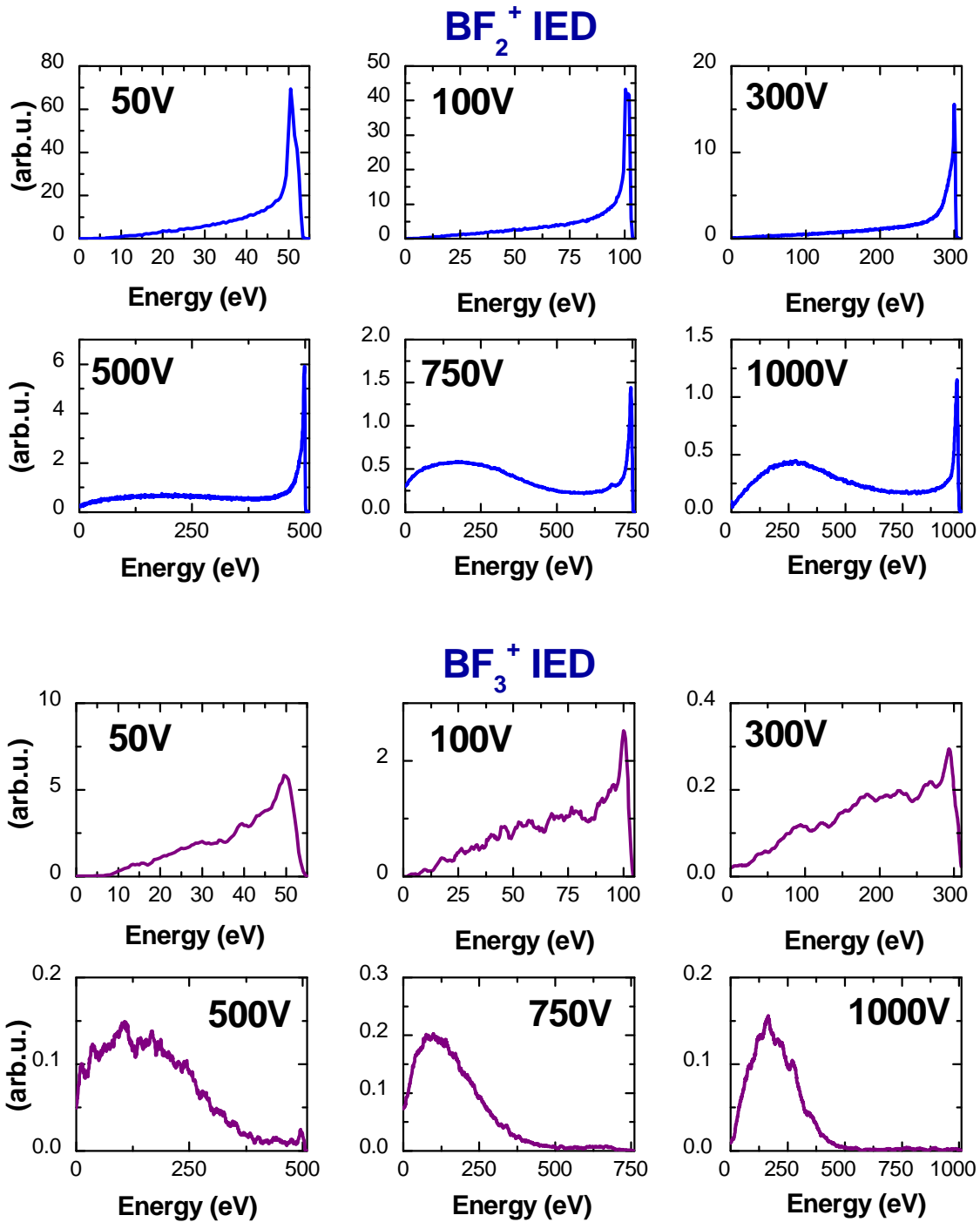


Figure 106: BF_2^+ and BF_3^+ IED normalized to the total ion flux for different cathode voltages (50, 100, 300, 500, 750 and 1000 V), for a 30 mTorr, 5sccm, 2500 Hz BF_3 glow discharge created using the hollow cathode at 1500V

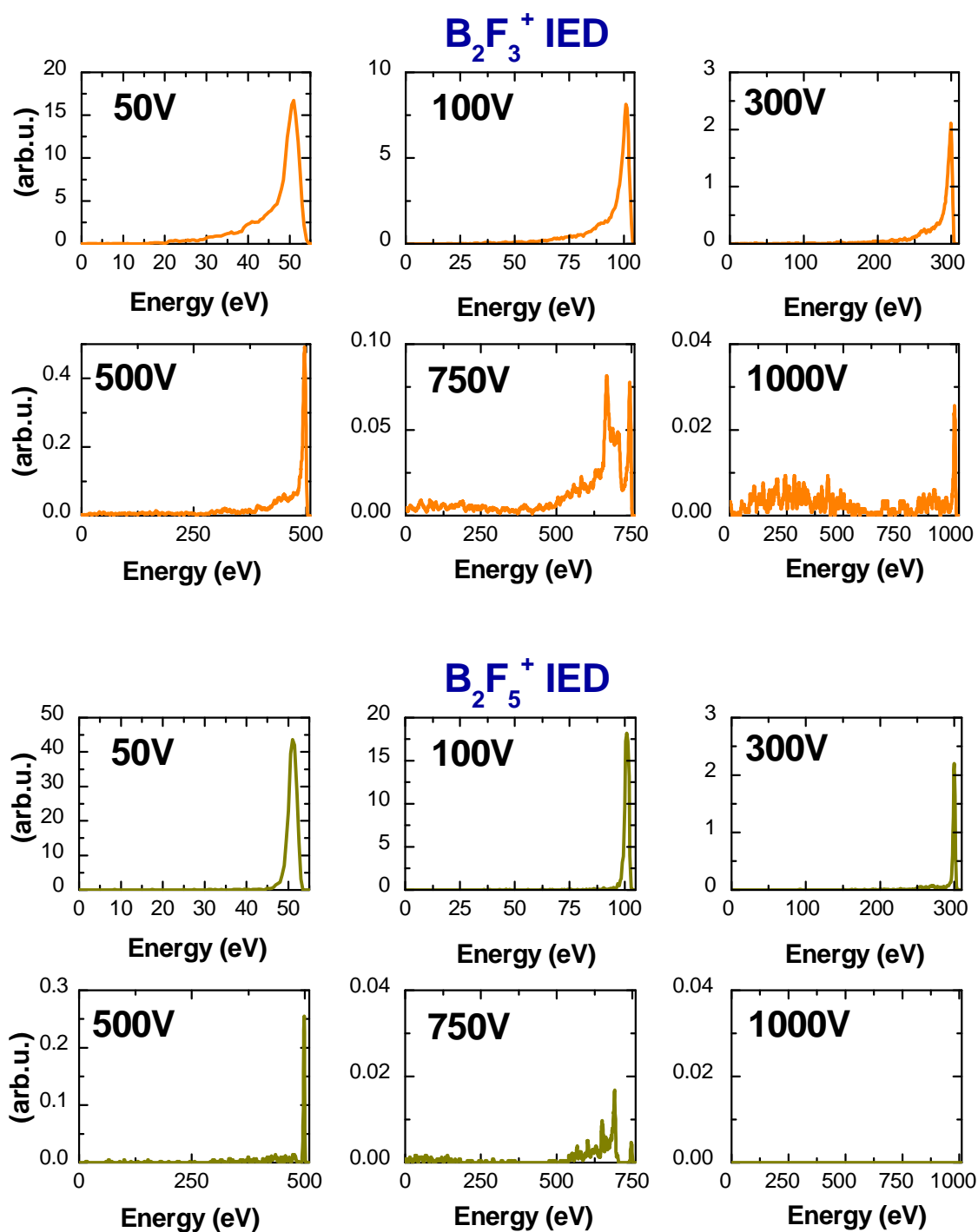


Figure 107: $B_2F_3^+$ and $B_2F_5^+$ IEDs normalized to the total ion flux for different cathode voltages (50, 100, 300, 500, 750 and 1000 V), for a 30 mTorr, 5sccm, 2500 Hz BF_3 glow discharge created using the hollow cathode at 1500V

For low cathode voltages (below 300V), all ions are mainly detected at the full energy showing that none or few collisions occur inside the sheath. When the cathode voltage is increased with a constant HC voltage, B⁺, BF⁺, BF₂⁺ and BF₃⁺ ion energy distributions are spread toward lower energy showing that more collisions occur inside the sheath. Therefore, this operational mode (triode configuration) allows for the observation of the transition between collision-less and collisional sheath. It should also be noted that B₂F₃⁺ and B₂F₅⁺ ion energy distributions are different. In this case, only ions with full acceleration are observed.

The B⁺ IED follows the same trend as BF₂⁺ IED and presents a two-peak distribution above 300 V. In the case of BF⁺, a two-peak distribution can be observed, even at a cathode bias of 50 V or 100 V. For a cathode bias higher than 300V, a tri-peak distribution can be observed on the BF⁺ IED.

Fig. 108 shows the fraction of the different boron containing ions at different cathode voltage under the same discharge conditions than previously discussed. BF₂⁺ remains the dominant ion under all the conditions.

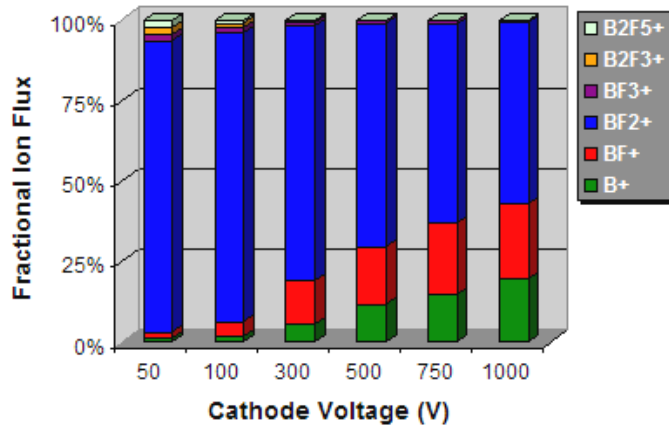


Figure 108: Boron ion fluxes normalized to the total boron ion flux measured for different cathode biases (50, 100, 300, 500, 750 and 1000V) during the pulse-on period of a 30 mTorr BF₃ glow discharge in the high-voltage sheath, with a constant hollow cathode bias at -1500V

For higher cathode biases, when the ion energy distributions are spread toward lower energy by the increase of collisions inside the sheath, the fraction of B⁺ and BF⁺ significantly increases up to 20 % of the total flux of boron ions. It seems to indicate that B⁺ and BF⁺ are mainly created inside the sheath and their fractions are correlated to the

number of collision inside the sheath. It should be noted that the fraction of BF_2^+ ions is also reduced.

Concerning $B_2F_3^+$ and $B_2F_5^+$, the complete absence of signal at low energy, shows that as soon as a kinetically excited heavy ions collide, they get destroyed. Furthermore, their percentage after crossing the sheath is always lower than in the bulk, showing that they never reach a non collisional regime, even for low cathode bias.

In order to have a better overview, another plasma condition with different anode-to-cathode spacings and with constant cathode and hollow cathode voltages is also briefly introduced here and will be discussed in detailed in section V.3.3.1.a. By changing the anode to cathode spacing, the effective hollow cathode surface area can be changed to control the plasma density (see section II.2.2.2.a). Lower anode-to-cathode spacing leads to lower plasma density and thus higher number of collisions inside the sheath.

The B^+ , BF^+ , BF_2^+ and BF_3^+ ion energy distributions for a 500 V, 30 mTorr BF_3 plasma with five different anode-to-cathode spacings are presented in Fig. 109.

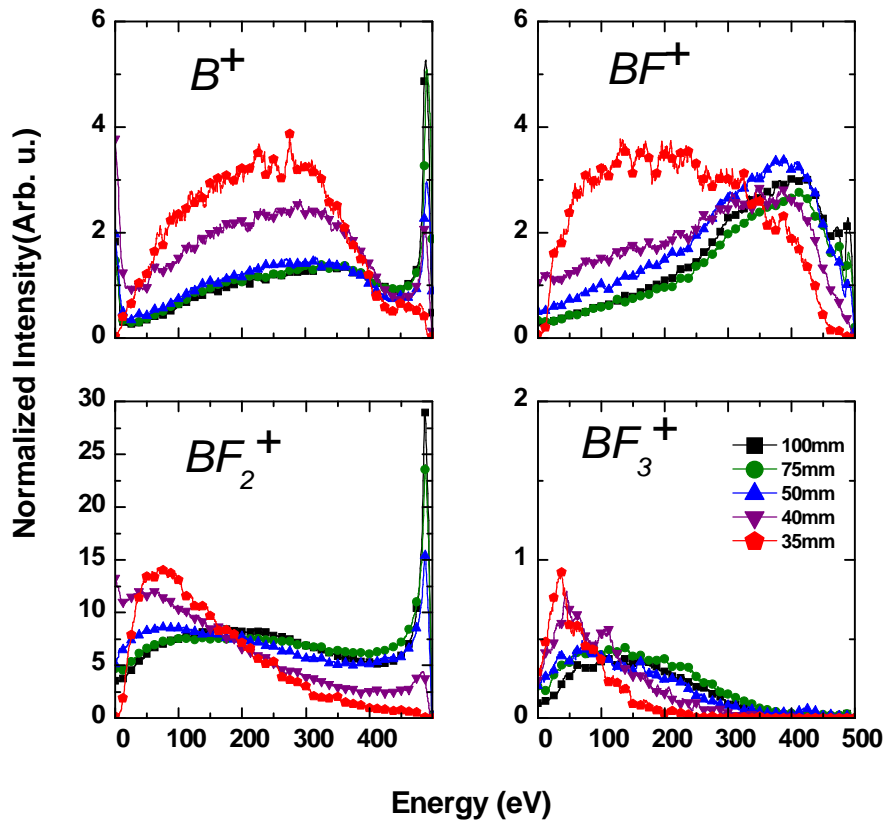


Figure 109: B^+ , BF^+ , BF_2^+ and BF_3^+ IED normalized to the total ion flux for anode-to-cathode spacing for a 500 V, 30 mTorr, 5sccm, 2500 Hz BF_3 glow discharge created using the hollow cathode at 1400V

The ion energy distribution obtained are similar to the ones obtained previously for different cathode bias. When the plasma density is increased, the fraction of ions colliding inside the sheath decreases, and less low-energy B^+ and BF^+ ions are observed. At the same time, the fractions of energetic B^+ and BF^+ ions increase.

The fraction of B^+ ions reaching the cathode with a full high-voltage acceleration increases from 0.2 to 1.4 % between 3.5 and 7.5 cm and is stabilized from 7.5 to 10 cm (see Fig. 110). The maximum fraction, 1.4% percent is close to the B^+ fraction measured in the bulk plasma with a 10 cm gap. It seems to indicate that the collision-less sheath regime is achieved for the B^+ ions in the case of a large gap, and all the B^+ ions present in the bulk reach the cathode with full energy acceleration. Even if the collision-free regime is reached for bulk B^+ ions in the case of a large gap, the mean energy of B^+ remains around 300 eV because of its double-peak distribution. Therefore, it can be concluded that low energy B^+ ions do not come from the bulk plasma but are created inside the sheath.

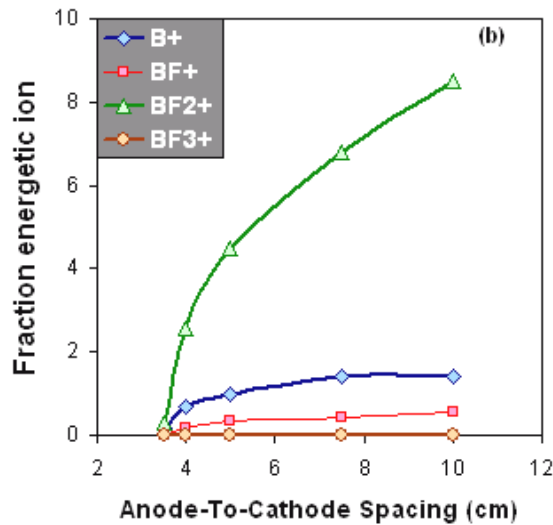


Figure 110: B^+ , BF^+ , BF_2^+ and BF_3^+ ion fractions of with the full high-voltage acceleration under the previously detailed conditions

The fraction of BF^+ energetic ions slightly increases from 0 to 0.56 % of the total flux of boron ions, but the fraction is not stabilized. In the case of BF_2^+ ions, the fraction of energetic ions increases quickly from 0 to 8.5 %, but never reaches a plateau. No BF_3^+ energetic ions can be detected. It appears that the collision-free regime inside the sheath

in this mode of operation is never reached for BF⁺, BF₂⁺ and BF₃⁺, even if the number of collisions is reduced. Nevertheless, as BF⁺ behavior is similar to B⁺ behavior (increase of its percentage after crossing the sheath and bi or tri-modal distribution). Consequently, one can assume that low energy BF⁺ ions are also created inside the sheath and do not come from the bulk plasma.

In this section, only two discharge conditions in the hollow cathode mode were presented even if various other hollow cathode plasmas or pulsed anode plasmas were studied. These cases also show the IEDs evolution between collisional and collision-less sheath and will be presented later in this manuscript or can be found in the Appendixes 5 and 6. The shape of the IEDs will be discussed in detail for each ion in this chapter.

e) Ion energy distribution for collisional sheath

When the hollow cathode is not used, the discharge is operated in a diode configuration (anode grounded and cathode negatively pulsed) and higher pressures are required to ignite the plasma. In this configuration, the electron density is lower than in the hollow cathode configuration. Lower plasma density implies larger sheath thickness. The number of collisions should thus increase. Therefore, the energy distribution of the ions reaching the cathode after acceleration inside the high-voltage sheath is expected to be strongly affected and spread to lower energy.

Fig. 111 shows the ion energy distributions for the different ions striking the high-voltage cathode under different gas discharge pressures during 1kV and 500V implantation. B⁺, BF⁺, BF₂⁺ and BF₃⁺ are the only ions that reach the cathode after crossing the collisional sheath. After the high voltage sheath acceleration, heavy ions such as B₂F₃⁺ and B₂F₅⁺ ions are not detected. BF₃⁺ is always a minor ion in pure BF₃ plasmas. BF₃⁺ IED shape is similar to argon and neon IED shapes shown on figure 101. The charge exchange of BF₃⁺ with its parent neutral molecule seems to govern its IED shape.

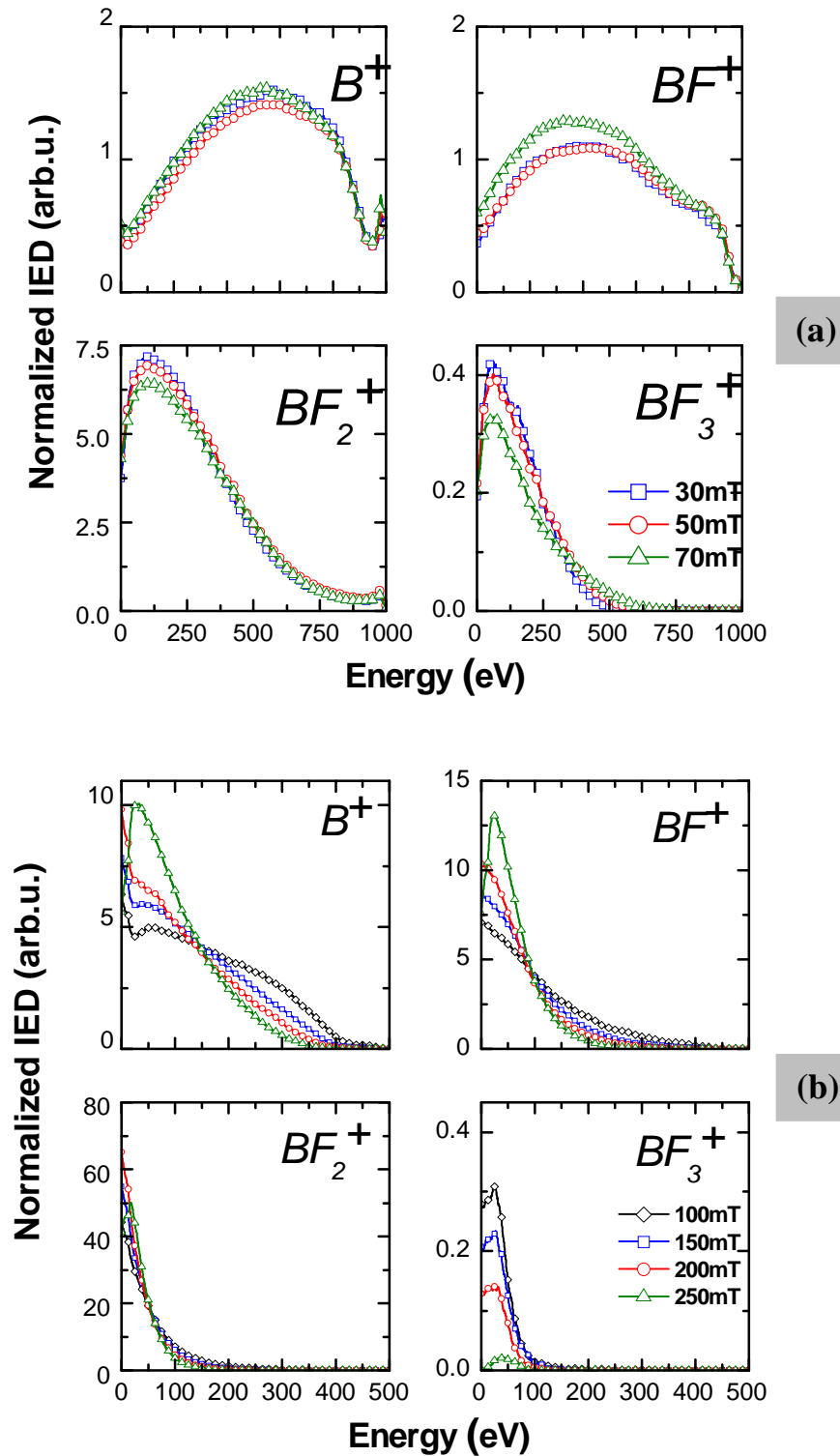


Figure 111: B^+ , BF^+ , BF_2^+ , BF_3^+ IEDs normalized to the total flux of boron ion. (a) 1 kV 2500 Hz BF_3 plasma at three different pressures: 30, 50, 70 mTorr, (b) 500 V 2500 Hz BF_3 plasma at four different pressures: 100, 150, 200, 250 mTorr

The shape of the BF₂⁺ IED seems also to be affected by the charge exchange with BF₂(g). BF₂⁺ remains the dominant ion but its fraction is significantly reduced from around 85 % to 50 or 60 % of the total flux of boron containing ions after crossing the high-voltage sheath (see Fig. 103 and 104, three first conditions). A large disparity in the relative ion abundance between the bulk plasma measurement and the cathode IEDs is also observed in the case of the collisional sheath. B⁺ and BF⁺ fractions increase by a factor of 10 after crossing the plasma sheath. In the 1kV case, the ion energy distribution of B⁺ and BF⁺ presents a two-peak distribution. Their IED shapes do not seem to be governed by charge exchange collision processes.

These observations seem to confirm that B⁺ and BF⁺ are created inside the sheath when the heavy ions such as BF₂⁺, B₂F₃⁺ or B₂F₅⁺ are destroyed inside the sheath by collisions.

f) Parameter driving the shape of ion energy distribution shapes

As discussed previously, IED shapes are strongly influenced by the number of collisions inside the sheath. The reduced electric field (E/N) can be used to estimate the variation of the number of collisions inside the sheath. Indeed, an increase of E/N, due to an increase of the electric field (increase electron density) or a decrease of the gas density, leads to a reduction in the number of collisions inside the sheath. The mean energies for B⁺, BF⁺, BF₂⁺, BF₃⁺, calculated from the measured IED using equation {IV.2.18}, as a function of the electric field-to-gas density ratio (E/N) under various operating discharge conditions for a collisional sheath in a BF₃ glow discharge is presented on Fig. 112. An increase of E/N, leads to a reduction in the number of collisions inside the sheath. As a direct effect, the ion mean energy is increased for a higher E/N. The E/N gives a good indication of how the number of collisions inside the sheath evolves, but does not provide an estimation of this number. Furthermore, the reduced electric field can not be easily estimated in the case of hollow cathode plasmas. Therefore an estimation of the number of collisions inside the sheath ($\frac{s}{\lambda}$) is necessary.

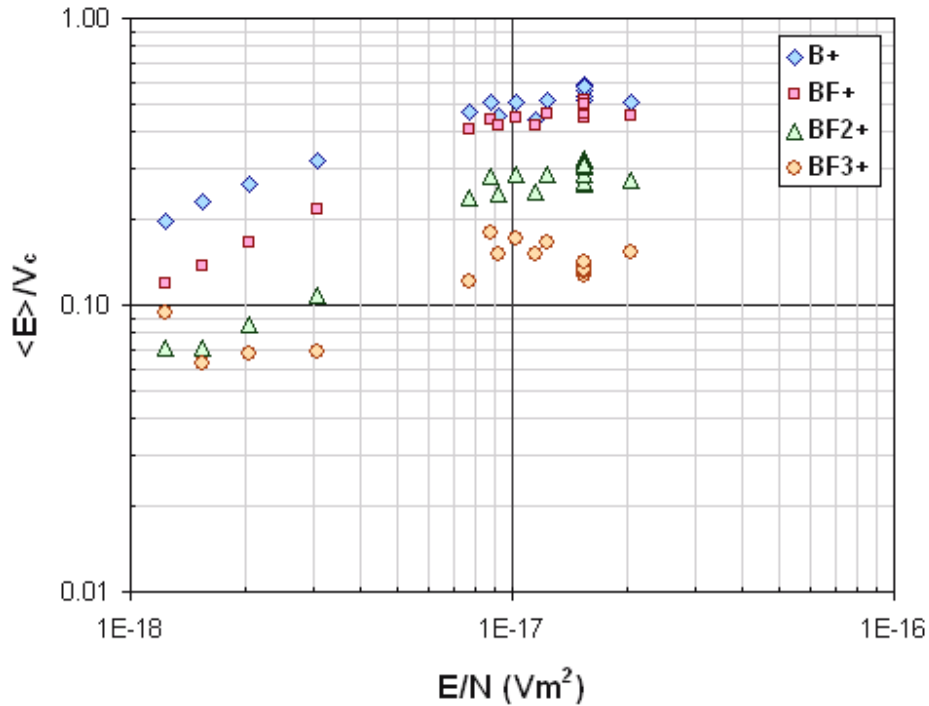


Figure 112: Mean ion energy normalized to the cathode voltage for B⁺, BF⁺, BF₂⁺ and BF₃⁺ ions reaching the cathode for a collisional and highly collisional sheath under various operating discharge conditions in a BF₃ glow discharge as a function of electric field-to-gas density ratio.

As the cathode ion current is known, the number of collisions s/λ can be estimated using the equation {IV.2.5 or IV.2.12}. Only BF₂⁺ will be considered for this calculation as it is the dominant ion under all the various conditions. The hard sphere model is used to estimate the ion-neutral cross section for a BF₂⁺ ion. A constant ion neutral cross-section of $2 \times 10^{-15} \text{ cm}^2$ is assumed.

Fig. 113 shows the ion mean energy as a function of the number of collisions inside the sheath for various BF₃ diode glow discharge conditions. As expected, the ion mean energy is strongly affected when s/λ increases. When the glow discharge is operated in a planar diode system, a collision-less sheath is not achievable due to the pressure limitation and the low plasma density. Under the planar diode system, the discharge is always operated in a collisional mode. The number of collisions inside the sheath is a relevant parameter that drives the IED shape and describes well the experimental conditions in the case of collisional sheath.

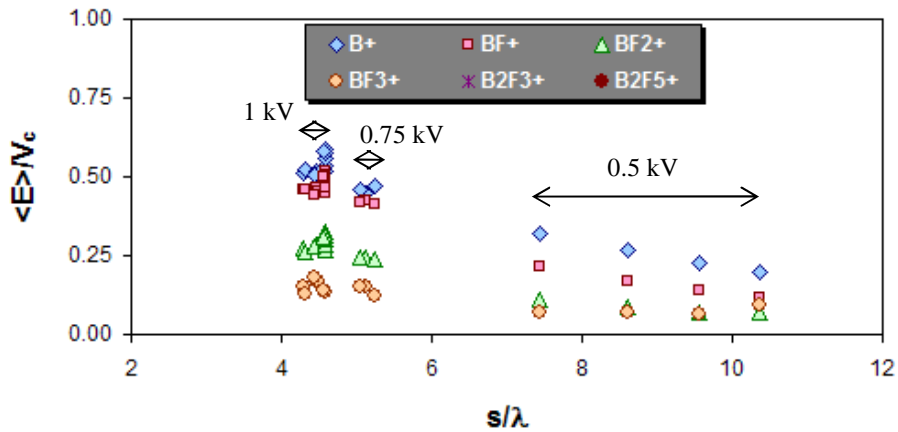


Figure 113: B^+ , BF^+ , BF_2^+ and BF_3^+ mean energies normalized to the cathode voltage, as a function of the number of collisions for various BF_3 glow discharge conditions

Fig. 114 shows the ion mean energy as a function of the number of collisions inside the sheath for many different BF_3 hollow-cathode glow discharge conditions. As the discharge can be ignited at lower pressures and lower cathode biases, higher ion mean energies are achievable when the hollow-cathode is turned-on. The discharge can thus be operated in a collision-free regime. When only a few collisions happen, the heavy molecular ions can be detected at the cathode.

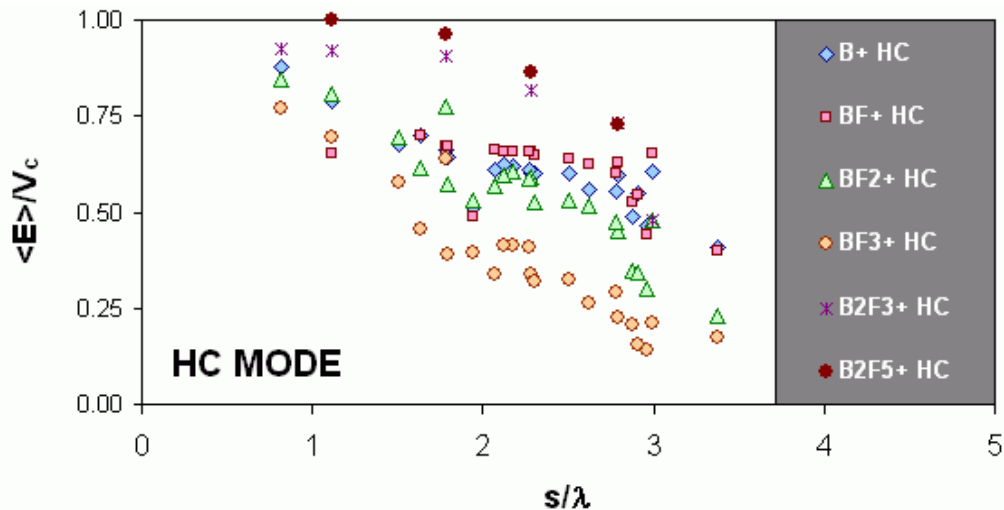


Figure 114: Experimentally calculated B^+ , BF^+ , BF_2^+ , BF_3^+ , $B_2F_3^+$ and $B_2F_5^+$ mean energies normalized to the cathode voltage, as a function of the number of collisions for many different BF_3 hollow cathode glow discharge conditions

To conclude, the common parameter that is governing the shapes of the IEDs for the ions reaching the cathode under various BF₃ glow discharge (HC, no HC, pulsed anode) is the number of collisions inside the sheath, s/λ .

Ion energy distributions discussion

g) Observations and comments

In summary, the major observations and comments discussed in the previous sections are:

- BF₃⁺ ion is always a minor ion in pure BF₃ plasmas. The charge exchange collisions of BF₃⁺ with its parent neutral molecule seem to govern its IED shape (see Fig. 106, 109, 111 and Appendices 5 and 7).
- BF₂⁺ ion is the dominant ion under all conditions in the bulk plasma and in the high-voltage sheath. As the fraction of BF₂⁺ ions is significantly reduced after the high-voltage sheath acceleration as soon as collisions take place. The BF₂⁺ ions seem to be lost by a collision process. The shape of the BF₂⁺ IED in the diode case seems also to be affected by the symmetric charge exchange between BF₂⁺ and BF₂(g) (see Fig 111 and Appendix 7).
- The heavy molecular ions do not survive any collisions during the acceleration across the sheath. If they are detected, only the energetic component of these ions is collected (see Fig 104 and Fig. 106). The exact structure of these ions is not known. However, a boron-boron bond is unlikely. By comparison to the diborane molecule (B₂H₆), we can make assumptions concerning their structure. The diborane molecule does not present a boron-boron bond. The two BH₃ monomers are weakly bonded through boron – hydrogen electrostatic interactions. B₂F₃⁺ and B₂F₅⁺ may have a similar

structure with a weak electrostatic interaction between fluorine and boron atoms. Therefore small energy is probably sufficient to dissociate these ions, and dissociation is certainly very efficient when kinetically excited ions collide with neutrals in the sheath. This is in agreement with the complete absence of low energy heavy ions reaching the cathode. Concerning bulk measurements, we can suppose that heavy ion fractions measured are correct since the sheath drop voltage is low enough ($V_p - V_f =$ some few eV) and the sheath is probably not collisional, even for heavy ions.

- As soon as few collisions take place, the fraction of B⁺ and BF⁺ is increased during the sheath acceleration. B⁺ and BF⁺ ions seem to be created inside the sheath. Since a double-peak distribution is observed for B⁺ and BF⁺, their IED shapes are not mainly due to charge exchange (see Fig 106, 109, 111 and Appendices 5, 6 and 7). The energetic peak of the IEDs for B⁺ and BF⁺ seems to be due to the B⁺ and BF⁺ ions present in the bulk plasma, which are accelerated inside the sheath without any collisions.
- In the collision-less regime, all the IEDs peak at the energy maximum defined by the cathode acceleration (see Fig. 106, 109, Appendices 5 and 6).

The shapes of the IED will now be detailed and quantified for each ion separately. The goal is to present the collision processes that can occur inside the high-voltage sheath for each ion, starting with B⁺, followed by BF⁺ and concluding with BF₂⁺, BF₃⁺ and the heavy molecular ions.

h) B⁺ ion energy distribution

As discussed previously, the relative abundance of B⁺ in the bulk plasma composition represents only a few percent (see Fig. 115).

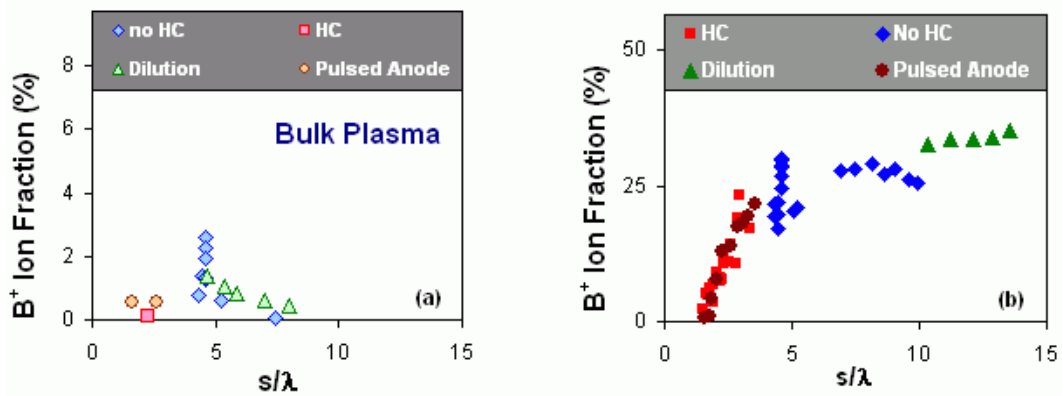


Figure 115: B^+ ion fraction as a function of the number of collisions under various BF_3 discharge conditions (HC, no HC, Pulsed anode, Neon dilution) for (a) bulk plasma, (b) ions reaching the cathode

The probability of creating B^+ , as compared to the probability of creating BF_2^+ by electron impact is low (see section IV.1.2). The fraction of B^+ thus remains small in the bulk plasma. However, a large fraction of B^+ ions, up to 35 % of the total ion flux can be measured as they reach the cathode. As can be seen on Fig 115b, the B^+ fraction crossing the sheath is strongly dependant on the number of collisions inside the sheath. The same amount of B^+ is detected in the bulk plasma and in the high voltage sheath when the sheath is collision-less, but as soon as the number of collisions increases, the fraction of B^+ quickly rises (when there are between 1 and 5 collisions). It reaches a plateau after 10 collisions. There are two different hypotheses that could explain the creation of B^+ inside the sheath:

- Ionization inside the high voltage sheath by secondary electron impact during their acceleration by the electric field inside the high voltage sheath.

When the secondary electrons emitted at the cathode are accelerated inside the sheath, the higher probability of collision is with BF_3 , as it is the major neutral species in the gas phase. Such a collision is more likely to create BF_2^+ ion than B^+ ion when the electron impact energy is lower than 100 eV, based on the electron impact dissociation of $BF_3(g)$ (see section IV.1.2). No data is available for higher electron impact energies, but the total ionization cross-section of $BF_3(g)$ shows that the highest probability of electron ionization is around 100 eV (see BF_3 cross-section {IV.1.1}).

To summarize, for energies below 100 eV, the ion most likely to be created by electron impact is BF₂⁺. For electron energies higher than a few hundred electronvolts, electron ionization is less likely to happen. Based on this observation, the first hypothesis can be ruled out.

- Heavier ions dissociation inside the sheath (BF₂⁺, B₂F₃⁺ or B₂F₅⁺).

A significant fraction of heavy molecular ions are measured in the bulk plasma (up to 25%) but only few of them reach the cathode. These ions are therefore lost in the sheath, either by transition into neutrals or lighter ions. Mizutani have reported similar behavior in the case of Ar-C₃F₈ mixture, where CF⁺ and CF₂⁺ were created inside the sheath by dissociation of fast CF₃⁺ [Mizutani 2000]. In order to verify this hypothesis, a number of measurements are performed on each B⁺ IED. A schematic of a typical B⁺ IED shape in a moderately collisional sheath is presented in Fig. 116 (see Fig 105, Appendices 5 and 6). When the sheath is very collisional, the two peaks cannot be distinguished, therefore, the highly collisional sheath case will not be used to verify the hypothesis.

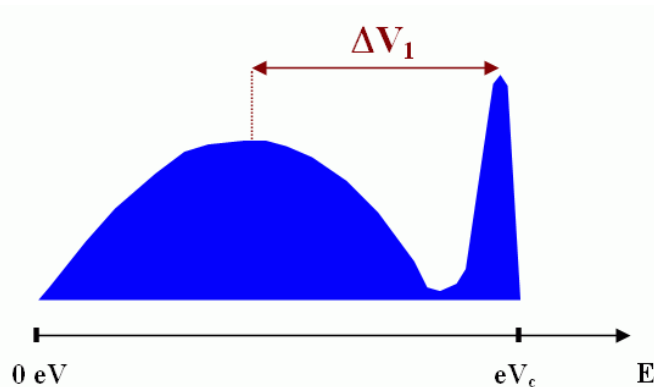


Figure 116: Schematic of the typical shape of B⁺ IED for a moderately collisional sheath ($s/\lambda < 6$ collisions)

If the hypothesis of heavy ion dissociation inside the sheath is valid, these ions should travel a certain distance inside the sheath before being destroyed. This distance is defined as their mean free path, λ_{iHeavy_1} . They are then dissociated into lighter ions such as BF⁺ or B⁺. The resulting B⁺ and BF⁺ will not appear with the full sheath acceleration

since they are created inside the sheath. The assumption that they are created at rest will be made. This is justified since only some few eV are probably sufficient to dissociate heavy ions, and the remaining energy of the dissociation reaction is probably low. Therefore, the difference between the energetic peak and the maximum of the second peak of the IED for B⁺, ΔV₁, should correspond to a distance x linked to λ_{iHeavy-1}. Using the collisional child Langmuir sheath (equation {IV.2.10}), ΔV₁ can be expressed by:

$$\Delta V_1 = \phi(x) - \phi(0) = -\frac{3}{5} \times \left(\frac{3}{2\varepsilon_0} \right)^{2/3} \times \frac{j_i^{2/3}}{(2e\lambda_{iBF_2^+} / \pi M)^{1/3}} \times x^{5/3} \quad \{\text{IV.2.18}\}$$

where φ(0) = V_p ≈ 0 and λ_{iBF₂⁺} is the BF₂⁺ mean free path. The assumption here is that BF₂⁺ ion defines the sheath potential as it is the dominant ion inside the sheath. The probability for a particle to do not undergo any collision over a distance x is e^{-x/λ_i} and the probability to have a collision on the distance x is (1 - e^{-x/λ_i}). For x ≈ 3λ_{iHeavy-1} ({IV.2.19}), 95 % of the heavy ions have collided.

Based on the potential equation {IV.2.18} and {IV.19}, the equation can be obtained:

$$\Delta V_1 = -\frac{3}{5} \times \left(\frac{3}{2\varepsilon_0} \right)^{2/3} \times \frac{j_i^{2/3}}{(2e\lambda_{iBF_2^+} / \pi M)^{1/3}} \times (3\lambda_{iHeavy-1})^{5/3} \quad \{\text{IV.2.20}\}$$

$$\lambda_{iHeavy} = \frac{kT}{p \times \sigma_{iHeavy-1}} = -\frac{1}{3} \left(5 \times \frac{(2\varepsilon_0)^{2/3}}{(3)^{5/3}} \times \frac{(2e\lambda_{iBF_2^+} / \pi M)^{1/3}}{j_i^{2/3}} \times \Delta V_1 \right)^{3/5} \quad \{\text{IV.2.21}\}$$

where σ_{iHeavy} is the cross section for dissociation of heavy ion inside the sheath.

$$p \times \sigma_{iHeavy-1} = -3kT \times \left(5 \times \frac{(2\varepsilon_0)^{2/3}}{(3)^{5/3}} \times \frac{(2e\lambda_{iBF_2^+} / \pi M)^{1/3}}{j_i^{2/3}} \times \Delta V_1 \right)^{-3/5} \quad \{\text{IV.2.22}\}$$

The following relationship should be obtained if the hypothesis of heavy ion dissociation creating B⁺ inside the sheath is valid:

$$U = \left(\frac{\Delta V_1 \times \left(\lambda_{iBF_2^+} \right)^{1/3}}{(j_i)^{2/3}} \right)^{-3/5} \propto P \times \sigma_{iHeavy_1} \quad \{IV.2.23\}$$

ΔV_1 is measured on B⁺ IEDs, j_i is deduced from measured cathode current and $\lambda_{iBF_2^+}$ is estimated using a BF₂⁺ ion neutral cross-section of $2 \times 10^{-15} \text{ cm}^2$.

As expected by the hypothesis, Fig 117 shows an excellent linear relationship between the U function and the pressure. This validates hypothesis of the creation of B⁺ by dissociation of the heavier ions by collision with neutral particles from the gas phase.

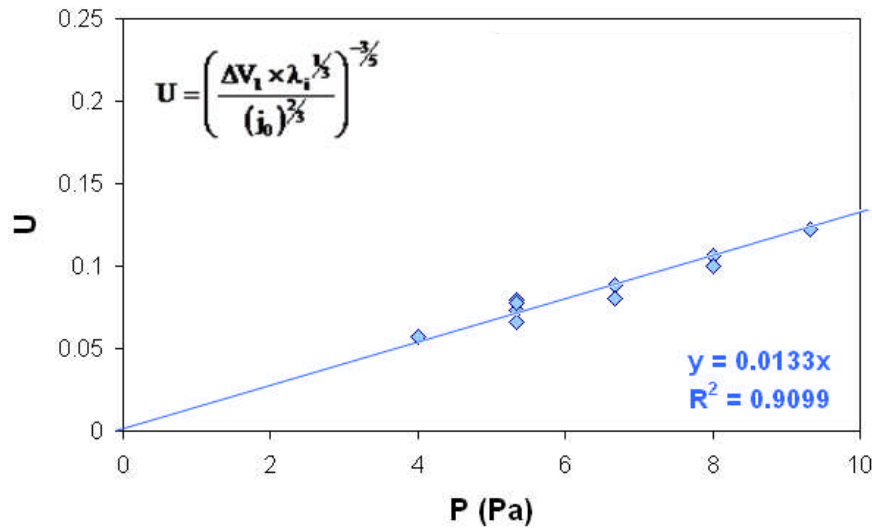
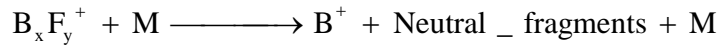


Figure 117: U function as a function of pressure for different plasma conditions in collisional pure BF₃ plasma

The average cross-section of heavy ions can thus be estimated based on the assumed BF₂⁺ cross-section. The calculated σ_{iHeavy_1} for heavy ions is equal to:

$$\sigma_{iHeavy_1} = 2.3 \times 10^{-19} \text{ m}^2 \pm 0.2 \times 10^{-19} \quad \{IV.2.24\}$$

where $\sigma_{BF_2^+} = 2 \times 10^{-19} m^2$. It should be noticed that the two values of $\sigma_{BF_2^+}$ and σ_{iHeavy_1} are of the same order of magnitude. However, the value σ_{iHeavy_1} must be taken with care as many assumptions are used to derive it. The creation of B^+ inside the sheath is probably due to the dissociation of heavier ions such as BF_2^+ , $B_2F_3^+$ or $B_2F_5^+$ into B^+ after a collision with a neutral particle during the acceleration inside the sheath (see following reaction).



where $x = 1$ or 2 and $y = 2, 3$ or 5 . The heavy ion that creates B^+ cannot be identified with this method.

i) BF^+ ion energy distribution

As discussed previously, similar observations to those made for B^+ can be made for BF^+ . The relative abundance of BF^+ in the bulk plasma only represents a few percent (see Fig. 118a). The probability of creating BF^+ through electron impacts is small compared to that of creating BF_2^+ (see section IV.1.2). The fraction of BF^+ in the bulk plasma thus remains small under all the different plasma conditions, as can be seen in Fig. 120a. In contrast a large fraction of BF^+ , representing up to 25 % of the total boron ion flux, can be measured at the cathode (see Fig. 118b).

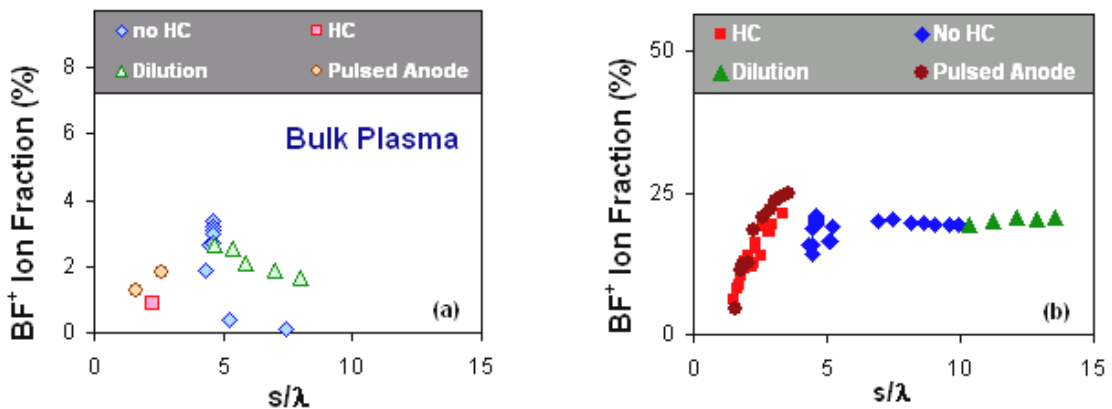


Figure 118: BF^+ ion fraction as a function of the number of collisions under many different BF_3 discharge conditions (HC, no HC, Pulsed anode, Neon dilution) for (a) the bulk plasma, (b) the ion reaching the cathode

BF⁺ presents the same behavior as B⁺, and the BF⁺ fraction is also strongly dependant on the number of collision inside the sheath. The amount of BF⁺ detected in the bulk plasma is slightly lower than the one detected across a collision-less sheath, but as soon as the number of collisions increases, between 1 and 5 collisions, the fraction of BF⁺ increases quickly. It reaches a plateau after 5 collisions. The same hypothesis as for B⁺ can still hold true in the case of BF⁺ and for the same reason, the creation of BF⁺ by secondary electron impact can be ruled out.

After reviewing all the different BF⁺ IED shapes under many different plasma conditions, the shape of the IED could be described as composed of three different convoluted peaks (see Fig 119): the first peak corresponds to the bulk plasma BF⁺ ions that reach the cathode without collision, and is followed by two other peaks (see Fig. 109, Appendices 5 and 6). The ratio between these two peaks appears to change with different plasma conditions (see Appendix 7).

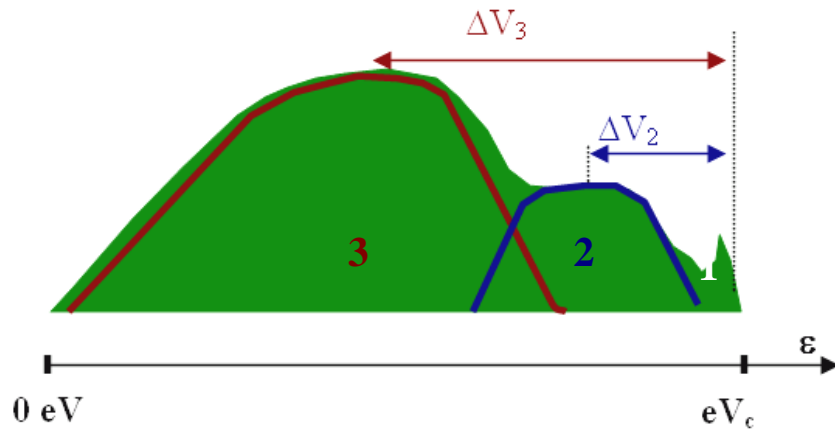


Figure 119: Schematic of a typical shape of BF⁺ IED for a moderately collisional sheath. Three different peaks can be observed

If the hypothesis of heavy ion dissociation inside the sheath is valid, these two peaks could be due to different heavy ion species. Each heavy ion species may have different mean free paths (λ_{iHeavy_2} and λ_{iHeavy_3} for example). The difference between the energetic peak and the maximum of the second and third peak of the IED for BF⁺, ΔV_2 and ΔV_3 (respectively) should be linked to λ_{iHeavy_2} and λ_{iHeavy_3} respectively. Using

the same calculation than for B⁺, similar relationship{IV.2.23}for ΔV₂ and ΔV₃ can be obtained:

$$U(\Delta V_2) = \left(\frac{\Delta V_2 \times \left(\lambda_{iBF_2^+} \right)^{1/3}}{(j_i)^{2/3}} \right)^{-3/5} \propto P \times \sigma_{iHeavy_2} \quad \{\text{IV.2.25}\}$$

$$\text{and } U(\Delta V_3) = \left(\frac{\Delta V_3 \times \left(\lambda_{iBF_2^+} \right)^{1/3}}{(j_i)^{2/3}} \right)^{-3/5} \propto P \times \sigma_{iHeavy_3} \quad \{\text{IV.2.26}\}$$

where σ_{iHeavy_2} and σ_{iHeavy_3} are the cross section for the dissociation of two different heavier ions.

As is expected with the hypothesis, Fig. 120 shows two different linear relationships between the U function and the pressures for ΔV₂ and ΔV₃. This validates the hypothesis of BF⁺ creation by dissociation of the heavier ions by collision with neutral particles from the gas phase. The two different linear relationships are probably signs of two different ways to create BF⁺ inside the sheath. The linear relationship is less evident for ΔV₂ since the position of the first peak is not well defined.

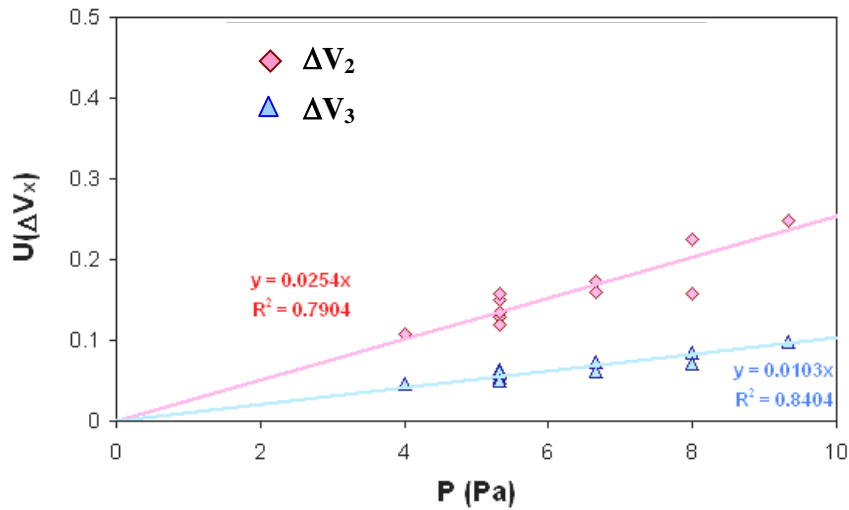


Figure 120: $U(\Delta V_x)$ function as a function of pressures for different plasma conditions in collisional pure BF₃ plasma (with $x = 2$ or 3)

The average cross section of heavy ions that create BF⁺ can thus be estimated by using a constant BF₂⁺ cross-section $\sigma_{BF_2^+} = 2 \times 10^{-19} m^2$ and by defining σ_{iHeavy_2} and

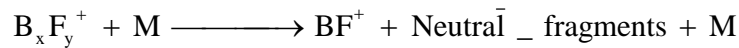
σ_{iHeavy_3} as the cross-sections of the two different heavy ions that dissociate inside the sheath to create the second and third peak (respectively) on the IED for BF⁺. The two cross-sections can thus be estimated through the following equations:

$$\sigma_{iHeavy(\Delta V 2)} = 4.6 \times 10^{-19} m^2 \pm 0.5 \times 10^{-19} \quad \{\text{IV.2.27}\}$$

$$\sigma_{iHeavy(\Delta V 3)} = 1.8 \times 10^{-19} m^2 \pm 0.25 \times 10^{-19} \quad \{\text{IV.2.28}\}$$

Again, these values must be taken with care as their calculation is based on many assumptions.

As σ_{iHeavy_2} is different than σ_{iHeavy_3} , the creation of BF⁺ inside the sheath is probably due to the dissociation of two different type of heavier ions such as BF₂⁺, B₂F₃⁺ or B₂F₅⁺ into BF⁺ after a collision with neutral particle during its acceleration inside the sheath (see following reaction).



where x = 1 or 2 and y = 2, 3 or 5. The heavy ion that creates BF⁺ cannot be identified using this method.

In contrast with the B⁺ ion, the BF⁺ ion energy distribution always presents a minimum of two peaks even when the sheath is collision-less for B⁺ and BF₂⁺ (see Fig. 105, 106 with a cathode bias at 50V and 100V). This seems to indicate that the second peak on the BF⁺ IED does not come from the dissociation of BF₂⁺ ion inside the high-voltage sheath. On the other hand the fraction of B₂F₃⁺ and B₂F₅⁺ is below 2 % of the total ion flux even for cathode bias voltage of 50 or 100 V. The second peak on the BF⁺ IED probably comes from the dissociation of B₂F₃⁺ or B₂F₅⁺ ion inside the high-voltage sheath. Similar observation can be made from measurements presented in the Appendix 5.

j) BF₂⁺ ion energy distribution

As expected according to the BF₃(g) dissociation by electron impact probability, BF₂⁺ is the dominant ion in the bulk plasma and remains so until it reaches the cathode after the high-voltage sheath acceleration. When the sheath is totally collision-less for BF₂⁺ (in the pulsed-anode case), the fraction of BF₂⁺ detected on the cathode is similar to the one measured from the bulk plasma (see Fig.121) and the ion energy distribution is

peaked at the maximum energy (see Fig. 106, cathode bias: 50 to 300V, and Appendix 6, HC bias: 2200 V). As soon as some collisions take place, the BF_2^+ ion fraction is significantly reduced after the high-voltage sheath acceleration; the BF_2^+ seems to be lost by a collision process. In this section we will try to explain the BF_2^+ IED shapes in the three regimes, the collision less regime ($s/\lambda < 1$), the fewly collisional regime ($1 < s/\lambda < 5$) and the highly collisional regime ($s/\lambda > 5$). We start with the collision less regimes.

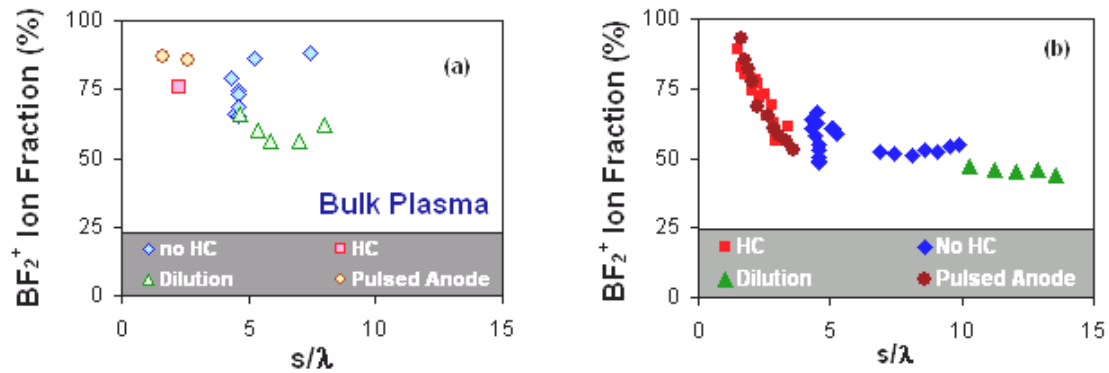


Figure 121: BF_2^+ ion fraction as a function of the number of collisions under many different BF_3 discharge conditions (HC, no HC, Pulsed anode, Neon dilution) for (a) the bulk plasma, (b) the ion reaching the cathode

When the sheath is not collisional for BF_2^+ ions (see Fig. 106, $V_c < 300V$; Appendix 5, HC voltage $> 1800V$), the energy distribution is peaked at maximum energy. A slight spread toward low energy is observed and corresponds to momentum transfer collisions. In these conditions, the BF_2^+ bulk fraction is equal to the BF_2^+ fraction reaching the cathode (see Fig. 121), and B^+ energy distribution present only one peak at maximum energy (see Fig 105, Fig.106, $V_c < 300V$; Appendix 5, HC voltage $> 1800V$). As soon as some collisions take place, the BF_2^+ ion fraction is reduced after the high-voltage sheath acceleration and the B^+ energy distribution present a second peak (see Fig.105 and Fig. 106, $V_c > 300V$; Appendix 5, HC voltage $< 1800V$). We may attribute this second peak on B^+ IED to BF_2^+ dissociation inside the sheath.

When the sheath is highly collisional ($s/\lambda > 5$ collisions, see Fig. 111b, 500 V, no HC and high pressure), the distribution is peaked at lower energy. The shape of the BF_2^+ IED seems to be affected by the symmetric charge exchange between BF_2^+ and $BF_2(g)$

(see Fig 111 and Appendix 7). Indeed, the shape of the BF_2^+ IED (see Fig. 109b) is similar to the shape of Ne^+ and Ar^+ IEDs in neon and argon plasma presented by Davis and Vanderslice (see Fig. 105). BF_2^+ IED during the 500 V high-pressure has been fitted with the modified Davis and Vanderslice model by adjusting the number of collisions inside the sheath. All the different IEDs can be well fitted using the Davis and Vanderslice model. The number of collisions obtained with the model is presented on Fig. 122.

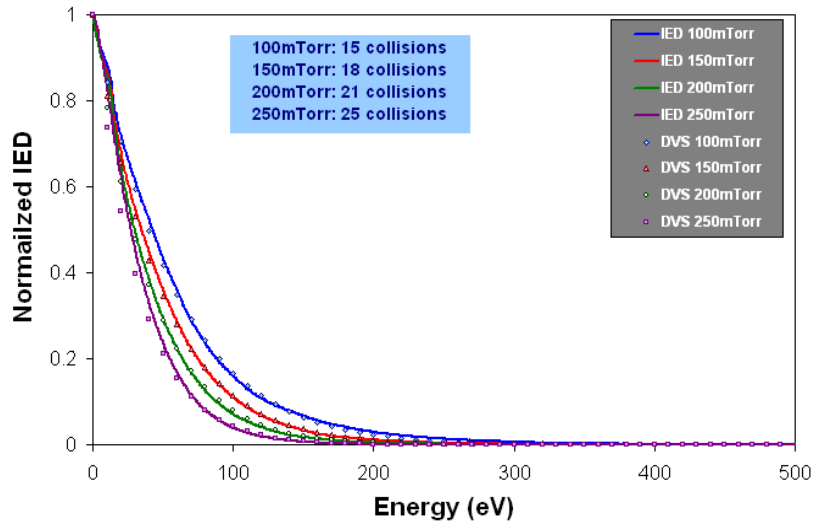


Figure 122: Normalized BF_2^+ IED in the case of a high-pressure, low-energy (500V) BF_3 discharge under different operating pressures (100, 150, 200 and 250 mTorr), fitted with the modified Davis and Vanderslice model (DVS) by adjusting the number of collisions inside the sheath

As could be expected, with the rising pressure the number of collisions increases. The number of collisions inside the sheath based on the Davis and Vanderslice (DVS) model does not match the one calculated using the ion current density in a collisional sheath. s/λ is higher in the case of the VDS model (see Table 11).

		BF_2^+	
		$\langle \sigma_{iBF_2^+} \rangle$ (m^2)	2.00E-19
Pressure (mTorr)	$s_{Measured}$ (cm)	s/λ (calculated)	s/λ (DVS)
100	1.15	7.4	15
150	0.9	8.6	18
200	0.74	9.6	21
250	0.65	10.4	25

Table 11: 500V high pressure, s/λ calculated based on BF_2^+ hard sphere model, s/λ measured with Davis and Vanderslice (VDS)

As already explained, the fraction of BF₂⁺ reaching the cathode is significantly lower than the BF₂⁺ bulk fraction in case of highly collisional sheath (see for example Fig. 103 and Fig. 104, first condition, and Fig.121). Moreover, the B⁺ and BF⁺ fractions are high at the cathode under the same conditions. This is a strong indication that BF₂⁺ dissociates inside the sheath and creates B⁺ ions and maybe BF⁺ ions. Therefore charge exchange is not the only inelastic process affecting the IED shape, and it could explain why the Davis and Vanderslice model overestimates the number of collisions inside the sheath.

The BF₂⁺ IED shape is more difficult to interpret in the transition regime, between the collision less and the collisional regimes. As soon as the sheath becomes collisional (between 1 and 5 collisions), a two peaks energy distribution is observed (Fig. 123). The first peak is composed of the BF₂⁺ ion extracted from the bulk plasma without collision. The second peak is located at lower energy than the sheath acceleration. The ratio between the two peaks is a function of the number of collisions inside the sheath (see Fig. 109 and 111a). In many other cases such as in Fig. 106 (for cathode bias of 750 and 1000V), Appendix 5 (for HC BF₂⁺ IED 1000V and 1200V) or Appendix 6 (pulsed anode mode 1200V), the BF₂⁺ IED shape presents a two peaks distribution, as illustrated in Fig 123.

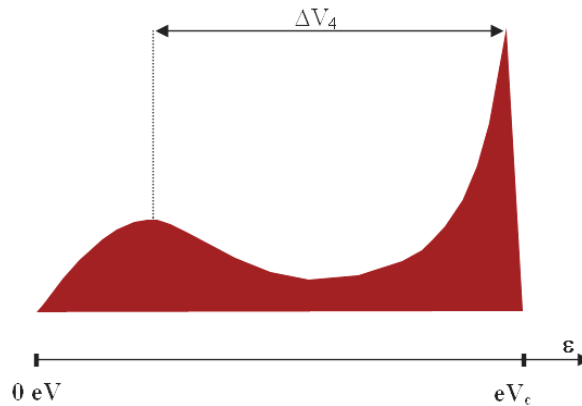


Figure 123: Schematic of a typical shape of BF₂⁺ for moderately collisional sheath

This second peak can not come from the dissociation of a heavy ion (B₂F₃⁺ or B₂F₅⁺). Indeed, the high value for ΔV₄ (Fig.123) corresponds to a position in the sheath

close to the cathode, and therefore to a high heavy ion mean free path, λ_{iHeavy_4} . Such high mean free path should imply the detection of heavy ions at the cathode under these conditions, while no signal is observed (Fig 106 and Fig.107, 1000V).

Since BF₂⁺ is the ion created preferentially by electron impact ionization of BF₃ (g) molecules, the second peak could also origin from ionization in the sheath by secondary electrons emitted by the cathode. However, in most conditions, the electron ionization mean free path is higher or of the same order of magnitude as the sheath thickness. For instance, in the case of hollow cathode pulsed at 800 V for a 500 V cathode voltage and a pressure of 20 mTorr, the electron mean free path calculated using the maximum of the electron ionization cross section (see Fig.89) is estimated to be 3.1 cm, while the sheath thickness is estimated to be 2.6 cm. Therefore, in any conditions, ionization can not take place close to the cathode and can not explain the second peak on BF₂⁺ IED. Furthermore ionization would tend to increase BF₂⁺ fraction while a reduction is observed

The last hypothesis to explain the second peak of the BF₂⁺ IED, is a combined effect of the two kind of inelastic collisions occurring inside the sheath, the charge exchange and the dissociation. In the slightly collisional regime, some ions may reach high energy at which dissociation may dominate charge exchange. Therefore, colliding ions with high energy ($\epsilon > e\Delta V_4$, Fig. 123) may lead to dissociation and not to charge exchange. No ion is thus created at rest close to the cathode and no ion is detected at low energy.

It is important to note that BF₂⁺ ion has covalent bonds between boron and fluorine atoms, and its dissociation requires high energy to occur efficiently (much more energy than for dissociation of heavier ions B₂F₃⁺ and B₂F₅⁺). Thus, the remaining energy of the dissociation reaction may be high, explaining why the B⁺ second peak position (ΔV_1 , Fig.116) does not correspond to ΔV_4 (Fig. 123).

In conclusion, the BF₂⁺ IED is composed of the energetic BF₂⁺ ions from the bulk plasma in case of a non collisional sheath. In case of highly collisional sheath, the BF₂⁺ IED shape is in agreement with the Davis and Vanderslice model, despite the number of collisions calculated by the model is too high. We showed that BF₂⁺ ions probably

dissociate inside the sheath to form B^+ and maybe BF^+ ions. The presence of two kind of inelastic collisions, charge exchange and ion dissociation, may explain the BF_2^+ IED shape for slightly collisional regimes, and may also explain why the calculated number of collisions by Davis and Vanderslice model is too high.

k) BF_3^+ ion energy distribution

Under all plasma conditions, BF_3^+ remains a small fraction of the total ion flux in the bulk plasma, below 5% of the total ion flux (see Fig. 125). The BF_3^+ fraction measured at the cathode remains similar to the one measured in the bulk plasma. This indicates that the probability of asymmetric charge transfer between BF_2^+ and BF_3 is unlikely.

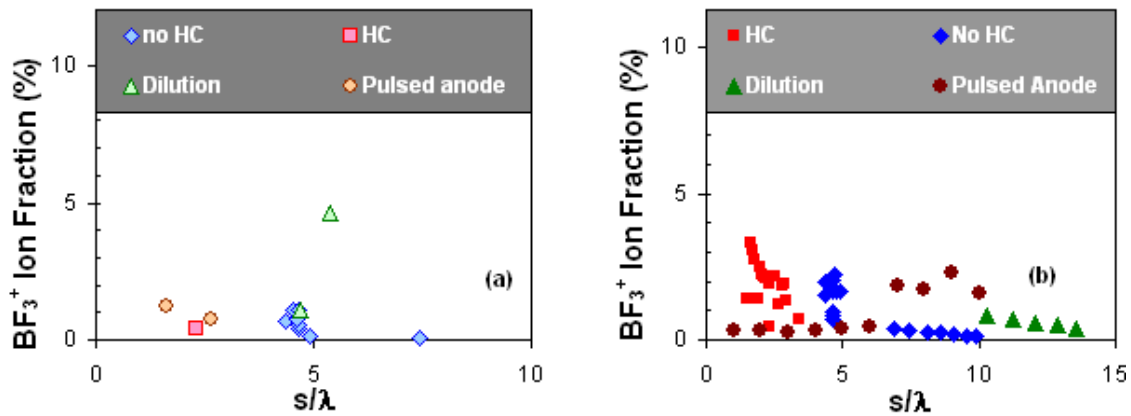


Figure 125: BF_3^+ ion fraction as a function of the number of collisions under many different BF_3 discharge conditions (HC, no HC, Pulsed anode, Neon dilution) for (a) the bulk plasma, (b) the ion reaching the cathode

In the case of a collisional sheath, the BF_3^+ IED shape is strongly affected by collisions and the mean energy is decreased to low energies. The shape of BF_3^+ (see Fig. 109, 111 a and b) is similar to the shape of measured Neon or Argon IEDs presented by Davis and Vanderslice. The BF_3^+ IED has been fitted with the modified Davis and Vanderslice model by adjusting the number of collisions inside the sheath.

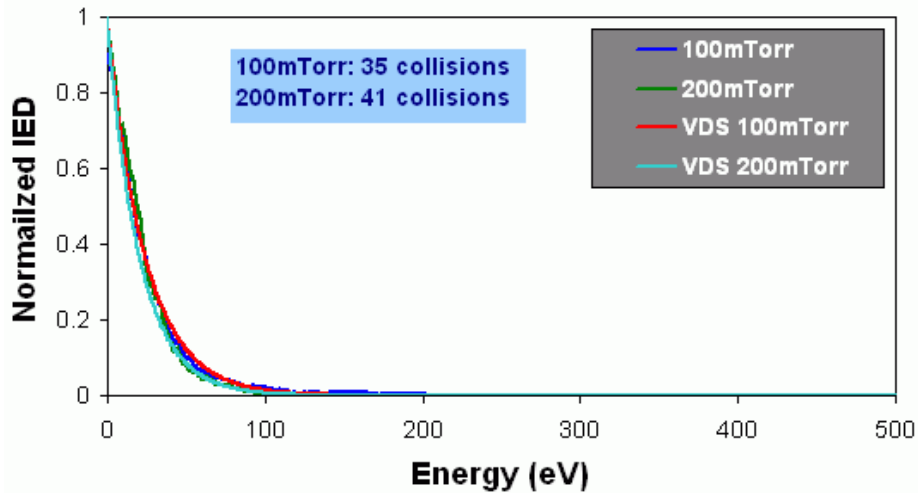


Figure 126: Normalized BF_3^+ IED in the case of high pressure low-energy (500 V) BF_3 discharge for different operating pressure (100 and 200 mTorr) fitted with the modify Davis and Vanderslice model (DVS) by adjusting the number of collisions inside the sheath

The fraction of neutral BF_3 in the gas phase is much higher than that for BF_2 . Therefore, the probability of a charge exchange between BF_3^+ and BF_3 is much higher than that between BF_2^+ and BF_2 . The number of collisions obtained for BF_3^+ is also higher than that for BF_2^+ under the same conditions. The BF_3^+ charge exchange cross-section $\sigma_{i\text{BF}_3^+}$ can be estimated by the following equation using the measured sheath thickness under the same plasma conditions:

$$\sigma_{i\text{BF}_3^+} = 8.8 \times 10^{-19} \text{ m}^2 \pm 0.25 \times 10^{-19} \quad \{\text{IV.2.19}\}$$

As expected, $\sigma_{i\text{BF}_3^+}$ is larger than the BF_2^+ charge exchange cross section $\sigma_{i\text{BF}_2^+}$. The calculated $\sigma_{i\text{BF}_3^+}$ based on the Davis and Vanderslice model is almost four times higher than the one calculated with the hard sphere model.

l) Heavy ions

As discussed previously in Fig. 103, the heavy molecular ions represent a large fraction of the bulk plasma population. In this section, the creation of these heavy ions is discussed as well as their dissociation inside the sheath by collision with neutral particle.

The heavy ion creation seems to be enhanced during the afterglow period. Under all the different plasma conditions studied (see Fig. 127), a substantial fraction of heavy ions such as $B_2F_3^+$ and $B_2F_5^+$ are measured during the afterglow.

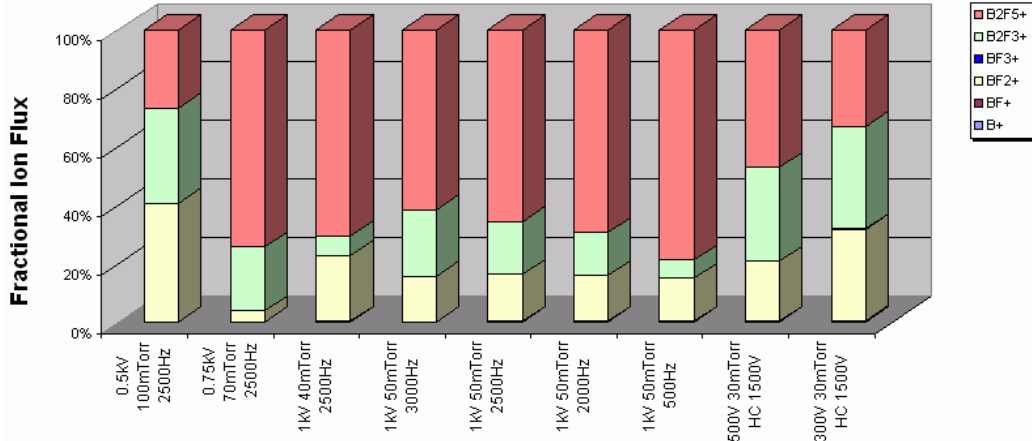


Figure 127: Bulk plasma boron ion fractions normalized to the total flux of boron containing ions during the afterglow in BF_3 plasma for different cathode voltage biases, pressures and frequencies as measured by the mass spectrometer installed on the anode

The fraction of heavy ions is significantly increased in the afterglow compared to the pulse-on period. For example, the $B_2F_5^+$ fraction reaches up to 70 % of the total boron ion flux during the afterglow and becomes the dominant boron ion. BF_2^+ fraction is strongly reduced and B^+ , BF^+ and BF_3^+ are not detected in the afterglow plasma. It should be noted that the $B_2F_5^+$ fraction measured during the pulse-on period (see Fig. 128a) and the afterglow (see Fig 128b) decreases with the frequency while BF_2^+ increases.

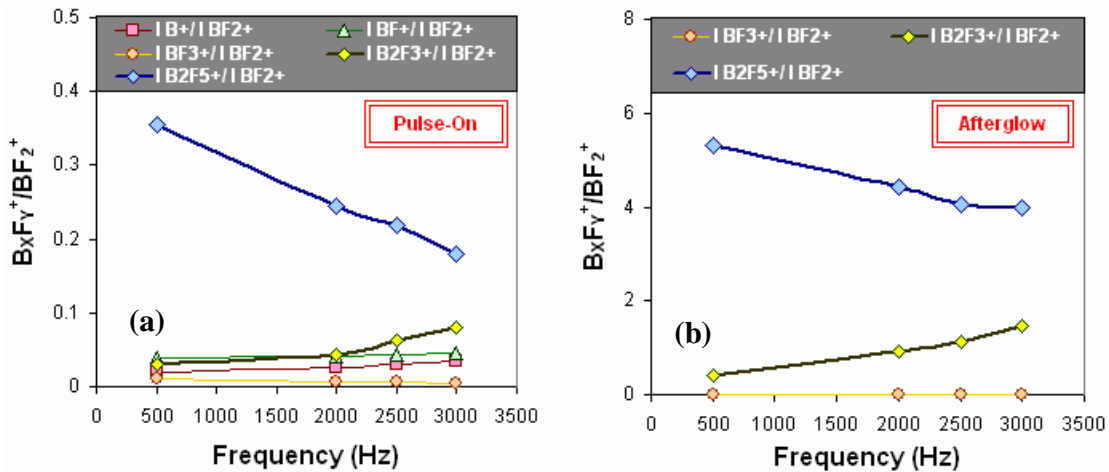


Figure 128: Fractions of boron containing ions normalized to the BF_2^+ fraction for a 1 kV 40 mTorr $50\mu s$ as measured in the bulk plasma during the pulse-on (a) and the afterglow (b)

Therefore, the suspected reaction channel that creates heavy ions such as B₂F₅⁺ is a three-body recombination, such as the one below:



This reaction channel is likely important in the afterglow since it is not balanced by a dissociation mechanism such as:



When the frequency is increased, while the pulse-on time remains constant, the afterglow period is reduced and the fraction of B₂F₅⁺ measured decreases. This indicates that the afterglow period is becoming lower than the three body reaction characteristic time.

In contrast, the fraction of B₂F₃⁺ increases when the frequency is raised. At low frequencies or low plasma densities, the B₂F₃⁺ may be destroyed by dissociation or dissociative recombination between the B₂F₃⁺ and electron either in the gas phase or on surrounding surfaces. The presence of negative ions in the BF₃ afterglow may also play a role in altering these processes. Another hypothesis could be that B₂F₃⁺ may also recombine to create heavier ions. Further studies are needed to conclude but the heavy ions (at least B₂F₅⁺) are for sure mainly created during the afterglow since no dissociation by electron impact occurs.

The bulk plasma fraction of heavy ions such as B₂F₃⁺ and B₂F₅⁺ fluctuates and seems to be strongly dependant on the process conditions in use (see Fig. 129). For example, in the no-hollow cathode case, the B₂F₅⁺ fraction fluctuates from 2 % to 35 % of the total ion flux.

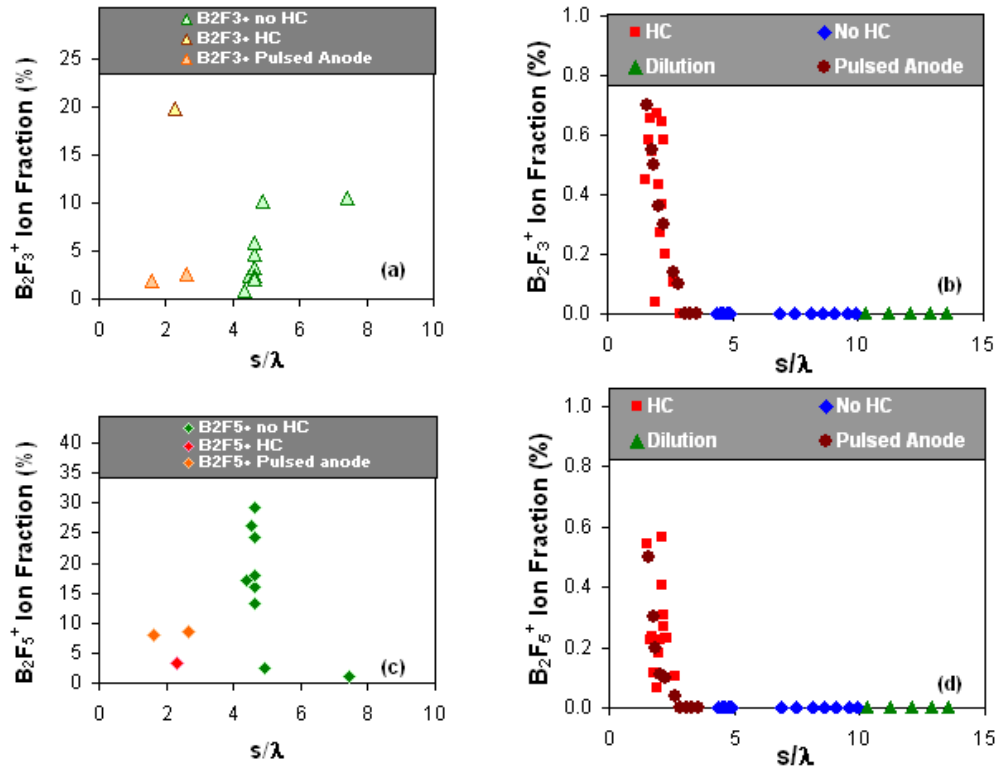


Figure 129: $B_2F_3^+$ (a) (b) and $B_2F_5^+$ (c) (d) ion fractions as a function of the number of collisions under many different BF_3 discharge conditions (HC, no HC, Pulsed anode, Neon dilution) for the bulk plasma (a), (c), and for the ion reaching the cathode (b), (d)

The totally collision-less regime is never reached in the case of heavy ions such as $B_2F_3^+$ and $B_2F_5^+$. The heavy ions only start to be detected on the cathode side when the sheath is close to being collision-less. These heavy ions dissociate inside the sheath by collision with neutral and form lighter ions.

In conclusion, the bulk plasma composition is changing when the frequency is increased and in particular the fraction of heavy molecular ions increases. The fraction of heavy molecular ion is significantly increased during the afterglow; the $B_2F_5^+$ becomes the dominant ions. The heavy ions seem to be created by three body recombination. These ions are still present when the negative pulse starts. Their probability of collisions inside the sheath is high and only a minor fraction of them is detected when the sheath becomes collision-less for BF_2^+ .

Role of negative Ion:

Usually, negative ions can not cross the sheath potential barrier and are trapped inside the plasma. To observe negative ions by mass spectrometry, one must pulse the plasma and detect negative ions in the afterglow when the sheath has completely collapsed [Overzet 1992, Overzet 1993, Howling 1993 and Howling 1994]. Negative ions observed during the pulse-on or during continuous plasma by mass spectrometry are highly energetic negative ions that have sufficiently energy to cross the sheath [Zeuner 1996, Stoffels 2001]. Under our experimental conditions it is possible to observe negative ions in the reverse bias scheme when the mass spectrometer is inside the grounded cathode and the anode is negatively biased.

Due to the positive overshoot, the negative ions cannot be extracted during the afterglow even if the plasma is pulsed. However, negative ions are also created inside the high-voltage sheath or at the cathode surface during the pulse-on period and are accelerated by the high voltage sheath toward the bulk plasma and the anode (where the mass spectrometer is installed). An example of F⁻ ion energy distribution measured during the pulse-on period at the grounded electrode during a 1 kV, 40 mTorr, 2500 Hz, 50 μs BF₃ glow discharge is presented in Fig. 130. The measured IED is peaked at low energy around 8 eV (which correspond to the measured plasma potential during the pulse-on period see Fig. 95a) and spread up to 200 eV. The F⁻ ions with energy lower than the plasma potential cannot cross the potential barrier and are trapped in the plasma. F⁻ ion is the dominant negative ion created inside the sheath but other ions such as BF₄⁻ are also detected.

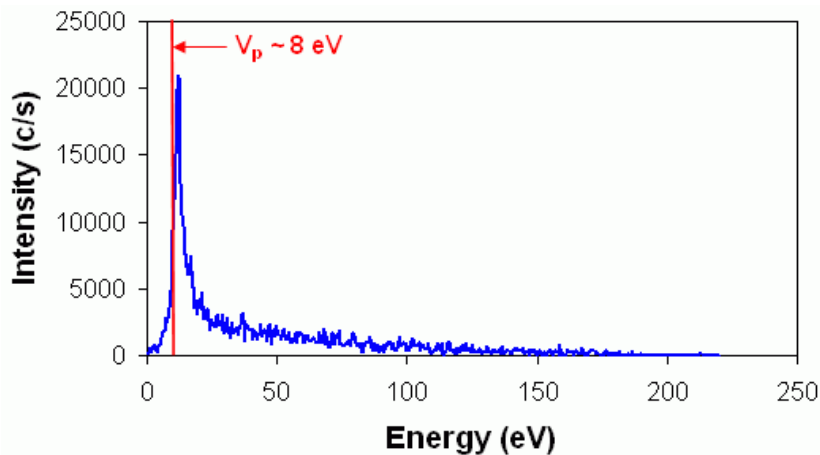


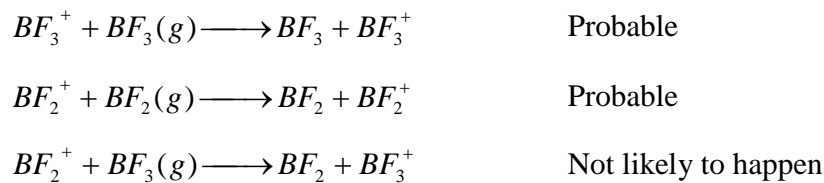
Figure 130: F⁻ IED measured on the anode side during the pulse-on period of a 1 kV, 40 mTorr, 2500 Hz, 50 μs, 4.5 cm BF₃ plasma

In conclusion, the negative ions probably play an important role in the kinetics of the BF₃ bulk plasma but are not implanted in the wafer; indeed, the negative ions are trapped in the bulk plasma and cannot be extracted even during the afterglow due to the power supply overshoot. During the pulse-on period, negative ions created inside the high-voltage sheath or at the wafer surface are accelerated toward the anode with a large energy spread.

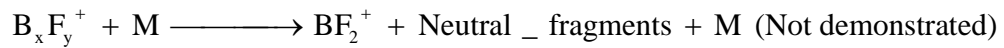
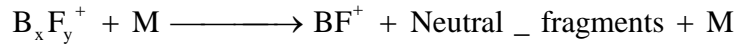
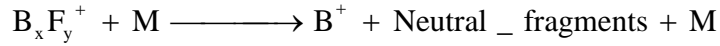
Concluding remarks

The IED shape for each ion was described in detail under this section. It was demonstrated that s/λ is a key parameter in understanding and explaining the shape of the IED measured in the high-voltage sheath. B⁺ and BF⁺ are created inside the sheath as their concentration in the bulk is far lower than at the cathode. The fraction of BF₂⁺ is also strongly reduced after crossing the high-voltage sheath. The main reaction channels that create B⁺, BF⁺ and BF₂⁺ inside the sheath were identified. Heavy molecular ions, such as B₂F₃⁺ and B₂F₅⁺, are created by a three-body recombination, probably destroyed in the bulk plasma by electron impact, and therefore their concentration increase in the afterglow. These ions are dissociated inside the sheath by colliding with neutral particles of the gas phase. The presence of a symmetric charge exchange for BF₂⁺ and BF₃⁺ was also demonstrated in the case of a collisional sheath. A list of the different reaction channels that take place in the high-voltage sheath is presented below.

➤ **Charge exchange:**



➤ **Ion dissociation inside the sheath:**



where x = 1 or 2 and y = 2, 3 or 5.

A more complete description of the exact mechanisms occurring inside the sheath would be interesting but requires further experiments. Nevertheless, it was observed that the B⁺ and BF⁺ fractions are strongly dependant on the number of collisions inside the sheath and can be reduced by minimizing the number of collisions during the high-voltage acceleration. The control of light ions, such as B⁺ and BF⁺, is vital to obtain shallower junctions during ion implantation. More details will be presented in Chapter V.

Chapter V Understanding, control and optimization of the process

V.1 PLAD process control

In this section, the chamber conditioning after maintenance, the plasma and R_s uniformity and the plasma etching with BF_3 chemistry will be presented and described.

Chamber conditioning

During PLAD maintenance, all the interior parts of the process chamber are exposed to the ambient atmosphere. After exposure to the BF_3 plasma, the process chamber walls are reactive to the ambient environment (H_2O , O_2 , $\text{CO}_2\dots$). An oxidation layer forms on all the chamber parts (anode, cathode, chamber wall) during exposure to the atmosphere.

In order to reach a stable process after maintenance, the chamber has to be conditioned. An understanding of the plasma surface interaction with the BF_3 chemistry is required to improve the conditioning step.

Observation

Following chamber maintenance, a shift in the R_s and R_s non-uniformity measured on annealed wafers can be observed. Fig. 131 shows the evolution of the R_s and R_s non-uniformity before and after the chamber maintenance in the case of a 3 kV PLAD implantation.

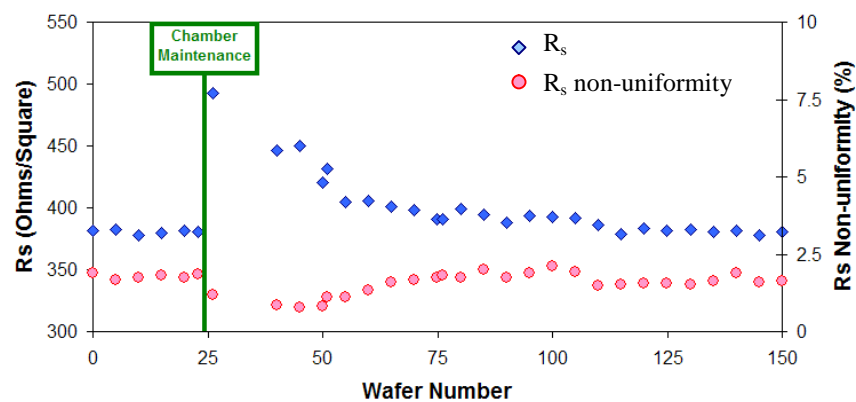


Figure 131: Sheet resistance (R_s) and its non-uniformity evolution before and after chamber maintenance during the conditioning step (3 kV, 18 mTorr, 28 μs , 10^{15} ions/ cm^2)

The wafer for the R_s measurement was implanted with a dose of $1 \times 10^{15} \text{ ions/cm}^2$. The wafers between the R_s monitor wafers were implanted with a higher dose of $2 \times 10^{16} \text{ ions/cm}^2$.

Just after the opening of the chamber, the R_s increases by thirty percent, while the non-uniformity is improved. Higher R_s means a lower boron dose implanted. A large number of implanted wafers is needed to recover the original R_s values. A similar observation can also be made for higher and lower implantation energies. As the time needed to stabilize the process after the chamber opening can reach up to six hours of plasma and wafer handling, opening the chamber can become very costly, and an optimization of the chamber conditioning step is thus needed.

In order to acquire a better understanding of the conditioning step, a detailed study using a Langmuir probe, mass spectrometry and R_s and SIMS measurements was performed at a low energy (300V) after chamber maintenance. It is discussed below.

Description of the experiments

When a base chamber pressure of 5×10^{-6} Torr is reached after chamber maintenance, the 300 V BF_3 plasma conditioning step is started (see Fig. 132).

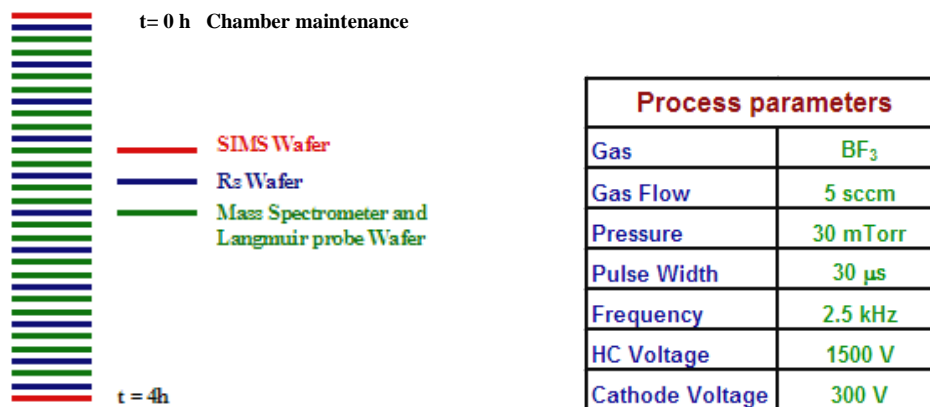


Figure 132: Experimental conditions of the conditioning step study

The first and the last wafer of the test were used for SIMS measurements and were implanted with a dose of $1 \times 10^{14} \text{ ions/cm}^2$. A R_s monitor wafer implanted with

5×10^{14} ions/cm² is included every third wafer. Low dose was used to increase sensitivity. The two wafers between the R_s monitors are special wafers that have a laser-cut hole in the center for mass spectrometry sampling. These wafers are implanted with a dose of 1×10^{16} ions/cm² to provide enough time so that the measurements can be performed. Langmuir probe measurements were also performed during the mass spectrometric measurements. During these experiments, the total number of pulses, the cathode current, the implant time and the cathode voltage waveforms were constantly recorded. As only a manual load lock is available on the PLAD test-stand, the wafer handling time is longer here than in the case of a production machine. The total duration of this test (with the maintenance) is around eight hours, with four hours of pulsed plasma-on time. The results of the test are detailed in the next section.

Conditioning test results

Fig. 133 shows the evolution of the sheet resistance, as measured at the center of the wafer before and after the chamber maintenance for a cathode bias of 300 V, a discharge pressure of 30 mTorr, a frequency of 2500 Hz, a pulse width of 30 μs under HC plasma at 1500 V and an anode-to-cathode gap of 5 cm.

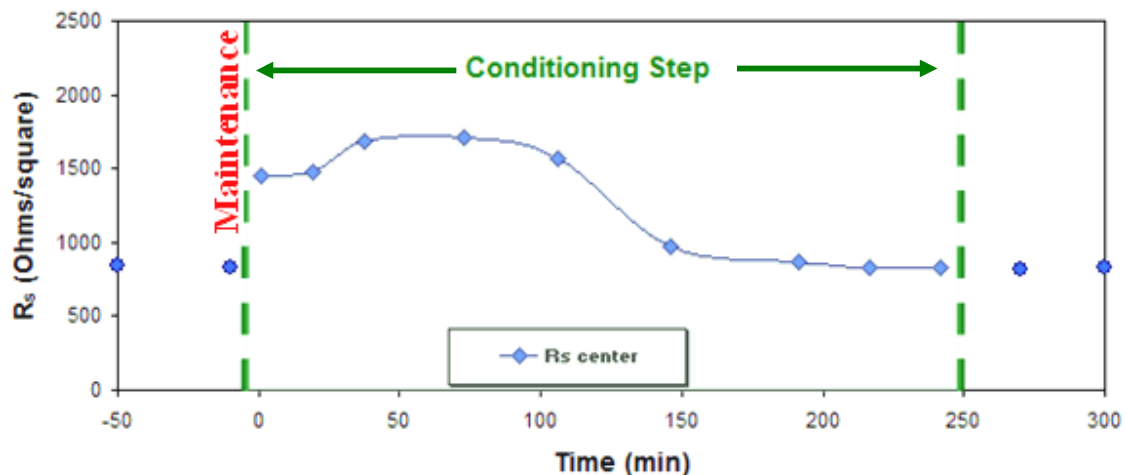


Figure 133: Sheet resistance evolution measured at the center of the wafer before and after the chamber maintenance for 300V 30 mTorr, 30 μs, 2500Hz, HC = 1500V, gap = 5cm, with an implanted dose of 10^{15} at/cm²

As expected from previous experiments, after maintenance, higher R_s values are observed immediately. In the case of low-energy implantation, the R_s values at the beginning of the conditioning are higher than for a well-conditioned chamber. A long conditioning time of 120 to 150 minutes is needed to recover a stable R_s .

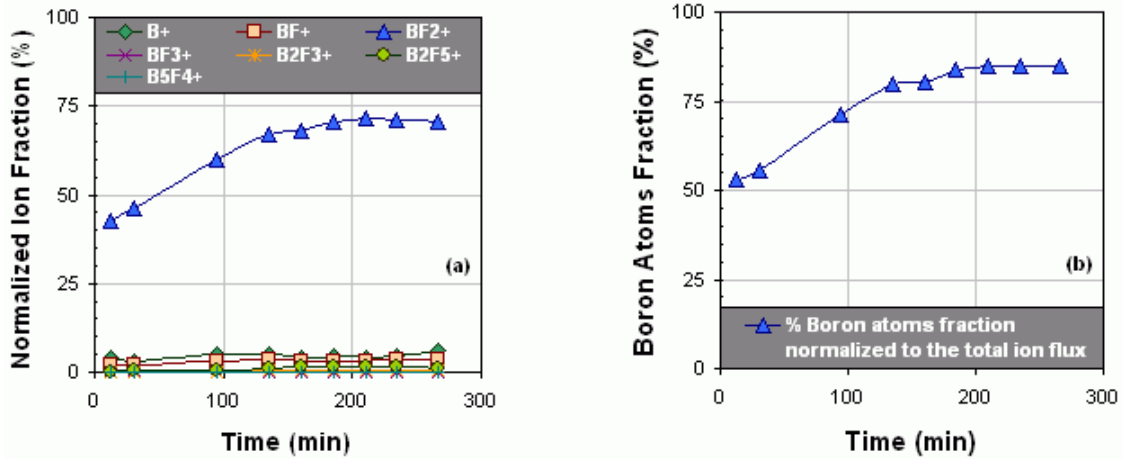


Figure 134: (a) Boron containing ion fluxes normalized to the total ion flux(%) during the conditioning step, (b) Evolution of the implanted boron atom fraction (see text) reaching the cathode during the conditioning step after maintenance, using a 300 V, 30mTorr HC PLAD implantation

The different boron-containing ions that are present during conditioning and reach the cathode with a fraction greater than 0.1% are B^+ , BF^+ , BF_2^+ , BF_3^+ , $B_2F_3^+$, $B_2F_5^+$ and $B_5F_4^+$. Their time evolution is shown on Fig. 134a. BF_2^+ is the dominant ion during of all the conditioning. Its fraction increases with the time during conditioning and reaches a stable level after 120 minutes. The recovery of the nominal boron ion flux correlates well with the recovery of the initial R_s when the chamber is correctly conditioned. Once the ion fractions are stabilized, the process becomes stable and repeatable.

All the other boron-containing ions are below 5 % of the total ion flux, and the total boron-containing ion percentage reaches 83 % once the process is stabilized. The remaining 17 % of the total ion flux mainly comes from a contaminant material, which was used inside the process chamber at the time of the experiment. The fraction of the contaminant ions was stable over time and was due to a reaction between the material used and the BF_3 chemistry. For industrial proprietary reasons, the contaminant material used at the time of these experiments will not be discussed here.

Fig. 134b shows the time evolution of the fraction of implanted boron dose, normalized by the total ion flux, during the conditioning step after exposure to the atmosphere. The boron dose fraction ($F_{B_{at}}$) is calculated using the following equation:

$$F_{B_{at}} = \frac{\sum_{x=1}^5 \sum_{y=0}^5 x \times \phi_{B_x F_y^+}}{\sum \phi_{allions}} \quad \{V.1.1\}$$

$\phi_{B_x F_y}$ is the $B_x F_y$ ion flux and $\phi_{allions}$ is the total ion flux. At the beginning of the conditioning step, the boron containing ion fraction represents less than 60 % of the total ion flux and reaches a stable state of 85.5 % after 140 minutes of plasma exposure. The PLAD dosimetry system detects all ions. During the conditioning step, many ions present in the plasma are implanted into the wafer and are counted by the dosimetry system. The implanted boron dose is thus lower than the dose measured by the Faraday cup, and the R_s value is higher than in the case of a well-conditioned chamber. Fig. 134b correlates well with Fig. 133. In order to avoid the boron surface saturation, a low dose of 1×10^{14} ions/cm² was implanted and analyzed by SIMS. In order to obtain the measured boron dose implanted into the silicon wafer, the SIMS profile is integrated.

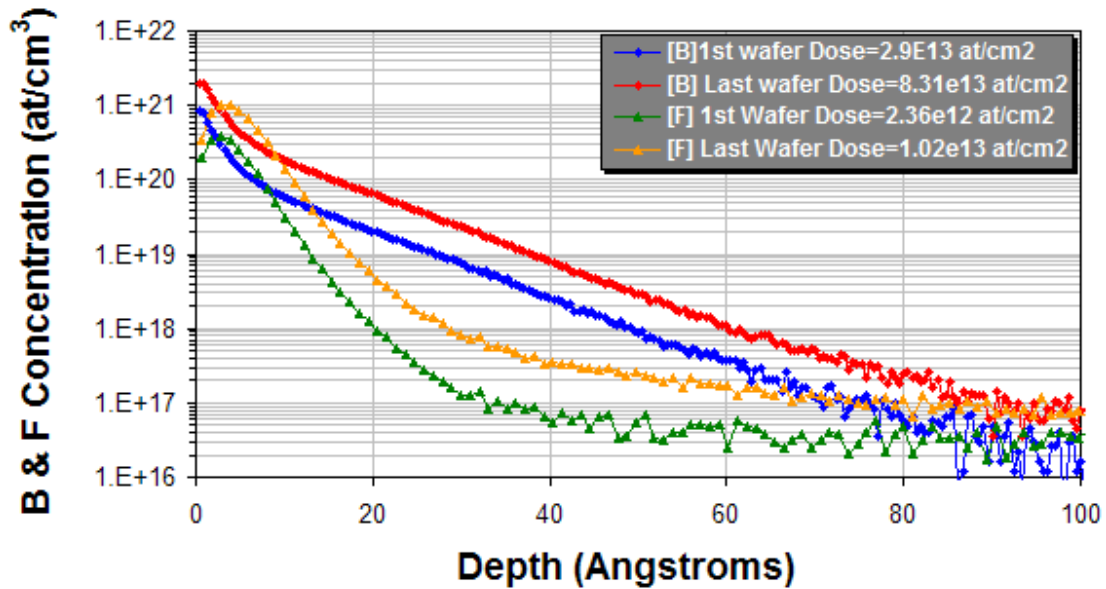


Figure 135: Boron and fluorine concentration at the beginning and the end of the conditioning step, as measured by SIMS for a 10^{14} ion/cm² 300 V BF_3 HC plasma

As expected, the SIMS measurement of the first implanted wafer gives a boron dose of only $2.9 \times 10^{13} \text{ at/cm}^2$ (see Fig. 135) for a $1 \times 10^{14} \text{ ions/cm}^2$ nominal dose, as measured by the dosimetry system. When the process returns to a steady state, the SIMS-measured boron dose is $8.31 \times 10^{13} \text{ at/cm}^2$.

Based on the fraction of boron ions predicted through mass spectrometry (see Fig. 134b) for a well conditioned chamber, a $1 \times 10^{14} \text{ ions/cm}^2$ dose measured by the Faraday cup should in fact represent a boron dose of $8.55 \times 10^{13} \text{ at/cm}^2$. With only 3 % less dopant implanted than expected, the measured SIMS boron dose matches the corrected Faraday cup dose well. The mass spectrometer measurement gives an indication of the trend of the boron concentration after the conditioning step and can be used to control or correct the dosimetry system for better accuracy.

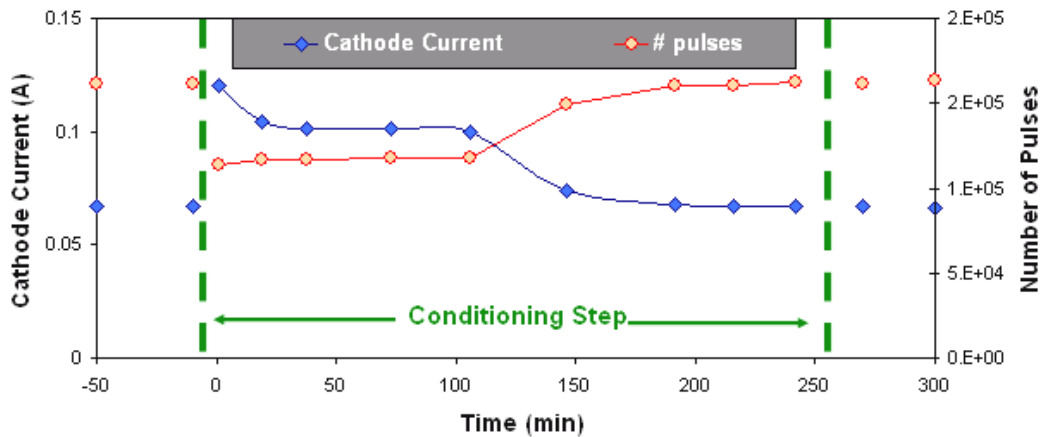


Figure 136: Cathode current and number of pulses to implant the $5 \times 10^{14} \text{ ions/cm}^2$

The evolution during the conditioning of the cathode current and the number of pulses for each R_s wafer implanted with a dose of $5 \times 10^{14} \text{ ion/cm}^2$ is presented in Fig. 136. At the beginning of the test, the power supply current is drastically increased up to twice its original value. The power supply current is then stabilized and back to its baseline at value around 140 minutes after the beginning of the conditioning. A possible explanation for this observation is an oxide layer created on the surface by the reaction of the boron-fluorine compounds with the air environment during the maintenance, the

cathode current increase at the beginning of the conditioning could be due to a change of the cathode surface during exposure to air.

The cathode current or the number of pulses needed to achieve a certain dose can also be used to monitor and control the conditioning step, and are simple methods compared to using mass spectrometry measurements.

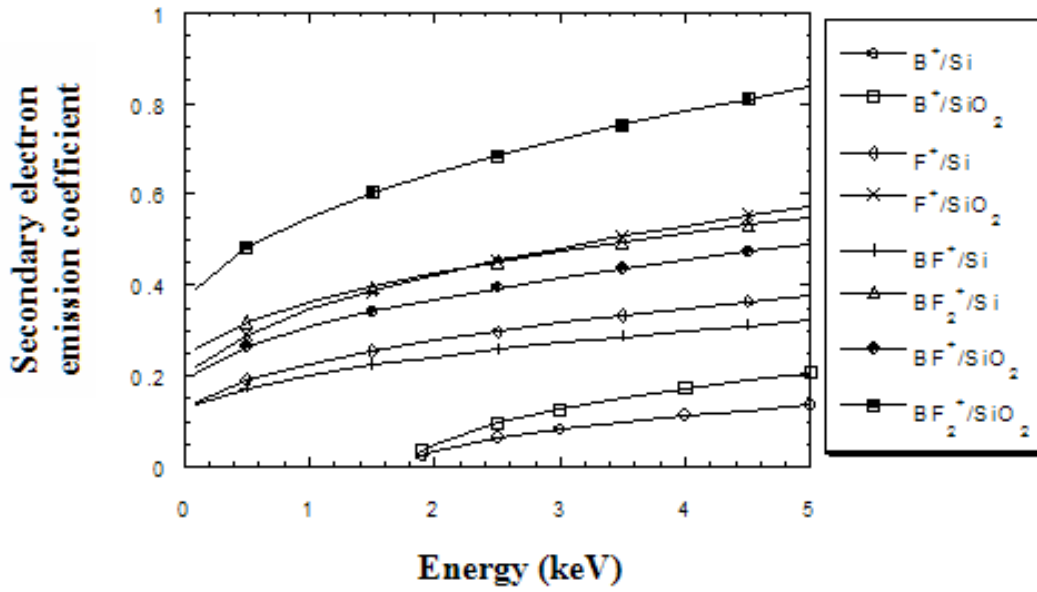


Figure 137: Values of the secondary electron emission coefficients of Si and SiO₂, as a function of the incident energy for the ions B⁺, F⁺, BF⁺, BF₂⁺ [Lenoble 2000]

It is well known that different surface materials have different secondary electron emission coefficients [Chapman 1980]. Based on the equation {V.1.2}, a surface material with a higher secondary electron emission (γ) coefficient will lead to a higher cathode current (I_c).

$$I_c = I_{ion}(1 + \gamma) \quad \{V.1.2\}$$

The secondary electron emission coefficient was calculated by Lenoble for a non-collisional sheath in the case of B⁺, F⁺, BF⁺ and BF₂⁺ ions impacting Si or SiO₂ targets at different energies normally to the surface [Lenoble 2000]. Fig. 137 shows the results of this calculation. The secondary electron emission yield following a BF₂⁺ impact

is higher for a SiO₂ target than for a Si target. The secondary electron emission coefficient for a 300 V BF₂⁺ incident ion is 60% higher in the case of a SiO₂ target than for the Si target.

If an oxide layer is created at the surface of the cathode, the ion accelerated by the high-voltage sheath will eject more secondary electrons from the cathode and a higher current will thus be observed. As the secondary electrons emitted from the cathode also contribute to the ionization inside the bulk during a DC glow discharge, more secondary electrons emitted from the cathode should also lead to higher plasma density. When an oxide layer is present at the surface of the cathode or hollow cathode, its current is increased. As soon as the majority of the oxide layer is etched or sputtered by the ion bombardment, the cathode current will decrease to its stable value.

To summarize, the hypothesis used here to explain the higher cathode current at the beginning of the conditioning is the creation of an oxide layer (not necessary silicon oxide) on the cathode surface, which leads to a higher secondary electron emission and thus a higher plasma density and cathode current.

The number of pulses is controlled by the dosimetry system, which measures the ion current (I_{ion}). Higher plasma density leads to a reduction in the number of pulses needed to reach the requested dose. In fact, the number of pulses needed to achieve the target dose decreases at the beginning of the conditioning. This seems to confirm the previous hypothesis. It should also be noted that similar observations (higher current and lower number of pulses) can be made when a wafer with a thick oxide is used.

A detailed analysis of the mass spectrometric and Langmuir probe data collected during the conditioning step has helped to understand the plasma-surface interaction during the exposure to the atmosphere and confirmed the hypothesis of an oxide layer formation during the exposure to the atmosphere.

Fig. 138 shows the evolution of the various etching products present during the conditioning step and detected by mass spectrometric measurements. The etching

products are ionized in the gas phase and implanted on the wafer after acceleration across the sheath.

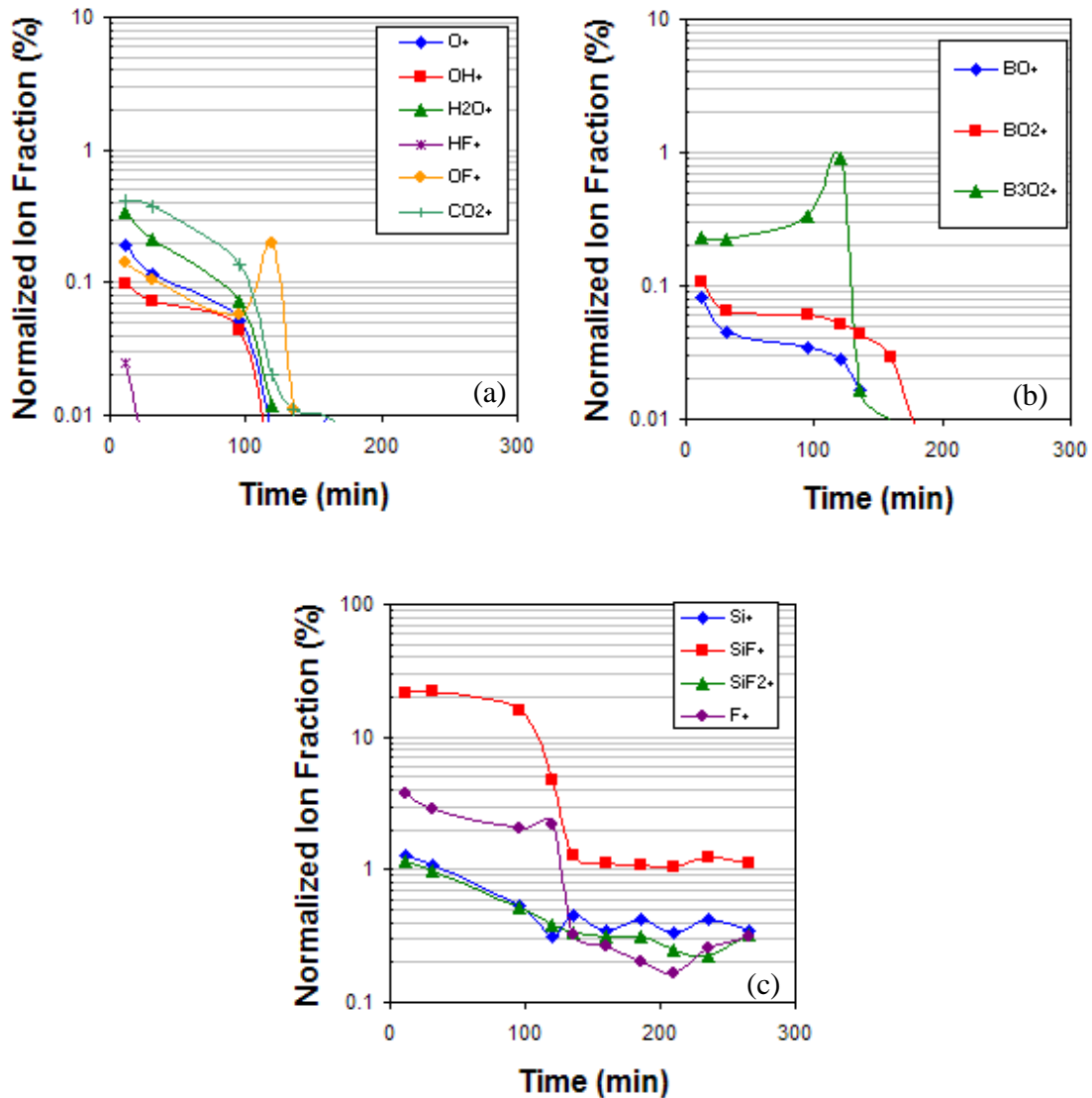


Figure 138: Evolution of the etching product fluxes, normalized to the total ion flux during the conditioning step with a 300 V, 30 mTorr, $HC BF_3$ plasma, (a) fraction of hydrogen, oxygen and carbon products, (b) fraction of boron oxide products, (c) fraction of silicon, silicon fluoride and fluorine products

At the start of the conditioning, molecules such as H_2O or CO_2 present inside the chamber after the exposure to the atmosphere are ionized in the plasma into O^+ , OH^+ , H_2O^+ or CO_2^+ and are implanted into the wafer (see Fig. 138a). The fraction of these ions

measured by the mass spectrometer is slowly reduced to zero during the conditioning step. This indicates that H₂O and CO₂ concentrations in the gas phase are slowly reduced.

Boron oxide ions (BO⁺, BO₂⁺ and B₂O₃⁺) are also detected during the first step of conditioning. They also disappear after 140 minutes of plasma exposure. It should also be noted that when new hardware parts are installed inside the process chamber, the boron oxide ions are not detected. The new parts are composed of spray-coated silicon and a clean silicon oxide layer is thus present on the surface of the new part. The absence of boron oxide ions with new hardware seems to indicate that the boron oxide ions come from the etching of a boron oxide layer created during the air exposure, and not from the reaction of BF₃ with silicon oxide or with molecules such as H₂O and CO₂. Once the boron oxide ions have disappeared from the mass spectrometry data, one can conclude that the boron oxide layer has been eliminated from the surface of the cathode.

Fig. 138c shows the evolution of the different silicon ions as a function of the conditioning time. Si⁺, SiF⁺ and SiF₂⁺ are the main silicon ions detected through mass spectrometry measurements and result from plasma etching of silicon. At the beginning of conditioning, these three ions represent up to 23% of the total ion flux. This fraction is constant during the first 100 minutes of conditioning, then suddenly drops down to 2% of the total ion flux. This coincides with the disappearance of the boron oxide ions. A boron oxide silicon layer is created during the exposure to the atmosphere. This layer is removed by reactive ion etching (RIE) combining fluorine chemical etching and ion bombardment. This process is quite long due to the roughness of the cathode surface. As the wafers are regularly replaced by new wafers (with a native oxide layer) during the conditioning, the silicon etching products are mainly coming from the cathode shield ring (surrounding the wafer) and not from the wafer itself.

To fully validate the previous hypothesis, experiments using the Langmuir probe were also performed to estimate the variation of plasma density at the beginning and end of the conditioning step. The Langmuir probe data are presented in Fig. 139. The pulse-on period electron density is twice as high at the beginning of conditioning than at the

end. It decreases from $7.9 \times 10^9 \text{ electrons/cm}^3$ to $3.8 \times 10^9 \text{ electrons/cm}^3$ (densities measured at the end of the pulse). The higher electron density measured at the beginning of conditioning indicates a higher plasma density and seems to confirm the hypothesis of higher ionization by the secondary electrons emitted from the cathode and accelerated by the high-voltage sheath.

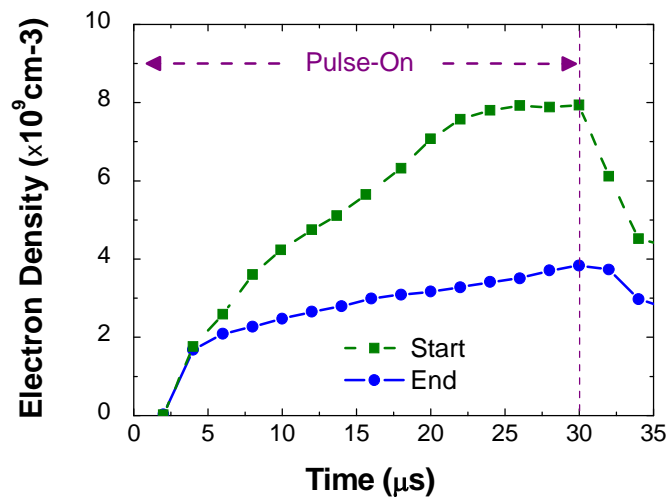


Figure 139: Evolution of the electron density measured with a Langmuir probe during the pulse-on period of a 300 V, 30 mTorr, hollow cathode BF_3 plasma at the beginning and at the end of the conditioning step

To summarize, when the chamber is exposed to atmosphere during maintenance, an oxidation of the spray-coated silicon cathode which had previously been implanted with boron ions, occurs and leads to the formation of a boron oxide silicon surface layer on the cathode. This layer presents a higher secondary electron emission yield than that of a well-conditioned hardware, which leads to higher plasma density. This layer is removed slowly by reactive ion etching. This process is quite long, due to the roughness of the cathode surface. As soon as all the silicon and boron oxide are etched, the process reaches a stable state and the chamber is well-conditioned.

When the chamber is exposed to the atmosphere, all its surfaces are exposed to the air and the boron silicon oxide layer is thus formed throughout the chamber. In the case of the cathode, the layer can be removed thanks to the RIE process. However in the case of the anode, the RIE rate is expected to be low due to the low ion energy at the anode.

The boron oxide material is known to be an insulator and the boron silicon oxide is suspected of being an insulating layer. The presence of insulating materials implies that there is no mass reference inside the chamber. This could explain why there is a plasma potential shift toward negative values each time the chamber was exposed to air. After each maintenance and conditioning, the plasma potential is shifted toward lower values due to the insulating layer on the anode. A negative V_p shift up to -35 eV, was observed after many maintenance cycles of the process chamber. As the acceleration inside the sheath is defined by $(V_p + |V_{cathode}|)$, the maximum energy of the ions accelerated inside the cathode sheath is thus reduced when an insulating layer is present on the anode, as can be see in Fig. 140. The impact of this V_p shift is minor in the case of high-energy implantation (10-1 kV). However, in the case of low-energy implantation, such shift to lower values can introduce some disturbances to the process repeatability each time the chamber is vented.

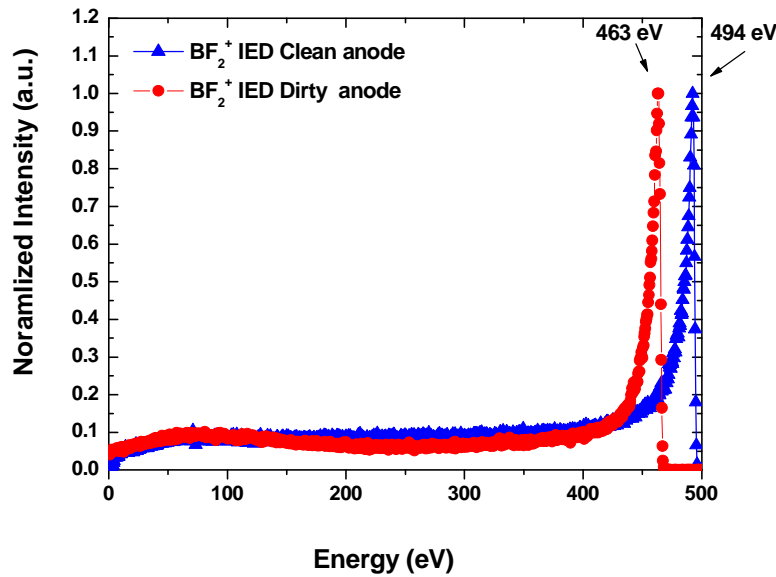


Figure 140: Normalized BF_2^+ ion energy distribution in the case of a clean hardware, and a dirty hardware, after many chamber maintenances and conditioning steps during a 500V, 30 mTorr, $50\mu s$ BF_3 glow discharge with hollow cathode biased at -1500 V

Positive V_p values are recovered only when the hardware inside the chamber is renewed. The insulating layer can be removed by ion bombardment (RIE) when the pulsed-anode mode is used. The plasma potential then returns to its original value.

Conditioning optimization

The mass spectrometer and Langmuir probe measurements have confirmed that an insulating layer is formed on the cathode and anode, which had been previously exposed to BF_3 chemistry, when the process chamber is exposed to air. The presence of the boron silicon oxide layer induces a higher secondary electron emission yield leading to a higher plasma density and thus a lower number of pulses needed to reach the target dose. Once the entire insulating layer on the cathode is etched away, a stable process is reached. Based on this study, the hardware material of the process chamber was modified. A different material roughness for the cathode and anode, as well as the use of the pulsed anode during the conditioning step has reduced the step to 30 minutes. This work also shows the importance of the Faraday cup when it comes to adjusting the number of pulses once the plasma density changes, due to the use of different types of substrate.

Plasma and R_s uniformity

Uniform implantation across the entire wafer is required in order to have a good device yield. The plasma uniformity is in turn very important to obtain a uniform plasma implant. In this section, radial plasma uniformity measured by Langmuir probe for different pressures will be presented during a 1 kV BF_3 glow discharge. The plasma uniformity will be correlated with wafer results such as sheet resistance (R_s) measurements. The observations and conclusions made for the 1 kV case are also valid for the 750 V and 500 V cases.

In the case of a DC glow discharge, the electron and ion densities should increase when the pressure is raised [Chapman 1980]. As expected, the plasma density measured in the center of the wafer by the Langmuir probe increases from 2.8×10^9 to 6.6×10^9 ions or electrons per cubic centimeter, when the pressure is raised from 40 to 70 mTorr during a 1 kV BF_3 glow discharge (see Fig. 141a).

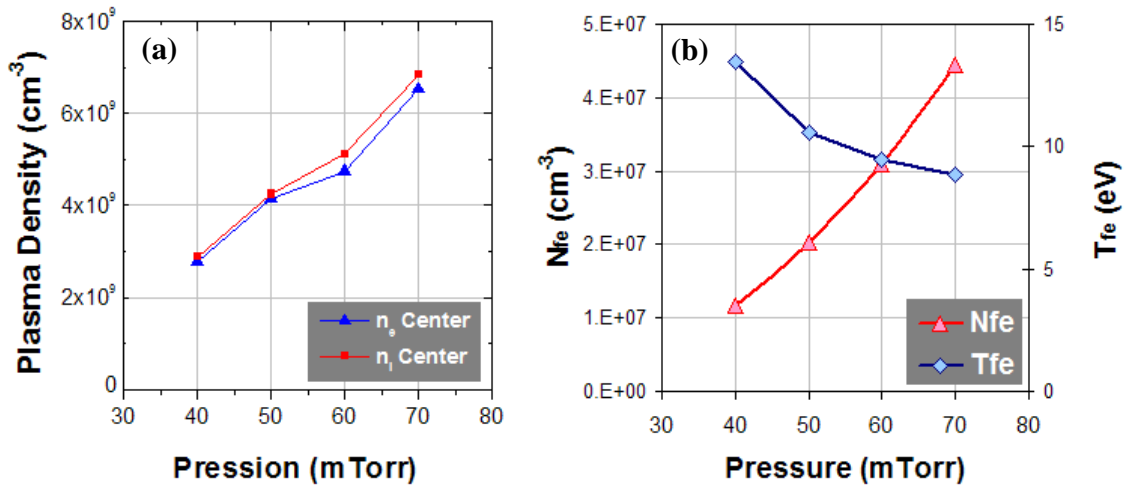


Figure 141: (a) Ion and electron densities measured at the center of the wafer, (b) fast electron temperature and density measured by the Langmuir probe during the pulse-on period, as a function of pressures ranging from 40 to 70 mTorr for a 1 kV 50 μs BF_3 glow discharge

It should also be noted that the densities of fast electrons also increase when the pressure is raised; they follow the same trend as the electron density that can be seen in Fig. 141b. As the electron mean free path is reduced when the pressure is raised from 40 to 70 mTorr, the probability of collisions for the fast electrons increases, and the average temperature of the fast electrons thus fall from 13.5 eV to 8.9 eV.

Fig. 142a shows the plasma potential radial distributions for different BF_3 gas discharge pressures during a 1kV, 50 μs PLAD implantation.

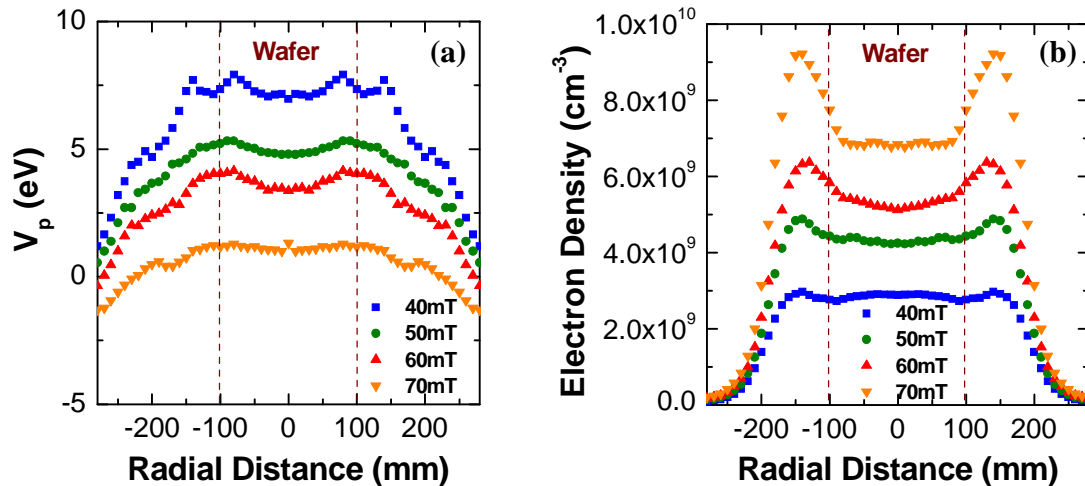


Figure 142: Plasma potential (a) and electron density (b) radial distributions for different pressures (40, 50, 60 and 70 mTorr), during a 1kV, BF_3 PLAD implantation

Under all the conditions, the plasma potential is uniform in the center of the discharge up to the annular Faraday cup, which is located 2.5 cm away from the wafer edge. However, the plasma potential (V_p) drops near the edge of the cathode shield ring. Some small uniformity distortions can be observed in the case of lower pressures. A pressure increase leads to a plasma density increase and in turn a reduction in the plasma potential.

The radial electron density distributions for different process chamber pressures are presented in Fig. 142b. As expected, higher pressure leads to higher electron density. Under all the conditions, the electron density is uniform above the wafer. Some uniformity distortions can be observed on the radial distributions above the shield ring. These distortions are more significant at higher discharge pressures. It should be noted that the shield ring materials used here were different from those of the silicon wafer. Under the original PLAD configuration, the shield ring that surrounds the wafer was made of aluminum and spray-coated with silicon. The roughness of the spray-coated silicon increases the effective shield ring surface, which creates locally higher secondary electron emissions, as well as higher ionization efficiency. In the case of lower pressures, the electrons created through ionization by the electron emitted from the shield ring diffuse faster than under high pressures, and the electron density thus becomes uniform. When the pressure is increased, the electron mean free path is reduced, higher non-uniformity and a maximum of plasma density can be observed above the shield ring near the edge of the silicon wafer. The maximum electron density is measured near the annular Faraday cup. When the same silicon spray-coated material is used on both the wafer and the shield ring, uniformity distortions are not observed.

The ion density radial distributions under the same conditions are presented in Fig. 143. As expected, the shape of the radial ion density is similar to the one for the electron density. As the dose is controlled by the Faraday cup, where the plasma density reaches its maximum, a lower implanted boron dose is expected in the center of the wafer when it comes to higher pressures. In the case of 60 mTorr, a degradation of the implantation uniformity is observed. With 3.9 % of non-uniformity, the higher R_s value in the center of the wafer indicates a lower implanted boron dose and is in good

agreement with the ion density radial distribution measurements (see Fig. 143). As expected by the ion density, the sheet resistance map becomes uniform for the 40 mTorr implantation, with only 1.2 % of non-uniformity. Based on Fig. 143, less boron dopants should be implanted in the center of the wafer in the 60 mTorr case if compared with the 40 mTorr case. This is confirmed by the average 60 mTorr R_s value, which is higher than in the case of 40 mTorr.

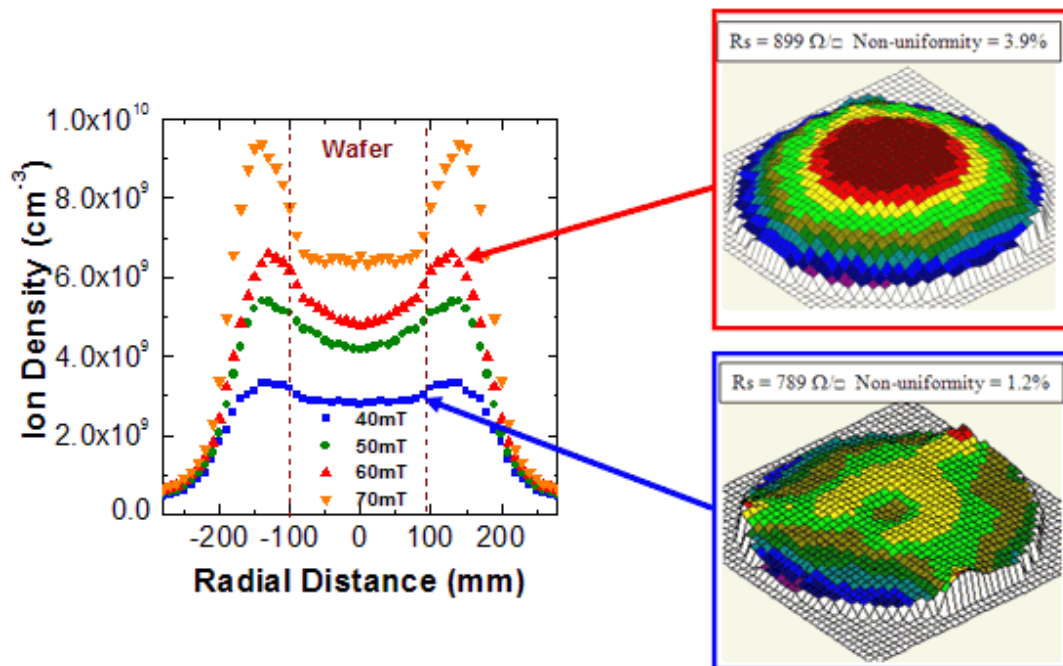


Figure 143: Ion density radial distributions for different pressures (40, 50, 60 and 70 mTorr), during a 1kV, BF_3 PLAD implantation

In conclusion, radial measurements of the plasma parameters can provide a good indication of the plasma uniformity and a good understanding of the sheet resistance uniformity after dopant activation. These measurements can also be used to estimate the error in dose expected after implantation. The selection of the material used on the surrounding shield ring is thus critical so as to obtain a uniform plasma. The spray-coated silicon shield ring was replaced by a bulk silicon shield ring, which is made of the same material as the wafer. The new silicon shield ring provides a larger operating window for controlling the implant uniformity.

Plasma etching

During a BF_3 plasma doping implantation, the silicon wafer is exposed to fluorine chemistry plasma, the etching of the wafer needs to be minimized in order to maintain device integrity. Lenoble has demonstrated that after a BF_3 plasma doping implantation into a patterned photoresist silicon wafer (at 600 V with a 3×10^{15} ions/cm² and 5 kV 1×10^{16} ion/cm²), the photoresist pattern is not affected by the BF_3 plasma exposure and the silicon wafer surface presents the same roughness (measured by atomic force microscopy) as a non implanted wafer [Lenoble 2000]. Due to the pulsed nature of the discharge, the etching of the substrate is thus minimized. Lower plasma duty cycle can further minimize the silicon etching from the cathode shield ring or hollow cathode.

As the residence time of the molecules and radicals is dependant on the gas flow inside the chamber as well as the pumping speed, the gas flow is an important process parameter. The typical gas flow value used during a BF_3 glow discharge is between 3 and 5 sccm. The effects of the gas flow on the energy distribution of the ions reaching the cathode are explored in this section.

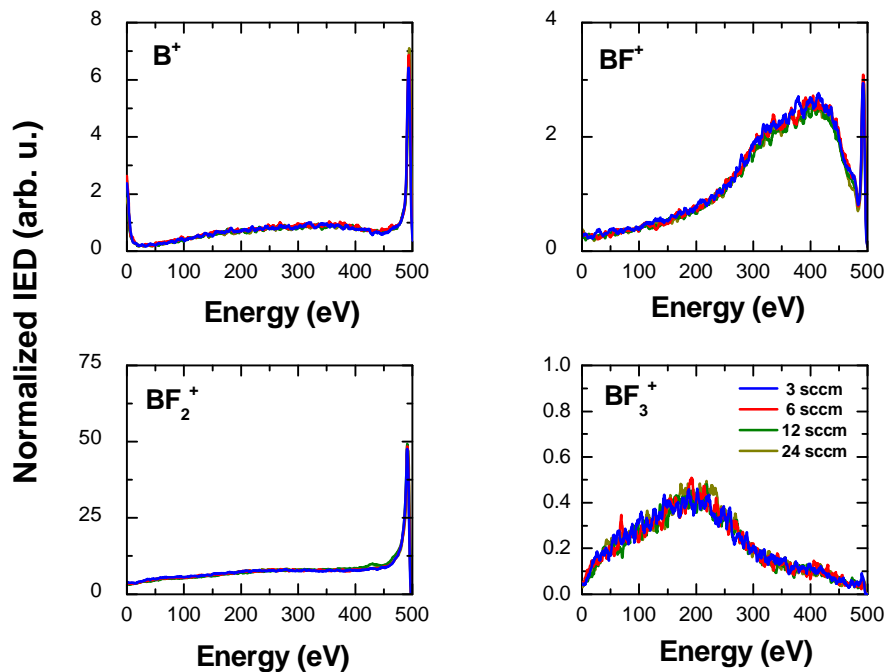


Figure 144: B^+ , BF^+ , BF_2^+ and BF_3^+ IEDs normalized to the total boron ion flux for different gas flows (3, 6, 12, and 24 sccm) during a 30 mTorr, 50 μs , 2500Hz BF_3 glow discharge for a hollow cathode plasma (1400V), with a cathode bias of 500V

Fig. 144 shows the B^+ , BF^+ , BF_2^+ and BF_3^+ IEDs normalized to the total flux of boron ions reaching the cathode for a 500 V, 30 mTorr hollow cathode plasma during BF_3 glow discharge. Identical IEDs can be observed for all the different gas flows studied.

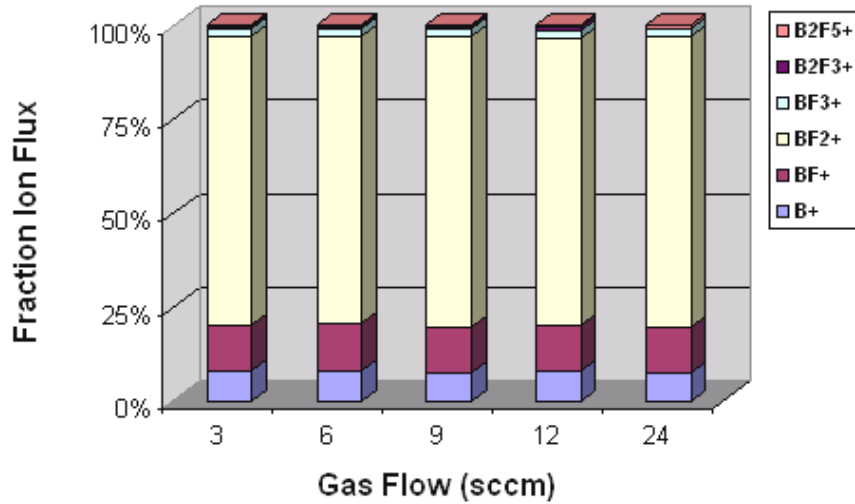


Figure 145: Boron ion fractions based on the flux of boron ions normalized to the total flux of boron ions measured for different gas flows during the pulse-on period for a 30 mTorr BF_3 glow discharge hollow cathode plasma (1400V) with a cathode bias of 500V

The abundances of all boron ions measured for different gas flows are presented in Fig. 145. The boron ion fractions remain constant when the gas flow is increased.

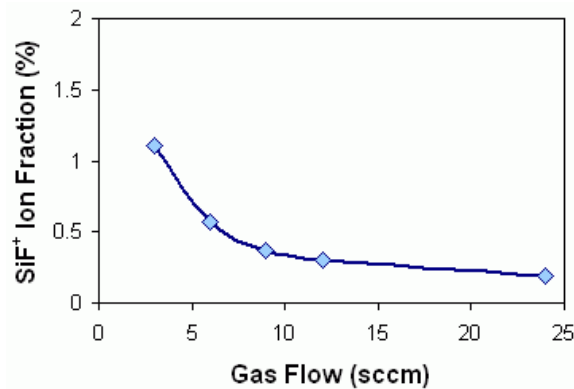


Figure 146: SiF^+ ion fraction based on the SiF^+ ion flux normalized to the total ion flux measured for different gas flows during the pulse-on period for a 30 mTorr BF_3 glow discharge hollow cathode plasma (1400V), with a cathode bias of 500V

The etching of silicon will generate some SiF_4 molecules, which will be desorbed from the silicon surface. These neutral molecules can then be ionized in the gas phase to

create SiF^+ , SiF_2^+ and SiF_3^+ . Only a minor fraction (typically below 1% of the total ion flux reaching the cathode under all the conditions used) of these ions can be detected on the cathode side. As expected, higher gas flows lead to a lower residence time for the etching species inside the process chamber and a lower fraction of SiF^+ (see Fig. 146).

In conclusion, changing the gas flow does not have an impact on the shape of the different boron IED reaching the cathode, but it reduces the residence time of the etching product inside the process chamber. The probability of ionization and implantation of the etching products is thus reduced.

Conclusion

In this section, a detailed study of the conditioning step following chamber maintenance was presented. Based on these experiments, the chamber hardware was modified to minimize the conditioning time necessary to obtain a stable process. Measurements of plasma uniformity has lead to a better understanding of the sheet resistance uniformity after plasma based ion implantation and the material of the cathode shield ring was replaced with same material as the wafer. When higher gas flow is used, the residence time of the etching product is strongly reduced and their implantation after ionization is thus reduced.

V.2 Depth profile simulation

For traditional beamline implantation, the incident ion mass and energy are well known parameters, and simulation programs are available to predict the implant profiles. For plasma-based ion implantation, all ionized species present in the plasma are extracted and implanted by applying negative voltage pulses to the wafer. Therefore, predicting an implant profile is more complicated, since one needs to know the relative abundance of the ion species, as well as their energy distribution (IED) prior to entering the wafer surface.

In this work, the plasma implant profile will be constructed using the profiles calculated at different energies, with their contributions proportional to the relative amount of ions at these energies. The information that is essential for calculating a profile is the ion mass and energy distribution, which are measured in-situ in the center of the wafer using an ion-mass and energy spectrometer. A computer simulation package was used to predict dopant profiles for all species and energies allowed by the PLAD voltage. The calculations are detailed below.

Principle

As soon as the voltage pulse is applied, a dynamic process starts in the discharge chamber, during which the neutrals and charged particles adjust their quantity, position and energy until a steady state is reached. Characterizing this dynamic process is difficult [Radovanov 2005]. One concern associated with the pulse rise and fall times is that they may affect the ion mass and energy distribution, thus changing the implant profile. This concern was ruled out in early studies of low-energy BF_3 PLAD implantation, as boron SIMS profiles showed no difference for various pulse-on widths (20 to 60 μs) [Lenoble 2000] with constant rise and decay times. The IEDs change during the rise and fall times of the pulse-on but the ion density and energy are much lower than during the flat part of the pulse and contribution to the dopant profile is low. In Fig. 79, the time evolution for the different ion fluxes measured with the mass spectrometer during the PLAD pulse are

reported. During the first 15 μs of the pulse-on, the sheath expands and the relative ion flux increases. After 15 μs , the relative total ion flux stabilizes and the IEDs of the different ions remain the same. During the decay, the total ion flux decreases as the sheath collapses. This observation allows us to improve the statistics of the EQP system by employing a wide TTL gate pulse, starting at 20 μs after the beginning of the pulse and ending at 50 μs . Only the constant portion of the pulse will thus be used to calculate the dopant depth profile. The rise and fall of the voltage pulse will not be included in the measurement and calculation, as they do not contain any critical information for implant profile calculation.

The measured IEDs for all the boron and fluorine ions implanted into the wafer were used as inputs [Walther 2006b] into implant-simulation software. 500V, 100 mTorr, BF_3 plasma IEDs are used here (Fig. 147) as an example.

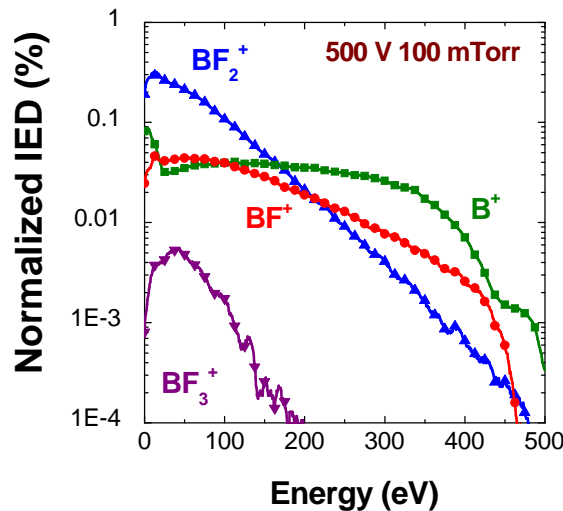


Figure 147: B^+ , BF^+ , BF_2^+ , and BF_3^+ IEDs, normalized to the total flux of boron ions for 500 V, 100 mTorr, BF_3 plasma

The Stopping and Range of Ions in Matter (SRIM) software [Ziegler 1996] (see section {I.2.2.2}) was used to simulate and predict implant profiles, to which the SIMS results were compared. Since SRIM only accepts atomic ions, the BF_x^+ ($x=1,2,3$) IEDs are normalized to the total ion flux and are converted into equivalent boron IED (B_{eq}^+) and equivalent fluorine IED (F_{eq}^+) by using the following formulas for each energy:

$$E(B_{eq}^+) = E(BF_x^+) \times \frac{m_B}{m_{BF_x^+}} \quad \{V.2.1\},$$

$$E(F_{eq}^+) = E(BF_x^+) \times \frac{m_F}{m_{BF_x^+}} \quad \{V.2.2\}$$

The results from the conversion of the ion energy distributions into boron equivalent energies are shown in Fig. 148 for each boron containing ion. The boron equivalent energy for each ion can then be used separately to estimate the impact of each ion on the final profile. They can also be combined together to give the total boron equivalent energy (B_{eqtot}^+) by using the following formula:

$$E(B_{eqtot}^+) = \sum_{x=0}^3 E(BF_x^+) \quad \{V.2.3\}$$

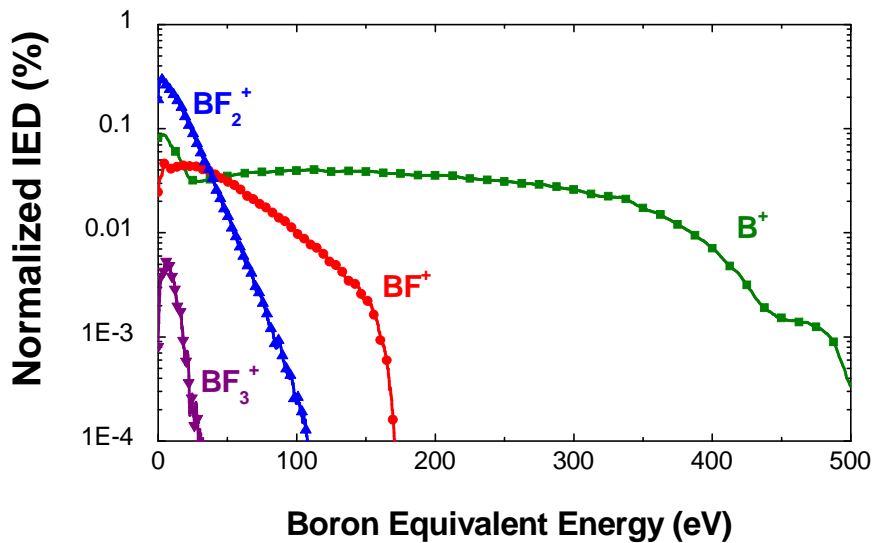


Figure 148: Calculated boron equivalent energy for each boron ion, normalized to the total flux of boron ions based on 500 V 100 mTorr IEDs of the ions reaching the wafer

Fig. 149 shows the equivalent boron and fluorine IEDs under the previously described discharge conditions. As expected, the main part of the boron and fluorine equivalent ion energies are below 250 eV.

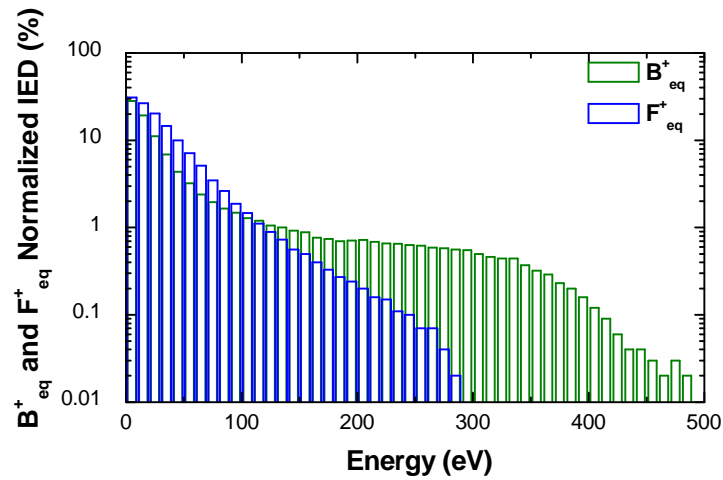


Figure 149: Boron and fluorine equivalent energy based on the 500V 100mTorr IED of the ions reaching the wafer

The equivalent boron and fluorine energies are partitioned into energy bins with 10eV increments. Each energy bin defines an ion dose fraction of the total flux of the boron ions coming onto the wafer. The average energy of each bin is used as the input energy for the SRIM simulation. All the output depth profiles from SRIM are then added up to represent the predicted depth profile, based on the IEDs of all the ions striking the wafer. A simulation of a beamline B^+ implanted at 1 keV was performed at various angles and the results are presented in Fig. 150.

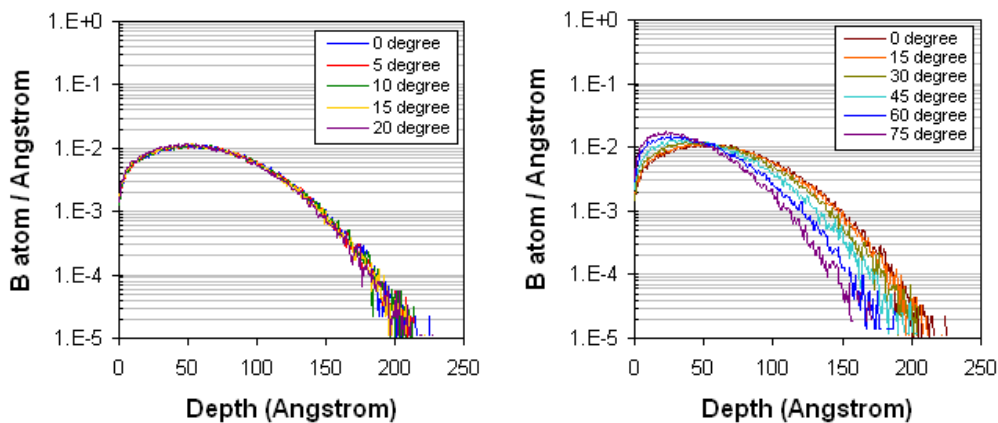


Figure 150: SRIM simulations of a 1keV B^+ implantation with different incident angles

Simulations for non-normal ion incident angles have also been performed and it should be noted that for angles below 15° , only minor differences can be observed on the

simulated profiles. In the following sections, only normal incident ions to the silicon surface will be considered.

Results and comparison

The predicted boron and fluorine profiles were calculated using the protocol described above and were then scaled up to the SIMS measured dose. A comparison between the predicted profile and the experimental boron and fluorine SIMS profiles is shown in Fig. 151.

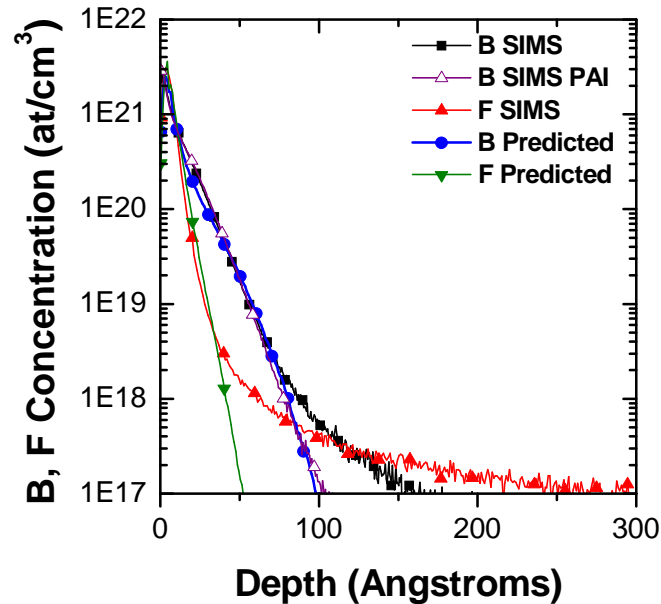


Figure 151: Boron and Fluorine predicted depth profiles, based on the measured ion mass and energy distributions for crystalline and pre-amorphized silicon wafer (PAI), compared with the measured SIMS depth profile for the same implant conditions (500V 100mTorr BF₃ PLAD)

When a crystalline wafer is used, a good correlation is obtained between the simulation and the experimental SIMS profiles of both elements in the shallower part of the profile, but the measured profile is deeper than the predicted one. In the boron and fluorine SIMS profiles, a typical channeling tail (see section I.2.2.3) inside the crystalline

wafer can be observed. This is not reflected in the predicted profiles, because SRIM simulation assumes amorphous target. This channeling tail, obtained at 0.5 kV with a crystalline silicon wafer, confirms that the majority of the ions are reaching the wafer with a small angle (lower than 15°). When a pre-amorphized substrate (PAI) is used, there is no channeling tail and the predicted boron profile then also matches the deeper part of the measured SIMS profile for the 0.5 kV case (see “B SIMS PAI” curve on Fig. 151).

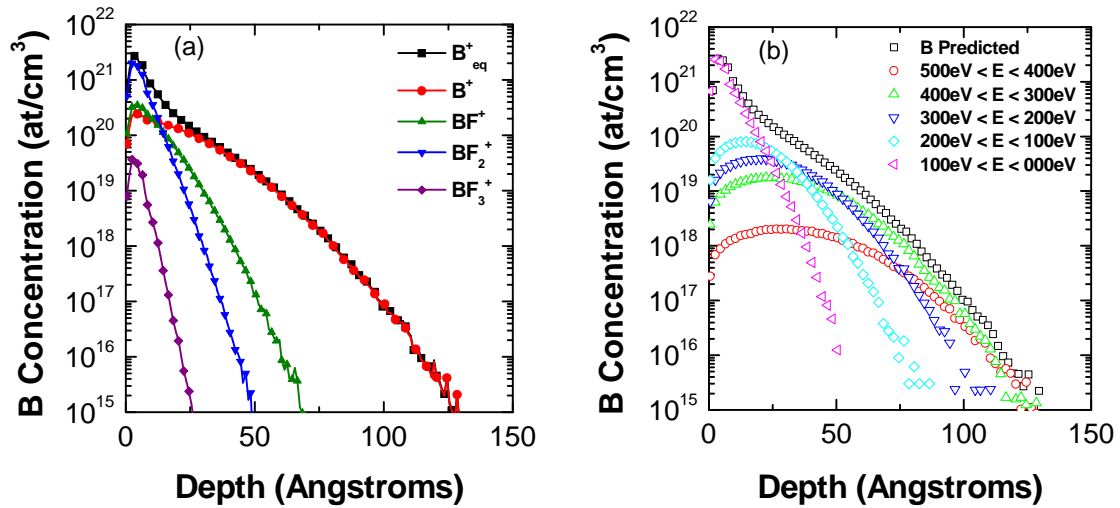


Figure 152: (a) Contribution of each ion reaching the wafer (B^+ , BF^+ , BF_2^+ and BF_3^+) onto the boron depth profile, (b) Contribution of each energy bin (0 to 100eV, 100 to 200eV, 200 to 300eV, 300 to 400eV and 400 to 500eV) equivalent boron energy onto the boron depth profile

By doing the simulation for each ion separately for the 0.5 kV 100 mTorr PLAD, the particularities of a PLAD dopant profile (surface peak and very shallow profile) can be explained. Fig. 152a shows the role of each ion species reaching the wafer: B^+ defines the depth of the implant, BF^+ and BF_2^+ are the main contributors to the surface dose, and BF_3^+ does not have any significant impact on the SIMS profile. Moreover, ions with equivalent energies between 0 to 100 eV are the main contributors to the dose. Under this

experimental condition, the surface peak of the PLAD SIMS profile represents about 50 % of the total dose (see Fig. 152b). Finally, the higher energy ions are found to define the final dopant depth.

Validation

In order to be more confident in the depth profile simulation, different plasma conditions, such as a higher cathode voltage and collisional or collision-less sheaths were used to compared the experimental data with prediction.

Mass transmission inside the mass spectrometer

In section {III.1.5.4}, the experimental mass transmission inside the mass spectrometer was compared to the theoretical transmission of the quadrupole and the channeltron. It was concluded that the experimental transmission does not follow the one provided by the mass spectrometer supplier, but was mostly constant for a range of ion masses studied here (11 to 68 amu). In order to confirm that the mass transmission does not follow a $\frac{1}{m}$ law, the IED was corrected through the transmission factor and then used as the input for the TRIM calculation to predict the boron depth profile. The new IEDs of the 500V 100mTorr BF₃ glow discharge are presented in Fig. 153a.

The B⁺ and BF⁺ fractions are reduced in the case of a $\frac{1}{m}$ transmission. The results of the simulation are presented in Fig. 153b. If a transmission factor of $\frac{1}{m}$ is used to correct the IED for the mass transmission inside the mass spectrometer, the predicted profile does not match at all the measured SIMS profile. This confirms that the mass transmission inside the mass spectrometer does not follow a $\frac{1}{m}$ law, and the IED must not be corrected but be used as measured.

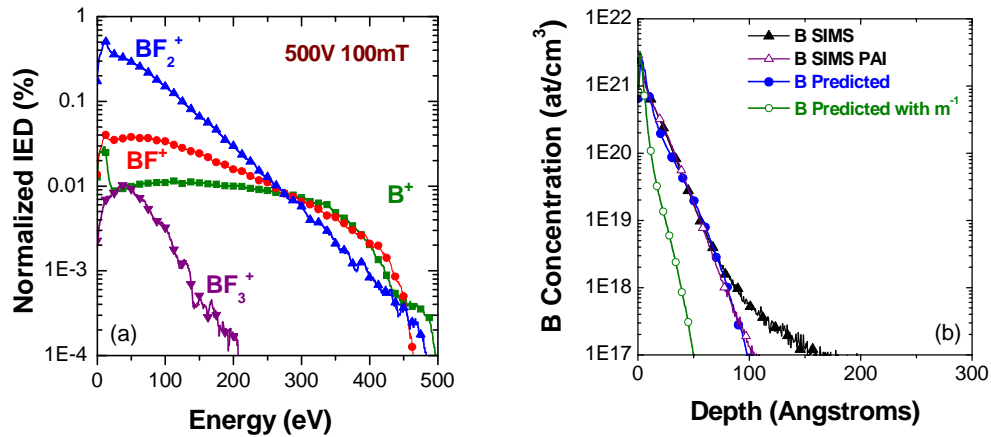


Figure 153: (a) B^+ , BF^+ , BF_2^+ , and BF_3^+ corrected IEDs normalized to the total flux of boron ions for 500 V, 100 mTorr, BF_3 plasma, (b) Boron predicted depth profile based on the measured IEDs, not corrected and corrected by a mass transmission in m^{-1} for crystalline and pre-amorphized silicon wafer (PAI), compared to the measured SIMS depth profile for the same implant conditions (500V 100mTorr BF_3 PLAD)

The next section will show that in many different cases, the measured SIMS profiles always match satisfactorily the predicted profiles.

Higher implantation energy

The boron molecular IED for a 1 kV 70 mTorr BF_3 plasma is shown in Fig. 154 (a) and used as an input for the calculation of the predicted boron profile.

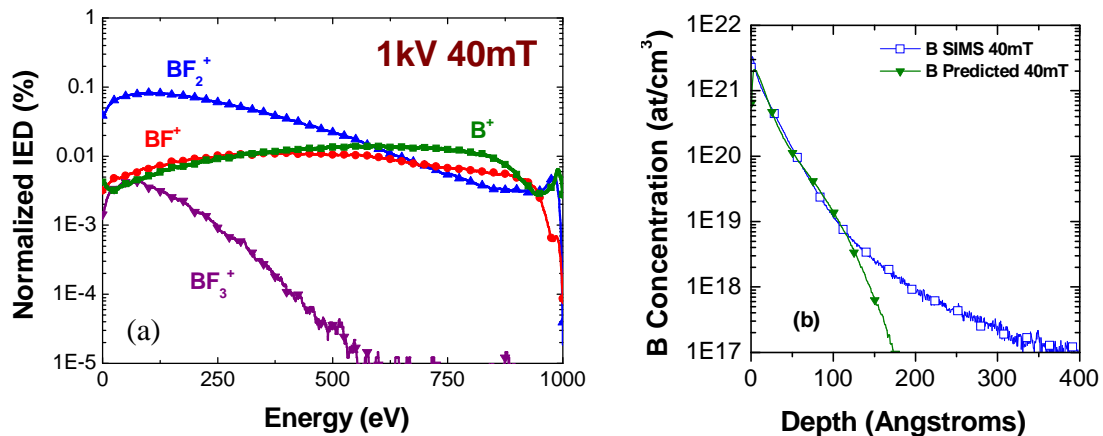


Figure 154: (a) B^+ , BF^+ , BF_2^+ , and BF_3^+ IEDs, normalized to the total flux of boron ions for 1kV, 40 mTorr, BF_3 plasma, (b) Boron predicted depth profile based on the measured IEDs for crystalline silicon wafer, compared to the measured SIMS depth profile for the same implant conditions (1kV 40 mTorr BF_3 PLAD)

Even at higher implantation energies, a good match is obtained between the SIMS profile and the predicted profile. The channeling tail can again be observed in the case of a 1 kV BF_3 implantation.

Collisional and collision-less sheath

As discussed previously [IV.2.3.1.d], when the hollow cathode is used, the plasma density can be modified while keeping the same mean free path. Two different plasma regimes can thus be obtained. In high density plasma, the discharge is operated in a collision-less sheath regime, and the majority of the ions extracted from the plasma reach the wafer with the full range of energy. The BF_2^+ IED peaks at high energy as can be seen in Fig. 155a.

In contrast, when it comes to low-density plasma, the discharge is operated in a collisional sheath regime, and the majority of the ions reach the cathode with lower energies than the voltage drop between the sheath edge and the cathode. As can be seen in Fig. 155b, the shape of the IED is very broad, with a BF_2^+ maximum intensity at very low energies.

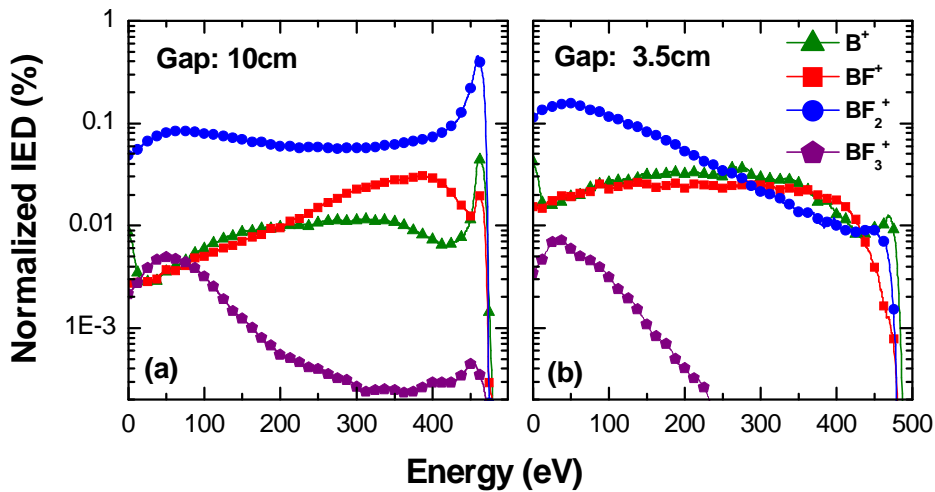


Figure 155: B^+ , BF^+ , BF_2^+ , and BF_3^+ IEDs, normalized to the total ion flux of a 500V, 30 mTorr, BF_3 hollow cathode plasma for a collisional sheath and a collision-less sheath

These two different cases were used as an input for the boron profile calculation. SIMS measurements were performed after PLAD implantation under the same conditions.

The SIMS profiles were then compared to the predicted boron profile as illustrated in Fig. 156.

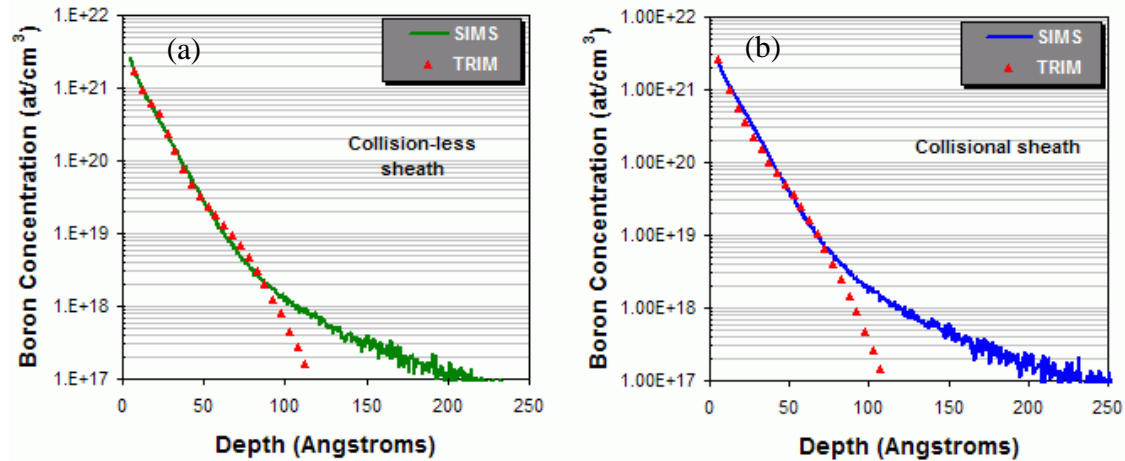


Figure 156: Boron predicted depth profile, based on the measured IED for crystalline silicon wafer, compared to the measured SIMS depth profile (500V 30 mTorr BF₃ PLAD) in the case of collisional and collision-less sheath

In both cases, the predicted profiles perfectly match the boron SIMS profiles very, even near the silicon surface.

Dopant profile prediction: Conclusion

To summarize, in-situ mass and ion energy distribution data was collected with an ion mass and energy spectrometer, which was installed in the middle of the cathode. Based on the spectrometer data, a series of SRIM simulations were performed to calculate the boron and fluorine dopant depth profiles. The calculated profiles will match the ones measured through secondary ion mass spectrometry for many different plasma conditions (cathode voltage, collisional sheath, collision-less sheath...). It was also confirmed that the mass transmission inside the mass spectrometer does not follow a $1/m$ law, the transmission function provided by the mass spectrometer supplier. When the IEDs are used without correction for the mass transmission, a good match to the SIMS profile is obtained. The predicted profiles also provide some additional explanations for the surface-peaked SIMS profile that is unique to plasma doping, and illustrate the role of

each ion. This knowledge will be useful to control and optimize implant profiles and dopant activation.

As with traditional ion implantation, the implant profile can now be predicted based on the ion energy distributions measured in the high-voltage sheath. This method can thus be used to optimize the as-implanted dopant profile for the junction engineering, by changing the plasma parameters and by understanding the sheath dynamics without using costly SIMS analysis. The other big advantage is that the dopant profile can be obtained instantaneously.

The dopant profile prediction method will be used in the following section, so as to optimize the plasma parameters and obtain shallower junctions.

V.3 Control of the dopant depth profile

In this section, a detailed BF_3 plasma characterization and dopant depth profile modeling will be used to tune the plasma and to optimize the process and the dopant depth profile. Three different approaches can be used to control the dopant depth profile. The first one consists of changing the energy of incident ion reaching the cathode by reducing the cathode voltage with or without the hollow cathode. The second one consists of increasing the number of collisions inside the sheath, and thus decreasing the ion mean energy. This can be accomplished by using higher discharge pressures or using a dilution gas, such as neon. The last approach consists of operating the discharge in a collision-less regime, with a minimized fraction of light ions. These three different ways to obtain shallower dopant depth profile after plasma-based ion implantation will be presented in the next section.

Cathode voltage

The effects of the cathode voltage on the ion energy distribution and the predicted boron dopant depth profile in a diode (anode and cathode) and triode (hollow cathode, anode and cathode) configuration are explored in this section.

Diode configuration: without hollow cathode

As discussed previously, in the diode configuration when the hollow cathode is unused, the discharge cannot be operated at energies below 450V due to Paschen curve limitations. In order to operate the discharge at lower cathode voltages, higher process pressures are required. The B^+ , BF^+ , BF_2^+ and BF_3^+ IEDs normalized to the total flux of boron ions as a function of the energy divided by the cathode voltage (eV_c) in the diode configuration, are presented in Fig. 157 for different cathode voltages (1000, 750 and 500V).

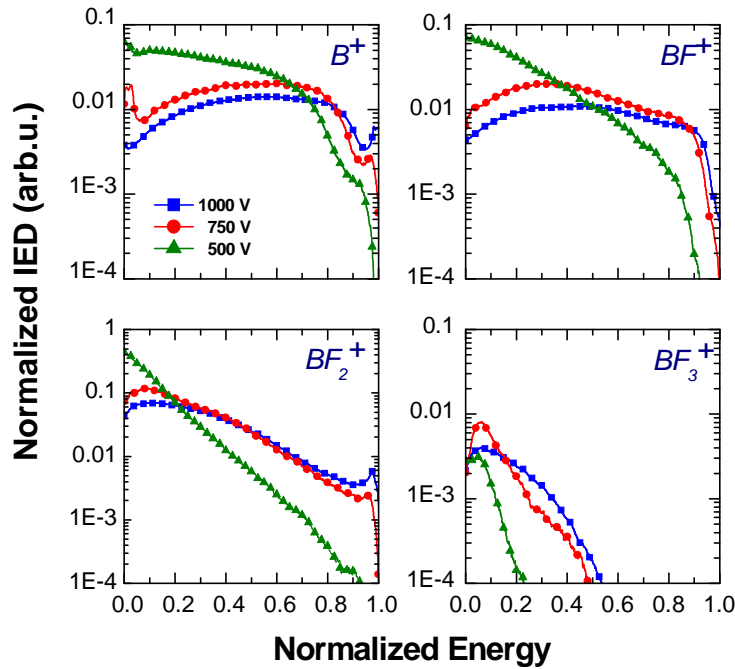


Figure 157: B^+ , BF^+ , BF_2^+ and BF_3^+ IEDs normalized to the total flux of the boron ions as a function of the normalized energy (ϵ / eV_c), for different cathode voltages, BF_3 glow discharge (1000 V 40 mTorr, 750 V 60 mTorr and 500 V 100 mTorr)

Between 1000 V and 750 V, only minor variations are observed. When the cathode voltage is reduced further (500 V), higher pressure is needed to ignite the plasma and the number of collisions is thus increased. Under such conditions, the mean energy of each ion is also reduced, and the shape of IEDs is strongly modified.

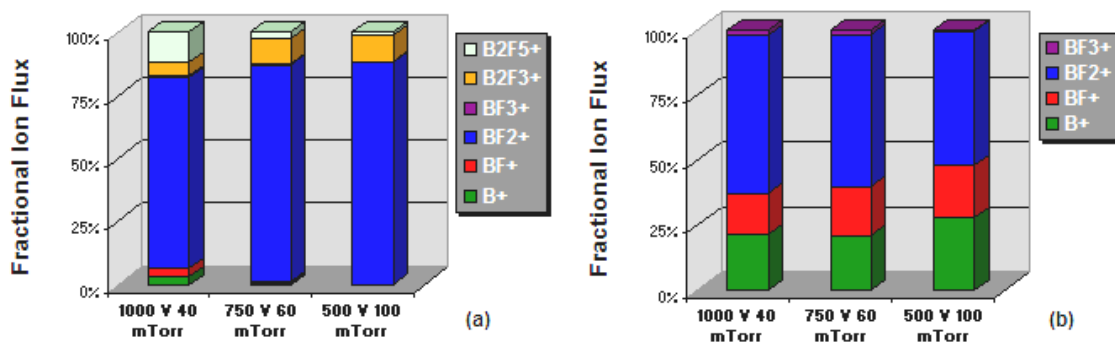


Figure 158: Boron ion fractions normalized to the total boron ion flux and measured for different cathode bias voltages (1000 V 40 mTorr, 750 V 60 mTorr and 500 V 100 mTorr), during the pulse-on period BF_3 glow discharge, as measured (a) in the bulk plasma and (b) in the high-voltage sheath

The fractions of boron ions, normalized to the total flux of boron ions measured during the pulse-on in the bulk plasma and in the high-voltage sheath, are presented in Fig. 158 (a) and (b), respectively. As the electron energy is reduced for higher pressure, the B^+ and BF^+ fractions from the bulk decrease to almost zero percent of the total flux of boron ions when the cathode voltage is reduced. In contrast, the fraction of $B_2F_3^+$ ions slightly increases, while the $B_2F_5^+$ fraction decreases.

During the high-voltage acceleration, the ions are subject to collisions by charge exchange or dissociation inside the sheath, as was demonstrated in section {IV.2.5}. As the sheath becomes more collisional once the cathode bias is reduced, the fraction of B^+ and BF^+ increases and is thus significantly higher than in the bulk plasma. As usual, no heavy ions are detected in the high-voltage sheath. As the number of collisions inside the sheath only slightly increases from 4.4 to 4.9, only minor changes in the fraction of boron ions for the 750 V, 60 mTorr and 1000 V, 40 mTorr conditions are observed.

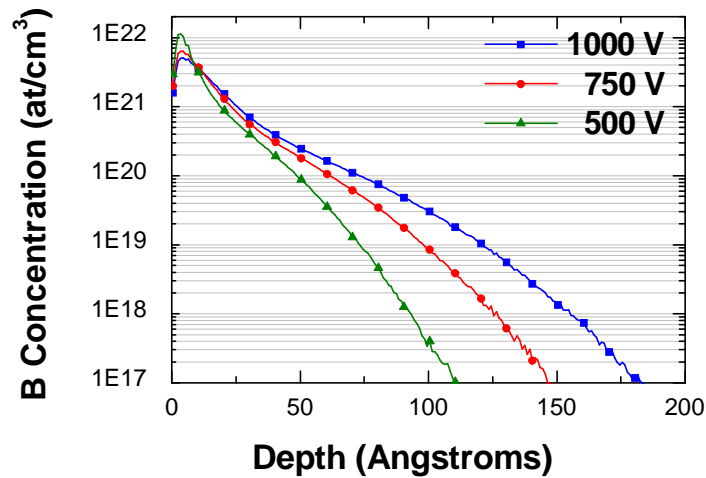


Figure 159: Boron predicted profile, based on the measured IEDs for different cathode biases and pressures (1000 V and 40 mTorr, 750 V and 60 mTorr and 500 V and 100 mTorr) during the pulse-on period BF_3 glow discharge measured in the high-voltage sheath for 10^{15} B ion/cm³

The boron predicted profile, based on the measured IEDs normalized to 10^{15} ion/cm² boron dose is presented in Fig. 159 for three different cathode voltages. As expected, the dopant depth profile decreases when the cathode is reduced from 1000 V to 500 V. Unfortunately, the fractions of B^+ and BF^+ remain quite high, and the profiles are

deeper than expected if only BF_2^+ was implanted. The challenges in obtaining shallower junctions with a constant cathode bias will be described in section V.3.2 and V.3.3.

Triode configuration: hollow cathode mode

The hollow cathode allows for the discharge to be operated at constant pressure for different cathode biases with an almost constant bulk plasma density (see section II.2.2.a). The ion energy distribution for the different boron ions, with a constant hollow cathode plasma and for different cathode bias voltages in a BF_3 glow discharge, are presented in Fig. 105, 106 and 107 of section {IV.2.5}. Fig. 160 is a summary of all the IEDs for the main boron ions, as measured inside the high voltage sheath.

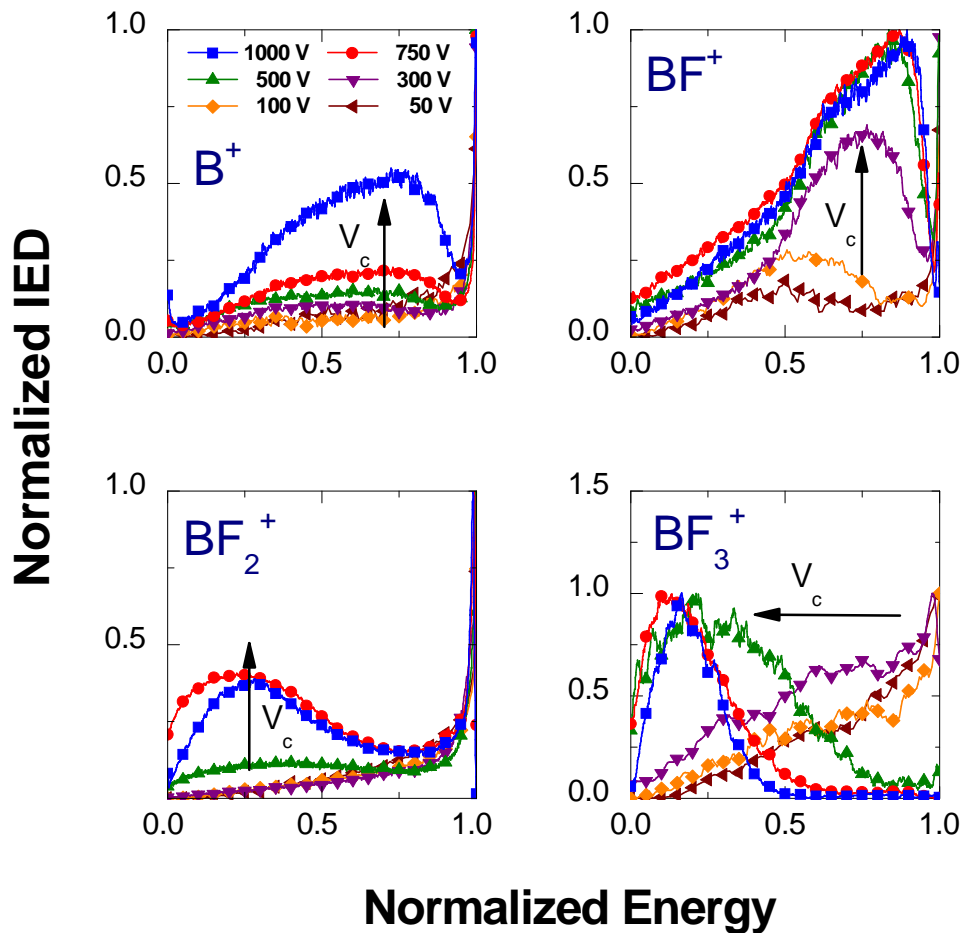


Figure 160: B^+ , BF^+ , BF_2^+ and BF_3^+ IEDs normalized to their maximum intensity as a function of the energy normalized to the cathode voltage, for different cathode voltages in a 30 mTorr, 2500 Hz, 50 μs , BF_3 glow discharge (50, 100, 300, 500, 750 and 1000V), with a constant hollow cathode bias at -1500 V

The IEDs were normalized to their maximum of intensity and plotted as a function of the normalized energy for the different cathode bias voltages (50, 100, 300, 500, 750 and 1000 V), with a constant hollow cathode plasma operated at 1500 V and 30 mTorr.

B^+ , BF_2^+ and BF_3^+ IEDs are characteristic of collision-less discharge for 50, 100 and 300 V. The shape of the IEDs starts to be affected by collisions inside the sheath at 500 V. The dominant ion, BF_2^+ starts to be affected by collisions for cathode biases above 300 V; a two-peak distribution can then be observed at higher cathode voltages, with an energetic peak at full acceleration and a peak at a lower energy. The low-energy peak increases when the cathode voltage is raised, which indicates that the sheath becomes collisional for the BF_2^+ ion population. The B^+ IED follows the same trend as the BF_2^+ IED and presents a bimodal distribution above 300 V.

In the case of BF^+ , a two peak distribution can be observed, even at a cathode bias of 50 V or 100 V. For a cathode bias higher than 300V, a tri-peak distribution can be observed on the IED. The IED shapes have been explained in details in Chapter IV. In the case of the BF_3^+ IED, the collisional sheath regime also appears for cathode biases above 300 V

The calculation of the number of collisions inside the sheath shows that at low cathode bias, the sheath is not collisional for BF_2^+ and becomes collisional only above 300 V (see Fig. 161a). For higher cathode biases the sheath becomes collisional for the BF_2^+ ion population.

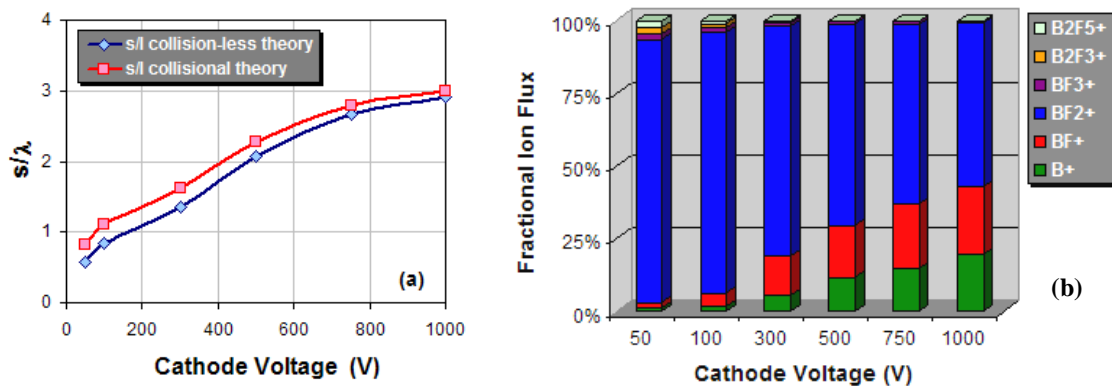


Figure 161: (a) Number of collisions and (b) boron ion fractions normalized to the total boron ion flux measured for different cathode biases (50, 100, 300, 500, 750 and 1000V) during the pulse-on period of a 30 mTorr BF_3 glow discharge in the high-voltage sheath, with a constant hollow cathode bias at -1500V

As previously discussed (see Chapter IV), when the number of collisions increases, the fractions of B^+ and BF^+ also rise, while the fractions of heavier ions almost totally disappear for cathode biases above 300 V (see Fig. 161b).

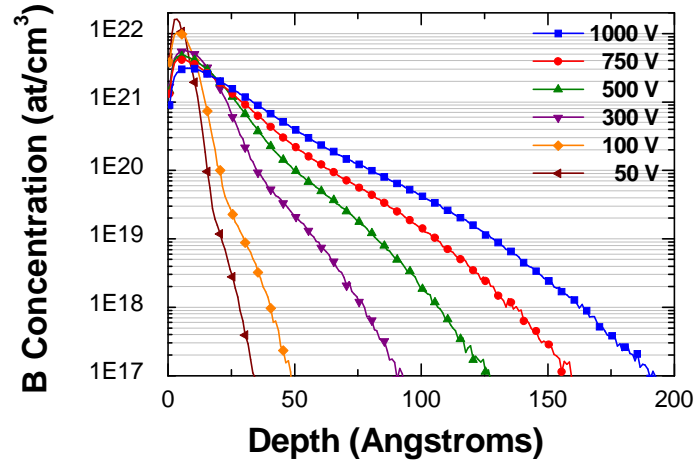


Figure 162: Boron predicted profiles based on the measured IEDs for different cathode biases (50, 100, 300, 500, 750 and 1000V) during the pulse-on period of a 30 mTorr hollow cathode BF_3 glow discharge measured in the high-voltage sheath for 10^{15} B ion/cm³

The boron predicted profiles, calculated using the previous ion energy distributions for different cathode biases with a constant hollow cathode voltage, is normalized to a total boron dose of 10^{15} ions/cm² and presented in Fig. 162. As expected, the dopant depth decreases with lower high-voltage acceleration. The use of the hollow cathode can thus provide very shallow junctions. With an appropriate activation of the dopant (Flash anneal for example), the junction depth needed to meet the ITRS can be achieved (9 nm for 2006). However, the difficulties that come to achieve the needed dose and match the R_s and X_j target values, may be an issue with such low-energy implantation. The optimization of higher energies, such as 500 V, may thus be a better approach. An optimized 500V BF_3 discharge plasma-based ion implantation (B^+ fraction minimized) will give very shallow junction with higher dopant concentration implanted under the solid solubility limit.

High pressure to increase the number of collisions

The second approach consists of increasing the number of collisions inside the sheath, and thus decreasing the mean energy by using higher discharge pressures or using a dilution gas, such as neon. Three different cases are presented in this section. The first case studied here is a 1 kV BF_3 glow discharge with pressures ranging from 30 to 70 mTorr. The second case involves a 750 V BF_3 glow discharge with pressures ranging from 40 to 60 mTorr and the last case covers a 500 V BF_3 glow discharge with pressures ranging from 75 to 250 mTorr.

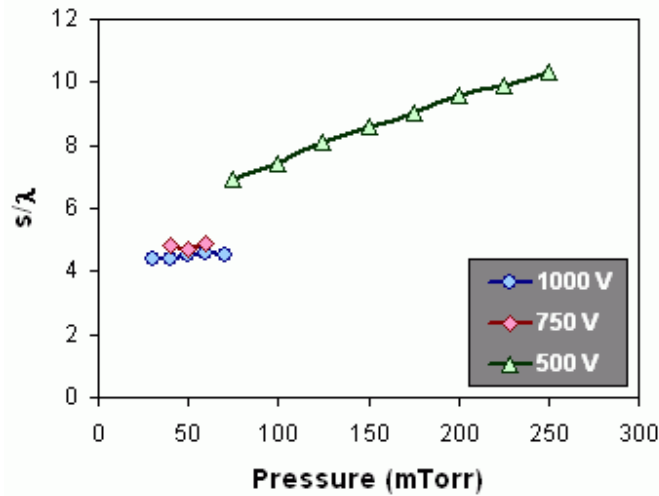


Figure 163: Ratio of sheath thickness over ion mean free path, as a function of the pressures for different cathode voltages (1000 V, 30 to 70 mTorr; 750 V, 40 to 60 mTorr and 500 V, 75 to 250 mTorr)

Fig. 163 shows the number of collisions inside the sheath, as calculated for the different cathode voltages and various gas pressures. When the cathode bias voltage is at 1000 V, the discharge pressure is limited by the Paschen curve (see section {II.2.2.1}) to a range of 30 to 70 mTorr. For this pressure range, the number of collisions (s/λ) inside the sheath calculated using formula {IV.2.12} for collisional sheath remains constant around 4 collisions. The decrease of the mean free path at higher pressures is compensated by the decrease of the sheath thickness, which is due to the plasma density increase at higher pressures. Consequently, minor changes in the shape of the IED are expected. The same conclusion holds true for the 750 V case. When a lower bias voltage is used (500 V), the discharge can be operated under a large range of pressures, from 75 to 250 mTorr. Within this pressure range, the number of collisions increases from 6.9 to 10.3. Significant changes on the IED can thus be expected.

The ion mass and energy distributions of a 1 kV BF_3 plasma under three different pressures are presented in Fig. 164.

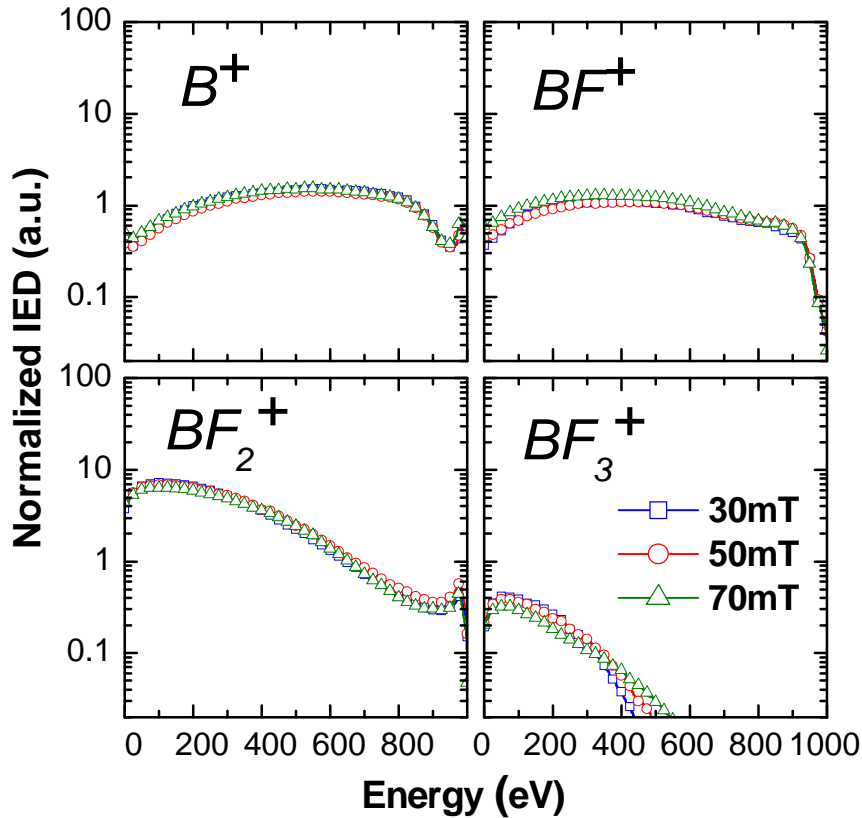


Figure 164: B^+ , BF^+ , BF_2^+ and BF_3^+ IEDs normalized to the total flux of the boron ions for a 1kV BF_3 plasma under three different pressures: 30, 50, 70mTorr

As expected with the number of collisions, the pressure changes do not significantly affect the shape of the IED, except for the BF_3^+ ion. In all the other cases, the BF_3^+ fraction remains very low (less than 2 %). BF_3^+ has a smaller energy spread, and the peak of the distribution is in a thermal range. BF_2^+ is the most abundant ion implanted into the wafer, with more than 60 % of the total boron ion flux composed of B^+ , BF^+ , BF_2^+ , and BF_3^+ . Only a few ions (<1 %) from the boron ion flux are able to reach the wafer with full energy (1000 eV). The majority of the ions strike the cathode with an energy below 500 eV.

The pressure needs to be significantly increased to influence the shape of the ion energy distribution and to reduce the ion mean energy. Indeed, there are no differences

between the boron SIMS profiles measured on crystalline wafer during a 1 kV implantation for pressures ranging from 30 to 70 mTorr (see Fig. 165). The SIMS profiles also match with the profiles predicted with the mass spectrometric measurements well. Similar observations can be made for the 750 V condition under the pressure range studied here.

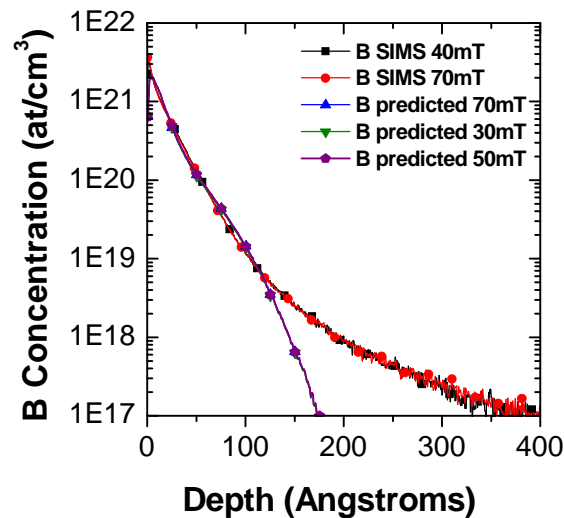


Figure 165: Boron predicted depth profile based on the measured ion mass and energy distribution, compared with the measured SIMS depth profile for the same implant conditions (1kV 30 to 70mTorr, 2500 Hz, 50 μ s BF_3 PLAD)

The normalized IEDs for a 0.5 kV BF_3 discharge (100 to 250 mTorr) are shown in Fig. 166. The ion energy distributions of the boron ions are strongly affected by the large rise in pressure. The maximum energies of B^+ , BF^+ and BF_2^+ decreases significantly when the pressure is raised from 100 to 250 mTorr. Compared to the 1 kV case, the number of collisions inside the sheath increases significantly. Only a few ions (<0.1 %) from the boron ion flux are able to reach the wafer with full energy (500 eV). The majority of these ions (91 %) strike the cathode with an energy below 250 eV. The ion energy and the lighter ion fraction slightly decrease with the pressure, which should provide shallower dopant depth profiles, as confirmed by previous experiments [Lenoble 2000].

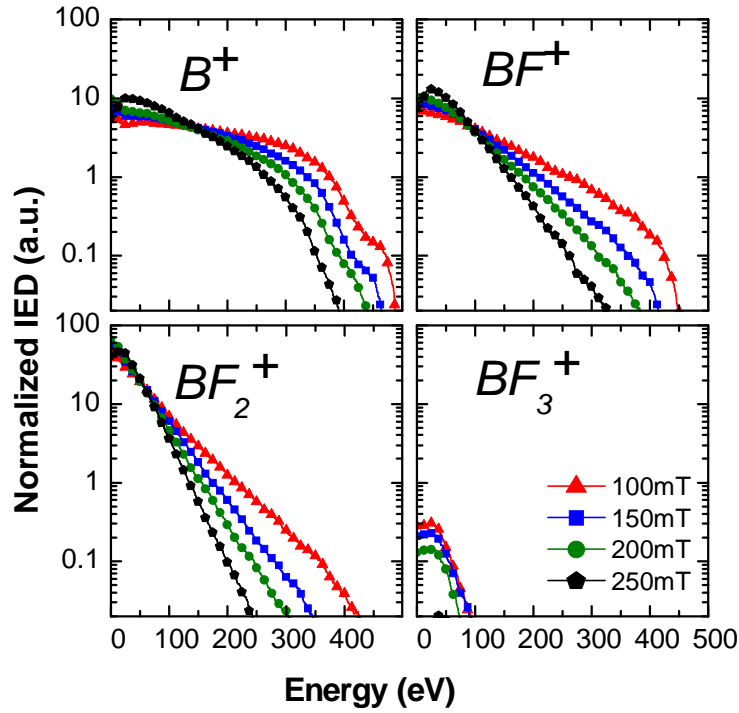


Figure 166: B^+ , BF^+ , BF_2^+ and BF_3^+ IEDs normalized to the total ion flux for a 500 V BF_3 plasma under four different pressures: 100, 150, 200, 250mTorr

Fig. 166 confirms that BF_2^+ is the dominant ion reaching the cathode for all the different process conditions, and the fraction of BF_3^+ is below one percent of the total ion flux.

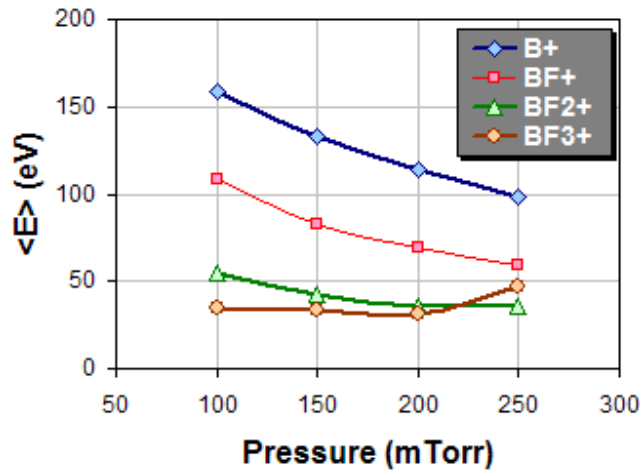


Figure 167: Experimentally determined mean ion energies for B^+ , BF^+ , BF_2^+ and BF_3^+ after their acceleration inside the high-voltage sheath for a 500V BF_3 glow discharge operated at different pressures (100, 150, 200 and 250 mTorr)

The experimentally determined mean ion energies for B^+ , BF^+ , BF_2^+ and BF_3^+ are presented in Fig. 167. As expected with the IEDs and the number of collisions inside the high-voltage sheath, the mean energies for B^+ , BF^+ and BF_2^+ are reduced when the pressure is increased.

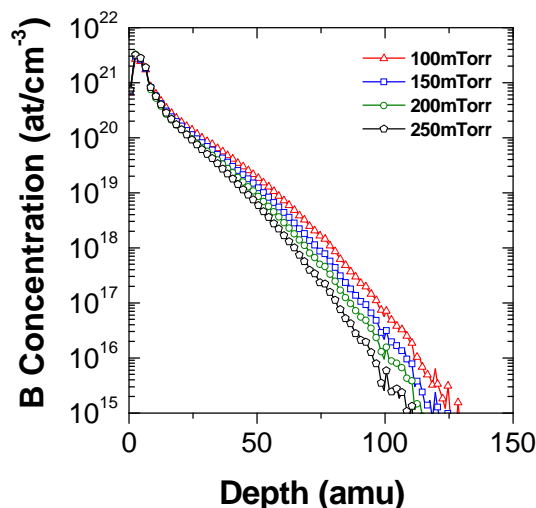


Figure 168: Boron predicted profiles based on the measured ion energy distribution for a 500V, 2500 Hz, 50 μ s BF_3 PLAD at 100, 150, 200 and 250mTorr

When the pressure is increased from 100 to 250 mTorr in the case of a 500 V PLAD implantation, the number of collisions rises significantly, while the mean ion energy decreases. This leads to shallower boron profiles when the pressure is increased from 100 to 250 mTorr (see Fig. 168), and is in good agreement with previous data presented by Lenoble for similar conditions [Lenoble 2000]. Unfortunately, the plasma could not be ignited for pressures above 175 mTorr at 500 V. For this experiments purpose, the discharge was ignited at a lower pressure. The pressure was then gradually increased up to the 250 mTorr with the plasma on. But this mode of operation to obtain shallower junctions is then limited by Paschen's curve. Moreover, with the annular Faraday cup installed inside the process chamber, some arcing could be observed inside the cup for pressures above 175 mTorr.

Another alternative to increase the number of collisions inside the sheath is the use of a rare gas with a high ionization potential such as neon, which is diluted with the BF_3 gas. Since neon has a higher ionization potential, the dilution of BF_3 with neon will decrease the plasma density. The number of collisions will thus increase, and the dopant

depth should be shallower. The ion energy distributions in the case of a 500 V BF_3 plasma diluted with neon at 50 % for different discharge pressures are presented in Fig. 174. In the case of the 500 V high-pressure neon dilution, the two isotopes $^{20}\text{Ne}^+$ and $^{22}\text{Ne}^+$ are detected. The fraction of B^+ slightly increases; as compared to the-no dilution case (see Fig. 169), but the shape of all the other ions remains similar. As expected, the Ne^+ IED present the same behavior as one measured by Davis and Vanderslice (see Fig. 101a). It can also be noticed that BF_2^+ and BF_3^+ follow the same shape as Ne^+ . Charge exchange inside the sheath for these two ions can thus be suspected.

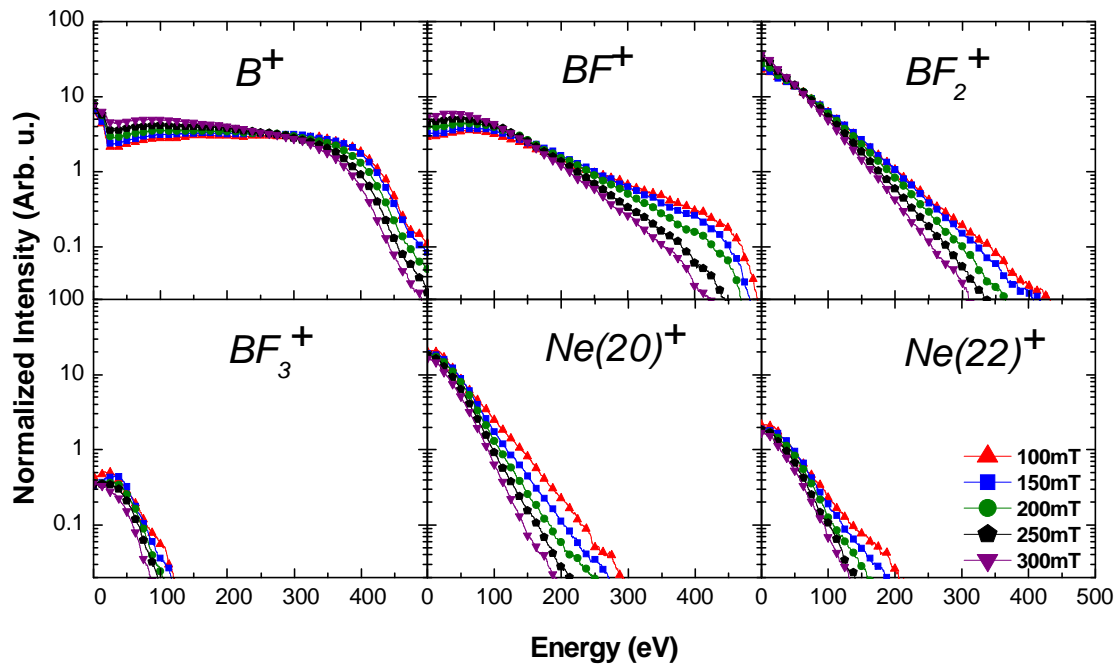


Figure 169: B^+ , BF^+ , BF_2^+ , BF_3^+ , Ne^+ IEDs normalized to the total ion flux for 500V 2500 Hz BF_3 , diluted at 50 % with neon for five different pressures: 100, 150, 200, 250 and 300 mTorr

Despite the fact that the number of collisions inside the sheath rise, the fractions of B^+ and BF^+ also increase with neon dilution. The predicted profile becomes deeper than in the case without dilution under the same discharge pressures (see Fig 170). No improvements in the dopant profile can be observed in the case of BF_3 diluted at 50% with argon.

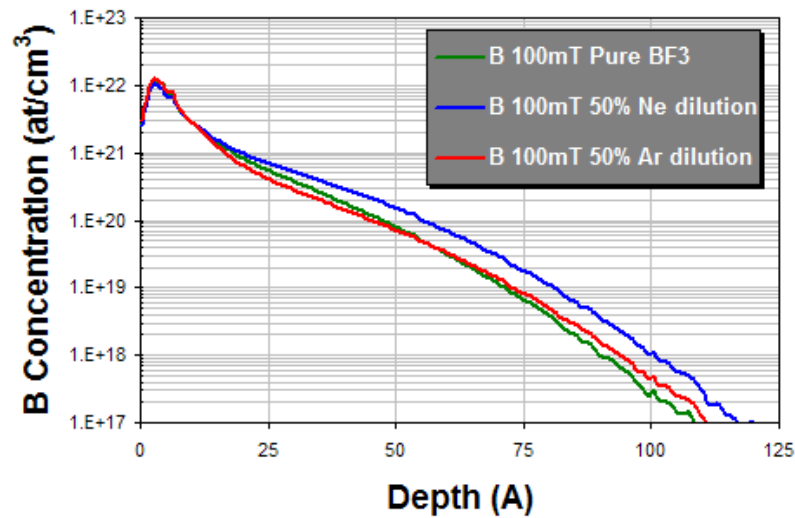


Figure 170: Boron predicted profile for a pure BF_3 plasma, a BF_3 -Ne plasma (with 50% neon) and a BF_3 -Ar plasma (with 50% argon) during a 500 V, 100 mTorr PLAD implantation

In conclusion, the depth of a dopant profile under high pressures, with or without dilution, is limited by the pressure and by the fraction of B^+ created inside the collisional sheath. These approaches do not appear to be the most effective approach to obtain very shallow junctions.

Reduction in the number of collisions

It was demonstrated in Chapter IV that, under a diode configuration with one electrode grounded and the other one negatively pulsed, the collision-less regime cannot be reached. Different configurations of the current PLAD system can be used to decouple the plasma creation from the negative cathode bias and to reach the collision-less regime. A configuration using a hollow cathode or another using a pulsed anode can thus be adopted to control the sheath dynamics. The advantages of the two different configurations will be discussed in the following section.

Hollow cathode mode

In order to modify the plasma density and the number of collisions inside the sheath, the anode-to-cathode spacing can be used to modify the effective surface of the

hollow cathode. In addition to electric field modification, the higher hollow cathode voltage should help to obtain higher plasma density. These two approaches will be introduced and discussed in the next two sections.

a) Anode-to-cathode spacing and process implications

In the diode configuration, the IEDs of the boron containing ions for different anode-to-cathode spacing remain constant. Similar observations can be made using SIMS measurement for different anode-to-cathode spacing. As no difference was observed for 3.5 cm and 10 cm gap, the data will not be presented.

In the case of the triode configuration with the hollow cathode, the moveable anode system offers an additional “knob” for process control and uniformity. The HC also provides a better control of sheath dynamics, as it allows transition from a collisional to a collision-less sheath while maintaining a constant mean free path. Once there is a constant pressure, the shape of the IED can then be modified by changing the number of collisions inside the sheath.

Fig. 171 shows the time evolution of the electron density during the pulse-on period for a 500 V, 30 mTorr, 50 μs BF_3 plasma with different anode-to-cathode spacings. As can be seen, the steady state is never reached for the electron population.

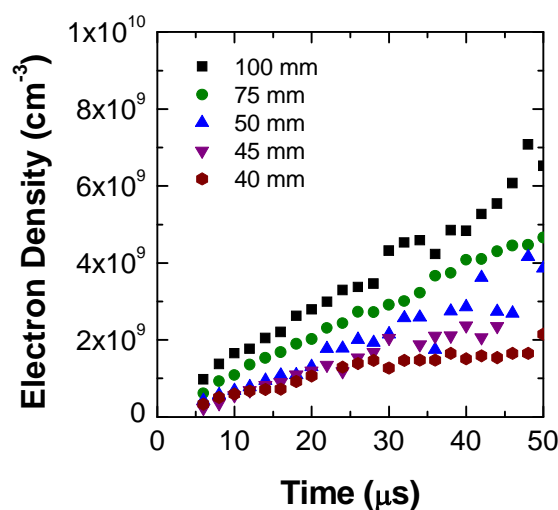


Figure 171: Time evolution of the electron density during the pulse-on period for a 1500 V HC plasma with different anode-to-cathode spacings (500 V, 30 mTorr, 50 μs , 2500 Hz)

The effective hollow cathode surface area increases when a larger anode-to-cathode spacing is used, which implies that there is an increase in the plasma density. As the pressure, HC and cathode voltages are maintained constant; the sheath thickness in turn decreases when the anode-to-cathode gap is increased. As can be seen in Fig. 172, the sheath thickness calculated using formula {IV.2.5} for a collision-less sheath in the steady state, decreases from 2.5 cm to 1.1 cm when the anode-to-cathode gap is increased from 40 to 100 mm.

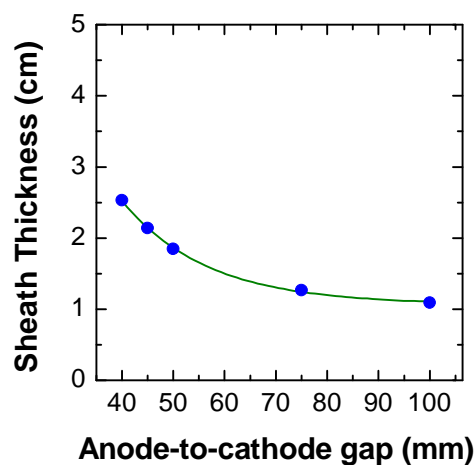


Figure 172: Calculated sheath thickness for a 500 V, 30 mTorr, 50 μ s, 2500 Hz BF_3 glow discharge with different anode-to-cathode spacings

The decrease in sheath thickness with a constant mean free path implies a reduction in the number of collisions inside the sheath. Assuming a constant ion-neutral cross-section of $2 \times 10^{-15} \text{ cm}^2$ for the dominant BF_2^+ ion, the ion mean free path is equal to 0.5 cm at 30 mTorr. The number of collisions inside the sheath can then be calculated. The estimated number of collisions inside the sheath changes from 5 to 2 when the anode-to-cathode gap is increased from 4 to 10 cm. Changes in the shape of the ion energy distribution are thus expected when the gap is increased.

Fig. 173 shows the BF_2^+ IEDs measured on the cathode side of a 500 V, 30 mTorr, 50 μ s HC plasma for different anode-to-cathode spacings. The IED shape for the dominant ion BF_2^+ is significantly affected as the sheath becomes more collisional when the anode-to-cathode spacing is reduced. In the case of small spacings, most of the BF_2^+ ions are low-energy ions. When the gap increases, the sheath becomes less collisional,

consequently more ions are able to reach the cathode with the full energy acquired through acceleration inside the high voltage sheath. As the sheath thickness only slightly increases for a gap larger than 75 mm, no significant difference is observed on the BF_2^+ IED shapes between 75 mm and 100 mm.

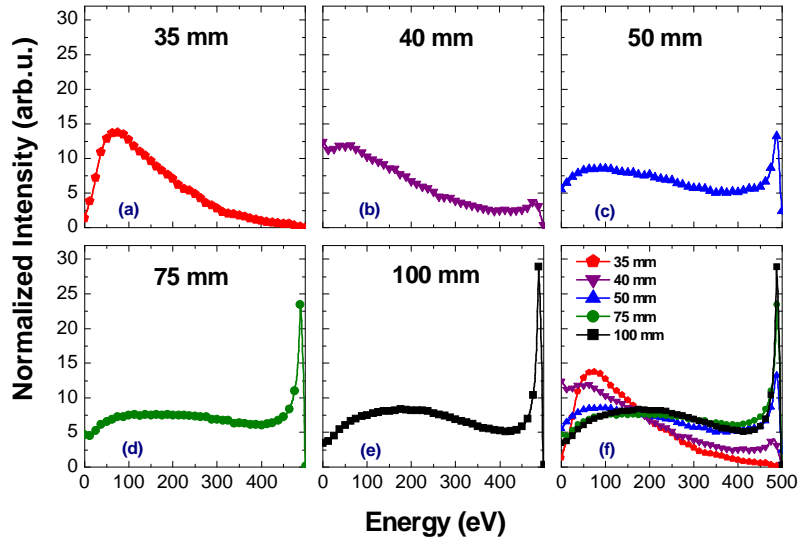


Figure 173: BF_2^+ IEDs normalized to the total flux of the boron ions for a 500 V, 30 mTorr, $50 \mu\text{s}$ BF_3 HC plasma (HC voltage of 1400 V) with different anode-to-cathode spacings equal to (a) 35mm, (b) 40 mm, (c) 50 mm, (d) 75 mm, (e) 100 mm. Also included in f is a summary of the BF_2^+ IED for different anode-to-cathode gaps

Under all these different conditions, the BF_2^+ ion is the dominant ion, constituting more than 50 % of the total boron ion flux, as can be observed on Fig. 174. As the sheath thickness increases when the anode-to-cathode gap is reduced, the ion fractions of B^+ and BF^+ , which are mostly created inside the sheath through the dissociation of heavier ions, also rise.

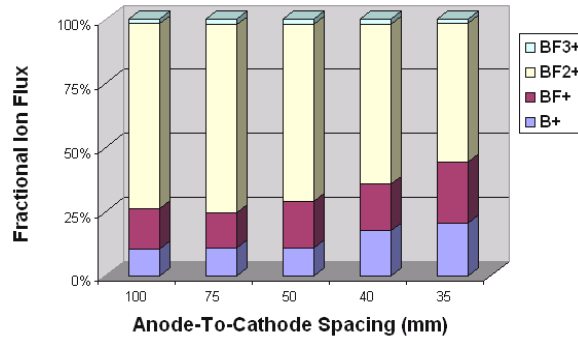


Figure 174: Boron ion and molecular fraction in a 500 V, 30 mTorr BF_3 HC glow discharge with anode-to-cathode spacings ranging from 3.5 to 10 cm at a constant hollow cathode bias (- 1400 V)

As discussed previously, the BF_3^+ ion fraction is always below 1 % of the total boron ion flux. Even if the B_2F_3^+ and B_2F_5^+ fractions inside the bulk plasma represent a significant fraction of the total boron ion flux, they do not “survive” inside the sheath when the collision probability is high. As there are still some collisions inside the sheath even once it reaches 10cm, the fractions B_2F_3^+ and B_2F_5^+ are always below 0.05 %, so they will be neglected in this discussion.

The B^+ , BF^+ and BF_3^+ ion energy distributions for a 500 V, 30 mTorr BF_3 plasma with five different anode-to-cathode spacings are presented in Fig. 175. When the plasma density is increased, the fraction of ions colliding inside the sheath decreases, and less low-energy B^+ and BF^+ ions are observed. At the same time, the abundance of energetic B^+ and BF^+ ions increase. As can be seen in Fig. 175, the maximum of the BF^+ IED peak shifts to a higher energy when the anode-to-cathode gap is increased.

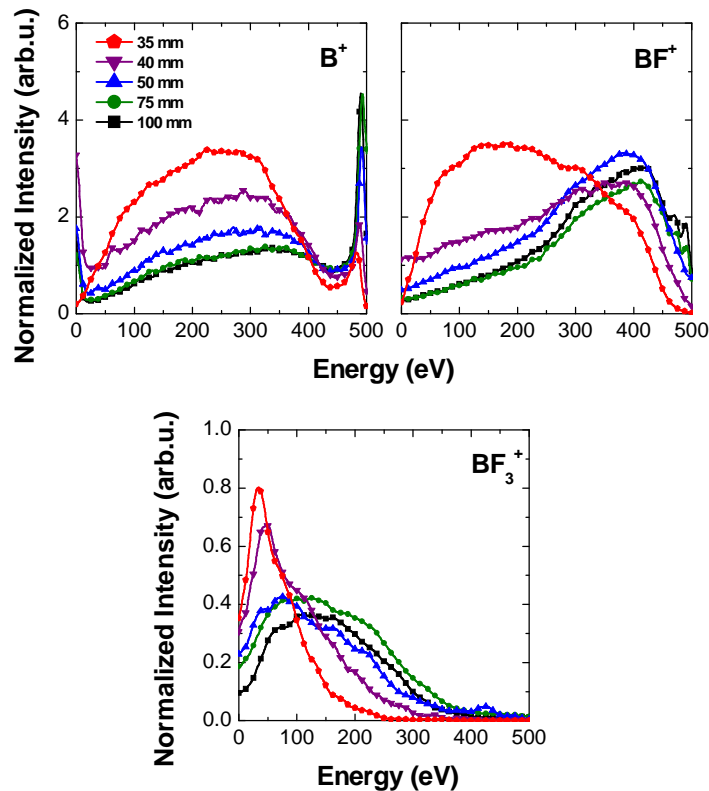


Figure 175: B^+ , BF^+ and BF_3^+ IEDs normalized to the total ion flux for a 500 V, 30 mTorr, 2500 Hz, 50 μs BF_3 plasma with different anode-to-cathode spacings

Due to the reduction in the number of collisions inside the sheath, BF_3^+ becomes more energetic, but its maximum of intensity still remains below 150eV. As the neutral molecule BF_3 dominates the gas phase, the probability of a charge exchange inside the sheath through a symmetric charge transfer between BF_3^+ and its parent molecule, BF_3 , is high. A symmetric charge exchange is a dominant collision process for BF_3^+ ions, and only a few BF_3^+ ions reach the cathode with the full acceleration energy. For an anode-to-cathode gap above 7.5 cm, only minor changes occur on the IED.

Fig. 176a shows the evolution of the B^+ , BF^+ , BF_2^+ and BF_3^+ mean energies experimentally calculated as a function of the anode-to-cathode spacing under the same plasma conditions as those presented previously. As expected, with the number of collisions and the shape of the IED, the mean energies of all the boron ions increase with a larger anode-to-cathode spacing, due to the reduction in the number of collisions inside the high-voltage sheath. The evolution in the fraction of ions that reach the wafer with a full acceleration, as a function of the anode-to-cathode spacing is presented in Fig. 176b. The fraction of energetic ions is calculated here by integrating a Gaussian curve under the energetic peak of the distribution.

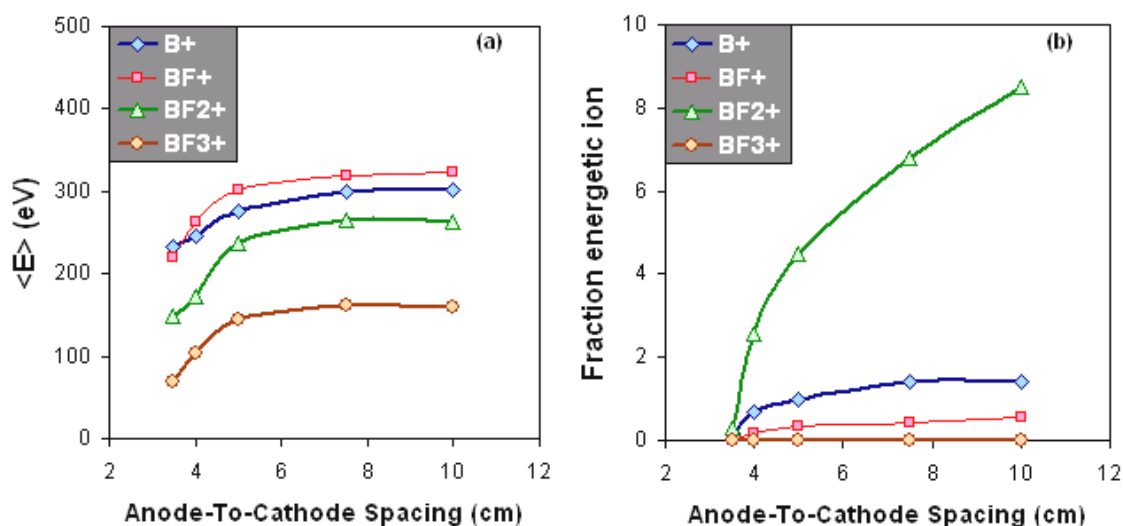


Figure 176:(a) Experimentally calculated B^+ , BF^+ , BF_2^+ and BF_3^+ ion mean energies, based on the ion energy distributions, as a function of the anode-to-cathode spacings; (b) B^+ , BF^+ , BF_2^+ and BF_3^+ ion fractions of with the full high-voltage acceleration under the previously detailed conditions

The fraction of B^+ ions reaching the cathode with a full high-voltage acceleration increases from 0.2 to 1.4 % and is constant from 7.5 to 10 cm. The maximum fraction,

1.4% percent is close to the B^+ fraction in the bulk plasma. It seems to indicate that the collision-less sheath regime is achieved for the B^+ ions in the case of a gap larger than 7.5 cm, and all the B^+ ions present in the bulk reach the cathode with full energy acceleration. Even if the collision-free regime is reached for bulk B^+ ions in the case of a large gap, the mean energy of B^+ remains constant around 300eV because of its bimodal distribution. The second peak of the ion energy distribution is mainly due to the dissociation of heavier ions inside the sheath.

The fraction of BF^+ energetic ions slightly increases from 0 to 0.56 % of the total flux of boron ions, but the fraction is not stabilized. In the case of BF_2^+ ions, the fraction of energetic ions increases quickly from 0 to 8.5 %, but never reaches a plateau. No BF_3^+ energetic ions can be detected. It appears that the collision-free regime inside the sheath is never reached for BF^+ , BF_2^+ and BF_3^+ , even if the number of collisions is reduced.

As the shapes of the ion energy distributions are very different between the 3.5 and 10 cm gaps (more energetic ions, reduced fraction of B^+ and BF^+), the dopant profile should show significant differences. The boron equivalent energy distribution, based on the IEDs for a 3.5 cm gap, is compared to that of a 10 cm gap in Fig. 177. Significant differences can be observed between the two cases. In the 10 cm case, three peaks are observed on the boron equivalent energy distribution. Each peak is due to the contribution of the B^+ (high energy peak), BF^+ (intermediate energy peak) and BF_2^+ energetic ions (low energy peak).

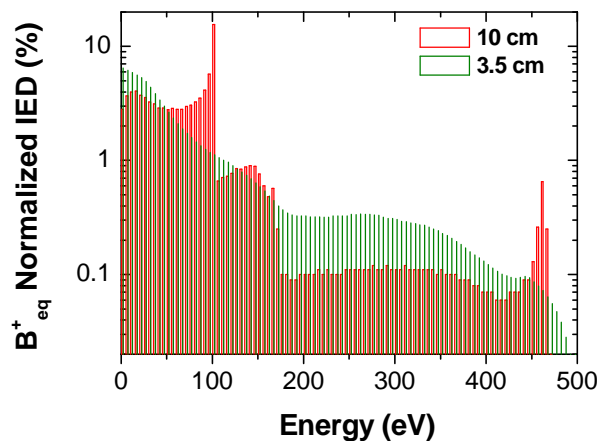


Figure 177: Boron equivalent normalized IED, based on the 500V 30mTorr IEDs of the ions reaching the wafer for 3.5 cm and 10 cm anode-to-cathode spacings

Based on the boron equivalent energy distribution, less boron ion dopant should be implanted near the target surface in the 10 cm case, and more BF_2^+ dopant ions should be implanted around 14 Angstroms, which corresponds to the projected range of B^+ ion implanted at 120 eV (see Fig.9.a).

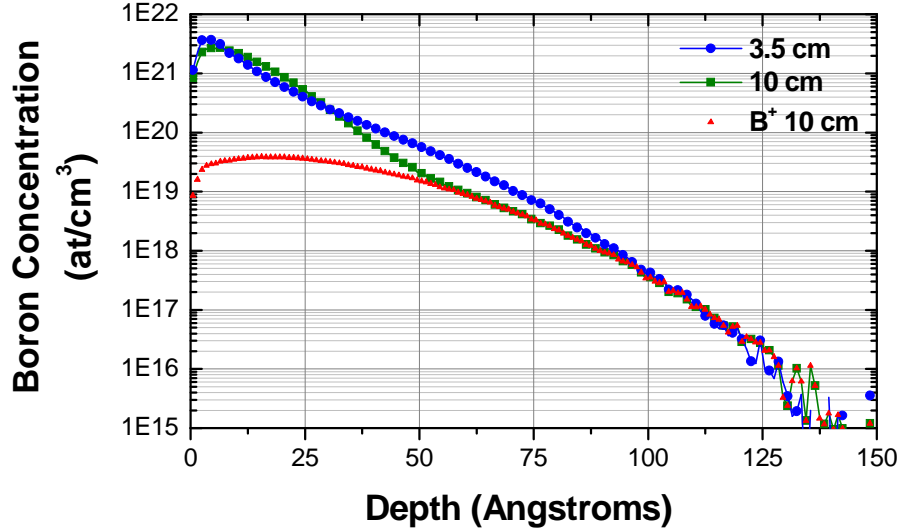


Figure 178: Boron predicted depth profile, normalized to 10^{15} dose, based on the measured IED for different anode-to-cathode spacings (500V 30 mTorr BF_3 PLAD)

Fig 178 shows the predicted boron profile for different anode-to-cathode spacings in the case of a 500 V, 30 mTorr PLAD implant. A good match between the SIMS and the predicted boron profile for the 3.5 and 10 cm anode-to-cathode gaps was obtained, as detailed in the previous section {V.2.3.3}. More dopant near the surface can be observed in the case of a small gap due to the low-energy tails of the different ion energy distributions. In the case of a large gap, more dopant is implanted around 14 Angstroms, due to the higher fraction of energetic BF_2^+ ions. Even if the whole B^+ ion fraction from the total ion flux is reduced when the large anode-to-cathode gap is used, the energetic fraction of B^+ is still present and define the junction depth (see Fig. 178). The dopant depth profile is only slightly shallower than in the case of a small gap

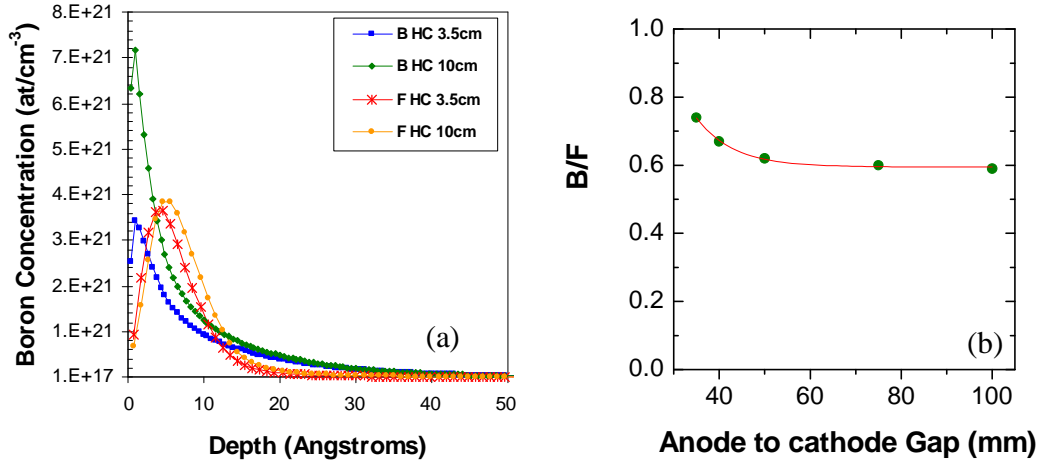


Figure 179: (a) Measured boron SIMS profile for a 500 V, 30 mTorr, 1×10^{15} ions/cm³ BF₃ PLAD implant with 3.5 and 10 cm anode-to-cathode spacings, (b) Boron over fluorine ratio, based on the IEDs at different anode-to-cathode spacings

When a larger gap is used, a higher plasma density is obtained, which implies a faster implantation time. For example, a 10^{15} cm⁻² nominal dose in the 3.5 cm case requires 60 seconds, while it requires 20 seconds in the 10 cm case. The retained dose (boron dose that is retained into the silicon after implantation) is also more important in the case of a larger gap, due to the higher fraction of BF₂⁺ energetic ions. The measured SIMS profile (see Fig. 179a) also shows a higher retained dose in the case of the 10cm gap ($7.6 \cdot 10^{14}$ of retained dose), as compared to the 3.5cm case ($2.9 \cdot 10^{14}$ cm⁻² of retained dose), for the same nominal dose of 10^{15} cm⁻² measured by the dosimetry system. A higher fluorine concentration is obtained in the larger gap cases (see Fig. 179b) due to the higher fraction of BF₂⁺ ions implanted onto the wafer. After the implantation of different doses, ranging from 2.5×10^{14} to 2×10^{15} ions / cm², and the dopant activation (1050 °C, 10 s, 100 ppm O₂), R_s measurements and boron SIMS profiles were performed on each sample.

The sheet resistance as a function of the junction depth at a level of 3×10^{18} boron atoms per cubic centimeter is plotted in Fig. 180. In the case of the 10 cm gap, lower R_s values can be obtained, with a deeper junction depth, despite the fact that the dopant depth profile was shallower before the dopant activation. Also shown on this plot are the theoretical R_s values for different X_j and boron solid solubility limits assuming a “box

profile” and a constant activation temperature. The results in both cases (large and small anode-to-cathode gap) are almost on the same curve, thus no real improvement in the ratio of R_s/X_j could be observed but the change in the anode-to-cathode gap allows for a larger operating window in the case of junction engineering.

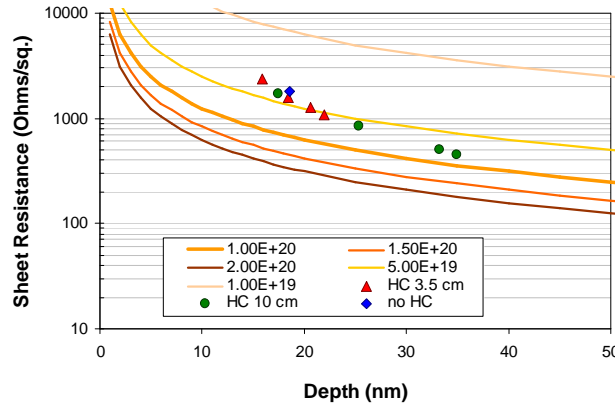


Figure 180: R_s as a function of X_j for a 500 V, 30 mTorr HC plasma implantation with different anode-to-cathode spacings, and calculated R_s based on different solid solubility levels in the silicon (a reference point at 500V, 100 mTorr without the HC is also included)

Fig. 181 shows the calculation of the dopant activation efficiency for different doses at 10 cm and 3.5cm anode-to-cathode spacings. For all the different doses from 2.5×10^{14} to 2×10^{15} boron atoms per cubic centimeter, the activation efficiency for the 10 cm gap is higher than the one for the 3.5 cm gap. The higher fluorine ratio seems to improve the dopant activation for the same initial thermal budget (i.e. time \times activation temperature). This results in a deeper junction depth than in the case of a small gap, even if the dopant profiles have almost identical depth (but different doses) before activation. Higher fluorine concentrations seem to enhance the boron activation.

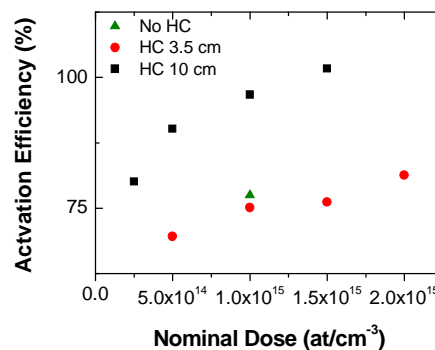


Figure 181: Activation efficiency for different anode-to-cathode gaps (3.5 and 10 cm) and different nominal doses, as measured with the PLAD dosimetry system (a reference point at 500V, 100 mTorr without the HC is also included)

In the case of diode configuration (green triangle), the activation efficiency of a $1 \times 10^{15} \text{ ions/cm}^3$, 500 V, 100 mTorr BF_3 glow discharge follows the same trend as in the case of the hollow cathode with a small gap. The B/F ratio is thus similar to the 3.5 hollow cathode case.

In conclusion, the use of a hollow cathode provides the possibility of operating the discharge at lower pressures, even at low-cathode voltages (lower than 500 V). The moveable anode acts as a supplementary “knob” to control the plasma density and the number of collisions inside the sheath. It is thus possible to control the shape of the ion energy distribution by changing the number of collisions inside the sheath. By reducing the number of collisions through a larger anode-to-cathode spacing, the fractions of B^+ and BF^+ ions implanted can be decreased. The larger gap provides many advantages compared to the 3.5 cm gap. With the 10 cm gap, the throughput is higher (higher plasma density), the dopant depth is shallower for the same boron dose implanted (less B^+ and BF^+), the retained dose is higher (more BF_2^+ energetic ions) and the dopant activation is better than in the case of a smaller gap. After activation of the dopant, no improvement in the R_s/X_j ratio could be observed between the 10 cm and the 3.5 cm case, but the change in the anode-to-cathode gap leads to a larger operating window for junction engineering.

b) Hollow cathode voltage

It has been demonstrated in the case of the hollow cathode mode that the anode-to-cathode spacing can be used to reduce the number of collisions inside the sheath. Unfortunately, fractions of B^+ and BF^+ , which are created through the dissociation of heavier ions, still remain too high to obtain very shallow junctions, as the collision-less regime of the heavier ions is not reached. Another approach consists of using a large anode-to-cathode spacing with a higher hollow cathode voltage, while keeping a constant cathode bias voltage. Higher plasma density can thus be reached. As expected, when the hollow cathode bias is increased during a constant cathode bias (500 V) at 20 mTorr, the plasma density increases and the ion current density rises linearly (see Fig. 182a).

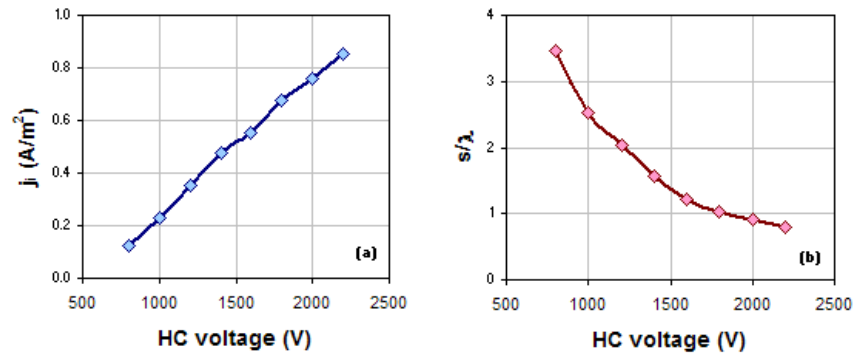


Figure 182: (a) Ion current density as a function of the hollow cathode voltage under a constant cathode voltage (500 V) and an anode-to-cathode spacing of 5 cm at 20 mTorr, (b) Calculated number of collisions, based on equation {IV.2.5}, under the same plasma conditions

The number of collisions inside the sheath is thus reduced when a higher plasma density is obtained for a higher hollow-cathode voltage (see Fig. 182b). The B^+ , BF^+ , BF_2^+ and BF_3^+ ion energy distributions for various hollow cathode voltages (800 to 2200 V) under a constant cathode bias voltage of 500 V in a BF_3 plasma at 20 mTorr are shown in Fig. 183.

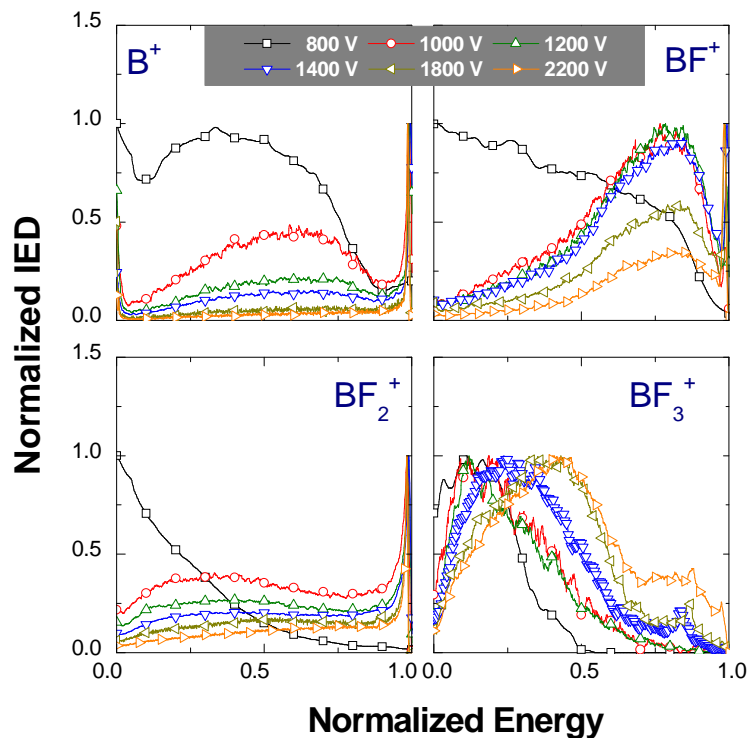


Figure 183: B^+ , BF^+ , BF_2^+ and BF_3^+ IEDs normalized to their maximum intensity of each ion, as a function of the energy normalized to the cathode voltage maintained at 500 V 20 mTorr for different hollow cathode voltages (800, 1000, 1200, 1400, 1800 and 2200 V)

As expected, the mean energy of the different ions increases when the plasma density rises with the hollow cathode voltage. The ion energy distributions are less and less affected by collisions inside the sheath. At 2200 V on the hollow cathode, only the energetic fraction of B^+ is present. This means that the sheath is collision-less for the B^+ population, and only B^+ ions present in the bulk plasma are implanted into the target. The dissociation of heavy ions into B^+ stops once the hollow-cathode voltage is above 2000 V. The BF_2^+ ions appear to follow the same trend as B^+ inside the sheath, and almost reach the collision-less sheath regime. In the case of BF^+ , the number of collisions also decreases, but the BF^+ ion fraction created through the dissociation of heavier ions still remains present, even at 2200 V. This appears to indicate that BF^+ ions are created through a different reaction channel than for B^+ ions. The regime of a collision-less sheath is not reached for the heavy ions that create BF^+ . It should also be noted that the fractions of heavy ions such as $B_2F_3^+$ and $B_2F_5^+$ is always lower than 2%. These ions may be dissociated to create BF^+ ions. The mean energy of all the different boron ions increases for higher hollow-cathode voltages.

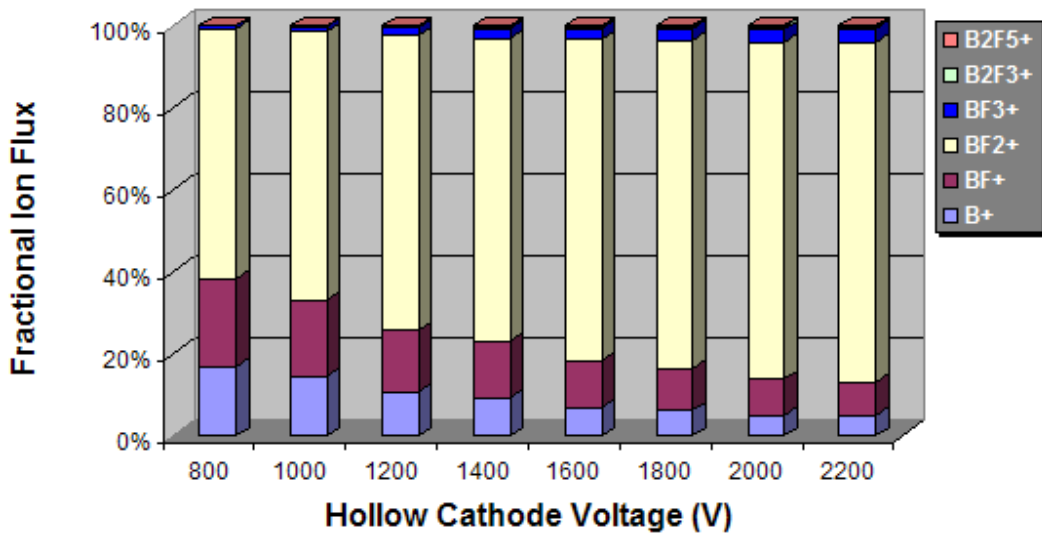


Figure 184: Boron ion fractions, based of the boron ion fluxes normalized to the total flux of boron ions for different hollow cathode voltages (800, 1000, 1200, 1400, 1800 and 2200 V) measured during the pulse-on period in a 20 mTorr, 500 V BF_3 glow discharge with a 50 μs pulse width

The boron ion fractions under the same discharge conditions detailed previously are presented in Fig. 184. As expected, the fractions of B^+ and BF^+ decrease when the number of collisions is reduced. When the hollow-cathode voltage rises above 1600 V, the fraction of B^+ ions with full energy (500 eV) is increased up to almost 5% of the total flux of boron ions. It was demonstrated by Koo and al that higher cathode voltages lead to higher B^+ fractions created in the bulk plasma [Koo 2004]. Similar observations can thus be made with the hollow cathode bias. The increased of fraction B^+ energetic ions will impact the deeper parts of the dopant profile. Even if the fraction of B^+ ions is reduced to 5 % of the total flux of boron ions implanted, the junction depth may not be shallower. A significant 8% fraction of BF^+ can still be detected in the 2200 V hollow-cathode voltage case.

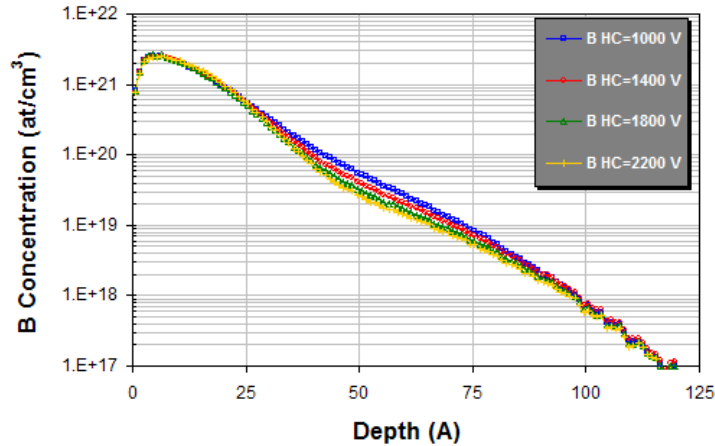


Figure 185: Boron predicted depth profile for different hollow cathode voltages, during a 500 V, 20 mTorr PLAD implantation

Fig. 185 shows the boron predicted depth profiles for different hollow cathode voltages (1000, 1400, 1800 and 2200 V) during a 500 V, 20 mTorr BF_3 glow discharge. As the fraction of B^+ energetic ions increases and the hollow cathode bias rises, while the B^+ fraction still remains superior to 5 %, no improvement in the junction depth can be observed.

In conclusion, by changing the hollow-cathode voltage, the fractions of B^+ and BF^+ ions can be reduced, but the fraction of energetic light ions significantly increase, therefore no improvement could be observed in the dopant depth profile. Another approach will now be presented in the next section.

Pulsed anode configuration

The use of a pulsed anode, in addition to the pulsed cathode, allows for the discharge to be operated at lower pressures and lower cathode biases. The pulsed anode is used to create and maintain the plasma (same role as the hollow cathode). The anode-to-cathode spacing is maintained at 4.5 cm during all the experiments. The electrons are now confined in the small gap between the two negatively pulsed electrodes. This provides higher ionization efficiency and thus a higher plasma density for the same pressure as in the hollow cathode case. The hollow cathode is used as the ground reference for the plasma. The electrons thus diffuse from the center of the discharge to the side of the chamber, where the hollow cathode is positioned. The discharge could be operated at pressures as low as 12 mTorr under this configuration.

Fig. 186a shows the cathode current for different pulsed anode voltages, from 400 V to 1200 V, during a 500V BF_3 discharge operated at 30 mTorr. The cathode current increases when the discharge is operated at higher anode voltages.

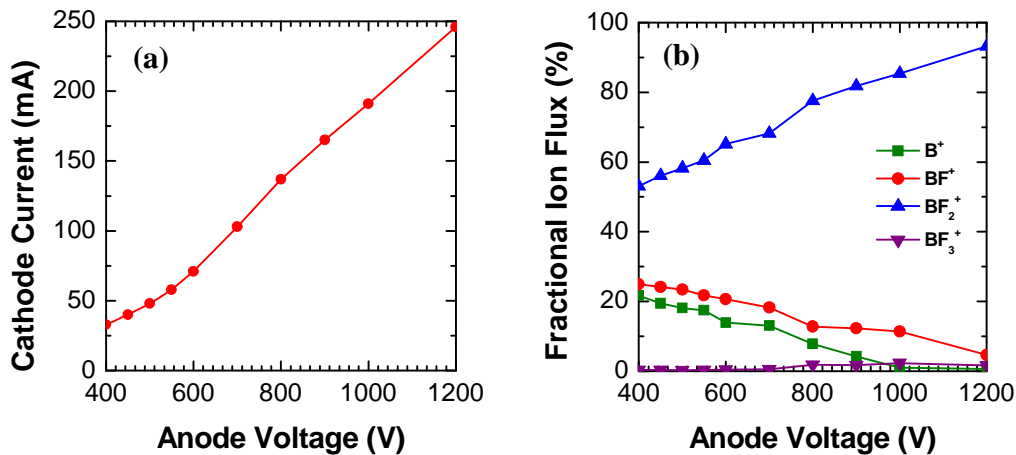


Figure 186: (a) Cathode current for different pulsed anode voltages with a 500 V, 30 mTorr, 50 μs , BF_3 plasma, (b) Ion ratios under the same plasma conditions for different pulsed anode voltages, ranging from 400 V to 1200 V

In agreement with the discussion in Chapter IV, when the discharge is operated at higher plasma densities under the same process pressure, the ion mean free path is

maintained constant and the sheath thickness decreases. The number of collisions is thus reduced and the fractions of B^+ and BF^+ decreases. Fig. 186b shows the evolution of the fractions of different boron ions under different anode voltages. The B^+ and BF^+ fractions slowly decrease for higher plasma densities. For a cathode bias above 1000 V, the fraction of B^+ falls below 1% of the total flux of boron ions. The fraction of BF^+ also decreases below 5% of the total flux of boron ions.

The B^+ , BF^+ , BF_2^+ and BF_3^+ ion energy distributions under different anode voltages for a constant pressure (30 mTorr) and a constant cathode voltage (500V) are presented in Fig. 187.

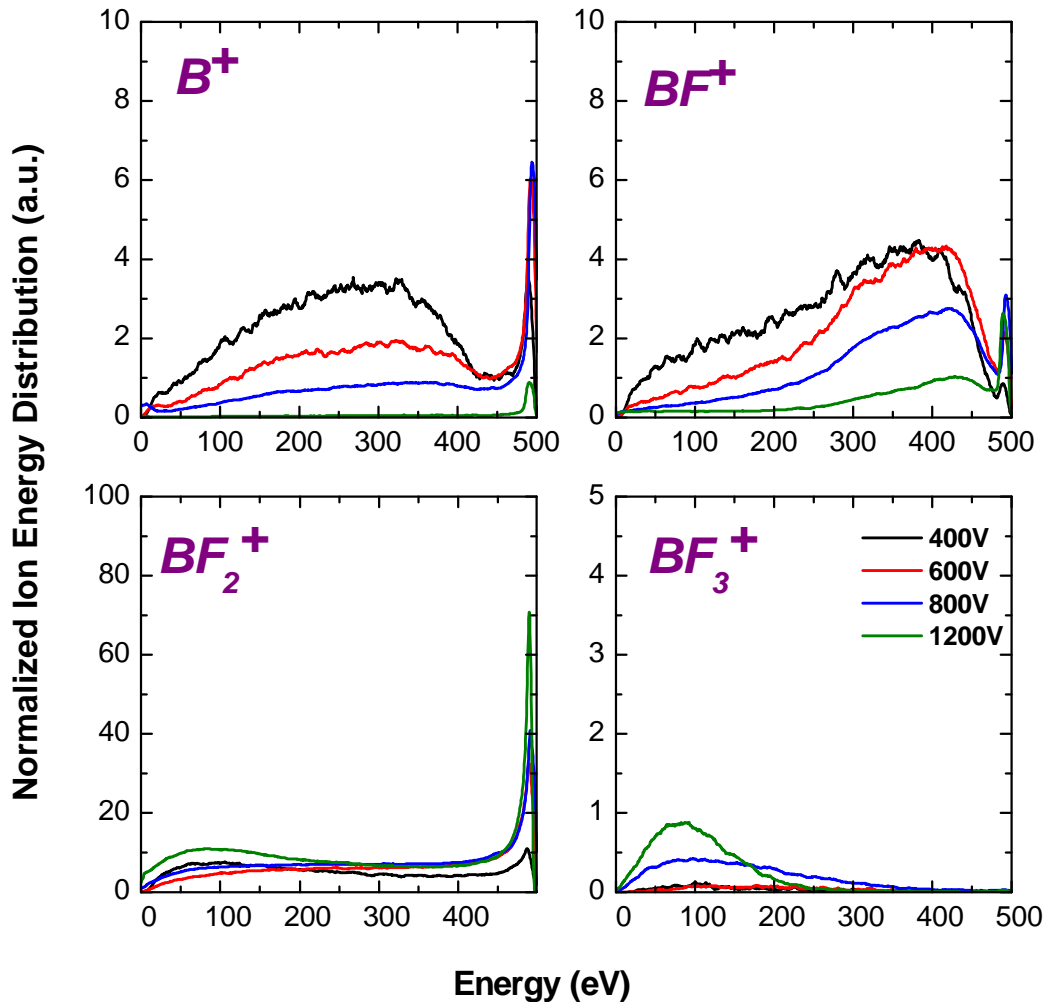


Figure 187: Boron ions, normalized to the total ion flux, reaching the cathode for a 500 V, 30 mTorr, $50\mu s$ BF_3 plasma under different pulsed anode voltages

In regard to the shape of the ion energy distributions, similar observations to the one in the previous section can be made. When the anode voltage is pulsed at 1200 V, the collision-less sheath regime is reached and the dissociation of heavier ions into B^+ ceases inside the sheath. The fraction of B^+ is then roughly equal to the measured B^+ fraction in the bulk plasma. The fraction of BF^+ decreases significantly under higher anode bias voltages, but the dissociation of heavier ions into BF^+ is still occurring inside the sheath. As the fraction of lighter ions is significantly decreases, the dopant depth profile is expected to be shallower in the case of the higher anode voltage.

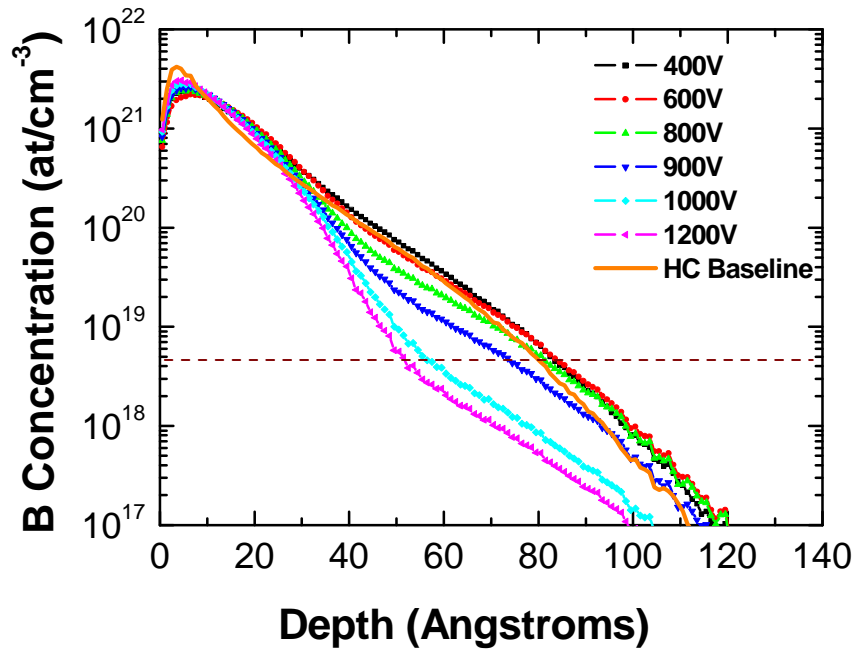


Figure 188: Boron predicted depth profile, normalized to a 5.10^{14} dose, based on the measured IEDs for different pulsed anode voltages (500V, 30 mTorr BF_3 PLAD)

The boron predicted profile under the previous discharge conditions is presented in Fig. 188. As predicted, a higher anode voltage leads to a higher plasma density, and the dopant depth profile at 3×10^{18} boron atoms per cubic centimeter significantly decreases and is up to 3 nanometers shallower than in the baseline case (with a hollow cathode plasma). The decrease of the B^+ fraction when the anode bias increases can clearly be seen in Fig. 189. The objective of this section is thus reached when the pulse anode is used with a low pressure. With an appropriate dopant activation (flash anneal for

example), shallower junctions can be achieved in the case of the pulsed anode configuration.

Optimum conditions and conclusions

To summarize, in this section, it has been demonstrated that through a good understanding of the BF_3 plasma, and in particular of the collision processes inside the sheath, shallower junctions can be reached. The approach using a collision-less sheath seems to be the best one. It is necessary to use an external plasma source, such as a hollow cathode or a pulsed anode, to be able to reach a collision-less sheath and to significantly reduce the fraction of B^+ and BF^+ inside the high-voltage sheath.

Using a high-density plasma created with a RF plasma source (pulsed or not pulsed) decoupled from the cathode bias voltage, tuning the plasma parameters (duty cycle, pressure, gas flow...) to enhance the BF_2^+ fraction and avoiding collisions inside the sheath, appear to be the optimum conditions to obtain the shallowest junction depth by using plasma implantation with BF_3 chemistry.

Chapter VI Conclusion

A brief review of the doping requirement for the next device node generation as well as the traditional beam line implantation technology was presented in Chapter I. In order to reach the new doping requirements for the source drain extension, the ion implantation energy needs to be further reduced with a higher dopant concentration. New doping technique such as plasma-based ion implantation is emerging for the future device nodes. In particular, pulsed PLAsma Doping (PLAD) offers the capability of operating at very low energies for a lower cost and at a higher ion flux than with the traditional beamline ion implantation. With the PLAD technique, the silicon wafer is directly immersed in the plasma. The ions present in the bulk plasma are extracted through the high voltage applied on the cathode and are implanted into the wafer with the desired energy. The principle of plasma doping as well as its advantages and performances were presented in Chapter II.

In traditional beamline implantation, the incident ion mass and energy are well-known parameters, and simulation programs are available to predict the implant profiles. In plasma-based ion implantation, all ionized species present in the plasma are extracted and implanted by applying negative voltage pulses to the wafer. Therefore, the prediction of implant profiles is more complicated since it requires the knowledge of each ion relative abundances, as well as their energy distributions, prior to entering the wafer surface. The plasma composition was studied by mass spectrometry measurements and the plasma parameters such as electron density or plasma potential were measured by Langmuir probe. The characterization of pulsed plasmas has lead to the modification of the existing system and has required the development of time-resolved measurements. A mass and energy spectrometer was installed inside the high-voltage electrode to measure the energy distribution of the different dopant ions reaching the silicon wafer after their acceleration inside the high-voltage sheath in BF_3 plasma (boron trifluoride). A 3D electrostatic model of the mass spectrometer was developed in order to optimize the ion transmission inside the mass spectrometer and has lead to modification of the mass spectrometer voltage set-up.

The identification and the quantification of the various plasma charged species, as well as the ion energy distribution measurements, were presented in Chapter IV. The different elastic and inelastic collisions for the BF_3 electron cross-section processes were briefly reviewed. Electron-impact ionization measurements for BF_3 have shown that BF_2^+ is the dominant ion created by this reaction channel. Its relative abundance intensity is two decades higher than that for B^+ , F^+ , BF^+ and BF_3^+ . The time evolution of the electron temperature and plasma density was also presented. Two different electron populations were measured: the low-energy electrons that make up the majority of the electrons and the fast electrons that represent less than 1 % of the electrons and are present only during the pulse-on period. The electron density increases during the pulse-on and decreases slowly during the afterglow period. As expected, higher electron density is measured when the hollow cathode is used. The characterization of the BF_3 plasma, including the ion kinetics, the description of different collision processes occurring inside the high-voltage sheath and a detail description of the energy distributions of ions reaching the cathode, was also presented in Chapter IV. It was demonstrated that s/λ is a key parameter that is governing the shape of the ion energy distribution measured in the high-voltage sheath. Under all the various plasma conditions, the BF_2^+ ion was measured as the dominant ion of the BF_3 discharge. The fraction of BF_2^+ is reduced after crossing the high-voltage sheath. The presence of a symmetric charge exchange for BF_2^+ and BF_3^+ was also demonstrated in the case of a collisional sheath. Heavy molecular ions, such as B_2F_3^+ and B_2F_5^+ were detected by mass spectrometry during the pulse-on period. These ions are probably created by a three-body recombination. It was demonstrated that B^+ and BF^+ are created inside the sheath. The main reaction channels that create B^+ , BF^+ inside the sheath were identified. The heavy molecular ions are dissociated inside the sheath by colliding with neutral particles of the gas phase into lighter ions. It was observed that the B^+ and BF^+ fractions are strongly dependant on the number of collisions inside the sheath and can be reduced by minimizing the number of collisions during the high-voltage acceleration. The control of light ions, such as B^+ and BF^+ , is vital to obtain shallower junctions during ion implantation.

The understanding, control and optimization of the process were introduced in Chapter V. The PLAD conditioning step is described in details and optimized. The

conditioning study and the plasma uniformity study have lead to a modification of the PLAD hardware material. A model, based on ion energy distribution measurements was developed to predict the dopant depth profile. The prediction results are in good agreements with the SIMS measurements. According to this depth profile prediction and to ion energy distribution measurements of chapter IV, we discussed and found in chapter V optimized experimental conditions to obtain shallower junctions.

This thesis research provides a better understanding of the key parameters that control the nature, the concentration and the depth distribution of the implanted species. With a better understanding of the collision processes that occur inside the high-voltage sheath, the doping process can be optimized. Based on the ion energy distributions measured with the mass spectrometer, the dopant depth profile can be predicted and the plasma parameters can be tuned in order to obtain shallower dopant depth distribution in the silicon after plasma doping implantation.

Reference

- [Anders 2000] “Handbook of plasma immersion ion implantation and deposition”, edited by A. Anders, Wiley Interscience, **2000**
- [Aston 1919] “A positive ray spectrograph” F. W. Aston, Philos. Mag., **38**, 707, **1919**
- [Arevalo] unpublished data
- [Armigliato 1977] A. Armigliato, D. Nobili, P. Ostoja, M. Servidori, S. Solmi, The Electrochem. Soc., Pro. Series P. V. 77-2, p. 638-647, USA, **1977**
- [Batten 1978] C. F. Batten, J. A. Taylor, B. P. Tsai, and G.g. Meisels, J. Chem. Phys. **69**, p2547, **1978**
- [Bayha 2002] “Dependence of junction depth and sheet resistance on the thermal budget in low temperature pre-stabilization regime”, B. Bayha, S. Paul, W. Lerch, D. F. Downey, E. A. Arevalo, X. Hebras, N. Cherkashin, Proc. Of 14th Conf. on Ion Implantation Technology, Taos, Sept 2002
- [Budtz-Jorgensen01] “Studies of electrical plasma discharges” Casper V. Budtz-Jorgensen, Thesis report, www.ifa.au.dk/~budtz, **2001**
- [Buyuklimanli 2006] “Near-surface SIMS analysis of plasma-based ion implant in Si”, USJ conference 2005 proceedings, to be published in JVST **2006**

-
-
- [Cecchi 1990] “Handbook of plasma processing Technology”, J. L. Cecchi, eds. S. M. Rossnagel, J.J. Cuomo, and W. D. Westwood, p14. Park Ridge, NJ: Noyes Publications, 1990.
- [Chapman 1980] “Glow Discharge Process, sputtering and plasma etching”, B. Chapman, Wiley Inter-science publication, **1980**
- [Cheung 1991] “Plasma Immersion Ion Implantation for ULSI Processing” Nucl. Instr. Meth. Vol. B55, p. 811-820, **1991**
- [Chevolleau 1998] T. Chevolleau, Thesis manuscript, University Nantes, **1998**, France
- [Child 1911] C. D. Child, Phys. Rev. **32**, 492, **1911**
- [Christophorou 1984] “Electron-molecule interactions and their applications”, L. G. Christophorou, D. L. McCorkle, and A.A. Christodoulides, L. G. Christophorou (ed), Academic, New York, Vol 1, **1984**
- [Christophorou 2004] “Fundamental electron interactions with plasma processing gases”, L. G. Christophorou, J. K. Olthoff, Physics of atoms and molecules, Kluwer Academic/Plenum Publishers, New York, **2004**
- [Chu 1999] “Plasma Doping: Progress and Potential”, P. K. Chu, S. B. Felch, P. Kellerman, F. Sinclair, L. A. Larson, B. Mizuno, Solid State Technology Millennium Series: Implantation, p 55 Sep 1999
- [Conrad 1987a] “Plasma source ion-implantation technique for surface modifications of materials” J. R. Conrad, J. L. Radtke, R. A. Dodd, F. J. Worzala, N. C. Tran, JAP, Vol. **62**, p 4591, **1987**

-
-
- [Conrad 1987b] “Sheath thickness and potential profiles of ion-matrix sheaths for cylindrical and spherical electrodes”, J. R. Conrad, JAP, Vol. **62**, p777, **1987**
- [Conrad 2000] Introduction to the “Handbook of plasma immersion ion implantation and deposition”, J. R. Conrad, ed. A. Anders, Wiley, New York, **2000**
- [Davis 1963] “Ion energies at the cathode of a Glow Discharge”, W. D. Davis and T. A. Vanderslice, Physical Review, Vol. **131**, Number 1, **1963**
- [Dawson 1995] “Quadrupole Mass spectrometry and its applications” P. H. Dawson, Elsevier, **1995**
- [Dieble 1968] V. H. Diebler and S. K. Liston, Inorg. Chem.. **7**, p1742, **1968**
- [Drawin 1968] “Mass spectrometry of plasmas”, H. W. Drawin, edition W. Lochte-Holtgreven, p.777, **1968**
- [Downey 2003] “Optimization of fluorine for increased activation and reduced diffusion to satisfy 65, 45 and 32nm nodes: the role of Ge, optical illumination, and low O₂ ppm content in the anneal ambient”, D. F. Downey, E. A. Arevalo, ECS 2003 proceeding
- [Dumont 2005] “ Plasma doping for S/D Extensions: Device integration, gate oxide reliability and dynamic behavior”, B. Dumont, A. Pouydebasque, F. Lallement, D. Lenoble, G. Ribes, J. M. Roux, S. Vanbergue, T. Skotnicki, Proceeding of ESSERDERC 2005, IEEE, p113-116, **2005**

-
-
- [Evans East] Evans Analytical group: specialist in material characterization, <http://www.eaglabs.com>
- [Fang 2005] “Plasma doping: production worthy solution for 65nm and beyond technology nodes”, Z. Fang, E. Arevalo, T. Miller, H. Persing, E. Windet, V. Singh, IWJT proceeding, IEEE CNF, p 71-74, June **2005**
- [Farber 1984] “Electron and thermal dissociation of $\text{BF}_3(\text{g})$ ”, M. Farber, R. D. Srivastava, J. Chem. Phys. **81**, p 241-244, **1984**
- [Felch 1992] “Characterization of a plasma doping system”, S. B. Felch, T. Sheng and C. B. Cooper III, 9th Conference on Ion Implantation Technology, Gainesvill, FL, September 20-24 1992
- [Felch 1998] “Characterization of ultra-shallow p+/n junctions formed by plasma doping with BF_3 and N_2 plasmas, S. B Felch, B. S. Lee, S. L. Daryanani, D. F. Downey, R.J. Matyi, Materials Chemistry and Physics, **54**, p37-43, **1998**
- [Felch 1999] “Characterization of shallow junction transistors manufactured with plasma doping”, S. B. Felch, G. Bersuker, L.A. Larson, B. S. lee and J. Shi, IEEE, p1246, **1999**
- [Gaboriau 2006] “Etching mechanisms of Si and SiO_2 in fluorocarbon ICP plasmas: analysis of plasma by mass spectrometry, Langmuir probe and optical emission spectroscopy”, F. Gaboriau, G. Cartry, M-C. Peignon, C. Cardinaud, J. Phys. D: Appl. Phys. **39**, p1830-1845, **2006**

-
-
- [Godet 2006] “Plasma doping implant depth profile calculation based on ion energy distribution measurements”, L. Godet, Z. Fang, S. Radovanov, S. Walther, E. Arevalo, F. Lallement, J. T. Scheuer, T. Miller, D. Lenoble, G. Cartry, C. Cardinaud, Submitted to JVST, 2006
- [Goeckner 1999] “Plasma doping for shallow junctions”, M. J. Goeckner, S. B. Felch, Z. Fang, D. Lenoble, J. Galvier, A. Grouillet, G. C-F. Yeap, D. Bang, M.-R. Lin, JVST B17, p2290, **1999**
- [Ha 1998] “High performance pMOSFET with BF₃ plasma doped Gate/Source/Drain and S/D Extension, J. M. Ha and al, IEDM 98, IEEE, p639-642, **1998**
- [HCP 1981] “Handbook of chemistry and physics, 62nd edition, **1981-1982**, CRC press
- [Hershkowitz 1989] “How Langmuir probe works” N. Hershkowitz, p113-183, **Chap.3** in Plasma Diagnostics (Eds. O. Auciello and D. L. Flamm) Academic Press, **1989**
- [Kae-nune 1995] P. Kae-nune, Thesis manuscript, University Paris 6, **1995**, France
- [Herzog 1934a] R. Herzog, J.H.E. Mattauch, Annalen der Physik, Leipzig **19**, 345, **1934**
- [Herzog 1934b] R. Herzog, Zeitschrift fur Physik, **89**, 447, **1934**
- [Hiden] “EQP analyzer operator’s manual” Hiden Analytical, <http://www.hidenanalytical.com>

-
-
- [Hippler 2001] “Low temperature plasma physics, fundamental aspects and applications” R. Hippler, S. Pfau, M. Schmidt, K. H. Schoenbach, Wiley- VCH, p199, **2001**
- [Hoffmann 2002] “Mass Spectrometer, Principles and Applications” E. de Hoffmann, V. Stroobant, John Wiley and sons, p4, **2002**
- [Hopkins 1986] M. B. Hopkins and W. G. Graham, Rev. Sci. Instrum., **57**, p. 2214, **1986**
- [Howling 1993] Howling A A, Dorier J L and Hollenstein Ch, Appl. Phys. Lett. 62 1341, **1993**
- [Howling 1994] “Time-resolved measurements of highly polymerized negative ions in radio frequency silane plasma deposition experiments”, A. A. Howling, L. Sansonnens, J. L. Dorier, Ch. Hollenstein, JAP, **75** (3), 1340-1353, **1994**
- [Ishida 1999] “The chemical effect of fluorine on boron transient enhanced diffusion”, E. Ishida, D. F. Downey, K. S. Jones, J. Lui, IEEE, Vol. **2**, p909-912, **1999**
- [ITRS 2005] International Technology Roadmap for Semiconductors – Front End Processes, Semiconductor Industry Association, p 23, **2005**, <http://www.itrs.net/Common/2005ITRS/FEP2005.pdf>
- [Jaeger 2002] “Introduction to microelectronic fabrication”, R. C. Jaeger, ed. G. W. Neudeck, R. F Pierret, Vol **5**, Published by Prentice Hall, p109, **2002**

-
-
- [Kaepelin 2002] Kaepelin Vincent, PhD thesis, Université de Provence, Marseille, France, 8 july **2002**
- [Kessels 1999] “Formation of cationic silicon clusters in a remote silane plasma and their contribution to hydrogenated amorphous silicon film growth”, W. M. M. Kessels, C. M. Leewis, M. C. M. Van de Sanden, D.c. Schram, JAP, **86**, 4029, **1999**
- [Koo 2004] “Plasma Diagnostics in Pulsed Plasma Doping (PLAD) System” B.-W. Koo, Z. Fang, L. Godet, S. Radovanov, C. Cardinaud, G. Cartry, A. Grouillet, D. Lenoble, IEEE, **April 2004**, Vol. **32**, Number 2
- [Lallement 2004] “Fabrication of an N+/P ultra-shallow junction by plasma doping for 65nm CMOS technology”, F. Lallement, A.Grouillet, M. Juhel, J.-P. Reynard, D. Lenoble, Z. Fang, S. Walther, Y. Rault, L. Godet and J. Scheuer, Surface & Coating Technology, Vol. 186, August 2004, p.17
- [Lallement 2005] F. Lallement, Thesis manuscript, INSA Toulouse, France, 2005
- [Langmuir 1924] I. Langmuir, H. M. Mott-Smith, General Electric Rev. **25**, p449, **1924**
- [Lieberman 2005] “Principles of Plasma Discharges and Materials processing” Michael A. Lieberman and Allan J. Lichtenberg, Wiley, New York **2005**
- [Lieberman 1989] “Model of plasma ion immersion ion implantation”, Michael A. Lieberman, JAP, Vol. **66**, p2926, **1989**

-
-
- [Liebert 2000] “Dose Monitor for plasma doping system”, U. S. Patent #6020592, Reuel B. Liebert, Bjorn O. Pedersen and Matthew Goeckner, Feb. 1, 2000
- [Liebert 2000a] “Plasma doping system for 200 and 300mm Wafers”, R. B. Liebert, S. R. Walther, S. B. Felch, Z. Fang, B. O. Pedersen, D. Hacker, IEEE, 0-7803-6462-7, p 472-475, **2000**
- [Lenoble 1999] “Evaluation of plasma doping for sub-0.18 μm ”, D. Lenoble, M. J. Goeckner, S. B. Felch, Z. Fang, J. Galvier and A. Grouillet, IEEE, p1222, **1999**
- [Lenoble 2000] D. Lenoble, Thesis manuscript, INSA Toulouse, France, **2000**
- [Lenoble 2006] “Enhanced performance of PMOS MUGFET via integration of conformal plasma-doped source/drain extensions”, D. Lenoble, K. G. Anil, A. De Keersgieter, P. Eybens, N. Collaert, R. Rooyackers, S. Brus, P. Zimmerman, M. Goodwin, D. Vanhaeren, W. Vandervorst, S. Radovanov, L. Godet, C. Cardinaud, S. Biesemans, T. Skotnicki, M. Jurczak, Submitted to VLSI, Hawaii, 2006
- [Low 1995] “An alternative method for determining the transmission function of secondary ion mass spectrometers”, M.H.S Low, C.H.A. Huan, A. T. S. Wee, K. L. Tan, Nuclear Instruments and Methods in Physics Research B **103**, p 482-488, **1995**
- [Marriott 1957] J. Marriott and J. D. Craggs, J. electron. Control **3**, 194, **1957**
- [Masetti 1983] G. Masetti, M. Severi, S. Solmi, IEEE Trans. On Elec. Dev., 30 (7), **1983**

-
-
- [Matyi 1998] “Process effects in shallow junction formation by plasma doping”
R. J. Matyi, S. B. Felch and al, JVST **B16**, p435-439, **1998**
- [Medved 1963] “Potential and Kinetic Electron Ejection from Molybdenum by
Argon Ions and Neutral Atoms”, D. B. Medved, P. Mahadevan, J.
K. Layton, Physical review, Vol **129**, Num **5**, p 2086-2087, **1963**
- [Mott-smith 1926] H. M. Mott Smith and I. Langmuir, Phys. Rev. **28**, p727, **1926**
- [Midha 2001] “Dynamics of ion-ion plasmas under radio frequency bias”, V.
Midha, D. J. Economou, JAP, **90**, p1102, **2001**
- [Miller] Unpublished data
- [Mizuno 1987] “Plasma doping into a sidewall of a sub-0.5 μ m width trench”, B.
Mizuno, I. Nakayama, N. Aoi and M. Kubota, Paper presented at
the 19th Conference on Solid State Devices and Materials, Tokyo,
Japan, p319-322, **1987**
- [Mizuno 1988] “New doping method for subhalf micron trench sidewalls by using
an electron cyclotron resonance plasma”, Appl. Phys. Lett. **53**,
p2059-2061, **1988**
- [Mizutani 2000] “Ion energy distribution at an r.f.-biased electrode in a inductively
coupled plasma affected by collision inside the sheath”, N.
Mizutani, T. Hayashi, Thin Solid Film, **374**, p 167-174, **2000**
- [Nastasi 1996] “Ion-Solid Interactions, Fundamentals and applications”, M.
Nastasi, J. W. Mayer and J. K. Hirvonen, Cambridge University
Press, Solid State Science Series, **1996**

-
-
- [O'Hanlon 2003] "A user's guide to vacuum technology", John F. O'Hanlon, Wiley-Inter-science, **2003**
- [Ohtake 1996] H. Ohtake, S. Samukawa, Appl. Phys. Lett., **68**, p2416, **1996**
- [Osberghaus 1950] O. Osberghaus, Z. Phys. **128**, p366, **1950**
- [Overzet 1992] Overzet L J, Lin Y abd Luo L, J. Appl. Phys. 72, 5579, **1992**
- [Overzet 1993] Overzet L J, J. Vac. Sci. Technol. A 11, 1114, **1993**
- [Paul 1953] W. Paul, H. Steinwedel, Z. Narturf. **8A**, 448, **1953**
- [Pauling 1964] L. Pauling, R. Hayward, "The architecture of Molecules", copyright W. H. Freeman, S. Francisco, 1964
- [Perel 2000] "Decaborane Ion Implantation", A.S Perel, W. Krull, D. Hoglund, K. Jackson and T. Horsky, Proc. 13th Conf. on IIT IEEE, 2000, pp. 304-307
- [Perrin 1997] "Mass spectrometry of reactive plasmas", J. Perrin, P.F. Williams(ed), Plasma Processing of semiconductors, 397-431, Kluwer Academic Publishers, **1997**
- [Pfeiffer] "Compact Cold Cathode Gauge IKR 260 operating manual" Pfeiffer Vacuum, BG805 153 BE/A, **p26**
- [Phelps] "Compilation of electron cross sections used by A. V. Phelps", A. V. Phelps, available online at ftp://jila.colorado.edu/collision_data/electronneutral/electron.txt

-
-
- [Qian 1991a] “Conformal implantation for trench doping with plasma immersion ion implantation”, X. Y. Qian, N. W. Cheung, M. A. Lieberman, R. Brennan, M. I. Current and N. Jha, Nuclear instruments and Methods in Physics Research, **B55**, p 898-901, **1991**
- [Qian 1991b] “Plasma immersion ion implantation of SiF₄ and BF₃ for sub-100nm P+/N junction fabrication”, X. Y. Qian, N. W. Cheung, M. A. Lieberman, S. B. Felch, R. Brennan, M. I. Current, Appl. Phys. Lett. **Vol 59**, p348-350, **1991**
- [Radovanov 2005] “Ion Energy Distributions in a Pulsed Plasma Doping System”, S.Radovanov, L.Godet, R. Dorai, Z.Fang, B. W. Koo, C. Cardinaud , G. Cartry, D. Lenoble, A. Grouillet, JAP, **98**, 113307, **2005**
- [Raizer 1997] “Gas discharge Physics”, Yu. P. Raizer, Spinger, New York, **1997**, p-128-135
- [Ramamurthi2002] “Two-dimensional pulsed-plasmas simulation of a chlorine discharge”, JVST, **A 20**, p467, **2002**
- [Reagan 1987] “Mass-dependent effect of channel electron multipliers in residual gas analyzers” N. R. Reagan, L. C. Frees, JVST, **Vol 5**, p2389, **1987**
- [Renau 2002] “Comparison of Plasma Doping and Beamline Technologies for Low Energy Ion Implantation”, A. Renau, J. T. Scheuer, Proc. Of 14th Conf. on Ion Implantation Technology, Taos, Sept 2002
- [Rolland 2000] L. Rolland, Thesis manuscript, University of Nantes, **2000**

-
-
- [Ruzic 1994] “Electric probes for low temperature plasmas” D. N. Ruzic , AVS monograph series, American Vacuum Society Education Committee, **1994**
- [Šašić 2005] “Electron Kinetic in BF₃ plasma“, O. Šašić, Z. Lj. Petrović, Z. Raspopović, L. Godet, S. Radovanov, GEC 2005 Proceeding
- [Scheuer 2004] “USJ formation using pulsed plasma doping,” J. T. Scheuer, D. Lenoble, J.-P. Reynard, F. Lallement, A. Grouillet, A. Arevalo, D. Distaso, D. Downey, Z. Fang, L. Godet, B.W. Koo, T. Miller and J. Weeman, Surface & Coating Technology, Vol. 186, August 2004, p. 57
- [Schwarzenbach1999] W. Schwarzenbach, Thesis, University of Grenoble 1, **1999**
- [Scientific Sys] “SmartProbe automated Langmuir probe plasma diagnostic”, Scientific System, <http://www.scisys.com>
- [Sheng 1994] “Characteristics of a plasma doping system for semiconductor device fabrication”, T. Sheng, S. B. Felch, C. B. Cooper III, JVST **B12**, p969-972, **1994**
- [Singh 1999] “Mass spectrometric detection of reactive neutral species: Beam-to-background ratio”, H. Singh, J. W. Coburn, D. B. Graves, JVST A, **17**, p2447, **1999**
- [Singh 2000] “Appearance potential mass spectrometry: discrimination of Dissociative ionization products” H. Singh, J. W. Coburn, D. B. Graves, JVST, **18**, p299-305, **2000**

-
-
- [Shockley 1957] “Dislocations and mechanical proprieties of crystals”, W. Shockley, ed. J. Fisher, W. G. Johnston, R. Thomson and T. Vreeland, Wiley, New York, p581, **1957**
- [Shockley 1958] “Forming Semiconductor Device by Ionic Bombardment”, W. Shockley, U.S. Patent 2 787 564, **1958**
- [Skotnicki 1996] “Electrical performance of retrograde versus conventional profile MOSFETs”, T. Skotnicki, P. Bouillon, Proc. On VLSI SYmp. Tech., pp. 327-328, 1996
- [Stewart 1991] “Model of plasma immersion ion implantation for voltage pulse with finite rise and fall times”, R. A. Stewart, M. A. Lieberman, JAP, **70**, p 3481-3487, **1991**
- [Stoffels 2001] “Near-surface generation of negative ions in low-pressure discharges”, E. Stoffels, W. Stoffels, V. M. Kroutilina, H. E. Wagner, J. Meichsner, JVST A, 19, **2001**
- [Strack 1963] “Ion bombardment of silicon in a glow discharge” H. Strack, JAP, **Vol. 34**, Number 8, p2405, **1963**
- [Suzuki 1987] “Dissociation and electron capture of CO⁺ and CF⁺ ions in collisions with He, Ne and Ar Atoms”, Y. Suzuki, T. Kaneko, M. Tomita, M. Sakisaka, Journalm of physical society of Japan, **Vol. 56**, No 2, pp 495-501, **1987**
- [Sze 2002] “Semiconductor Devices, Physics and Technology”, S. M. Sze, Ed Wiley & Sons, p 169-223, **2002**

-
-
- [Takagi 1978] “Proprieties of an ionized Cluster Beam from a vaporized Cluster Source”, T. Takagi, I. Yamada, A. Sasaki, Inst. Phys. Conf. Ser. N^o 38, IOP, 1978, pp. 229-235
- [Thompson 1913] “Rays of positive electricity and their applications to chemical analysis” J. J. Thompson, Longmans, Green and Co. ltd., London, **1913**
- [Van Zant 2004] “Microchip Fabrication”, Peter Van Zant, Mc Graw Hill book, 5th Edition, p438-441, **2004**
- [Vahedi 1991] “ A one-dimensional collisional model for plasma-immersion ion implantation”, V. Vahedi, M. A. Liebermann, M.V Alves, J. P. Verboncoeur, C. K. Birdsall, JAP, **69**, p 2008-2014, **1991**
- [Vahedi 1992] “Analytical model of the ion angular distribution in a collisional sheath”, V. Vahedi, R. A. Stewart, and M. Lieberman, JVST A, vol. **11**, p1275-1282, **1992**
- [Vasile 1989] “Mass spectrometry of plasmas” M. J. Vasile, H. F. Dylla, from the book: “Plasma Diagnostics, Discharge parameters and chemistry” O. Auciello and D. L. Flamm, Academic Press, **Vol. 1**, p185, **1989**
- [Walther 2006a] “Development of plasma-based implant for silicon devices”, S. Walther, R. Liebert, JVST, **B24**, p482-488, **2006**
- [Walther 2006b] “Plasma implanted ultra shallow junction boron depth profiles: effect of plasma chemistry and sheath conditions” S. Walther, L.Godet, T. Buyuklimanli, J. Weeman, JVST, **B24**, p489-493, **2006**

-
-
- [Yeap 1999] “High Performance Sub-0.2mm Gate Length PMOSFETs with Source/Drain Extensions Fabricated by Plasma Doping”, G. C-F. Yeap, S. B. Felch, D. Bang, B. Lee, M-R. Lin, IEEE, 0 7803 4538 X, p 114, **1999**
- [Zeuner 2001] “High energy negative ions in a radio-frequency discharge”, M. Zeuner, J. Meischner, J. A. Rees, JAP, **79**, p9379-9381, **2001**
- [Ziegler 1985] Stopping and Range of Ions in Matter (SRIM), a numerical simulation by J. F. Ziegler, and J. P. Biersack, 1985,
<http://www.srim.org>
- [Ziegler 1996] F. Ziegler, Ion Implantation Science and Technology, ed. J. F. Ziegler, Ion Implantation Technology Co., **1996**

List of Figures

<i>Figure 1: Schematic representation of a MOS Transistor type-N.....</i>	24
<i>Figure 2: Evolution of V_{th} for different gate lengths as a function of the drain voltage ..</i>	27
<i>Figure 3: Schematic representation of the channel-effective length and the spread under the gate</i>	28
<i>Figure 4: Representation of the in-series resistance's components [Lallement 2005]</i>	28
<i>Figure 5: Schematic of the different zones implanted for a MOS transistor</i>	30
<i>Figure 6: A map of application areas for high-current (H/C), medium-current (M/C) and high-energy (H/E) implanters as a function of dose and energy</i>	30
<i>Figure 7: Schematic drawing of a typical ion implanter showing (1) the ion source, (2) the ion-analyzing mechanism, (3) the accelerating column, (4) the scanning system, (5) the target chamber [Jaeger 2002]</i>	31
<i>Figure 8: Schematic of the ion range and projected range R_p</i>	34
<i>Figure 9: (a) Projected range simulated for B^+ implanted into silicon with an energy ranging from 10 to 5000 eV, (b) TRIM calculation example of B^+ 5000 eV implant into silicon.....</i>	34
<i>Figure 10: (a) The silicon lattice viewed along the $\langle 110 \rangle$ axis [Pauling 1964], (b) Comparison of a boron as-implanted SIMS profile after 500V implantation into a crystalline and a pre-amorphized (PAI) silicon wafer [Godet 2006]</i>	36
<i>Figure 11: Comparison of drift and decel implants of 1 keV $5E^{14}$ boron [Renau 2002] .</i>	41
<i>Figure 12: PLAD concept.....</i>	42
<i>Figure 13: Hans Strack's plasma immersion system [Strack 1963]</i>	45
<i>Figure 14: Plasma-Immersion Ion Implantation (PIII) [Conrad 2000]</i>	46
<i>Figure 15: Varian plasma-doping system first prototype [Lenoble 2000].....</i>	47
<i>Figure 16: Principle of PLAD</i>	48
<i>Figure 17: Experimental Paschen's curves showing the evolution of the breakdown voltage of a BF_3 discharge as a function of the product $P \times d$.....</i>	50

<i>Figure 18: Ion current density as a function of cathode bias voltage and anode-to-cathode spacing at 30mTorr for a hollow cathode plasma operated at -1500 V.....</i>	<i>51</i>
<i>Figure 19: Electric field distribution calculated using Opera 3D with -500 V on the cathode and -1500 V on the hollow cathode for two different anode-to-cathode spacing (100 and 35 mm)</i>	<i>52</i>
<i>Figure 20: Electric field distribution calculated using Opera 3D with -500 V on the cathode and -1200 V on the pulsed anode for an 5cm anode-to cathode spacing.....</i>	<i>53</i>
<i>Figure 21: Voltage distribution in a dc glow discharge process [Chapman 1980].....</i>	<i>53</i>
<i>Figure 22: Cathode voltage and current waveforms for a 1kV, 40mTorr, 50μs, 2.5 kHz BF₃ discharge</i>	<i>54</i>
<i>Figure 23: Typical cathode voltage overshoot for 1kV, 40mTorr, 50μs, 2.5 kHz BF₃ discharge</i>	<i>55</i>
<i>Figure 24: Secondary electron coefficient at different cathode voltages [Miller]</i>	<i>56</i>
<i>Figure 25: Displacement current measured without gas inside the process chamber.....</i>	<i>57</i>
<i>Figure 26: VISta PLAD system layout</i>	<i>58</i>
<i>Figure 27: PLAD parameter control screen.....</i>	<i>59</i>
<i>Figure 28: Varian Control System's, vacuum control screen</i>	<i>60</i>
<i>Figure 29: Gas delivery control system.....</i>	<i>61</i>
<i>Figure 30: Typical BF₃ ion spectrum for bulk plasma during the pulse-on period at 1kV 50μs</i>	<i>62</i>
<i>Figure 31: Typical AsF₅ ion spectrum for bulk plasma during the pulse-on period at 1kV 50μs</i>	<i>63</i>
<i>Figure 32: PLAD process chamber with spray-coated silicon anode and cathode</i>	<i>64</i>
<i>Figure 33: As-implanted boron SIMS profile after a 2.10¹⁵ PLAD implant at different cathode voltage using crystalline wafers</i>	<i>66</i>
<i>Figure 34: Particle contamination on 200mm wafers for AsH₃ and BF₃ implants.....</i>	<i>67</i>
<i>Figure 35: Metal contamination during 5E15 BF₃ PLAD implantation at 5 and 10kV... </i>	<i>67</i>

Figure 36: PLAD Uniformity and repeatability of a 1kV, 7.10^{14} dose, 40mTorr, PAI: Ge^+ 30keV $1e15$ dose, SPE annealed by RTP 650°C 60sec in 100ppm O_2 [Arevalo]	68
Figure 37: Across wafer X_j uniformity for 500V, BF_3 PLAD as- implanted SIMS boron profiles.....	68
Figure 38: A cross section of a 65 nm transistor fabricated by plasma implant without a sacrificial offset spacer [Lallement 2004, Walther 2006]	70
Figure 39: Photodiode implanted area [Lallement 2005]	71
Figure 40: Schematic representation of a FinFET transistor	72
Figure 41: SEM picture of the fabricated MUGFETs with BF_3 plasma-doped SDE. TiCN/HfO ₂ gate stack is used on 20nm width/60nm height Fin.....	73
Figure 42: Diagram of the Hiden EQP mass spectrometer	76
Figure 43: Linear relation between EQP pressure and PLAD process chamber for BF_3 77	
Figure 44: Mass spectrometer extraction section	78
Figure 45: Principle of an ionization chamber by electron impact.....	79
Figure 46: Schematic of the first sections of the EQP mass spectrometer	80
Figure 47: Equipotential distribution inside the mass spectrometer, (right) after the drift tube and before the quad lens, (left) inside the quad lens sector	80
Figure 48: Electrostatic sector analyzer	81
Figure 49: Quadrupole with cylindrical rods and applied potentials.....	83
Figure 50: Mathieu diagram of stability of the ion movement in a quadrupole field for two different mass ($M_1 < M_2$).....	84
Figure 51: Channeltron Electron Multiplier [Hiden]	86
Figure 52: Typical Detector operating curve.....	86
Figure 53: Schematic timing diagram of the time-resolved ion mass and energy measurements. Shown above are the timing scales for time-resolved ion mass and energy measurements: (a) the wafer bias voltage, (b) delay signal, and (c) gating pulse [Koo 2004].	87
Figure 54: Transit time inside the mass spectrometer divided in four sections [Hiden] .	88
Figure 55: Calculated transit time into the mass spectrometer for different masses with the calibration set-up of a 500V 75mTorr PLAD implantation	89

<i>Figure 56: 3D electrostatic model of the EQP</i>	<i>90</i>
<i>Figure 57: Beam trajectory inside the mass spectrometer model and divergence angle of a 500eV BF₂⁺ measured at the exit plane of the energy analyzer and zoom on the exit of the electrostatic energy analyzer of the mass spectrometer model</i>	<i>91</i>
<i>Figure 58: Calculated transmission efficiency of 100 to 500eV BF₂⁺ ion with normal incidence at the entrance of the mass spectrometer.....</i>	<i>92</i>
<i>Figure 59: BF₂⁺ ion energy distribution measured during the pulse-on period at different cathode voltage from 100 V to 500 V at 30 mTorr, 2500 Hz with 10 cm anode to cathode spacing in the hollow cathode mode pulsed at 1500 V.....</i>	<i>92</i>
<i>Figure 60: Mass spectrometer voltage set-up</i>	<i>94</i>
<i>Figure 61: BF₂⁺ transmission efficiency inside the mass spectrometer with different cone angle at the entrance of the EQP with the experimental settings of a 500V 100mT PLAD implant.....</i>	<i>95</i>
<i>Figure 62: Mass spectrometer corrected pressure P_s versus the PLAD process chamber pressure for helium, neon, argon and xenon.....</i>	<i>97</i>
<i>Figure 63: Experimental and calculated entrance aperture transmission factor as a function of mass.....</i>	<i>98</i>
<i>Figure 64: Schematic of the experimental system</i>	<i>98</i>
<i>Figure 65: Mass spectrometer global transmission factor as a function of mass.....</i>	<i>100</i>
<i>Figure 66: Mass spectrometer transmission factor as a function of mass normalized to the argon transmission using the experimentally measured and calculated K(M) and compared to the theoretical mass spectrometer transmission....</i>	<i>101</i>
<i>Figure 67: Schematic diagram of PLAD process chamber with an ion mass and energy analyzer installed in the center of the anode.....</i>	<i>103</i>
<i>Figure 68: Time-resolved IEDs of Ar⁺ ion incident to a grounded anode surface, 3 kV bias, 30 μs pulse, 2500 Hz frequency, and 30 mTorr. (a) Pulse-on, (b) pulse-off [Radovanov 2005].....</i>	<i>104</i>
<i>Figure 69: Schematic diagram of the mass spectrometer installed in the middle of the PLAD cathode</i>	<i>105</i>
<i>Figure 70: Design of EQP Mass spectrometer inside the PLAD cathode.....</i>	<i>106</i>

<i>Figure 71: Mass spectrometer insulated from the cathode</i>	<i>107</i>
<i>Figure 72: Wafer, platen and Mass spectrometer extraction optics set up.....</i>	<i>108</i>
<i>Figure 73: B⁺, BF⁺, BF₂⁺, BF₃⁺ IED normalized to the total ion flux for a 500 V BF₃ plasma at 100 mTorr and 2500 Hz.....</i>	<i>109</i>
<i>Figure 74: Bulk plasma time average Energy scan spectrum of Ar⁺ during a 3kV 30mTorr 10cm 2500 Hz Argon glow discharge</i>	<i>111</i>
<i>Figure 75: Time evolution of maximum intensity of BF₂⁺ ion, -1 kV, 41 mTorr, 2500 Hz and of Ar⁺ ion, 3 kV, 30 mTorr, 30 μs.....</i>	<i>112</i>
<i>Figure 76: Pulse-on period time-resolved measurement of Ar⁺ reaching the cathode for a 1 kV 50 mTorr 50μs 2500 Hz 5 sccm, 5 cm implantation. Reference scan measurement is used.....</i>	<i>113</i>
<i>Figure 77: Pulse-on period time-resolved measurement of Ar⁺ IED measured at the cathode for a 1 kV 50 mTorr 50μs 2500 Hz implantation</i>	<i>113</i>
<i>Figure 78: Time resolved BF₂⁺ IED measured by the mass spectrometer installed in the center of the high-voltage cathode, with a time resolution of 10 μs for a 500 V, 100 mTorr, 50 μs, 5sccm, BF₃ glow discharge plasma at 2500Hz.....</i>	<i>115</i>
<i>Figure 79: Evolution during the pulse of the relative total ion flux and B⁺, BF⁺ and BF₂⁺ ion relative fluxes measured through time resolved mass spectrometry.....</i>	<i>116</i>
<i>Figure 80: Correct and incorrect setting of the Vert parameter during its calibration are represented in (a) and (b), both of which are monitored with a fast- acquisition oscilloscope. The ion energy was set to 1000 eV. T_{on} is the pulse- on period and T_{ion} is the time over which the energetic ions are detected..</i>	<i>117</i>
<i>Figure 81: Relative total ion flux measured with the mass spectrometer as a function of the ion current density for 1kV (30 to 70mTorr, 500Hz to 3000Hz), 750V (40 to 70mTorr) and 500V (75 to 250mTorr) BF₃ plasma</i>	<i>118</i>
<i>Figure 82: Example of a typical I-V characteristic measured in argon plasma at 300V 45mTorr. Three regions can be distinguished (I,II,III) as well as the potentials V_p and V_f. A zoom of the ion saturation current is also presented.</i>	<i>120</i>
<i>Figure 83: Schematic diagram of a Langmuir probe installed on the PLAD process chamber.....</i>	<i>122</i>

<i>Figure 84: Pulse-on period (a) and afterglow (b) time resolved Langmuir probe for a 1kV 40mT 30μs BF₃ implant,</i>	123
<i>Figure 85: Experimental time-resolved EEPF for Argon plasma under two different plasma conditions</i>	125
<i>Figure 86: Primary ion interaction with the solid target and sputtering effects. The SIMS technique is based on the analysis of the secondary ions ejected from the target through mass spectrometry</i>	128
<i>Figure 87: Four-Point probe schematic</i>	130
<i>Figure 88: Solid-solubility and electrically active impurity-concentration limits in silicon for antimony, arsenic, boron and phosphorus [Jaeger 2002]</i>	132
<i>Figure 89: BF₃ cross section calculated by S. Biagi [Šašić 2005] for direct and indirect electron collision processes</i>	137
<i>Figure 90: Ions produced through electron impact fragmentation of BF₃(g), as function of electron energy</i>	139
<i>Figure 91: (a) Electron and fast electron density evolution (n_e and n_{fe}) and (b) electron and fast electron temperatures (T_e and T_{fe}) during an entire period of a BF₃ 1 kV 40 mTorr, 30μs, 2500 Hz glow discharge plasma,</i>	142
<i>Figure 92: Calculated EEDF time evolution extracted from the I-V curves during the pulse-on period of a 1 kV, 40 mTorr, 30μs, 2500Hz, 5sccm PLAD implantation</i>	143
<i>Figure 93: EEDF time evolution extracted from the I-V curves during the pulse-off period of a 1 kV, 40 mTorr, 30μs, 2500Hz, 5sccm PLAD implantation</i>	144
<i>Figure 94: Time evolution during the pulse-on period of the electron density radial distribution measured by the Langmuir probe during a 1 kV 40 mTorr 30μs BF₃ glow discharge</i>	144
<i>Figure 95: (a) Plasma potential and floating potential evolution (V_p and V_f) and (b) ion density evolution (n_i) during the whole period of a 1 kV 40 mTorr, 30μs, 2500 Hz BF₃ glow discharge plasma</i>	146
<i>Figure 96: (a) Time evolution during the pulse-on period of the plasma potential radial distribution as measured by the Langmuir probe during a 1 kV 40 mTorr 30μs BF₃ glow discharge (b)</i>	148

<i>Figure 97: Sheath thickness calculated using {IV.2.8} for a 1kV 40mTorr 30μs BF₃ glow discharge the plasma parameters, such as $n(t)$, were measured by a Langmuir probe.....</i>	<i>153</i>
<i>Figure 98: Representation of the different particle interaction in a collision-less sheath or collisional sheath, as well as the secondary electron emission from the cathode</i>	<i>154</i>
<i>Figure 99: Modified Davis and Vanderslice model for the ion energy distribution measured at the cathode.....</i>	<i>158</i>
<i>Figure 100: Theoretical cathode ion energy distributions for different numbers of collisions inside the sheath (from 1 to 100). All the curves have been normalized at $E = 0$ eV.....</i>	<i>160</i>
<i>Figure 101: Energy distribution for Ne⁺ in Neon discharge (660 V 470 mTorr) and for Ar⁺ in Argon discharge (600 V 60 mTorr). The circles are the experimental data and the full lines are the theoretical curve fitted to the experimental points [Davis 1963].....</i>	<i>160</i>
<i>Figure 102: Calculated mean energy as a function of the number of collisions based on the Davis and Vanderslice model.....</i>	<i>161</i>
<i>Figure 103: Bulk plasma boron ions fractions normalized to the total flux of boron containing ions in BF₃ plasma for different cathode voltage biases, pressures and frequencies measured by the mass spectrometer during the <u>pulse-on period</u> installed on the anode in a reversed bias configuration.....</i>	<i>162</i>
<i>Figure 104: Boron ions and molecular ions fraction normalized to the total flux of boron ions of the ions reaching the cathode, as measured during the <u>pulse-on period</u> in BF₃ plasma for different cathode voltage biases, pressures and frequencies by the mass spectrometer installed on the cathode.....</i>	<i>163</i>
<i>Figure 105: B⁺ and BF⁺ IEDs normalized to the total ion flux for different cathode voltages (50, 100, 300, 500, 750 and 1000 V), for a 30 mTorr, 5sccm, 2500 Hz BF₃ glow discharge created using the hollow cathode at 1500V.....</i>	<i>165</i>
<i>Figure 106: BF₂⁺ and BF₃⁺ IED normalized to the total ion flux for different cathode voltages (50, 100, 300, 500, 750 and 1000 V), for a 30 mTorr, 5sccm, 2500 Hz BF₃ glow discharge created using the hollow cathode at 1500V.....</i>	<i>166</i>

<i>Figure 107: $B_2F_3^+$ and $B_2F_5^+$ IEDs normalized to the total ion flux for different cathode voltages (50, 100, 300, 500, 750 and 1000 V), for a 30 mTorr, 5sccm, 2500 Hz BF_3 glow discharge created using the hollow cathode at 1500V.....</i>	<i>167</i>
<i>Figure 108: Boron ion fluxes normalized to the total boron ion flux measured for different cathode biases (50, 100, 300, 500, 750 and 1000V) during the pulse-on period of a 30 mTorr BF_3 glow discharge in the high-voltage sheath, with a constant hollow cathode bias at -1500V</i>	<i>168</i>
<i>Figure 109: B^+, BF^+, BF_2^+ and BF_3^+ IED normalized to the total ion flux for anode-to-cathode spacing for a 500 V, 30 mTorr, 5sccm, 2500 Hz BF_3 glow discharge created using the hollow cathode at 1400V</i>	<i>169</i>
<i>Figure 110: B^+, BF^+, BF_2^+ and BF_3^+ ion fractions of with the full high-voltage acceleration under the previously detailed conditions.....</i>	<i>170</i>
<i>Figure 111: B^+, BF^+, BF_2^+, BF_3^+ IEDs normalized to the total flux of boron ion. (a) 1 kV 2500 Hz BF_3 plasma at three different pressures: 30, 50, 70 mTorr, (b) 500 V 2500 Hz BF_3 plasma at four different pressures: 100, 150, 200, 250 mTorr</i>	<i>172</i>
<i>Figure 112: Mean ion energy normalized to the cathode voltage for B^+, BF^+, BF_2^+ and BF_3^+ ions reaching the cathode for a collisional and highly collisional sheath under various operating discharge conditions in a BF_3 glow discharge as a function of electric field-to-gas density ratio.</i>	<i>174</i>
<i>Figure 113: B^+, BF^+, BF_2^+ and BF_3^+ mean energies normalized to the cathode voltage, as a function of the number of collisions for various BF_3 glow discharge conditions</i>	<i>175</i>
<i>Figure 114: Experimentally calculated B^+, BF^+, BF_2^+, BF_3^+, $B_2F_3^+$ and $B_2F_5^+$ mean energies normalized to the cathode voltage, as a function of the number of collisions for many different BF_3 hollow cathode glow discharge conditions</i>	<i>175</i>
<i>Figure 115: B^+ ion fraction as a function of the number of collisions under various BF_3 discharge conditions (HC, no HC, Pulsed anode, Neon dilution) for (a) bulk plasma, (b) ions reaching the cathode</i>	<i>178</i>

<i>Figure 116: Schematic of the typical shape of B^+ IED for a moderately collisional sheath ($s/\lambda < 6$ collisions)</i>	<i>179</i>
<i>Figure 117: U function as a function of pressure for different plasma conditions in collisional pure BF_3 plasma</i>	<i>181</i>
<i>Figure 118: BF^+ ion fraction as a function of the number of collisions under many different BF_3 discharge conditions (HC, no HC, Pulsed anode, Neon dilution) for (a) the bulk plasma, (b) the ion reaching the cathode</i>	<i>182</i>
<i>Figure 119: Schematic of a typical shape of BF^+ IED for a moderately collisional sheath. Three different peaks can be observed</i>	<i>183</i>
<i>Figure 120: $U(\Delta V_x)$ function as a function of pressures for different plasma conditions in collisional pure BF_3 plasma (with $x = 2$ or 3)</i>	<i>184</i>
<i>Figure 121: BF_2^+ ion fraction as a function of the number of collisions under many different BF_3 discharge conditions (HC, no HC, Pulsed anode, Neon dilution) for (a) the bulk plasma, (b) the ion reaching the cathode</i>	<i>186</i>
<i>Figure 122: Normalized BF_2^+ IED in the case of a high-pressure, low-energy (500V) BF_3 discharge under different operating pressures (100, 150, 200 and 250 mTorr), fitted with the modified Davis and Vanderslice model (DVS) by adjusting the number of collisions inside the sheath</i>	<i>187</i>
<i>Figure 123: Schematic of a typical shape of BF_2^+ for moderately collisional sheath ...</i>	<i>188</i>
<i>Figure 125: BF_3^+ ion fraction as a function of the number of collisions under many different BF_3 discharge conditions (HC, no HC, Pulsed anode, Neon dilution) for (a) the bulk plasma, (b) the ion reaching the cathode</i>	<i>190</i>
<i>Figure 126: Normalized BF_3^+ IED in the case of high pressure low-energy (500 V) BF_3 discharge for different operating pressure (100 and 200 mTorr) fitted with the modify Davis and Vanderslice model (DVS) by adjusting the number of collisions inside the sheath.....</i>	<i>191</i>
<i>Figure 127: Bulk plasma boron ion fractions normalized to the total flux of boron containing ions during the <u>afterglow</u> in BF_3 plasma for different cathode voltage biases, pressures and frequencies as measured by the mass spectrometer installed on the anode.....</i>	<i>192</i>

<i>Figure 128: Fractions of boron containing ions normalized to the BF_2^+ fraction for a 1 kV 40 mTorr 50μs as measured in the bulk plasma during the pulse-on (a) and the afterglow (b).....</i>	<i>192</i>
<i>Figure 129: $B_2F_3^+$ (a) (b) and $B_2F_5^+$ (b) (d) ion fractions as a function of the number of collisions under many different BF_3 discharge conditions (HC, no HC, Pulsed anode, Neon dilution) for the bulk plasma (a), (c), and for the ion reaching the cathode (b), (d).....</i>	<i>194</i>
<i>Figure 130: F IED measured on the anode side during the pulse-on period of a 1 kV, 40 mTorr, 2500 Hz, 50 μs, 4.5 cm BF_3 plasma.....</i>	<i>195</i>
<i>Figure 131: Sheet resistance (R_s) and its non-uniformity evolution before and after chamber maintenance during the conditioning step (3 kV, 18 mTorr, 28 μs, 10^{15} ions/cm²).....</i>	<i>199</i>
<i>Figure 132: Experimental conditions of the conditioning step study.....</i>	<i>200</i>
<i>Figure 133: Sheet resistance evolution measured at the center of the wafer before and after the chamber maintenance for 300V 30 mTorr, 30 μs, 2500Hz, HC = 1500V, gap = 5cm, with an implanted dose of 10^{15} at/cm².....</i>	<i>201</i>
<i>Figure 134: (a) Boron containing ion fluxes normalized to the total ion flux(%) during the conditioning step, (b) Evolution of the implanted boron atom fraction (see text) reaching the cathode during the conditioning step after maintenance, using a 300 V, 30mTorr HC PLAD implantation.....</i>	<i>202</i>
<i>Figure 135: Boron and fluorine concentration at the beginning and the end of the conditioning step, as measured by SIMS for a 10^{14} ion/cm² 300 V BF_3 HC plasma.....</i>	<i>203</i>
<i>Figure 136: Cathode current and number of pulses to implant the 5×10^{14} ions/cm²</i>	<i>204</i>
<i>Figure 137: Values of the secondary electron emission coefficients of Si and SiO₂, as a function of the incident energy for the ions B^+, F^+, BF^+, BF_2^+ [Lenoble 2000].....</i>	<i>205</i>
<i>Figure 138: Evolution of the etching product fluxes, normalized to the total ion flux during the conditioning step with a 300 V, 30 mTorr, HC BF_3 plasma, (a) fraction of hydrogen, oxygen and carbon products, (b) fraction of boron</i>	

oxide products, (c) fraction of silicon, silicon fluoride and fluorine products	207
Figure 139: Evolution of the electron density measured with a Langmuir probe during the pulse-on period of a 300 V, 30 mTorr, hollow cathode BF_3 plasma at the beginning and at the end of the conditioning step.....	209
Figure 140: Normalized BF_2^+ ion energy distribution in the case of a clean hardware, and a dirty hardware, after many chamber maintenances and conditioning steps during a 500V, 30 mTorr, $50\mu\text{s}$ BF_3 glow discharge with hollow cathode biased at -1500 V	210
Figure 141: (a) Ion and electron densities measured at the center of the wafer, (b) fast electron temperature and density measured by the Langmuir probe during the pulse-on period, as a function of pressures ranging from 40 to 70 mTorr for a 1 kV $50\mu\text{s}$ BF_3 glow discharge	212
Figure 142: Plasma potential (a) and electron density (b) radial distributions for different pressures (40, 50, 60 and 70 mTorr), during a 1kV, BF_3 PLAD implantation.....	212
Figure 143: Ion density radial distributions for different pressures (40, 50, 60 and 70 mTorr), during a 1kV, BF_3 PLAD implantation.....	214
Figure 144: B^+ , BF^+ , BF_2^+ and BF_3^+ IEDs normalized to the total boron ion flux for different gas flows (3, 6, 12, and 24sccm) during a 30 mTorr, $50\mu\text{s}$, 2500Hz BF_3 glow discharge for a hollow cathode plasma (1400V), with a cathode bias of 500V.....	215
Figure 145: Boron ion fractions based on the flux of boron ions normalized to the total flux of boron ions measured for different gas flows during the <u>pulse-on</u> <u>period</u> for a 30 mTorr BF_3 glow discharge hollow cathode plasma (1400V) with a cathode bias of 500V	216
Figure 146: SiF^+ ion fraction based on the SiF^+ ion flux normalized to the total ion flux measured for different gas flows during the <u>pulse-on period</u> for a 30 mTorr BF_3 glow discharge hollow cathode plasma (1400V), with a cathode bias of 500V.....	216

<i>Figure 147: B^+, BF^+, BF_2^+, and BF_3^+ IEDs, normalized to the total flux of boron ions for 500 V, 100 mTorr, BF_3 plasma.....</i>	<i>219</i>
<i>Figure 148: Calculated boron equivalent energy for each boron ion, normalized to the total flux of boron ions based on 500V 100mTorr IEDs of the ions reaching the wafer</i>	<i>220</i>
<i>Figure 149: Boron and fluorine equivalent energy based on the 500V 100mTorr IED of the ions reaching the wafer</i>	<i>221</i>
<i>Figure 150: SRIM simulations of a 1keV B^+ implantation with different incident angles</i>	<i>221</i>
<i>Figure 151: Boron and Fluorine predicted depth profiles, based on the measured ion mass and energy distributions for crystalline and pre-amorphized silicon wafer (PAI), compared with the measured SIMS depth profile for the same implant conditions (500V 100mTorr BF_3 PLAD).....</i>	<i>222</i>
<i>Figure 152: (a) Contribution of each ion reaching the wafer (B^+, BF^+, BF_2^+ and BF_3^+) onto the boron depth profile, (b) Contribution of each energy bin (0 to 100eV, 100 to 200eV, 200 to 300eV, 300 to 400eV and 400 to 500eV) equivalent boron energy onto the boron depth profile</i>	<i>223</i>
<i>Figure 153: (a) B^+, BF^+, BF_2^+, and BF_3^+ corrected IEDs normalized to the total flux of boron ions for 500 V, 100 mTorr, BF_3 plasma, (b) Boron predicted depth profile based on the measured IEDs, not corrected and corrected by a mass transmission in m^{-1} for crystalline and pre-amorphized silicon wafer (PAI), compared to the measured SIMS depth profile for the same implant conditions (500V 100mTorr BF_3 PLAD).....</i>	<i>225</i>
<i>Figure 154: (a) B^+, BF^+, BF_2^+, and BF_3^+ IEDs, normalized to the total flux of boron ions for 1kV, 40 mTorr, BF_3 plasma, (b) Boron predicted depth profile based on the measured IEDs for crystalline silicon wafer, compared to the measured SIMS depth profile for the same implant conditions (1kV 40 mTorr BF_3 PLAD).....</i>	<i>225</i>
<i>Figure 155: B^+, BF^+, BF_2^+, and BF_3^+ IEDs, normalized to the total ion flux of a 500V, 30 mTorr, BF_3 hollow cathode plasma for a collisional sheath and a collisionless sheath.....</i>	<i>226</i>

<i>Figure 156: Boron predicted depth profile, based on the measured IED for crystalline silicon wafer, compared to the measured SIMS depth profile (500V 30 mTorr BF₃ PLAD) in the case of collisional and collision-less sheath.....</i>	<i>227</i>
<i>Figure 157: B⁺, BF⁺, BF₂⁺ and BF₃⁺ IEDs normalized to the total flux of the boron ions as a function of the normalized energy (ϵ / eV_c), for different cathode voltages, BF₃ glow discharge (1000 V 40 mTorr, 750 V 60 mTorr and 500 V 100 mTorr)</i>	<i>230</i>
<i>Figure 158: Boron ion fractions normalized to the total boron ion flux and measured for different cathode bias voltages (1000 V 40 mTorr, 750 V 60 mTorr and 500 V 100 mTorr), during the pulse-on period BF₃ glow discharge, as measured (a) in the bulk plasma and (b) in the high-voltage sheath</i>	<i>230</i>
<i>Figure 159: Boron predicted profile, based on the measured IEDs for different cathode biases and pressures (1000 V and 40 mTorr, 750 V and 60 mTorr and 500 V and 100 mTorr) during the pulse-on period BF₃ glow discharge measured in the high-voltage sheath for 10¹⁵ B ion/cm³</i>	<i>231</i>
<i>Figure 160: B⁺, BF⁺, BF₂⁺ and BF₃⁺ IEDs normalized to their maximum intensity as a function of the energy normalized to the cathode voltage, for different cathode voltages in a 30 mTorr, 2500 Hz, 50 μs, BF₃ glow discharge (50, 100, 300, 500, 750 and 1000V), with a constant hollow cathode bias at -1500 V.....</i>	<i>232</i>
<i>Figure 161: (a) Number of collisions and (b) boron ion fractions normalized to the total boron ion flux measured for different cathode biases (50, 100, 300, 500, 750 and 1000V) during the pulse-on period of a 30 mTorr BF₃ glow discharge in the high-voltage sheath, with a constant hollow cathode bias at -1500V... </i>	<i>233</i>
<i>Figure 162: Boron predicted profiles based on the measured IEDs for different cathode biases (50, 100, 300, 500, 750 and 1000V) during the pulse-on period of a 30 mTorr hollow cathode BF₃ glow discharge measured in the high-voltage sheath for 10¹⁵ B ion/cm³</i>	<i>234</i>
<i>Figure 163: Ratio of sheath thickness over ion mean free path, as a function of the pressures for different cathode voltages (1000 V, 30 to 70 mTorr; 750 V, 40 to 60 mTorr and 500 V, 75 to 250 mTorr).....</i>	<i>235</i>

<i>Figure 164: B^+, BF^+, BF_2^+ and BF_3^+ IEDs normalized to the total flux of the boron ions for a 1kV BF_3 plasma under three different pressures: 30, 50, 70mTorr ...</i>	236
<i>Figure 165: Boron predicted depth profile based on the measured ion mass and energy distribution, compared with the measured SIMS depth profile for the same implant conditions (1kV 30 to 70mTorr, 2500 Hz, 50 μs BF_3 PLAD.....</i>	237
<i>Figure 166: B^+, BF^+, BF_2^+ and BF_3^+ IEDs normalized to the total ion flux for a 500 V BF_3 plasma under four different pressures: 100, 150, 200, 250mTorr.....</i>	238
<i>Figure 167: Experimentally determined mean energies for B^+, BF^+, BF_2^+ and BF_3^+ after their acceleration inside the high-voltage sheath for a 500V BF_3 glow discharge operated at different pressures (100, 150, 200 and 250 mTorr)</i>	238
<i>Figure 168: Boron predicted profiles based on the measured ion energy distribution for a 500V, 2500 Hz, 50 μs BF_3 PLAD at 100, 150, 200 and 250mTorr.....</i>	239
<i>Figure 169: B^+, BF^+, BF_2^+, BF_3^+, Ne^+ IEDs normalized to the total ion flux for 500V 2500 Hz BF_3, diluted at 50 % with neon for five different pressures: 100, 150, 200, 250 and 300 mTorr.....</i>	240
<i>Figure 170: Boron predicted profile for a pure BF_3 plasma, a BF_3-Ne plasma (with 50% neon) and a BF_3-Ar plasma (with 50% argon) during a 500 V, 100 mTorr PLAD implantation.....</i>	241
<i>Figure 171: Time evolution of the electron density during the pulse-on period for a 1500V HC plasma with different anode-to-cathode spacings (500 V, 30 mTorr, 50 μs, 2500 Hz).....</i>	242
<i>Figure 172: Calculated sheath thickness for a 500 V, 30 mTorr, 50 μs, 2500 Hz BF_3 glow discharge with different anode-to-cathode spacings.....</i>	243
<i>Figure 173: BF_2^+ IEDs normalized to the total flux of the boron ions for a 500 V, 30 mTorr, 50μs BF_3 HC plasma (HC voltage of 1400 V) with different anode-to-cathode spacings equal to (a) 35mm, (b) 40 mm, (c) 50 mm, (d) 75 mm, (e) 100 mm. Also included in f is a summary of the BF_2^+ IED for different anode-to-cathode gaps</i>	244
<i>Figure 174: Boron ion and molecular fraction in a 500 V, 30 mTorr BF_3 HC glow discharge with anode-to-cathode spacings ranging from 3.5 to 10 cm at a constant hollow cathode bias (- 1400 V).....</i>	244

<i>Figure 175: B^+, BF^+ and BF_3^+ IEDs normalized to the total ion flux for a 500 V, 30 mTorr, 2500 Hz. 50 μs BF_3 plasma with different anode-to-cathode spacings</i>	245
<i>Figure 176:(a) Experimentally calculated B^+, BF^+, BF_2^+ and BF_3^+ ion mean energies, based on the ion energy distributions, as a function of the anode-to-cathode spacings; (b) B^+, BF^+, BF_2^+ and BF_3^+ ion fractions of with the full high-voltage acceleration under the previously detailed conditions</i>	246
<i>Figure 177: Boron equivalent normalized IED, based on the 500V 30mTorr IEDs of the ions reaching the wafer for 3.5 cm and 10 cm anode-to-cathode spacings</i>	247
<i>Figure 178: Boron predicted depth profile, normalized to 10^{15} dose, based on the measured IED for different anode-to-cathode spacings (500V 30 mTorr BF_3 PLAD)</i>	248
<i>Figure 179: (a) Measured boron SIMS profile for a 500 V, 30 mTorr, 1×10^{15} ions/cm³ BF_3 PLAD implant with 3.5 and 10 cm anode-to-cathode spacings, (b) Boron over fluorine ratio, based on the IEDs at different anode-to-cathode spacings</i>	249
<i>Figure 180: R_s as a function of X_j for a 500 V, 30 mTorr HC plasma implantation with different anode-to-cathode spacings, and calculated R_s based on different solid solubility levels in the silicon (a reference point at 500V, 100 mTorr without the HC is also included)</i>	250
<i>Figure 181: Activation efficiency for different anode-to-cathode gaps (3.5 and 10 cm) and different nominal doses, as measured with the PLAD dosimetry system (a reference point at 500V, 100 mTorr without the HC is also included)</i>	250
<i>Figure 182: (a) Ion current density as a function of the hollow cathode voltage under a constant cathode voltage (500 V) and an anode-to-cathode spacing of 5 cm at 20 mTorr, (b) Calculated number of collisions, based on equation {IV.2.5}, under the same plasma conditions</i>	252
<i>Figure 183: B^+, BF^+, BF_2^+ and BF_3^+ IEDs normalized to their maximum intensity of each ion, as a function of the energy normalized to the cathode voltage maintained at 500 V 20 mTorr for different hollow cathode voltages (800, 1000, 1200, 1400, 1800 and 2200V)</i>	252

<i>Figure 184: Boron ion fractions, based of the boron ion fluxes normalized to the total flux of boron ions for different hollow cathode voltages (800, 1000, 1200, 1400, 1800 and 2200 V) measured during the pulse-on period in a 20 mTorr, 500V BF₃ glow discharge with a 50 μs pulse width.....</i>	<i>253</i>
<i>Figure 185: Boron predicted depth profile for different hollow cathode voltages, during a 500 V, 20 mTorr PLAD implantation.....</i>	<i>254</i>
<i>Figure 186: (a) Cathode current for different pulsed anode voltages with a 500 V, 30 mTorr, 50μs, BF₃ plasma, (b) Ion ratios under the same plasma conditions for different pulsed anode voltages, ranging from 400 V to 1200 V.....</i>	<i>255</i>
<i>Figure 187: Boron ions, normalized to the total ion flux, reaching the cathode for a 500 V, 30 mTorr, 50μs BF₃ plasma under different pulsed anode voltages</i>	<i>256</i>
<i>Figure 188: Boron predicted depth profile, normalized to a 5.10¹⁴ dose, based on the measured IEDs for different pulsed anode voltages (500V, 30 mTorr BF₃ PLAD).....</i>	<i>257</i>
<i>Figure 189: Potential distribution at the entrance of the mass spectrometer tube with the original mass spectrometer configuration</i>	<i>295</i>
<i>Figure 190: Divergence angle of a 500 eV BF₂⁺ at the end of the mass spectrometer drift tube with the original mass spectrometer configuration.....</i>	<i>295</i>
<i>Figure 191: Potential distribution at the entrance of the mass spectrometer tube with the new mass spectrometer configuration.....</i>	<i>296</i>
<i>Figure 192: Divergence angle of a 500 eV BF₂⁺ at the end of the mass spectrometer drift tube with the new mass spectrometer configuration</i>	<i>296</i>
<i>Figure 193: PLAD modified chamber with the mass spectrometer installed in the center of the cathode and the cathode power supply unit</i>	<i>297</i>
<i>Figure 194: PLAD diagnostic test stand, which include a Langmuir probe, a mass spectrometer, an optical spectrometer, a fast data acquisition oscilloscope, a video camera to monitor the plasma and a manual loadlock</i>	<i>297</i>
<i>Figure 195: B⁺ and BF⁺ IED normalized to the total boron ion flux for different HC voltage (800, 1000, 1200, 1400, 1800 and 2200 V) for a 20 mTorr BF₃ glow discharge with a cathode bias at 500 V</i>	<i>301</i>

<i>Figure 196: BF_2^+ and BF_3^+ IED normalized to the total boron ion flux for different HC voltage (800, 1000, 1200, 1400, 1800 and 2200 V) for a 20 mTorr BF_3 glow discharge with a cathode bias at 500 V</i>	<i>302</i>
<i>Figure 197: B^+, BF^+, BF_2^+ and BF_3^+ IED normalized to the total boron ion flux for different pulsed-anode voltage (400, 600, 800, 1200 V) for a 30 mTorr BF_3 glow discharge with a cathode bias at 500 V.....</i>	<i>303</i>
<i>Figure 198: B^+, BF^+, BF_2^+ and BF_3^+ IED normalized to the total boron ion flux for different frequency (500, 1000, 1500, 2000, 2500 and 3000Hz) for a 40 mTorr BF_3 glow discharge with a cathode bias at 1 kV</i>	<i>304</i>

List of Tables

<i>Table 1: Key Ultra-Shallow Junction (USJ) doping requirements for CMOS [ITRS 2005]</i>	38
<i>Table 2: Boron equivalent energies and projected range of different molecular boron ions implanted with an energy of 10 keV</i>	40
<i>Table 3: Conversion factor for different gases for the cold cathode pressure gauge Pfeiffer Vacuum model TSF 012</i>	97
<i>Table 4: Ionization cross section at 70eV for different gases [Phelps]</i>	100
<i>Table 5: Principal direct elastic and inelastic electron scattering processes</i>	135
<i>Table 6: Principal indirect elastic and inelastic electron scattering processes</i>	136
<i>Table 7: Products of electron impact in BF₃ (g)</i>	139
<i>Table 8: Electron and ion plasma frequency, matrix sheath time length after the beginning of the pulse as a function of the plasma density</i>	150
<i>Table 9: Time necessary to establish the steady-state Child law sheath for different plasma density and cathode voltage</i>	152
<i>Table 10: Products of dissociation of fast molecular ion (AB⁺) by collision with the background gas (C) inside the high-voltage sheath [Suzuki 1986]</i>	156
<i>Table 11: 500V high pressure, s/λ calculated based on BF₂⁺ hard sphere model, s/λ measured with Davis and Vanderslice (VDS)</i>	187

Appendix 1a: Mass spectrometer old configuration

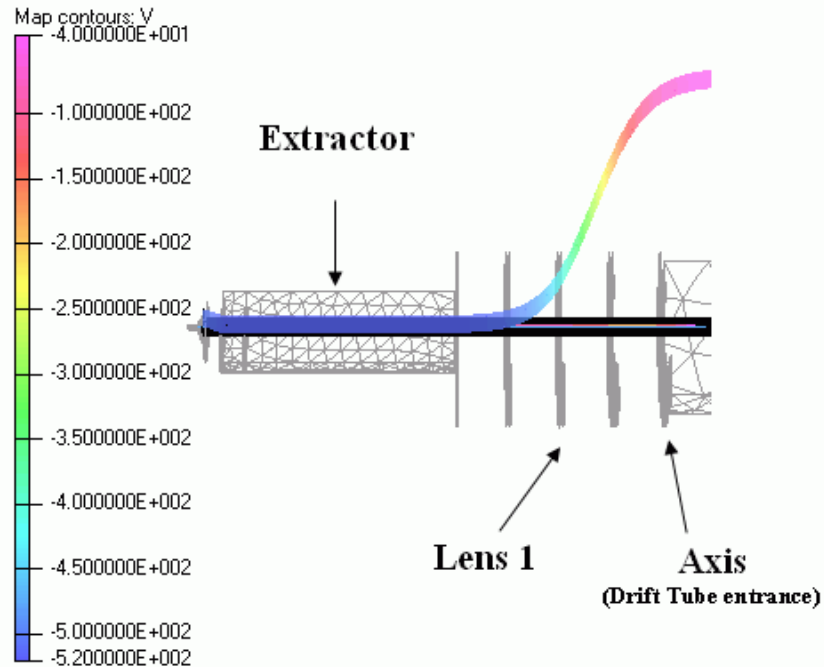


Figure 189: Potential distribution at the entrance of the mass spectrometer tube with the original mass spectrometer configuration

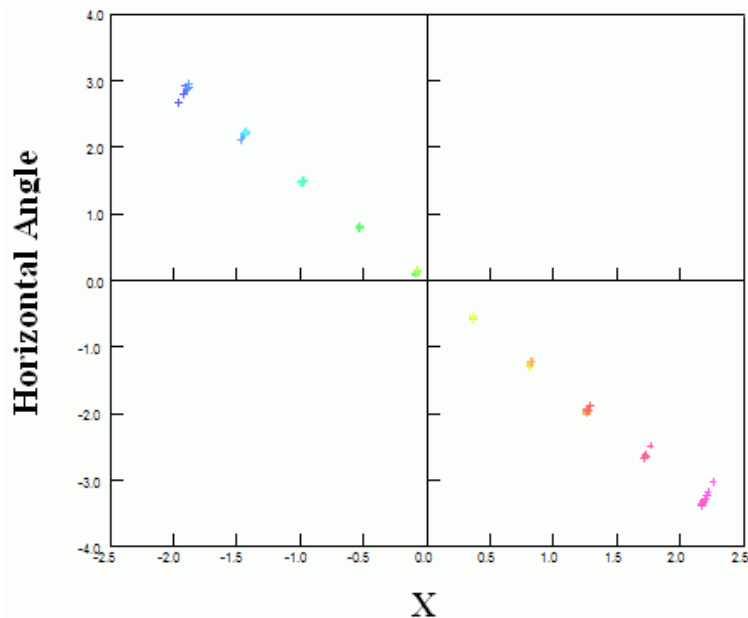


Figure 190: Divergence angle of a 500 eV BF_2^+ at the end of the mass spectrometer drift tube with the original mass spectrometer configuration

Appendix 1b: Mass spectrometer new configuration

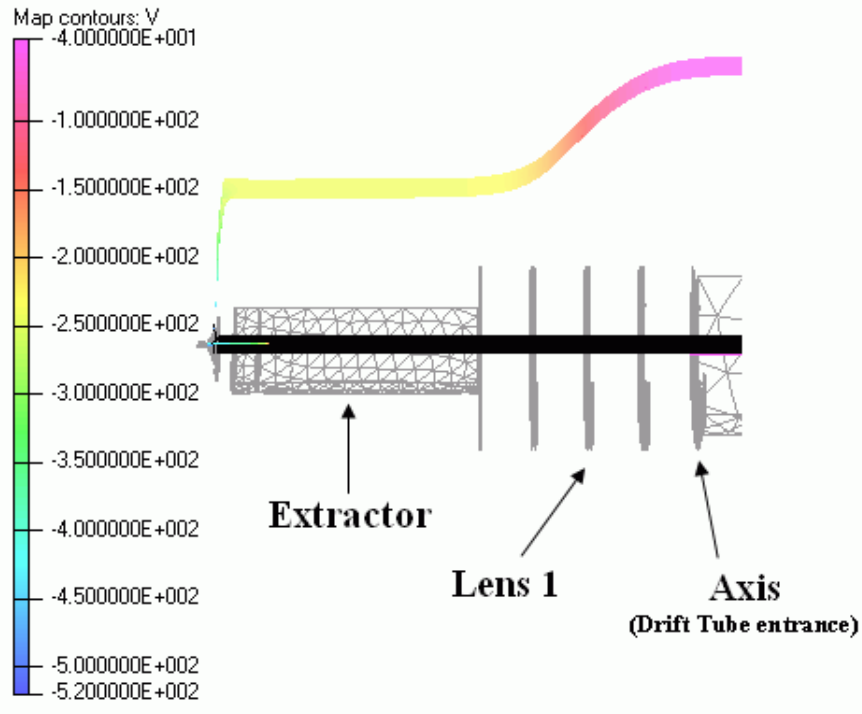


Figure 191: Potential distribution at the entrance of the mass spectrometer tube with the new mass spectrometer configuration

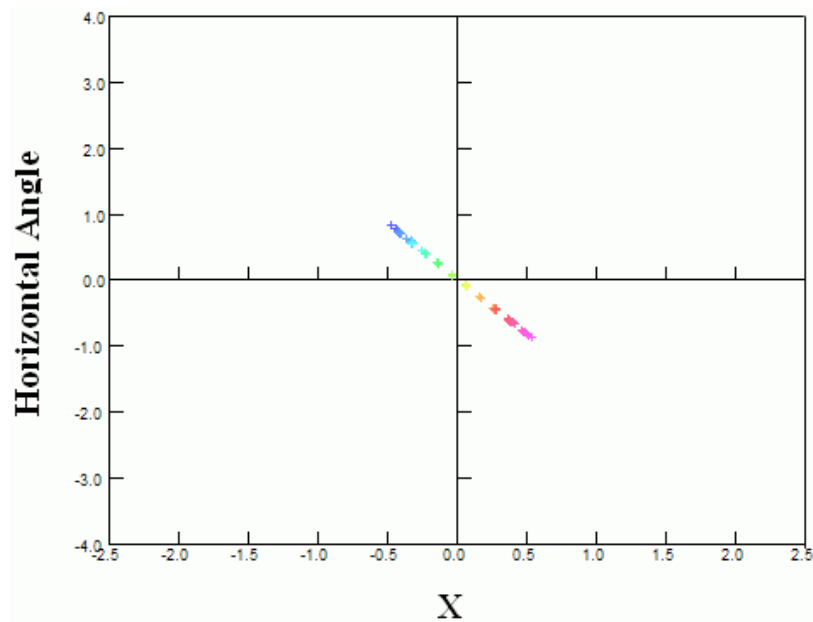


Figure 192: Divergence angle of a 500 eV BF_2^+ at the end of the mass spectrometer drift tube with the new mass spectrometer configuration

Appendix 2: PLAD chamber diagnostic

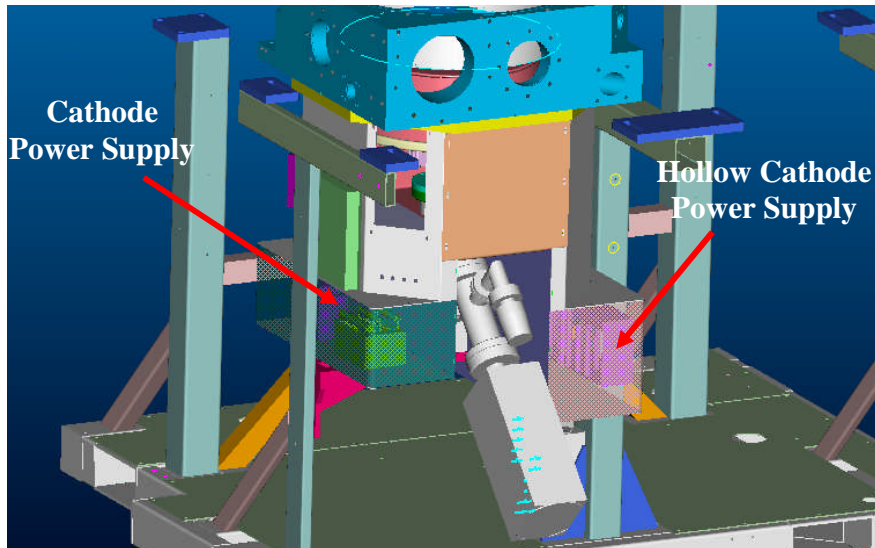


Figure 193: PLAD modified chamber with the mass spectrometer installed in the center of the cathode and the cathode power supply unit

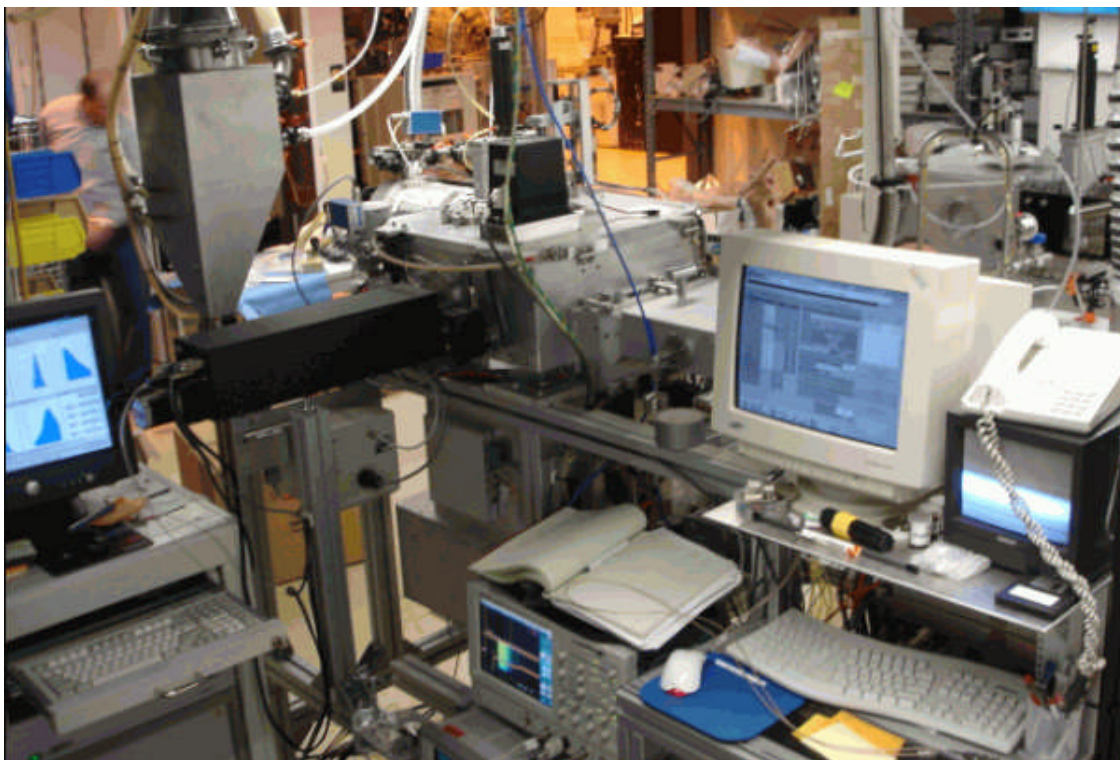


Figure 194: PLAD diagnostic test stand, which include a Langmuir probe, a mass spectrometer, an optical spectrometer, a fast data acquisition oscilloscope, a video camera to monitor the plasma and a manual loadlock

Appendix 3: Electron temperature calculation

(By the software SmartProbe [Smartsoft])

The total current I is assumed to be only the electron current I_e :

$$I \approx I_e = I(V_p) \times \exp\left(-\frac{e(V_p - V_b)}{kT_e}\right)$$

Then

$$\begin{aligned} \int_{V_f}^{V_p} I(V_b) dV_b &= I(V_p) \int_{V_f}^{V_p} \exp\left(-\frac{e(V_p - V_b)}{kT_e}\right) dV_b \\ &= I(V_p) \times \exp\left(-\frac{eV_p}{kT_e}\right) \times \frac{kT_e}{e} \times \left[\exp\left(\frac{eV_b}{kT_e}\right) \right]_{V_f}^{V_p} \\ &= I(V_p) \times \frac{kT_e}{e} \left(1 - \exp\left(-\frac{e(V_p - V_f)}{kT_e}\right) \right) \\ &= I(V_p) \times \frac{kT_e}{e} \times \left(1 - \frac{I(V_f)}{I(V_p)} \right) \end{aligned}$$

As $I(V_f) = 0$

$$\int_{V_f}^{V_p} I(V_b) dV_b = I(V_p) \times \frac{kT_e}{e}$$

Finally,

$$\frac{kT_e}{e} = \frac{\int_{V_f}^{V_p} I(V_b) dV_b}{I(V_p)}$$

Appendix 4: EEDF and EEPF calculation

(Based on Lieberman calculation [Lieberman 2005])

For an arbitrary distribution function, current in the retarding field $V_p - V_b > 0$ can be written as

$$I_e = eA_p \int_{-\infty}^{\infty} dv_x \int_{-\infty}^{\infty} dv_y \int_{v_{\min}}^{\infty} dv_z v_z f_e(v) \quad \{1\}$$

where $v_{\min} = \left[\frac{2e(V_p - V_b)}{m} \right]^{1/2}$ {2}

is the minimum velocity along z for an electron at the plasma-sheath edge to reach the probe. For an isotropic distribution, spherical polar coordinates in velocity can be introduced to obtain:

$$I_e = eA_p \int_{v_{\min}}^{\infty} dv \times \int_0^{\theta_{\min}} d\theta \times \int_0^{2\pi} d\phi \times v \times \cos\theta \times v^2 \sin\theta \times f_e(v) \quad \{3\}$$

Where A_p is the physical collecting area of the probe and where

$$\theta_{\min} = \cos^{-1}\left(\frac{v_{\min}}{v}\right) \quad \{4\}$$

The ϕ and θ integration are easily done, yielding

$$I_e = \pi e A_p \int_{v_{\min}}^{\infty} v^3 \times \left(1 - \frac{v_{\min}^2}{v^2}\right) \times f_e(v) dv \quad \{5\}$$

Introducing the changing of variable $\varepsilon = \frac{1}{2} \frac{mv^2}{e}$, {5} becomes

$$I_e = \frac{2\pi e^3 A_p}{m^2} \int_V^{\infty} \varepsilon \times \left[\left(1 - \frac{V}{\varepsilon}\right) \times f_e[v(\varepsilon)] \right] \times d\varepsilon \quad \{6\}$$

Where $v(\varepsilon) = (2e\varepsilon/m)^{1/2}$. Differentiating twice I_e we obtain:

$$\frac{d^2 I_e}{dV^2} = \frac{2\pi e^3}{m^2} A_p f_e[v(V)] \quad \{7\}$$

It is usual to introduce the electron energy distribution function (EEDF) $g_e(\varepsilon)$ by

$$g_e(\varepsilon) d\varepsilon = 4\pi v^2 f_e(v) dv \quad \{8\}$$

Using the relation between ε and v , we find

$$g_e(\varepsilon) = 2\pi \left(\frac{2e}{m}\right)^{3/2} \varepsilon^{1/2} f_e[v(\varepsilon)] \quad \{9\}$$

Using this to eliminate f_e from {7}, we obtain

$$g_e(V) = \frac{2m}{e^2 A_p} \left(\frac{2eV}{m}\right)^{1/2} \frac{d^2 I_e}{dV^2} \quad \{10\}$$

which gives $g_e(V)$ directly in terms of the measured value of $d^2 I/dV^2$. The electron probability function (EPPF) $g_p(\varepsilon) = \varepsilon^{-1/2} g_e(\varepsilon)$ is sometimes introduced instead.

Appendix 5: IED for different HC voltage 20mTorr with 500 V cathode bias

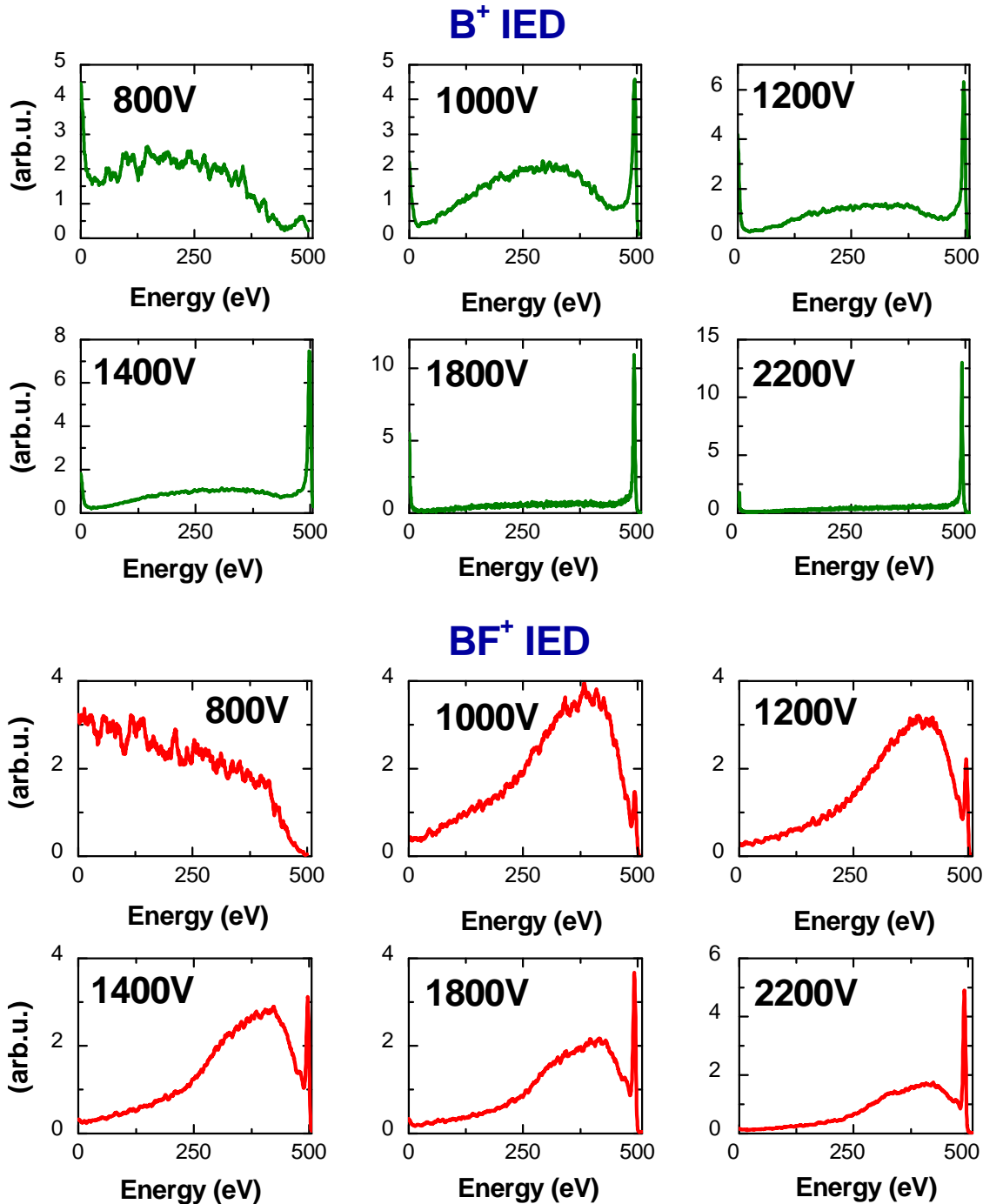


Figure 195: B⁺ and BF⁺ IED normalized to the total boron ion flux for different HC voltage (800, 1000, 1200, 1400, 1800 and 2200 V) for a 20 mTorr BF₃ glow discharge with a cathode bias at 500 V

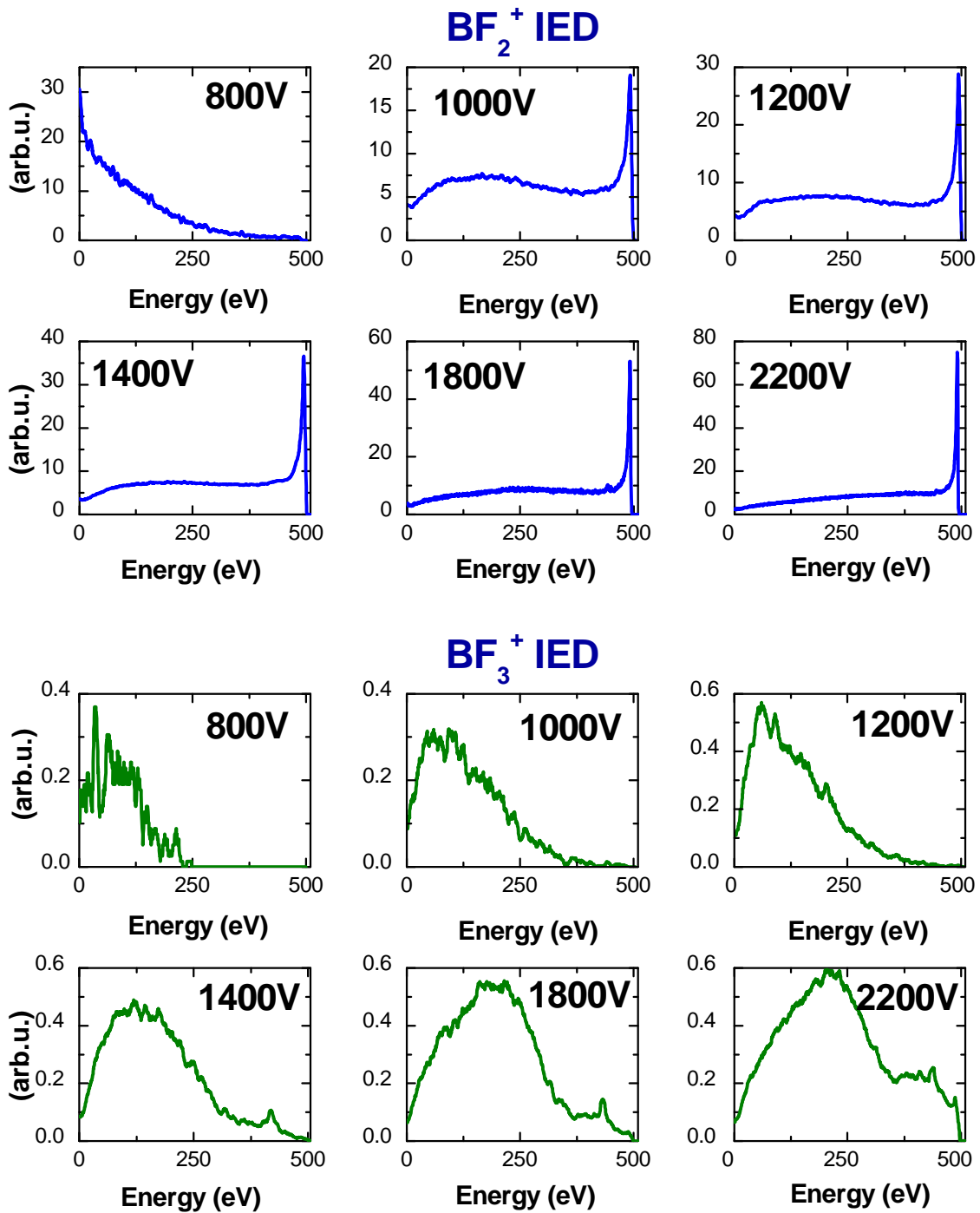


Figure 196: BF_2^+ and BF_3^+ IED normalized to the total boron ion flux for different HC voltage (800, 1000, 1200, 1400, 1800 and 2200 V) for a 20 mTorr BF_3 glow discharge with a cathode bias at 500 V

Appendix 6: Pulsed anode voltage variation

500V 30 mTorr BF_3 2500 Hz, 50 μs

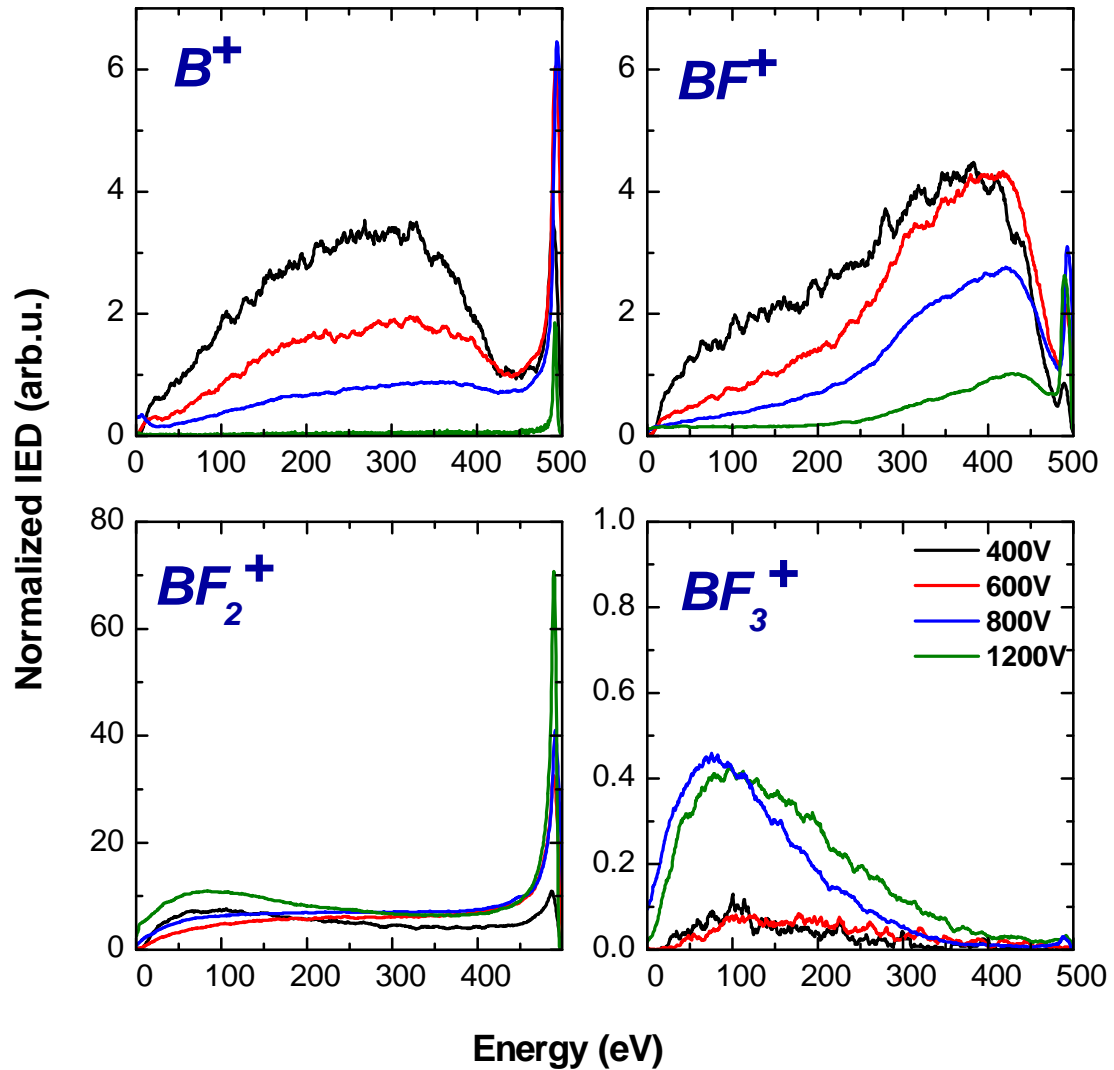


Figure 197: B^+ , BF^+ , BF_2^+ and BF_3^+ IED normalized to the total boron ion flux for different pulsed-anode voltage (400, 600, 800, 1200 V) for a 30 mTorr BF_3 glow discharge with a cathode bias at 500 V

Appendix 7: 1kV no HC Frequency Variation

(1kV 40mTorr 50 μ s 10scm)

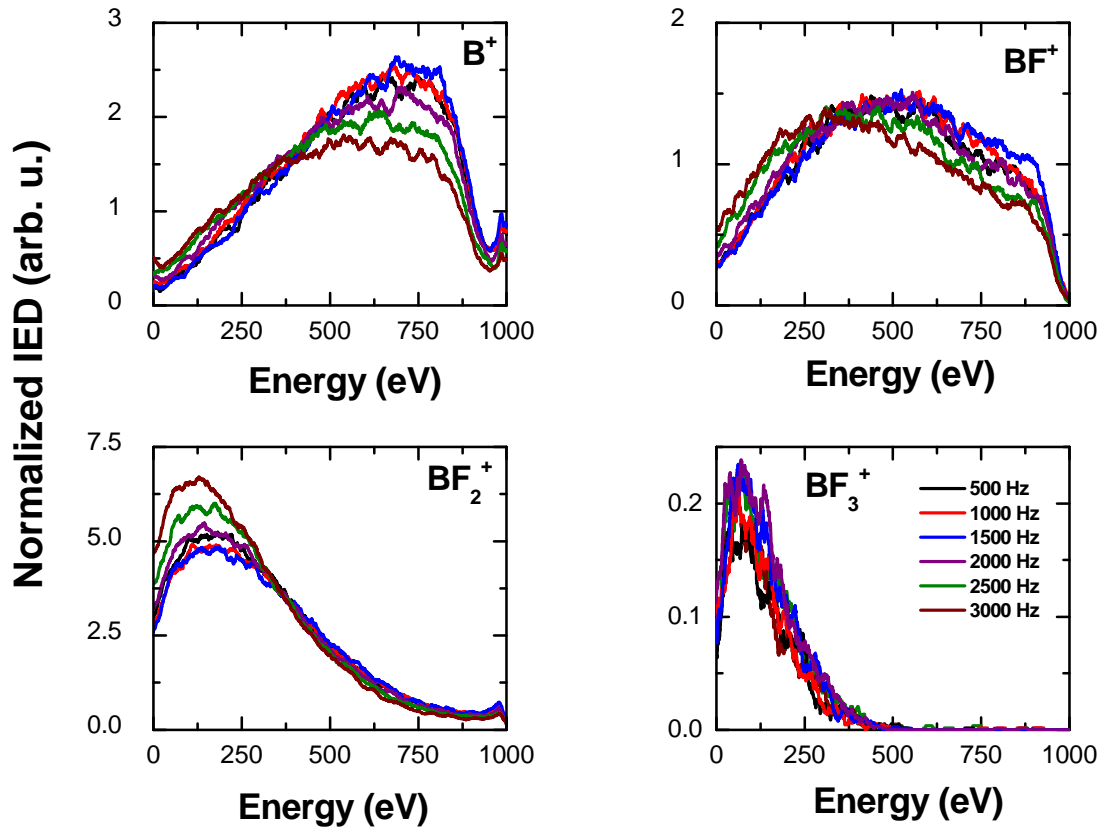


Figure 198: B^+ , BF^+ , BF_2^+ and BF_3^+ IED normalized to the total boron ion flux for different frequency (500, 1000, 1500, 2000, 2500 and 3000Hz) for a 40 mTorr BF_3 glow discharge with a cathode bias at 1 kV